UNIVERSITY OF OXFORD

Topochemical Synthesis of Novel Electronic Materials

Fabio Denis Romero

Wadham College

Michaelmas Term 2013

A thesis submitted to the Board of the Faculty of Physical Sciences in partial fulfilment of the requirements for the degree of Doctor of Philosophy

Topochemical Manipulation of Some Complex Oxides

This investigation is based on the topochemical modification of three set of phases: $Sr_3Co_2O_5Cl_2$, $SrO(Sr(Ru_{0.5}M_{0.5})O_3)_n$ (M = Ti, Mn, Fe; n = 1, 2, ∞), and $SrO(SrVO_3)_n$ (n = 1, 2, ∞).

The topochemical reduction of $Sr_3Co_2O_5Cl_2$ using sodium hydride as a solid state reducing agent results in the formation of a reduced phase containing cobalt centres with an average oxidation state of +2 and an overall composition of $Sr_3Co_2O_4Cl_2$. The resulting material adopts a structure containing double sheets of square-planar corner-sharing CoO_2 units separated by rock salt SrCl layers. Variable-temperature diffraction measurements reveal that these sheets undergo a cooperative Jahn-Teller distortion at T ~ 200 K due to unevenly filled degenerate (d_{xy}, d_{yz}) orbitals. This material adopts a magnetic structure in which the moments within each sheet are ordered antiferromagnetically, but the sheets are aligned ferromagnetically.

An investigation was carried on the reduction behaviour of Ru-doped $Sr(Ru_xFe_{1-x})O_3$. It was found that the reduction was non-topochemical for values of $x > 0.5$. For values of $0 < x < 0.5$, no single phase precursor material could be formed. For the material with $x = 0.5$, reduction with CaH_2 produced a new phase with composition $Sr(Ru_{0.5}Fe_{0.5})O_2$. This material is the first reported instance of Ru^{2+} in an extended transition metal oxide. DFT calculations reveal that, while the iron centres adopt a high-spin configuration, the ruthenium centres are in an intermediate-spin S = 1 configuration. Resulting competing magnetic interactions lead to frustration and lack of ordering.

In order to further study the reduction behaviour of extended transition metal oxides containing ruthenium, the reduction of $Sr_2(Ru_{0.5}Fe_{0.5})O_4$ and $Sr_3(Ru_{0.5}Fe_{0.5})_2O_7$ was performed using CaH_2 as a solid state reducing agent. In these cases, reduction leads to segregation of the materials into multiple phases adopting closely related structures that differ mainly in their oxygen content. In these materials, the ruthenium centres are preferentially reduced, such that starting from materials containing Ru^{5+} and Fe^{3+}, materials containing $Ru^{(3-\delta)+}$ and Fe^{3+} are produced.

Similarly, the low-temperature oxidation using CuF_2 as a solid state fluoride source was performed on materials with composition $Sr_3(Ru_{0.5}M_{0.5})_2O_7$ (M = Ti, Mn, Fe). In the case of M = Mn and Ti, materials with composition $Sr_3(Ru_{0.5}M_{0.5})_2O_7F_2$ are produced in which the ruthenium centres are oxidised to Ru^{6+}. For the M = Fe material, oxidation results in partial exchange of O for F and a material with composition $Sr_3(Ru_{0.5}Fe_{0.5})_2O_{5.5}F_{3.5}$ in which the ruthenium centres are oxidised from +5 to +5.5 while the iron centres remain in a +3 oxidation state. While fluorination of the M = Ti leads to increasing itinerant electronic behaviour, fluorination of the M = Mn and Fe materials induces a twisting of the MX_6 octahedra that enables magnetic order to emerge at low temperatures.

Finally, reaction of the $SrO(SrVO_3)_n$ (n = 1, 2, ∞) series of phases with CaH_2 results in the formation of phases with composition $SrO(SrVO_2H)_n$ (n = 1, 2, ∞), the first examples of stoichiometric oxyhydride materials. $SrVO_2H$ is magnetically ordered at room temperature, while the n = 1 and n = 2 materials order at 170 K and 240 K respectively. The high magnetic ordering temperature arises from strong interactions between (d_{xy}, d_{yz}) orbitals in a manner analogous to the reduced iron-containing phases $SrO(SrFeO_2)_n$.

Declaration

The work described in this thesis was carried out at the Inorganic Chemistry Laboratory at the University of Oxford between October 2010 and November 2013 under the supervision of Dr. Michael A. Hayward. All the work presented herein is my own except where I have either acknowledged help from a named person or given reference to a published source, and has not been submitted by the author for any other degree at any other university.

Fabio Denis Romero

November 2013

For everyone who ever believed in me.

Acknowledgements

First of all, I would like to thank my supervisor, **Dr. Michael Hayward**, for his inexhaustible passion and knowledge. I tried my best to soak up as much as I could. I need to thank the various researchers whom I collaborated with: **Prof. Paul A. Bingham** and **Dr. Susan D. Forder** for Mössbauer spectroscopy data, **Prof. Stephen Blundell**, **Francesca Foronda**, and **Dr. Johannes Moeller** who collected μSR data despite near constant beam stoppages, **Dr. Diego Gianolio** and **Dr. Gianantonio Cibin** for XANES data. All of the beam scientists and technicians at ISIS, Diamond and the ILL; especially **Dr. Ron Smith** and **Dr. Emma Suard**.

I would also like to thank **Dr. Edward Dixon**, for teaching me all I know and more about working in a lab. **Dr. Kun Luo** for company during long summers. **Miss Midori Amano** for taking a lot of the burden from me when I needed it. I also need to thank all the other members of the group over the years, too many to list.

I owe a great debt to my parents for giving me the opportunity to study, and allowing to pursue my goals.

Last but not least, I would like to thank **Mrs. Newman**, my high school chemistry teacher, for opening my eyes to the wonders of the natural world. I haven't closed them since.

Table of Contents

Chapter 1 Introduction

1.1 Complex Metal Oxides

Complex transition metal oxides are an important class of materials due to the wide range of electronic, magnetic, dielectric, and transport properties they exhibit.[1,2] In these materials, unpaired electrons in the transition metal *d*-orbitals can couple to each other either via direct-exchange mechanisms, or via super exchange interactions involving the oxygen *p*-orbitals.[3] Many of these interesting and technologically useful properties are the result of electron-electron and electron-lattice correlations and couplings. These lead to materials with a wide range of applications in areas such as catalysis,[4] energy storage,[5] and information processing.[6]

Of particular interest are materials adopting the perovskite structure with the general formula ABO_3, where A is a Group I or Group II metal or a lanthanide, and B is a transition metal. The mineral perovskite, $CaTiO_3$, is composed of an infinite three-dimensional network of vertex-sharing TiO_6 octahedra. In this material, the size mismatch between the constituent cations leads to a cooperative twisting of the TiO_6 octahedra, and consequent distortion away from perfect cubic symmetry and 180 ° B–O–B bond angles.[7] $SrTiO_3$, on the other hand, adopts the same structure, but in this case the sizes of the cations allow for perfect 180 ° bond angles B–O–B as shown in Figure 1.1 (a).[8]

The cooperative distortion in certain materials adopting the perovskite structure occurs in order to compensate for the mismatch in size between the constituent cations, which can be quantified using the Goldschmidt tolerance factor:[9]

$$t = \frac{< A - O >}{\sqrt{2} < B - O >}$$

Where $< A - O >$ and $< B - O >$ refer to the A–O and B–O bond lengths respectively. When $t = 1$, as in $SrTiO_3$, the structure adopts perfect cubic symmetry. If $t < 1$, a cooperative distortion arises, resulting in a deviation from perfect cubic symmetry and a subsequent decrease of the B–O–B angles to less than 180 °. If $t > 1$, on the other hand, the structure will crystallise in a hexagonal space group.[10]

The extended 3-dimensional transition-metal-oxide network in materials adopting the perovskite structure permits partially occupied *d*-states in transition metals to couple to each other strongly through superexchange mechanisms and orbital overlap, and gives rise to a wide range of resulting electronic properties.

Furthermore, the flexibility of the perovskite structure allows for tuning of the electronic properties. Deviations of B–O–B angles from 180 ° will reduce the orbital overlap, and consequently the interactions between transition metal cations. Control of the tolerance factor *t* therefore allows for some measure of control over the properties of the resulting materials.

Related to the perovskite structure, materials adopting the Ruddlesden-Popper structures typified by Sr_2TiO_4 and $Sr_3Ti_2O_7$ (Figure 1.1 (c) and (d)), are of similar interest due to the similar extended transition metal oxide network. These structures can be described by the general formula $AO(ABO_3)_n$, of which the perovskite is the $n = \infty$ end member.

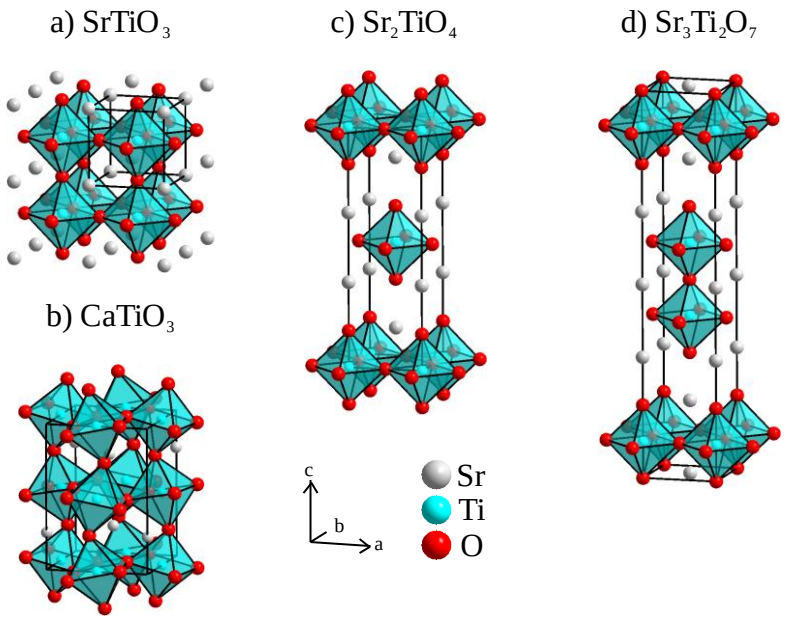

Figure 1.1 The structures of the perovskites $SrTiO_3$ (a) and $CaTiO_3$ (b), and the Ruddlesden-Popper Sr_2TiO_4 (c) and $Sr_3Ti_2O_7$ (d).

The behaviour of materials adopting these structures is strongly dependent on the metal oxygen framework. Consequently, this behaviour is strongly influenced by the transition metal oxidation state and coordination environment, which define the local transition metal electronic configuration, and the long-range connectivity, which influences the nature and strength of the interactions between centres. Control of these factors and understanding of the resulting behaviour would therefore enable materials synthesis by design.

1.2 The Hubbard Model

In many extended solids, the overlap of orbitals can be approximated by the formation of crystal orbitals that extend throughout the solid. With enough orbitals, the energy difference between them can be neglected, and can be thought of as forming continuous bands of energy levels. (Figure 1.2)

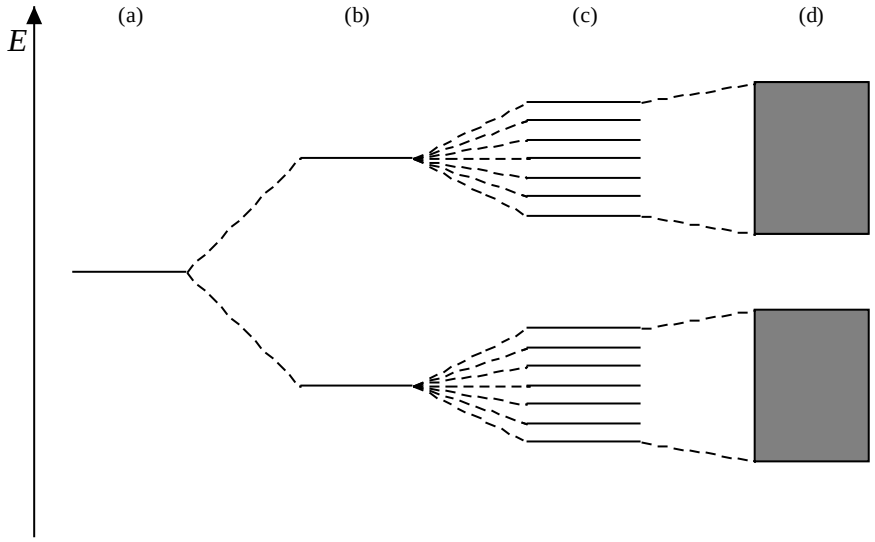

Figure 1.2: Orbital energies of (a) an atom, (b) a small molecule, (c) a large molecule, (d) a solid.

A partially occupied band can give rise to metallic conductivity as unpaired electrons near the Fermi level move into orbitals where they give rise to a net motion of charge in the solid, such that an electric current flows.

Many transition metal compounds, such as NiO or CoO, are not metallic, despite appearing to have partially filled *d*-bands.[11] When the inter-atomic overlap is small, such that only narrow bands are formed, electron-electron repulsion becomes much more important. In these compounds, standard band theory does not work, and the electrons are localised by their mutual repulsion.

The Hubbard model provides a useful approach to understanding the nature of the electronic behaviour of transition metal compounds, usually written down in the form:

$$H = -t \sum_{(i,j)\sigma} (c_{i,\sigma}^{\dagger} c_{j,\sigma} + h.c.) + U \sum_{i=1}^{N} n_{i\uparrow} n_{i\downarrow}$$

For a one-band system (one orbital per site). (i, j) represent nearest neighbour interactions on the lattice. *t* corresponds to the kinetic energy of electrons hopping between atoms, and favours itinerant electrons.

U, the repulsion energy between two electrons on the same atom can be thought of as the difference between the ionisation energy and the electron affinity. That is to say, the difference between the energy required to remove an electron from one atom and adding it to its neighbour. This term describes the Coulomb repulsion between electrons. In the Hubbard model, it is assumed to be the only interaction between electrons.

The Hubbard model thus describes the competition between chemical bonding (*t*) favouring itinerant electrons and short range on-site Coulomb repulsion (*U*). Once the energy scales have been extracted, a dimensionless ratio of t/U can be used to determine which of the chemical bonding or repulsion forces is strongest.

On-site repulsion will force electron transfer from atom to its neighbour to be accompanied by an energy penalty *U*. This in turn leads to the formation of sub-bands separated by a Mott-Hubbard gap *U*, making half-filled bands insulating when the overlap is small (Figure 1.3).

As the interatomic overlap increases, and the sub-bands become broader, they will meet when the width *W* and the repulsion parameter *U* are approximately equal. Beyond this point, there is no energy gap and the solid is metallic (Figure 1.3).[11] Simplistic band theory is thus a case in which $W > U$.

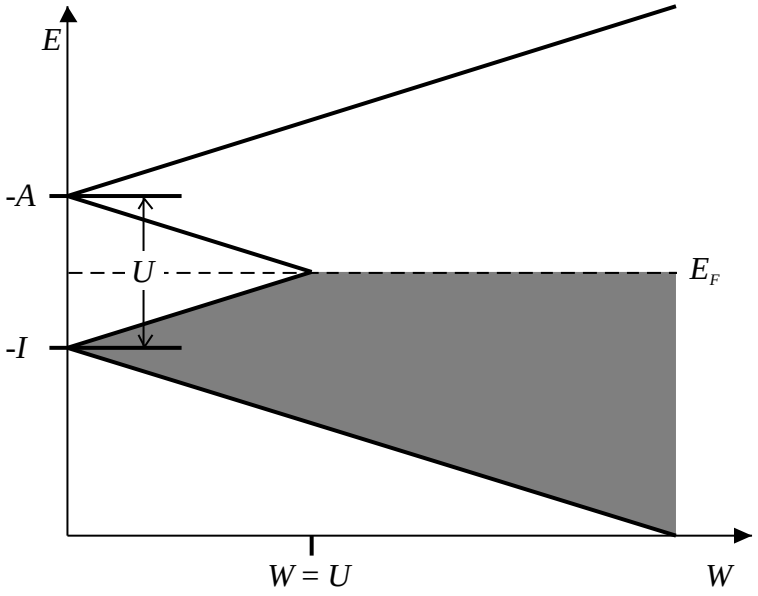

Figure 1.3: Hubbard sub-bands as a function of band width *W*.

However, materials with $U \approx W$ are of particular interest. The competition between forces that favour localisation such as the on-site repulsion, and those that favour delocalisation such as the band width, often result in the system adopting a so-called 'third option' in order to satisfy it various energetic requirements. For example, the ferromagnetic behaviour of elemental iron, cobalt, and nickel, or the onset of superconductivity in the cuprate superconductors.[12,13] Thus, tuning the electronic behaviour of materials around this point and achieving control over the properties represents an important goal in solid-state synthesis by design.

1.3 Topochemical Manipulation

Complex metal oxides are traditionally synthesised using high-temperature methods in order to overcome the high energetic barriers to ion diffusion in the solid state. Invariably, this results in the formation of thermodynamically stable materials as the ions adopt positions so as to minimise the free energy of the system. As a result, only a small fraction of possible oxidation state and coordination environment combinations are available for study. The study

of structure-property relations is necessarily limited by the phases that it is possible to synthesise. Consequently, the development of reactions that operate at low temperatures under 'kinetic' conditions is necessary to enable the preparation of a wide range of metastable phases that cannot be prepared using traditional synthesis techniques.

Such kinetically controlled reactions take advantage of the differing reactivities within systems. One of the most useful ones is the greater mobility of anions compared to cations at relatively low temperatures. This allows reactions that modify the anion sublattice while leaving the cation sublattice intact.

One of the prime examples of this type of reaction is topochemical reduction using binary metal hydrides, such as the reduction of $LaNiO_3$ to form $LaNiO_2$ (Figure 1.4).[14] Oxide ions are removed from a suitable manner in a topochemical fashion. The cation framework remains intact. In order to maintain charge neutrality, the transition metal centres are reduced.

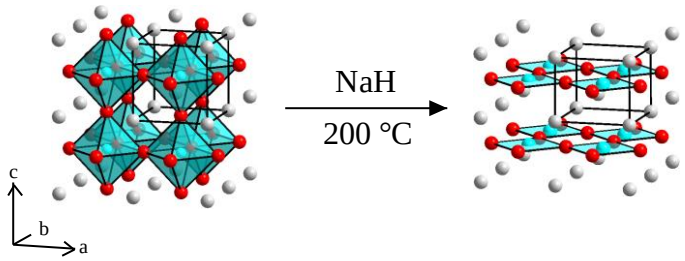

Figure 1.4: The reduction of $LaNiO_3$ to form $LaNiO_2$ using sodium hydride.

1.4 Hydride Reduction

Topochemical reduction of complex transition metal oxides using binary metal hydrides has been used to prepare a range of novel reduced phases containing the latter first-row transition metals (Mn, Fe, Co, Ni) in unusual oxidation states and/or coordination environments, such as square-planar Ni^{I} and Co^{I} and octahedral Mn^{I}.[14-16]

In order to be able to carry out topochemical reduction in a directed fashion to achieve target phases, it is important to understand the factors influencing selectivity of anion deintercalation. One strategy involves the strong interaction between the anion and cation lattices to exert control over the reduction behaviour of complex transition metal oxides. For example, the reduction of the isostructural and isoelectronic phases $YBaCo_2O_5$ and $LaBaCo_2O_5$ with NaH proceed to form markedly different products due solely to the directing behaviour of the A-cation identity (Figure 1.5).[16]

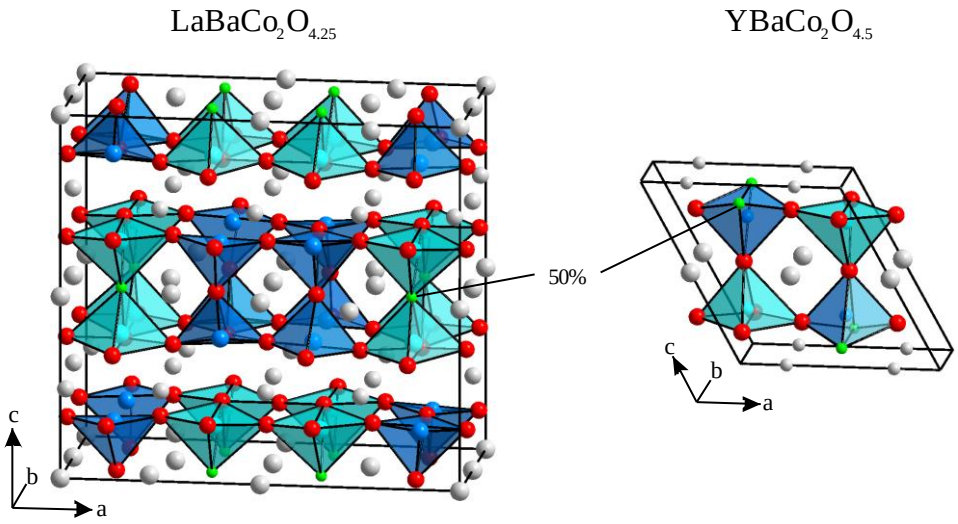

Figure 1.5: The structures of the topochemically reduced phases $LaBaCo_2O_{4.25}$ (left) and $YBaCo_2O_{4.5}$ (right).

Similarly, the nature of the B-cation can influence the selectivity of the topochemical reduction reactions. For instance, the *n*= 2 Ruddlesden-Popper phases $Sr_3Mn_2O_{7-\delta}$ and $Sr_3Fe_2O_{7-\delta}$ can be topochemically reduced to form phases with composition $Sr_3Mn_2O_{6+\delta}$ and $Sr_3Fe_2O_6$. In the manganese-containing phases, the oxide ions are removed from the equatorial sites, whereas in the iron case, they are removed from the bridging apical sites (Figure 1.6).[17,18]

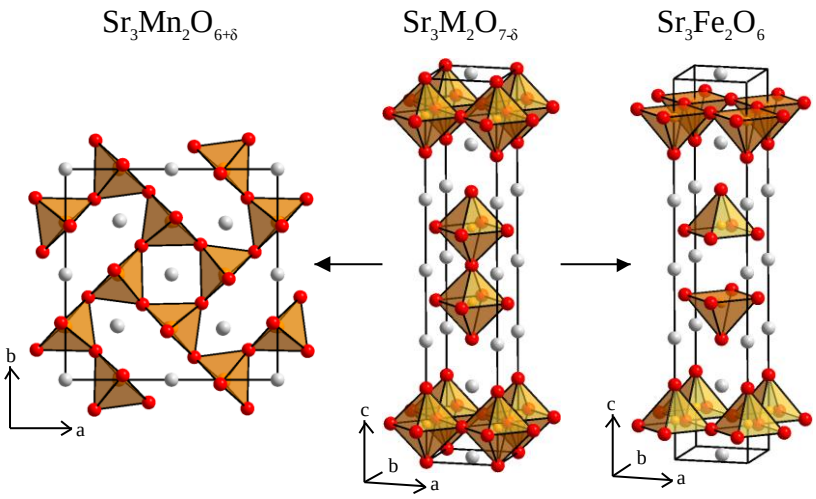

Figure 1.6: The structure of the *n* = 2 Ruddlesden-Popper phases $Sr_3M_2O_7$ (M = Mn, Fe) and their anion-deficient analogues.

Furthermore, the presence of heteroanions affords another way in which to exert control over the selectivity of these reactions. Reduction of the *n*= 2 Ruddlesden-Popper phase $Sr_3Fe_2O_{7-\delta}$ with CaH_2 can be performed to form a phase with composition $Sr_3Fe_2O_5$ (via the formation of $Sr_3Fe_2O_6$) containing double chains of square-planar $Fe^{II}O_4$ units (Figure 1.7).[19] The oxychloride $Sr_3Fe_2O_5Cl_2$, in which the outer apical oxide ions are replaced by chloride ions, can be reduced with LiH to form $Sr_3Fe_2O_4Cl$, a phase containing double infinite layers of square-planar $Fe^{II}O_4$ (Figure 1.7).[20]

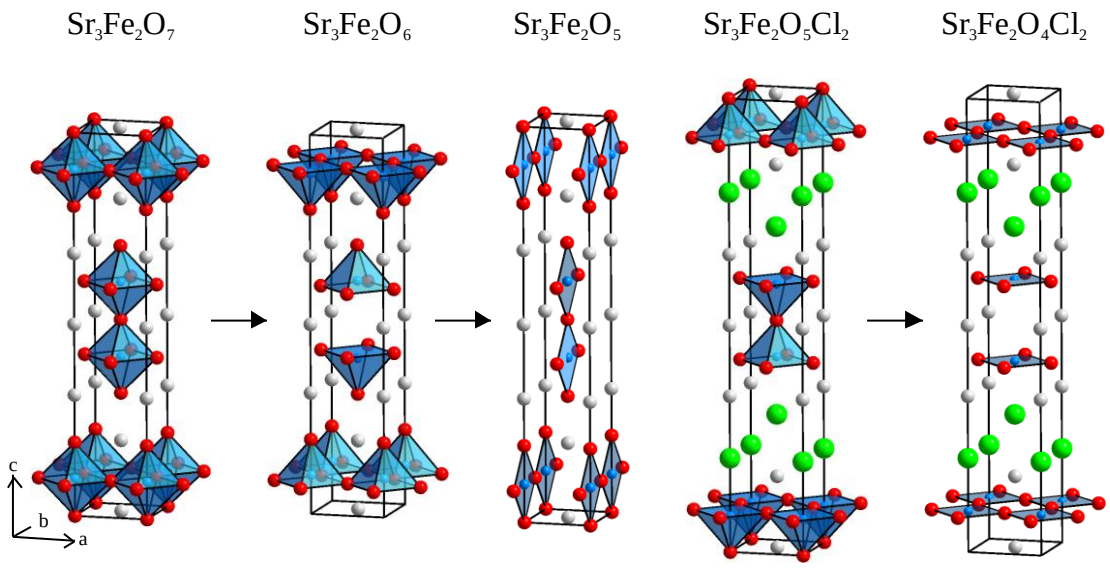

Figure 1.7: Structures of some iron-based *n* = 2 Ruddlesden-Popper phases and their anion-deficient analogues.

It has been shown that $Sr_3Fe_2O_5Cl_2$ can be doped with up to 50% cobalt without altering the selectivity of the reduction reaction. The resulting material is magnetically frustrated.[21] In order to further understand the selectivity and the behaviour of the resulting material, $Sr_3Co_2O_5Cl_2$ was synthesised and reduced using sodium hydride.

1.5 Electronic Behaviour of Reduced Phases

Reduction of first-row transition metal oxides will tend to lead to insulating behaviour for two reasons:

- As electrons are introduced into the systems, the on-site repulsion *U* will tend to increase due to greater repulsion between electrons, leading to more insulating behaviour.[22]
- As transition metals are reduced, their ionic radius will increase. Since the reactions are topochemical, this can induce a twisting of the bonds (lowering of the tolerance factor *t*) and a consequent decrease in the band width *W*.[11]

In addition, the introduction of anion vacancies in complex metal oxides serves to pin charges via two different mechanisms: the partial positive charge due to a vacant anion site can serve to trap electrons, and the presence of multiple cation coordination environments can serve to segregate charge due to the preference of certain cations and oxidation states for particular coordination environments. This can be seen in the electronic behaviour of some manganese-containing perovskites: $CaMnO_3$ and the reduced materials $CaMnO_{3-x}$ ($0 < x \leq 0.5$) are insulators.[23,24] It is, however, possible to prepare isoelectronic analogues with the general formula $Ca_{1-y}La_yMnO_3$ by doping with lanthanum on the A-site, and these materials are metallic for $0.17 \leq y \leq 0.5$.[25]

Many interesting electronic properties of complex transition metal oxides are due to the competition between several stabilising effects when U ≈ W. For example, Sr_2RuO_4 has been shown to be close to antiferromagnetic, ferromagnetic, and superconducting instabilities, and is the only known *p*-type superconductor with a $T_c \sim 1.5$ K.[26] Given the increase in U associated with lowering transition metal oxidation states, the reduction of 4*d* and early 3*d* was thought to be especially conducive to phases exhibiting these competing interactions and associated correlated electronic behaviour.

The larger orbitals present in 4*d* and early 3*d* transition metals will lead to smaller values of *U*, and the better overlap will lead to an increase in the width of the bands.[11] For instance, TiO and VO display metallic behaviour, while MnO and FeO are insulators.[27] Similarly, $SrFeO_3$ and $SrMnO_3$ are insulating, while $SrRuO_3$ displays metallic behaviour.[28]

Furthermore, the electronic behaviour of complex 4*d* transition metal oxides is strongly influenced by even very small changes in structure. This leads to the observation of a wide range of electronic properties in structurally related systems. For example, Sr_2RuO_4 is the only known *p*-type superconductor, with a rigidly tetragonal structure in which the Ru–O–Ru

angles are 180 ° (Figure 1.8).[29,30] Ca_2RuO_4, on the other hand, in which the bond angles deviate from 180 ° due to tilting of the RuO_6 octahedra, is a Mott insulator (Figure 1.8).[31] Sr_2IrO_4, in which twisting of the octahedral also leads to deviation from perfect 180 ° Ir–O–Ir bond angles, is also an insulator (Figure 1.8).[30,32] The solid solution $Sr_2Ru_xIr_{1-x}O_4$ displays a metal-insulator itinerant-localised transition at $x = 0.7$.[33]

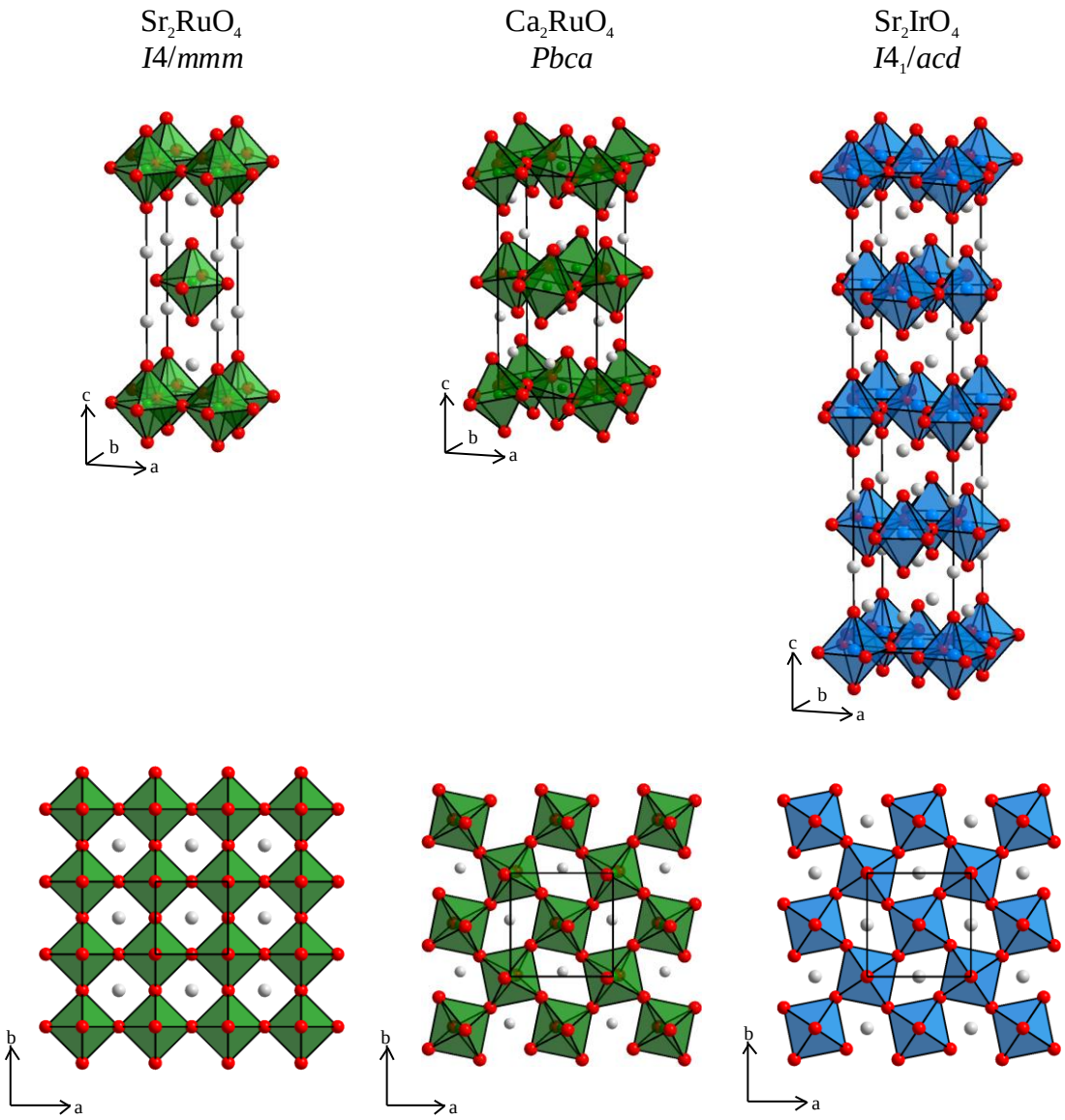

Figure 1.8: Structures of Sr_2RuO_4 (left), Ca_2RuO_4 (middle), and Sr_2IrO_4 (right)

The interesting electronic and magnetic properties of complex 4*d* transition metal oxides and their tunability makes these materials ideal for synthesis by design. In order to investigate the reduction behaviour and resulting properties of these materials, the reduction of the pervoskite $SrRuO_3$ and the $n = 1$ and $n = 2$ Ruddlesden-Popper phases Sr_2RuO_4 and $Sr_3Ru_2O_7$ was attempted, as well as the reduction of the iron-containing solid solutions $SrO(Sr(Ru_{1-x}Fe_x)O_3)_n$ ($n = 1, 2, \infty$).

Similarly, in order to investigate the reduction behaviour of early 3*d* complex transition metal oxides and the resulting electronic and magnetic properties, the reduction of the vanadium-containing $SrO(SrVO_3)_n$ ($n = 1, 2, \infty$) materials was attempted.

1.6 Topochemical Fluorination

Another method to prepare phases containing novel combinations of transition metal oxidation states and coordination environments involves topochemical fluorination of transition metal oxides to form oxyfluorides. Fluorination of complex oxides can result in either: 1. the insertion of fluorine into interstitial sites (oxidative); 2. the incorporation of two fluorines for each oxygen lost (redox neutral); or 3. the substitution of one fluorine for one oxygen (reductive).[34] Fluorination of a generic A_2BO_4 Ruddlesden-Popper phase using a fluorine source can be described as follows:

$$A_2BO_4 + 1/2F_2 \rightarrow A_2BO_4F \quad (1)$$

$$A_2BO_4 + F_2 \rightarrow A_2BO_3F_2 + 1/2O_2 \quad (2)$$

$$A_2BO_4 + 1/2F_2 \rightarrow A_2BO_3F + 1/2O_2 \quad (3)$$

Fluorinating agents for these reactions can be either fluorine gas[35] (undesirable due to its toxic nature) or solid-state fluorides such as NH_4F[36] or MF_2 (M = Cu, Zn, Ni, Ag) in the presence of oxygen[37]. While the use of F_2 gas favours insertion, a substitution of O for F is more prevalent for reactions with NH_4F which appear to proceed via the incorporation of HF

followed by loss of H_2O.[38] A combination of the processes has been reported for reactions involving MF_2 solid-state reagents.[34]

Of particular interest is the topochemical fluorination of Ruddlesden-Popper phases, where fluoride can be oxidatively intercalated in tetrahedral sites between the layers, far from the transition metal coordination environment (Figure 1.9). This allows the oxidation of the transition metals without altering their local environment, allowing the electronic behaviour to be tuned solely by changing the oxidation state, rather than both as in the case of reduction using binary metal hydrides.

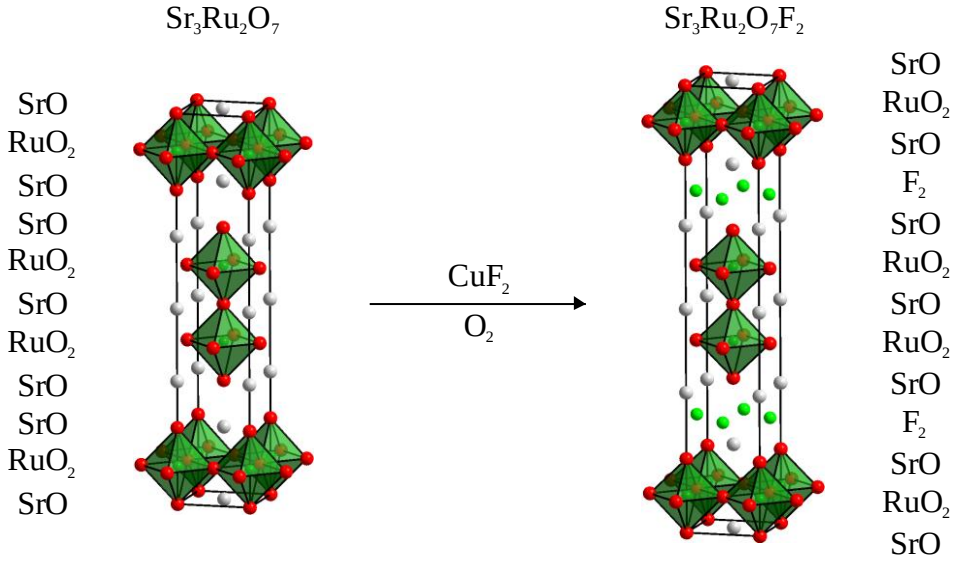

Figure 1.9: The fluorination of $Sr_3Ru_2O_7$ to form $Sr_3Ru_2O_7F_2$.[39]

This approach is attractive as removing electrons from the transition metal centres will lower the on-site repulsion *U*, leading to more metallic behaviour.[11]

Previous work has shown that the topochemical fluorination in this manner of $Sr_3Ru_2O_7$ produces $Sr_3Ru_2O_7F_2$, a phase in which the RuO_6 octahedra are twisted relative to each other, leading to Ru–O–Ru bond angles of 158.1 ° and 154.1 °. This decreases the overlap, and

consequently the band width, leads to localised electronic behaviour in the fluorinated phase and an antiferromagnetic ordering temperature of 185 K.[39]

In order to investigate this behaviour further, the topochemical fluorination of $Sr_3(Ru_{0.5}M_{0.5})O_7$ (M = Ti, Mn, Fe) was attempted.

Chapter 2 Experimental Methods

2.1 Standard Ceramic Synthesis

During the course of this investigation, standard ceramic synthesis techniques were used to prepare thermodynamically stable solids. The basic procedure involved the thorough mixing of suitable quantities of the appropriate starting materials (metal oxides, chlorides or carbonates) using an agate mortar and pestle. The resulting powders were pressed into 13 mm diameter pellets of no more than 2 g under 5 tonnes of force, in order to minimise the required diffusion length within the solid. These were then heated to suitably high temperatures in order to overcome the large energetic barrier to diffusion within solids. After each firing, the samples were thoroughly reground and re-pressed into pellets. The use of metal carbonates require an initial firing for 24 hours at 900 °C in order to decompose the carbonate into the appropriate oxide before being heated to the required temperature. Exact details of the procedures for each phase are included in the appropriate chapters. Reaction progress was monitored via X-ray powder diffraction. The reactions were judged to be complete when X-ray powder diffraction patters collected after consecutive firings showed no change.

2.2 Arc Furnace

The synthesis of some materials was carried out using an arc furnace, which provides a convenient combination of extremely high temperatures and highly reducing conditions. 13 mm diameter pellets of intimately mixed precursors were prepared via conventional methods. These were then place on a water cooled stage within the arc furnace. The chamber was pump-filled three times with argon and then placed under a flowing argon atmosphere. A DC arc welding torch operating with a 60 amp current was used to ionise the argon gas. The hot plasma was then repeatedly passed over the pellet until it melted. The pellet was then allowed

to cool to room temperature, at which point it was flipped over and melted once again. This process was repeated a minimum of four times. Reaction progress was monitored via X-ray powder diffraction.

2.3 Pechini Method

Samples requiring a high degree of homogeneity were prepared using the method first described by M. Pechini in 1967.[40] Suitable quantities of the appropriate starting materials (metal oxides, chlorides or carbonates) were dissolved in a 1:1 solution of nitric acid in distilled water. An excess of citric acid was added, followed by ethylene glycol. The solution was then heated to drive the polymerisation of citric acid, resulting in the formation of a polyester network complexing a homogeneous array of coordinated metal cations. This was used to prepared homogeneous powders which were then treated as in standard ceramic synthesis.

2.4 Hydride Reductions

Recent work has shown that binary metal hydrides (namely NaH, CaH_2 and LiH) can be used to reduce a wide range of materials at relatively low temperatures (180 °C to 630 °C) to form anion-deficient metastable phases.[14,41,42] Reduction of a generic ABO_3 phase with NaH can be described as follows:

$$ABO_3 + x\text{NaH} \rightarrow ABO_{3-x} + x\text{NaOH}$$

As sodium-containing by-products can be easily removed from the sample (see section 2.4.4) and the reaction does not produce H_2 gas, NaH was used as the reducing agent whenever possible. However, the low decomposition temperature of NaH placed an upper limit on possible reaction temperatures (~ 250 °C). When reactions were found to require higher temperatures, CaH_2 was used as the reducing agent at reaction temperatures up to 650 °C.[42] The reduction of a generic ABO_3 phase with CaH_2 can be described by:

$$ABO_3 + xCaH_2 \rightarrow ABO_{3-x} + xCaO + xH_2$$

The metal hydrides were kept in an argon-filled glovebox (O_2 and H_2O < 1 ppm) due to their air and moisture-sensitive nature. Furthermore, any mixtures containing these reagents were also kept under an inert atmosphere at all times. Substrates to be reduced were typically ground with 2 stoichiometric equivalents of the appropriate binary metal hydride in a glovebox and then placed within a suitable reaction vessel.

2.4.1 Reactions in Sealed Tubes

For small-scale test samples (typically ≤ 300 mg), the substrate and hydride reducing agent were sealed under vacuum in either Pyrex (cheaper and easier to handle, but cannot be used at reaction temperatures above 400 °C) or quartz ampoules. These were then heated to the desired temperatures at a ramp rate of 1 °C min^{-1} to ensure that the temperature of the furnace did not overshoot the relatively low reaction temperature. After being held at the required temperature for a suitable length of time, the ampoules were opened in the glovebox and the sample reground. Reaction progress was monitored using X-ray powder diffraction.

2.4.2 Modified Pressure Venting Apparatus

Due to the hazards associated with the production of H_2 gas as a by-product of reductions with CaH_2,[42] large-scale samples suitable for neutron diffraction experiments could not be prepared in sealed glass tubes. A modification of the pressure venting apparatus[42] was employed where the spring-loaded valve was removed in order to minimise the number of connections and thus any potential leaks.

The substrate was ground together with CaH_2 in an argon-filled glovebox and then placed in an alumina boat. This was then placed in a large quartz tube and closed with a steel end-cap equipped with a rubber O-ring and a 3-way tap. The tube and end-cap were connected to a flow of argon via a three-way connection as shown in Figure 2.1.

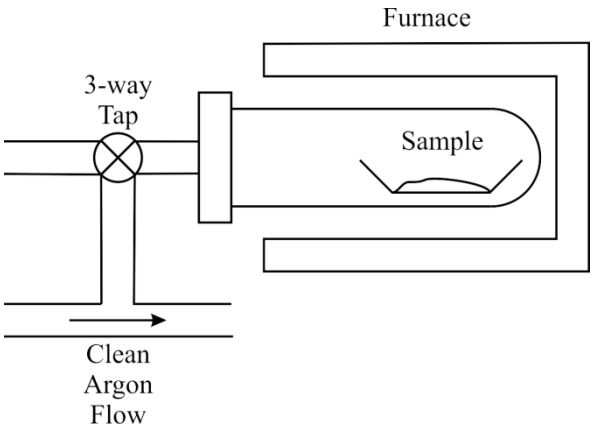

Figure 2.1: Modified pressure venting system.

The tube was then heated to the desired reaction temperature. After a suitable time period, the apparatus was cooled and the 3-way tap closed. It could then be disconnected from the flow of argon, evacuated, and moved into the glovebox. Reaction progress was monitored using X-ray powder diffraction.

2.4.3 High-Pressure Apparatus

Another method to prepare large samples using CaH_2 as a reducing agent utilised a Parr Series 4740 Pressure Vessel capable of withstanding pressure of up to 128bar. This reaction vessel could withstand the hydrogen pressures produced during the reductions reactions and was used to prepare samples suitable for neutron powder diffraction.

In an argon-filled glovebox, appropriate substrates were ground together with suitable amounts of CaH_2 into fine powders and placed in a silica finger. This was then fitted with a loose glass top to prevent sample contamination and placed in a steel vessel. The vessel was fitted with a screw cap housing six bolts which compress a PTFE O-ring. The screw cap was connected to a gauge block assembly using a coned pressure fitting to create an air-tight seal. A tap on the gauge block assembly was closed and the vessel removed from the glovebox. The gauge block assembly was connected by way of a three-way tap to a vacuum pump and an argon cylinder and pump-filled three times. The vessel was then placed under static

vacuum by closing the tap. It was then heated to the desired temperature. The large steel pressure vessel acted as a heat-sink. Additionally, the cap remained outside the furnace during heating and a thermocouple was attached to the outside of the pressure vessel. These resulted in a temperature gradient between the furnace temperature measured by the thermocouple, and the sample temperature inside. This could be accounted for by heating 50 °C hotter than an equivalent reaction performed in a sealed glass ampoule. Once the reaction was judged to be complete, the vessel was moved into the glovebox, where the hydrogen pressure could be safely released. Reaction progress was monitored using X-ray powder diffraction.

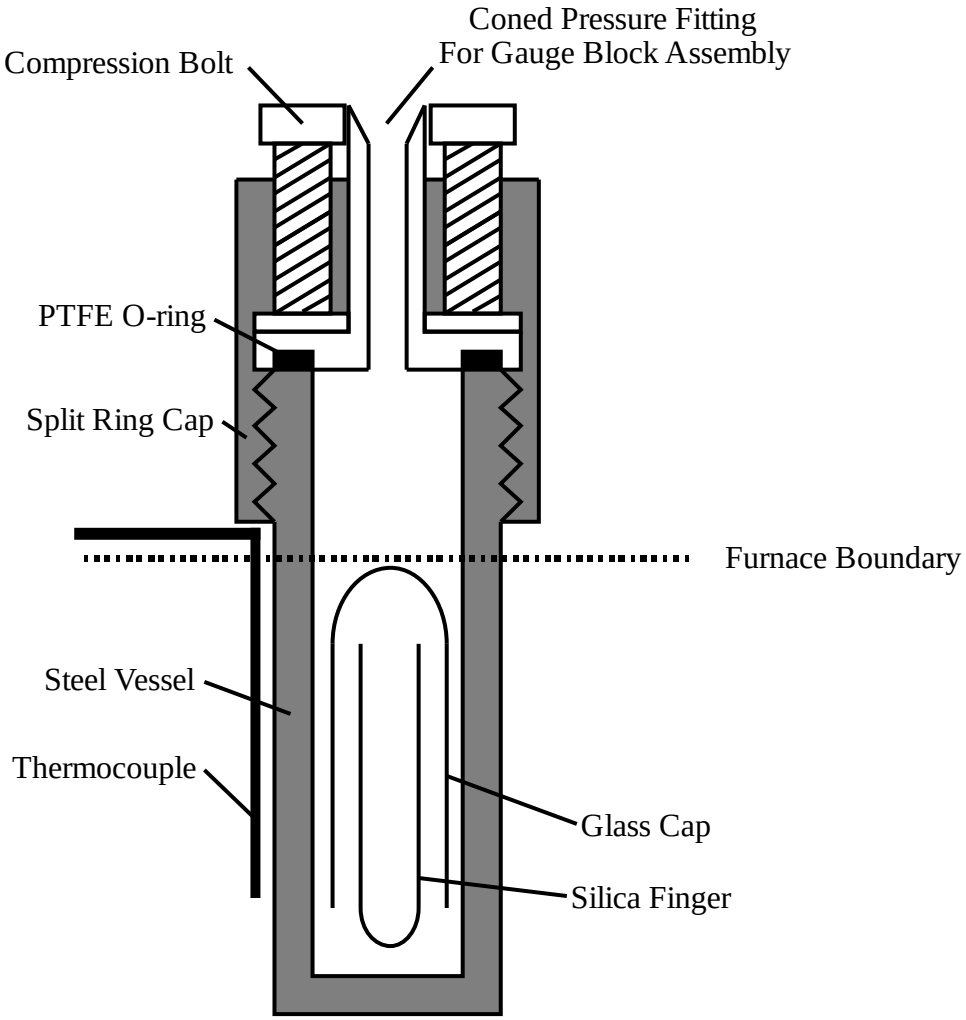

Figure 2.2: Slice through pressure vessel.

2.4.4 Removal of Reaction By-products

Reduction reactions were considered to be complete when X-ray powder diffraction data collected from products after successive heating cycles showed no change. Once reached, the products were washed to remove unwanted reaction by-products (NaOH, CaO and/or unreacted metal hydrides). When using NaH as the reducing agent, the samples were washed with 4 x 100 ml of methanol. As CaO is insoluble in methanol, its removal required washing with a 0.1 M solution of NH_4Cl in methanol (4 x 100 ml), followed by 4 x 100 ml of methanol to removed any remaining NH_4Cl. All washing procedures were performed under nitrogen using standard Schlenk line techniques. The samples were then dried under vacuum before being returned to the glovebox.

2.5 Fluorination Reactions

The manipulation of anion lattices in the solid state can also be performed via fluorination reactions. These reactions can either be performed using F_2 gas or solid state fluorinating agents such as NH_4F or MF_2 (M = Cu, Zn, Ni, Ag) in the presence of oxygen.[34]

2.5.1 F_2 Gas

Reactions were performed using a mixture of 10% F_2 in N_2. Substrates were placed in an alumina boat, which was then placed inside a large silica tube. This was then fitted with brass end-caps equipped with 3-way taps (Figure 2.3). A source of N_2 gas was connected, which was then used to purge the tube of any moisture in order to avoid the formation of HF before exposing the sample to the 10% F_2/N_2 mixture.

The sample could either be heated to the desired temperature under a flow of 10% F_2/N_2 or under N_2 before being exposed to fluorine once the desired temperature was reached. After a suitable length of time has passed, the sample was cooled and the tube purged with clean N_2

to remove any remaining fluorine. The sample could then be ground and reaction progress monitored via X-ray powder diffraction.

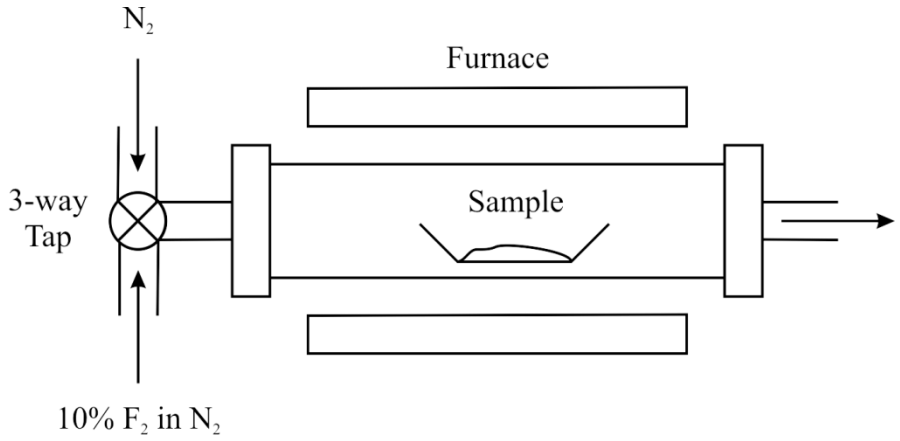

Figure 2.3: F_2 gas apparatus.

2.5.2 CuF_2

The substrate was ground together with a suitable amount of CuF_2 and placed in an alumina boat. This was then heated under a flow of oxygen for a desired time period. The oxygen drives the decomposition of CuF_2 to CuO, releasing fluorine.

$$A_2BO_4 + CuF_2 + 1/2O_2 \rightarrow A_2BO_{4-x}F_y + CuO$$

Reactions using CuF_2 result in contamination of the sample with CuO, but are more controllable and less hazardous than those carried out with F_2 gas.

2.6 Powder Diffraction

Powder diffraction techniques are the most widespread structural characterisation techniques used in solid state chemistry. X-ray and neutron powder diffraction methods were integral to the structural characterisation presented in this thesis.

Diffraction arises from the periodic arrangement of atoms within a crystal. A beam of X-rays or neutrons with a wavelength similar to the spacing between the lattice planes in the crystal can be diffracted according to Bragg's Law:

$$n\lambda = 2d_{hkl}\sin(\theta)$$

where λ is the wavelength of the incident beam, d_{hkl} is the interplanar distance and θ is the angle between the beam and the lattice plane (Figure 2.4).

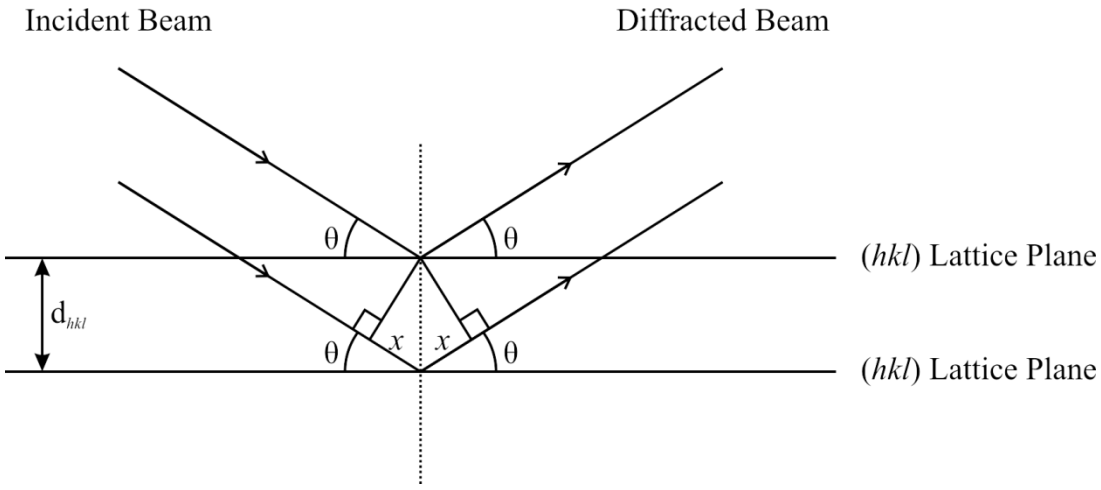

Figure 2.4: Bragg's approach to diffraction.

The unit cell dimensions define the *d*-spacing (d_{hkl}) of a given reflection, while the intensity (I_{hkl}) is given by:

$$I_{hkl} \propto LmA|F_{hkl}|^2$$

where L is the sample-independent Lorentz-polarisation function, *m* is the reflection multiplicity, *A* is the absorption factor and F_{hkl} is the structure factor.

The structure factor determines how the intensity of a given reflection depends on the particular arrangement of atoms in the unit cell:

$$F_{hkl} = \sum_n f_n \exp[2\pi i(hx_n + ky_n + lz_n)] \exp\left[\frac{-8\pi^2 U_{iso_n} \sin^2\theta_{hkl}}{\lambda^2}\right]$$

where f_n is the atomic scattering factor and x_n, y_n, and z_n are the fractional coordinates of the n^{th} atom in the unit cell. The exponential term containing the atomic isotropic thermal factor (U_{iso_n}) determines the reduction in intensity as a function of scattering angle.

2.6.1 X-ray Powder Diffraction

X-ray powder diffraction was routinely used to characterise structures due to the ready availability of monochromatic X-ray sources. A given atom's scattering factor (f_n) is related to its atomic number (Z_n). Therefore, the intensity is relatively insensitive to changes in the fractional occupancy or position of atomic sites occupied by light elements in the presence of relatively heavy elements. Consequently, the complete elucidation of structures containing mixtures of light and heavy elements (i.e. the majority of the complex transition metal oxides and oxyhalides detailed in this thesis) using X-ray powder diffraction data only was not always possible.

2.6.1.1 Philips PW1710

A Philips PW1710 diffractometer was routinely used to monitor reaction progress. It operates in Bragg-Brentano focusing geometry and uses both Cu $K_{\alpha1}$ and $K_{\alpha2}$ radiation. Data were collected from air-stable samples using an aluminium plate. Samples were loaded into a recess in the plate measuring 20 mm x 10 mm x 0.5 mm. Additional diffraction reflections from the aluminium plate sample holder were present in the resulting data. Data were collected over the range $3 < 2\theta / ° < 70$ with a continuous scan speed of 0.04 $°s^{-1}$.

When X-ray powder diffraction data had to be collected from air-sensitive samples, the samples were loaded into gas-tight holders (Figure 2.5) in an argon filled glovebox. The samples were placed on a glass slide coated with a small amount of Dow-Corning high-vacuum grease. This was then placed inside a gas-tight holder equipped with a thin Mylar window and sealed with a rubber o-ring and a brass cap. Data were collected over the range

$10 < 2\theta / ° < 70$ using a continuous scan speed of 0.02 $°s^{-1}$ to compensate for the intensity loss due to absorption by the Mylar window.

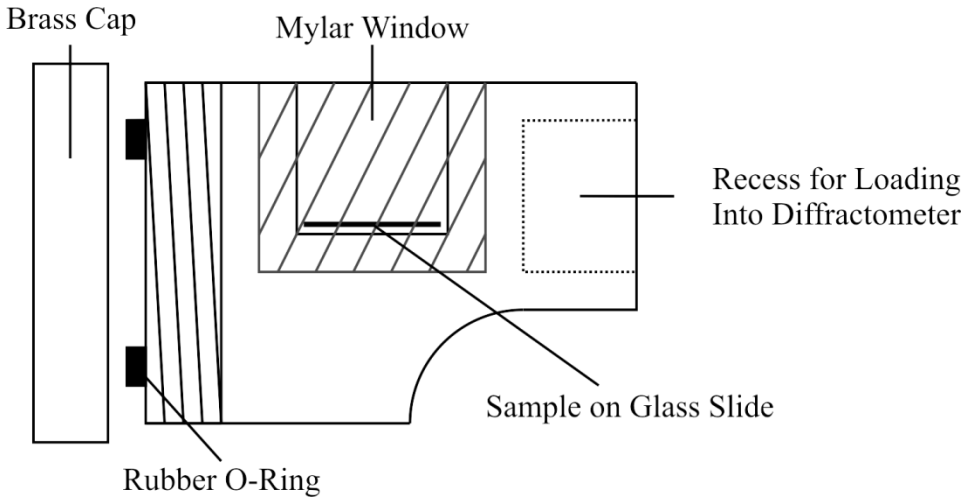

Figure 2.5: Sample holder for collecting X-ray powder diffraction data from air-sensitive samples

2.6.1.2 PANalytical X'Pert

A PANalytical X'Pert diffractometer was used to collect high-quality data sets suitable for Rietveld refinement. It operates in Bragg-Brentano geometry and utilises a crystal monochromator to exclusively select Cu $K_{\alpha 1}$ radiation. Additionally, 0.02 mm Söller slits were added to further collimate both the incident and diffracted beams, allowing for very high resolution diffraction patterns.

Non-air-sensitive samples were loaded onto a silicon wafer coated with a thin layer of Dow-Corning high vacuum grease. This wafer is cleaved along the systematically absent [110] plane, permitting the collection of diffraction patterns with no contributions from the holder. During measurement, the wafer is rotated at 30 rpm in order to minimise contributions from a non-uniform distribution of the sample. Data from air-sensitive samples were collected from samples loaded in the holders described in Section 2.6.1.1. Particular details of each measurement range and speed are described in the appropriate chapters.

2.6.1.3 Siemens D5000 with PheniX Cryostat

A Siemens D5000 diffractometer equipped with an Oxford Cryosystems PheniX cryostat was used to collect X-ray powder diffraction at low temperatures. The diffractometer operates in Bragg-Brentano geometry and utilises a crystal monochromator to exclusively select Cu $K_{\alpha 1}$ radiation. The PheniX cryostat uses compressed helium to cool samples down to 13 K.

Samples were loaded onto glass slides coated with a thin layer of Dow-Corning high vacuum grease. Air sensitive samples were prepared in the glovebox and kept under argon until they could be placed inside the cryostat in order to minimise exposure to the air. This could then be placed inside the cryostat, evacuated and cooled to the desired temperature. Data were collected in the range $3 < 2\theta / ° < 70$ using a continuous scan speed of 0.01 $°s^{-1}$.

2.6.2 Neutron Powder Diffraction

While X-rays are scattered by the periodic electron density in a crystalline solid, neutrons are scattered by the interaction with atomic nuclei. Thus, neutron diffraction differs from X-ray diffraction in a number of ways:

- The neutron scattering lengths of all atoms are much more similar than the X-ray scattering lengths, and follow no linear relationship with atomic number.[43] The contribution to the total scattering from a structure is therefore much more evenly distributed among its constituent elements, and neutron powder diffraction can therefore be used to locate light atoms in the presence of heavier elements and can distinguish between isoelectronic elements.
- Unlike the X-ray scattering form factor, which drops off rapidly with the scattering angle, the neutron scattering form factor can be regarded as essentially independent of the scattering angle. In contrast to X-ray diffraction data, there is no fall-off of intensity with increasing scattering angle.

- Neutron scattering interaction is relatively weak. Therefore, most neutron diffraction experiments require large sample sizes (2 g – 4 g), while X-ray diffraction data can be collected from mg-scale samples.
- Neutrons are spin-1/2 particles, and can therefore interact with unpaired electrons. Scattering from an ordered array of unpaired electrons produces magnetic reflections in the diffraction pattern which allow the determination of the magnetic structures in materials.

The magnetic scattering structure factor (F_{mag}^{hkl}) for an unpolarised neutron source can be expressed as follows:

$$F_{hkl,mag} = \sum_{j} q_j p_j e^{2\pi i h x_j}$$

where q_j is the magnetic interaction vector, p_j is the magnetic scattering length, h the magnetic scattering vector and x_j the position vector of magnetic atoms in the unit cell. The observed intensity of a magnetic reflection ($I_{hkl,mag}$) is proportional to the square of the projection of the magnetic structure factor onto the scattering vector:

$$I_{hkl,mag} = |F_{hkl,mag}|^2 cos^2\alpha$$

where α is the angle between the magnetic scattering structure and the relevant lattice plane.

For all neutron powder diffraction, the samples were loaded into vanadium cans (chosen for its low coherent scattering length (-0.3824 fm)[43] to minimise contributions from the holder). These cans were sealed with either indium washers for measurements in the range 5 < T / K < 300 or copper gaskets for measurements above 300 K.

Neutron powder diffraction data were collected at two facilities: the Institut Laue-Langevin (ILL) in Grenoble, France and ISIS, at the Rutherford Appleton Laboratory in Oxfordshire.

2.6.2.1 Institut Laue-Langevin (ILL)

At the ILL, diffraction experiments use a beam of neutrons produced from a ^{235}U fission nuclear reactor. 'Fast' neutrons produced from this fission reaction have energies in the MeV range, whereas the cross-section for neutron-induced fission of ^{235}U is highest for neutrons in the meV range. In order to sustain the fission process, a moderator filled with D_2O is used to reduce the energy of produced neutrons. These neutrons are then of suitable energies to perform diffraction experiments, with appropriate wavelengths selected using a crystal monochromator. The instrument used at the ILL was D2B.

D2B is a high-resolution two-axis diffractometer with a high take-angle (135 °) for the monochromator. Scans were performed over the range $5 < 2\theta / ° < 160$ with several scans being summed to improve the statistics. The wavelength of the incident neutron beam can be selected by rotation within the (*hhl*) plane of a germanium crystal monochromator. A wavelength of 1.594 Å was used for all experiments in this investigation.

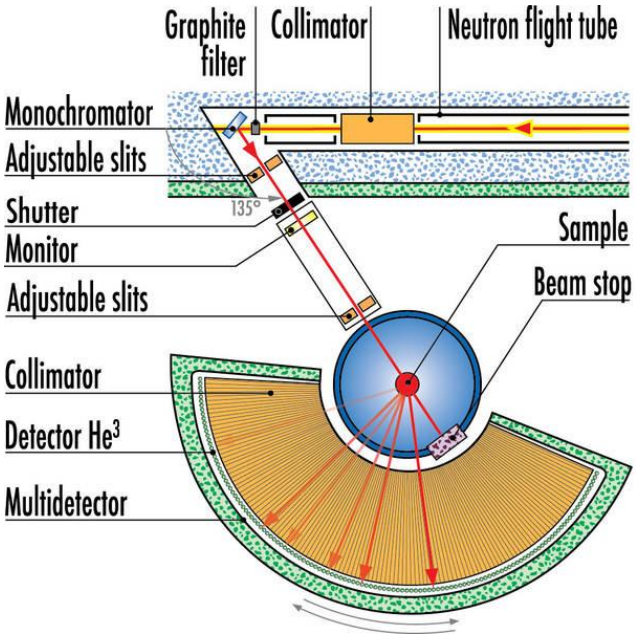

Figure 2.6: D2b instrument at the ILL facility.[44]

2.6.2.2 ISIS

The ISIS neutron facility at the Rutherford Appleton Laboratory uses a spallation neutron source.[45] Pulses of protons are accelerated to 800 MeV in a synchrotron and fired at a tantalum target. This causes an intranuclear cascade, resulting in a pulse of neutrons. These have very high thermal energies and must be slowed down using a hydrogenous moderator (H_2O in the case of the POLARIS instrument) so that their wavelength is suitable for diffraction. This method produces a pulse of neutrons with a range of wavelengths suitable for time-of-flight measurements.

Time-of-flight diffractometers use fixed-angle detectors to measure diffraction patterns as a function of wavelength, which can be related to the velocity of the neutrons using the de Broglie relationship:

$$\lambda = \frac{h}{m} \times \frac{t}{L}$$

where h is Planck's constant, m the neutron mass, and t the time taken to travel distance L from the moderator to the detector via the sample. POLARIS is a high-intensity, medium resolution powder diffractometer equipped with six banks of detectors (Table 2.1).

Detector Bank		**2θ Range / °**	**d_{max} / Å**
Very Low Angle	1	6 – 14	19.6
Low Angles	2	19 – 34	8.7
	3	40 – 67	7.0
90 °	4	75 – 113	3.2
Back-scattering	5	135 – 143	2.7
	6	146 – 168	2.7

Table 2.1: Detector banks following the POLARIS upgrade.

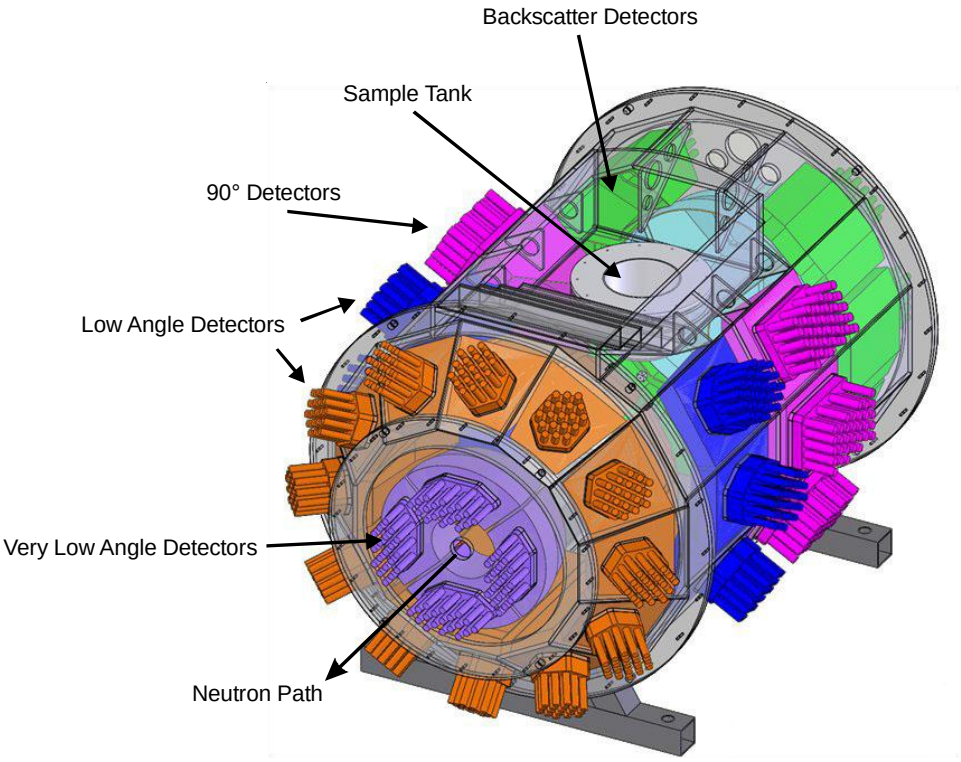

Figure 2.7: New POLARIS instrument at the ISIS facility.[46]

2.7 Rietveld Refinement

X-ray and neutron powder diffraction data were analysed using the Rietveld method of profile refinement with the GSAS suite of programs.[47,48] The Rietveld methods allows structural information to be extracted from powder diffraction data where peak overlap and d_{hkl} degeneracy prevent exact structure factors being calculated from reflection intensities.

A diffraction pattern is generated from diffraction and structural parameters and the calculated intensity at each point compared to the observed intensity in an experimental diffraction pattern using the following expression:

$$S = \sum_i w_i (y_{io} - y_{ic})^2$$

where w_i is the weighting factor, y_{io} the observed intensity at point i and y_{ic} the calculated intensity at point i. Diffraction and structural parameters are then refined against the experimental data using a least squares optimisation technique in order to minimise S.

The quality of the fit to the data can be assessed using three 'goodness of fit' functions: reduced χ^2, the residual function (R_p) and the weighted residual function (wR_p). These functions are defined as follows:

$$\chi^2 = \frac{\sum w_i(y_{io} - y_{ic})^2}{n_{obs} - n_{var}}$$

$$R_p = 100 \times \frac{\sum |y_{io} - y_{ic}|}{\sum y_{io}} \%$$

$$wR_p = 100 \times \sqrt{\left(\frac{\sum w_i(y_{io} - y_{ic})^2}{\sum w_i y_{io}^2}\right)} \%$$

where n_{obs} is the number of observations in all histograms and n_{var} is the number of variables in the least squares refinement.

2.7.1 Peak Shapes

The accurate description of experimentally observed peak shapes in diffraction patterns is fundamental to the success of Rietveld refinement. Peak widths in diffraction data are dependent on three main factors:

1. The Darwin width: due to the uncertainty principle, exact knowledge of the position of a photon necessarily implies an uncertainty about its momentum, and therefore, its wavelength. This leads to reflections possessing a finite width. However, broadening due to uncertainty is generally negligible compared to other experimental considerations.

2. Instrumental factors, such as imperfect measuring geometry (e.g. ambiguity in the height of the sample) and optical effects (e.g. diffraction by parts of the instrument rather than the sample).
3. The theory of diffraction assumes an infinite perfect crystal. Deviations from this hypothetical perfect crystal lead to a broadening of peaks in the diffraction pattern. This broadening can contain information about the sample, such as particle size or strain.

Instrumental peak broadening can be well modelled using a Gaussian profile,[49] but the use of a Lorentzian function is required to model the broadening from structural features. Thus, the overall profile function can be modelled as an integral of the Pseudo-Voigt function $(F(\Delta T))$[48,50] involving a linear combination of both Gaussian and Lorentzian components:

$$F(\Delta T) = \eta L(\Delta T, \Gamma) + (1 - \eta) G(\Delta T, \Gamma)$$

where ΔT is defined as the deviation of a reflection from its calculated position, correcting for asymmetry, Γ is a function of the Full Width at Half-Maximum (FWHM) and η is the mixing parameter which is used to include the optimal contribution from each component function.[49]

2.8 X-ray Absorption Near-Edge Structure (XANES) Spectroscopy

Sufficiently energetic X-rays can be used to ionise core electrons from an atom or ion. An atom or ion's absorption spectrum can therefore be collected by recording the absorption of X-rays as a function of the energy of the incident radiation. The energy at which the absorption of incident photons increases dramatically is defined as the absorption edge. The absorption edge corresponds to the energy at which incident photons are able to ionise core electrons.

The energy of the absorption edge is characteristic of the element and the oxidation state. Information about the latter can thus be gained by comparing the absorption edge of an unknown with those of the same element in known standards. It is thus a way to independently probe the oxidation states of ions in a sample.

In addition to the ionisation of core electrons, X-rays can cause excitation of core electrons to higher energy shells, e.g. 1*s* → 5*p*. This gives near-edge fine structure, which can be affected by the coordination environment (which will alter the relative energies of the orbitals).

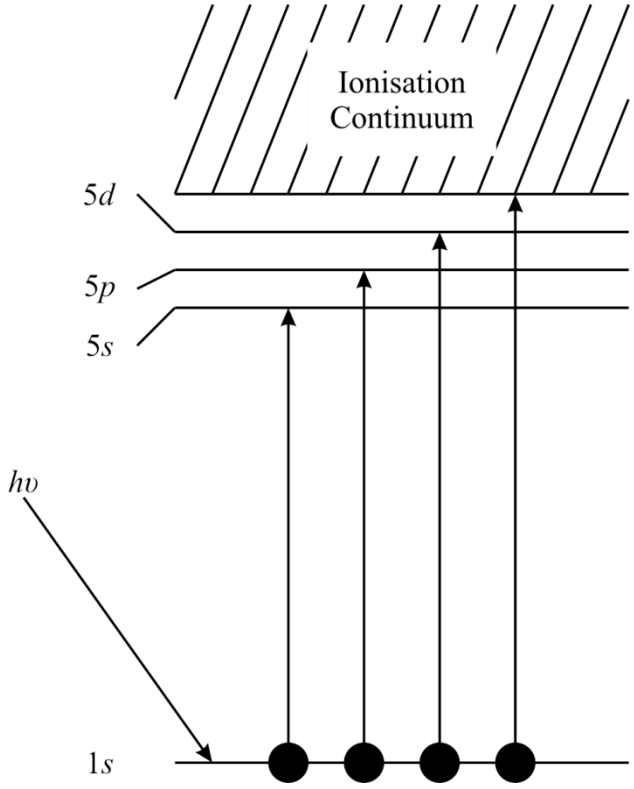

Figure 2.8: Cartoon depiction of the ionisation of core electrons by incident X-rays.

Samples suitable for characterisation by XANES were prepared by grinding together a suitable amount of product with 100 mg of cellulose using an agate mortar and pestle. The amount of sample was calculated in order to obtain an edge jump close to one. The cellulose acts as an inert matrix, allowing the resulting powder to be pressed into robust pellets.

In the case of air-sensitive samples, samples suitable for characterisation by XANES were prepared under an inert atmosphere. A suitable amount of product was ground together with

100 mg of cellulose (dried at 120 °C to prevent the introduction of moisture into the samples) in an argon-filled glovebox using an agate mortar and pestle. The mixture was then loaded into a pellet die and sealed inside two tied plastic bags in order to maintain an inert atmosphere. Once the pellet had been pressed outside the glovebox the die was returned to the glovebox and the pellet removed.

XANES data were collected at the B18 beamline at Diamond Light Source.[51]

2.9 ^{57}Fe Mössbauer Spectroscopy

Mössbauer spectroscopy relies on the emission and absorption of gamma rays. In a gas the energy of an emitted gamma ray is smaller than the energy of the nuclear transition due to energy lost to recoil. Similarly, the energy of an absorbed gamma ray must be greater than that of the nuclear transition. This causes resonance (emission and absorption of the same gamma ray) to be unobservable with free nuclei as there is no significant overlap between the emission and absorption spectra.

In a solid crystal, however, the nuclei are bound in place and therefore not free to recoil. The energy of emission or absorption can still be affected by lattice vibrations (phonons). During an event, any number of phonons can be emitted, including zero, which results in a 'recoil-free' event in which the entire crystal acts as the recoiling body. Since this results in a negligible loss of energy, the emission and absorption spectra overlap sufficiently for resonance to occur.

^{57}Fe Mössbauer spectroscopy utilises a ^{57}Co source which decays by electron capture to an excited state of ^{57}Fe, that subsequently decays to a ground state with emission of a gamma ray. The energy of the emitted gamma rays is modified via the Doppler effect. Transmission of gamma rays through a sample can then be plotted as a function of velocity, with sharp dips corresponding to absorption at energies where resonance can occur.

The energies at which transitions occur are modified by the local environment of the atoms or ions:

- The chemical shift represents a change in the resonance energy of a nucleus due to the presence of electrons in *s* orbital. This causes the entire pattern to be shifted depending on the electron charge density. In turn, this provides information about the oxidation state of the iron ions (e.g. Fe^{3+} ions have lower isomer shifts than Fe^{2+} due to weaker screening by *d* electrons, which increases the *s* electron density at the nucleus).[52]
- Quadrupole splitting arises because nuclei in states with non-spherical charge distributions (i.e. I > 1/2) produce an asymmetrical electric field which splits the nuclear energy levels and produce a nuclear quadrupole moment. ^{57}Fe possesses a I = 3/2 excited state, so the 1/2 to 3/2 transition is split into two substates, appearing as a doublet in the spectrum (Figure 2.9).

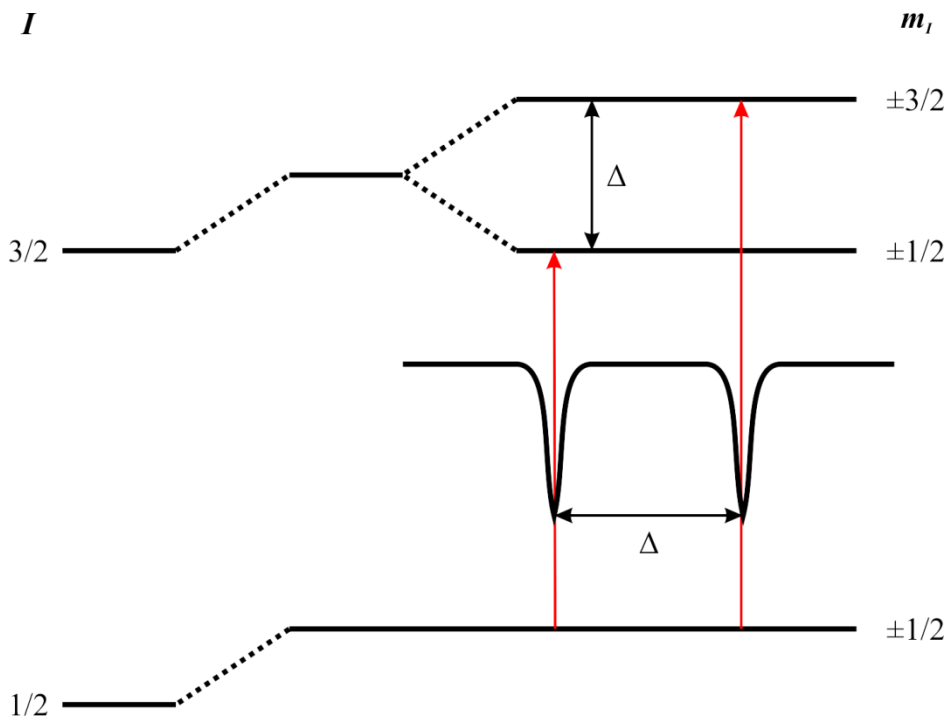

Figure 2.9: Quadrupole splitting from a 3/2 to 1/2 transition. The magnitude of the quadrupole splitting, Δ, is shown.

- Interaction between a nucleus with spin I and a surrounding magnetic field will cause a splitting into $2I + 1$ sub-energy levels. This splitting gives rise to additional features in the observed spectrum due to possible transitions between these states (Figure 2.10). These transitions are limited to those in which m_I changes by 0 or ±1.

Together, these features provide information about the oxidation state, chemical environment, and magnetic behaviour of Fe centres in a sample.

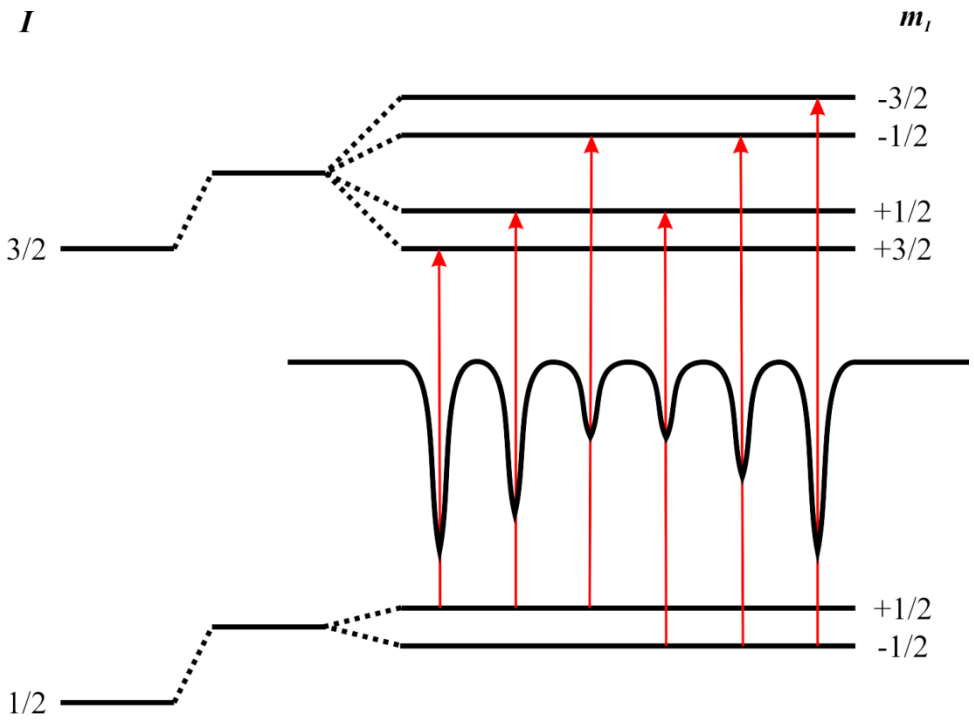

Figure 2.10: Magnetic splitting of nuclear energy levels.

Samples were diluted with graphite and contained within airtight plastic holders. ^{57}Fe Mössbauer spectroscopy data was collected relative to an α-Fe standard using a 36 mCi ^{57}Co in Rh source. The spectra were recorded over a velocity range ±5 mm/s. All spectra were collected and fitted by Dr. Paul A. Bingham and Dr. Susan D. Forder at the University of Sheffield.

2.10 Thermogravimetric Analysis (TGA)

Thermogravimetric analysis measures the mass of a sample as a function of temperature. By heating the sample under a flowing gas, chemical information about samples can be obtained. Reoxidative TGA, in which the sample was heated under flowing O_2, and reductive TGA, in which the sample was heated under H_2 (as 5-25% H_2 in N_2) were useful in determining the anion content of samples. For a generic, reduced ABO_{3-x} perovskite:

$$ABO_{3-x(s)} + O_{2(g)} \rightarrow ABO_{3(s)}$$

$$ABO_{3-x(s)} + H_{2(g)} \rightarrow AO_{(s)} + B_{(s)} + H_2O_{(g)}$$

In both cases, from knowledge of the mass of the sample at the beginning and end points and the composition at the end point, the amount of oxygen gained or lost can be calculated, and thus the initial composition of the sample can be determined.

Thermogravimetric data was collected from approximately 50 mg of powdered sample using a Netzsch STA 409PC balance.

2.11 Muon Spin Relaxation Spectroscopy (μSR)

Muon Spin Relaxation Spectroscopy (μSR) is a technique used to probe the internal magnetic field within materials. It functions by implanting a positively charged antimuons within a material and measuring the decay process.

Muons are produced by collisions between high-energy protons and a light element target such as graphite, which produce pions that subsequently decay into leptons (muons or electrons in a ratio of approximately 8000:1) and neutrinos with a mean lifetime of 26 ns. Beampipes are then used to focus the muon beam and discard unwanted particles, guiding the muons into the sample such that they arrive with correct energies and well-oriented spins.

Once the muon penetrates the sample, it sheds kinetic energy in a series of stages through ionisation of the sample and capture and loss of electrons before coming to rest within a crystal vacancy. These interactions are mainly electrostatic and do not significantly alter the muon spin.

Since the muon is a S = 1/2 particle, it undergoes Larmor precession in the presence of a magnetic field. In an ordered magnet, the muon will see the magnetic field without perturbing it. Muons decay into positrons and two neutrinos. The distribution of angles at which the

positron is emitted relative to the original muon spin is asymmetrical. In a typical experimental set up, scintillation detectors are set up around the sample. The difference in the numbers of positrons detected by pairs of detectors on opposite sides of the sample is normalised by the total count to account for the ever-decaying population of muons in the sample, and plotted as a function of time. The resulting oscillations give a measure of the muon precession frequency and thus the internal field it experiences.

μSR data was collected at the Paul Scherrer Institute in Switzerland by Prof. Stephen J. Blundell, Dr. Johannes Moeller, and Francesca Foronda.

2.12 DC SQUID Magnetometry

DC SQUID (Superconducting Quantum Interference Device) magnetometry was used to measure the magnetic properties of systems arising from spin and orbital momentum of electrons. A measurement is performed by moving the sample through a superconducting detection coil as shown in Figure 2.11, which induces a current in the ring.

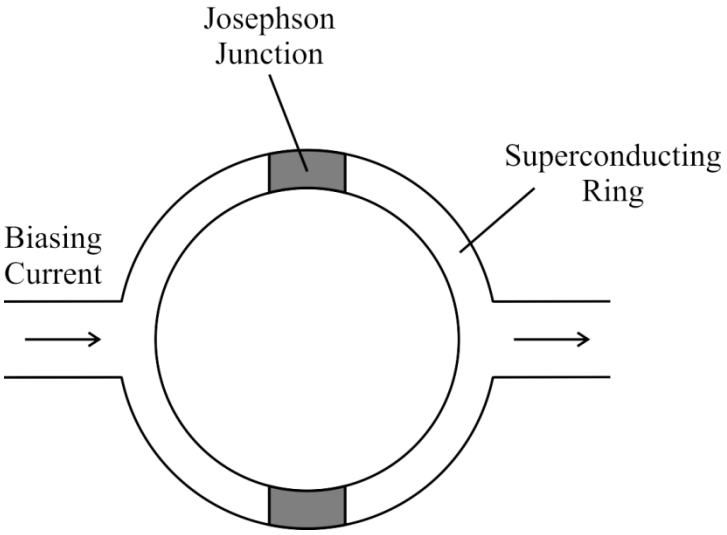

Figure 2.11: Schematic of a SQUID detection coil

The Josephson junctions force the current in the ring to become quantised. Variations in the ring current produce equivalent variations in the output voltage, which is therefore proportional to the magnetic moment of the sample.

All data was collected using a Quantum Design MPMS XL SQUID magnetometer. Approximately 50 mg of sample were weighed and suspended in a gelatine capsule inside a drinking straw, with four empty capsules on either side. The outermost capsules were covered in a layer of diamagnetic tape to hold the sample in place. Air sensitive samples were prepared in the glovebox and kept under an inert atmosphere until they could be loaded into the magnetometer.

Magnetisation data from samples was collected either as a function of temperature, usually from 5 K to 300 K in a constant applied field (normally 100 Oe), both when cooling in the absence of a magnetic field and when cooled in the presence of the measuring field, or as a function of applied field (typically $-50\,000 \leq H / Oe \leq 50\,000$) at a constant temperature (both 5 K and 300 K).

For samples containing trace amounts of ferromagnetic impurities, such as elemental cobalt, a 'ferrosubtract method' was used.[16] The paramagnetic susceptibility could be measured by measuring the gradient of magnetisation-field isotherms in fields of at least 35 000 Oe, which saturate the ferromagnetic contribution. The magnetisation of samples was measured in a series of 7 fields between 35 000 Oe and 50 000 Oe. The magnetisation-field isotherms were then fitted to a linear function, excluding points with large errors. All fits had at least 5 data points. This procedure was repeated at 5 K intervals between 5 K and 300 K in order to obtain the temperature-dependant susceptibility of samples.

2.12.1 Curie-Weiss Law

Paramagnetic susceptibility can be modelled using the Curie-Weiss law:

$$\chi_m = \frac{C}{T - \theta}$$

where θ is the Weiss constant, a measure of the strength of the interactions present, and C, the Curie constant, can be defined as:

$$C = \frac{N_A \mu_B g^2 S(S+1)}{3k_B} \approx \frac{1}{8}\mu_{eff}^2$$

where N_A is Avogadro's number, μ_B is the Bohr magneton, g is the Landé factor, S is the spin quantum number of the magnetic ion, k_B is Boltzmann's constant and μ_{eff} is the effective magnetic moment. A temperature-independent paramagnetic contribution can be accounted for in the Curie-Weiss law by the inclusion of a further constant K:

$$\chi_m = \frac{C}{T - \theta} + K$$

2.13 Bond Valence Sums (BVS)

Bond valence calculations allow the estimation of the valence of an ion based on the bond length and identity of the contacts in its coordination sphere.[53] The total valence, V_i, of an ion is defined as the sum of the valence contributions for the individual bonds within its coordination sphere:

$$V_i = \sum_j v_{ij}$$

where the valence v_{ij} of a bond between atoms *i* and *j* is given by:

$$v_{ij} = e^{(R_{ij} - d_{ij})/b}$$

where *b* is an empirical constant (taken to be equal to 0.37)[54], R_{ij} is the 'bond-valence parameter', and d_{ij} is the bond length. Bond valence calculations performed in this investigation used R_{ij} values published by Brese and O'Keefe.[53]

Chapter 3 The Reduction of $Sr_3Co_2O_5Cl_2$

3.1 Introduction

There are a large number of published examples of topochemical reactions involving metal hydrides as a reducing agent. These typically lead to the formation of materials with transition metals in unusual oxidation states and/or coordination environments. Of particular interest are the reduction of $SrFeO_3$ to $SrFeO_2$ and $Sr_3Fe_2O_{7-\delta}$ to $Sr_3Fe_2O_5$ via $Sr_3Fe_2O_6$. Both reduced phases contain networks of vertex-sharing $Fe^{II}O_4$ square planes (Figure 3.1).[19,55] High-spin Fe^{II} appears to show an unexpected affinity for square-planar coordination when undergoing topochemical reduction.

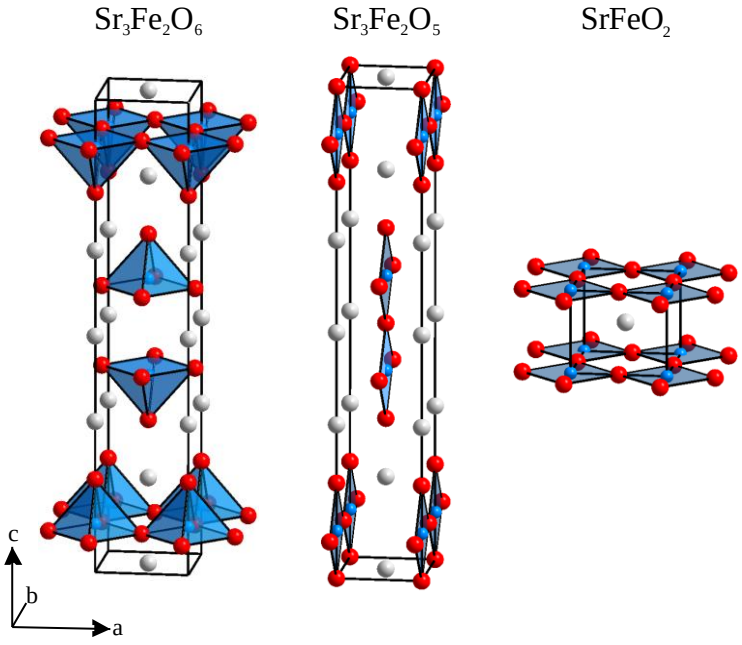

Figure 3.1: Structures of some topochemically reduced iron phases.

The topochemical reduction of complex cobalt oxides, in contrast, tends to result in phases in which the coordination around the Co centres is less rigorously square-planar. The topochemical reduction of $LaBaCo_2O_5$ to $LaBaCo_2O_{4.25}$ results in a phase that contains Co

centres in square-planar environments, along with square-based pyramidal and tetrahedral environments. The formation of this unusual anion arrangement appears to be driven more by the A-cation ordering than any particular coordination requirement of cobalt, as reduction of the isostructural starting phase $YBaCo_2O_5$ to $YBaCo_2O_{4.5}$ results in an entirely different structure type (Figure 3.2).[16]

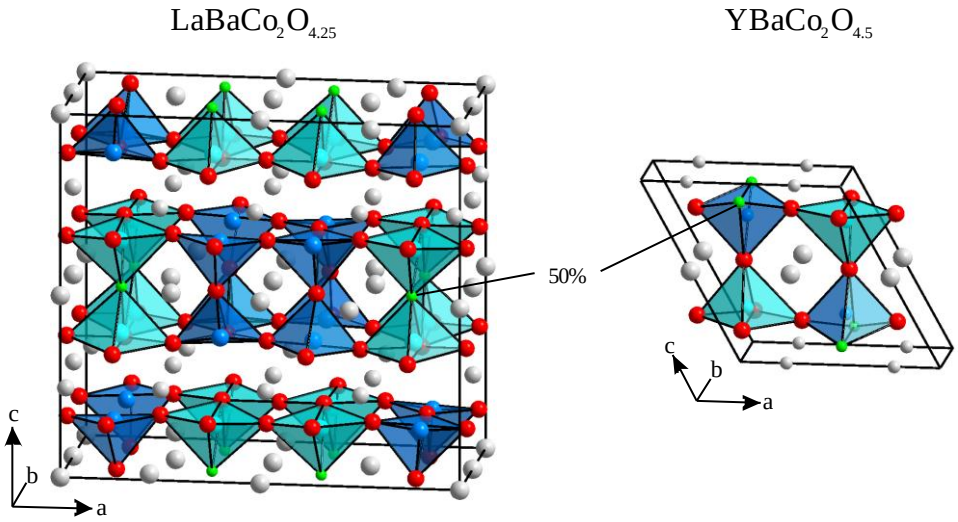

Figure 3.2: The structures of the topochemically reduced phases $LaBaCo_2O_{4.25}$ (left) and $YBaCo_2O_{4.5}$ (right).

The influence of cobalt on the arrangement of anion vacancies can also be observed in the structures adopted by $Sr_3(Fe_{1-x}Co_x)_2O_y$ phases.[18,56-59] In the case of the $x = 0$, all-Fe phase, there are no reports of isolated phases with an oxygen content $5 < y < 6$. The reported structures of $Sr_3Fe_2O_5$ and $Sr_3Fe_2O_6$ all show rigorous anion vacancy ordering.[18,19] Phases with $x = 0.5$, 1, in contrast, show increasing levels of anion vacancy disorder correlating to the level of Co doping (Figure 3.3).[56,57] This effect can also be observed in the reduction of $Sr(Fe_{1-x}Co_x)O_3$ where only phases with $x \leq 0.3$ form the infinite-layer structure.[60] This suggests that, in the absence of strong directing effects from the structure, the selectivity of topochemical reduction reactions is strongly dependent on the transition metal d-electron count.

Recent work by Dixon *et al.* has led to the successful topochemical reduction of the layered oxychloride phases $Sr_3(Fe_{1-x}Co_x)_2O_5Cl_2$ ($0 \leq x \leq 0.5$) to form $Sr_3(Fe_{1-x}Co_x)_2O_4Cl_2$ (Figure 3.4).[20,21] The selectivity of the reduction reactions of these phases appears indifferent to the identity of the transition metal B-cation, with isotructural end-points for all compositions studied.

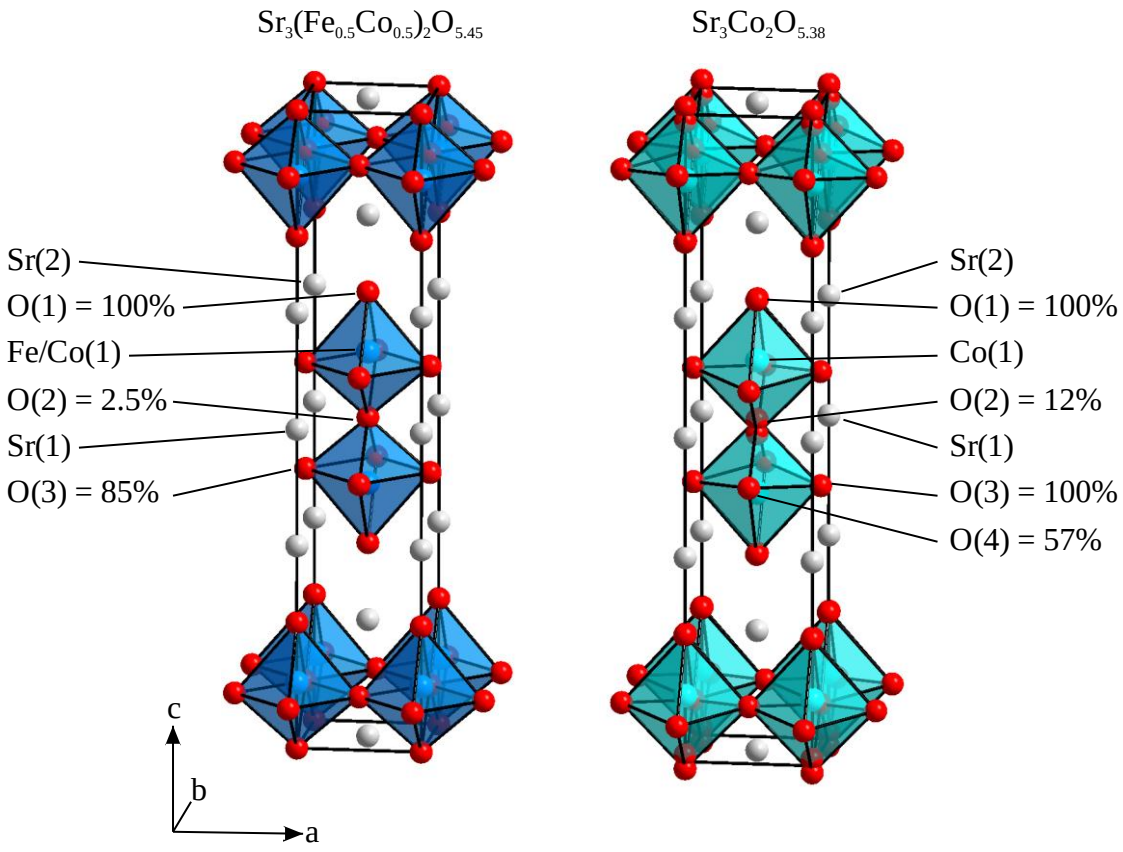

Figure 3.3: The structures of $Sr_3(Fe_{0.5}Co_{0.5})_2O_{5.45}$ (left) and $Sr_3Co_2O_{5.38}$ (right).

Substitution of the transition-metal B-cation site with Co led to a decrease in the magnetic ordering temperature and eventual formation of a spin-glass in $Sr_3(Fe_{0.5}Co_{0.5})_2O_4Cl_2$. This chapter details the synthesis and reduction of the $x = 1$ end-member of the series in order to analyse the effects of complete Co-substitution on the structural and magnetic properties of $Sr_3(Fe_{1-x}Co_x)_2O_4Cl_2$.

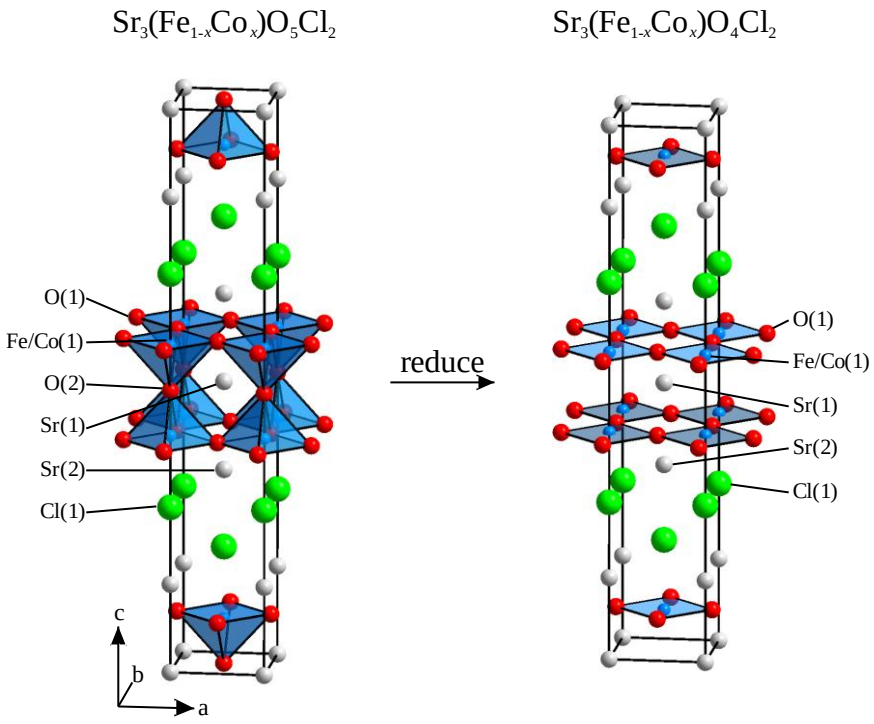

Figure 3.4: Topochemical reduction of $Sr_3(Fe_{1-x}Co_x)_2O_5Cl_2$.

3.2 Experimental

3.2.1 Synthesis of $Sr_3Co_2O_5Cl_2$

$Sr_2Co_2O_5$ was used as a precursor in the synthesis of $Sr_3Co_2O_5Cl_2$. This was synthesised using the method described by Grenier *et al.*[61] Suitable stoichiometric quantities of $SrCO_3$ (Alfa Aesar 99.99%) and Co_3O_4 (Alfa Aesar 99.9985%) were thoroughly mixed together using an agate mortar and pestle. The resulting powders were placed in an alumina crucible and then heated in air to 1100 °C for 12 hours to decompose the carbonates. The powders were then pressed into pellets and heated at 910 °C for two periods of two days with one intermediate grinding.

Samples of $Sr_3Co_2O_5Cl_2$ were prepared via the route previously described by Weller *et al.* for the synthesis of $Sr_3FeCoO_5Cl_2$.[62] Due to the moisture-sensitive nature of $SrCl_2$, all samples were kept under an inert atmosphere at all times. Suitable stoichiometric quantities of $Sr_2Co_2O_5$ and $SrCl_2$ (Alfa Aesar 99+ %, dried at 180 °C under vacuum) were thoroughly

mixed using an agate mortar and pestle in an argon-filled glovebox (O_2 and H_2O levels < 1 ppm). The resulting mixtures were then sealed under vacuum in silica ampoules and heated to 850 °C for two periods of 24 hours with one intermediate grinding. X-ray powder diffraction data collected from this material were consistent with a single phase with lattice parameters *a* = 3.91(1) Å and *c* = 24.00(1) Å, in good agreement with previously reported values (*a* = 3.89(1) Å and *c* = 23.88(1) Å).[63]

3.2.2 Reduction with Metal Hydrides

Previous research on the reduction of the related series of phases $Sr_3(Fe_{1-x}Co_x)_2O_4Cl_2$ (x = 0, 0.1, 0.3, 0.4 and 0.5) has shown that LiH can act as an effective solid state topochemical reducing agent for these materials.[20,21] The reduction of the x = 2 member of the series, $Sr_3Co_2O_5Cl_2$, with LiH was therefore attempted. Small samples (~ 200 mg) of $Sr_3Co_2O_5Cl_2$ were ground together with a 1:4 molar excess of LiH using an agate mortar and pestle in an argon-filled glovebox. These mixtures were then sealed under vacuum in Pyrex ampoules and heated to temperatures in the range 250 < T / K < 300 for periods of two days.

Reduction was also attempted in an analogous manner with a 1:2 molar excess of NaH in the temperature range 170 < T / K < 230. Preparation of large samples suitable for neutron diffraction were prepared using NaH at 200 °C for two periods of two days with an intermediate grinding. Removal of unwanted reaction by-products (NaOH and unreacted NaH) was performed by washing the samples under nitrogen with 2 x 100 ml of a 0.1 M solution of NH_4Cl, followed by 4 x 100 ml of clean methanol. The samples were then dried under vacuum before being returned to the glovebox.

3.3 Results

3.3.1 Reactivity

X-ray powder diffraction data were collected from the products of reaction with LiH. At temperatures ≤ 250 K, no reaction was observed to have taken place. At 260 K and above, samples decomposed to binary oxides, chlorides and elemental cobalt. Attempts were then made to reduce $Sr_3Co_2O_5Cl_2$ with NaH. X-ray powder diffraction collected from the products of small-scale test reactions performed in the range 170 < T / °C < 240 revealed the formation of a body-centred phase with lattice parameters similar to those of $Sr_3Fe_2O_4Cl_2$,[20] indicative of the successful topochemical reduction of $Sr_3Co_2O_5Cl_2$. Reaction temperatures above 240 °C resulted in decomposition to binary oxides, chlorides and elemental cobalt.

Examination of X-ray powder diffraction patterns before and after washing with methanol alone revealed a significant quantity (~ 50 % by weight) of the reduction products had reoxidised to the $Sr_3Co_2O_5Cl_2$ starting material during this procedure.

Use of a slightly acidic solvent (0.1 M NH_4Cl in methanol) was found to significantly reduce the amount of product undergoing reoxidation, but could not completely eliminate the problem. The high degree of air-sensitivity of reduced $Sr_3Co_2O_5Cl_2$ is consistent with the pyrophoric behaviour observed in the $Sr_3Fe_{2-x}Co_xO_5Cl_2$ series of phases.[21]

3.3.2 Structural Characterisation

3.3.2.1 X-ray Powder Diffraction at 298 K

X-ray powder diffraction data collected using a Siemens D5000 diffractometer from the washed product of the reaction between $Sr_3Co_2O_5Cl_2$ and NaH are shown in Figure 3.5.

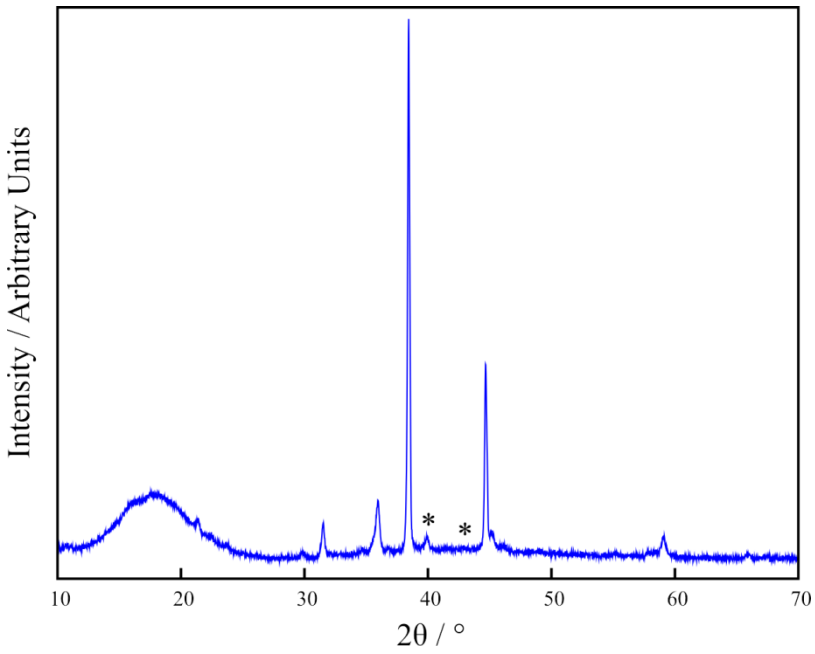

Figure 3.5: X-ray powder diffraction data collected from the washed products of reaction between $Sr_3Co_2O_5Cl_2$ and NaH. Reflections marked with an asterisk are due to the presence of reoxidised $Sr_3Co_2O_5Cl_2$. The large lump at 2θ ~ 18 ° is due to grease used to mount the sample.

The reflections in the data could be readily indexed on the basis of a body-centred tetragonal unit cell with lattice parameters a = 4.007(1) Å and c = 22.282(1) Å. This was consistent with topochemical reduction to form $Sr_3Co_2O_4Cl_2$. The presence of $Sr_3Co_2O_5Cl_2$ from reoxidation during the washing process is evident in the data (reflections marked with an asterisk in Figure 3.5).

3.3.2.2 Neutron Powder Diffraction at 298 K

Neutron powder diffraction data were collected from $Sr_3Co_2O_4Cl_2$ at 298 K using the POLARIS instrument at ISIS. These could be readily indexed using a body-centred tetragonal unit cell similar to those used for the $Sr_3(Fe_{1-x}Co_x)_2O_4Cl_2$ ($0 \leq x \leq 0.5$).[20,21] A structural model based on the refined structure of $Sr_3Fe_2O_4Cl_2$ was constructed and refined against the data. A small amount of $Sr_3Co_2O_5Cl_2$ was added as a second phase. The refinement converged readily to give a good statistical fit (χ^2 = 2.506).

Attempts were made to insert an oxide ion into the 'bridging' site of the structural model, but proved unsuccessful. The occupancy of this site consistently refined to zero, confirming the composition of the bulk phase as $Sr_3Co_2O_4Cl_2$.

Observed, calculated, and difference plots are shown in Figure 3.6. Full details of the structural parameters are given in Table 3.1 and selected bond lengths are given in Table 3.2.

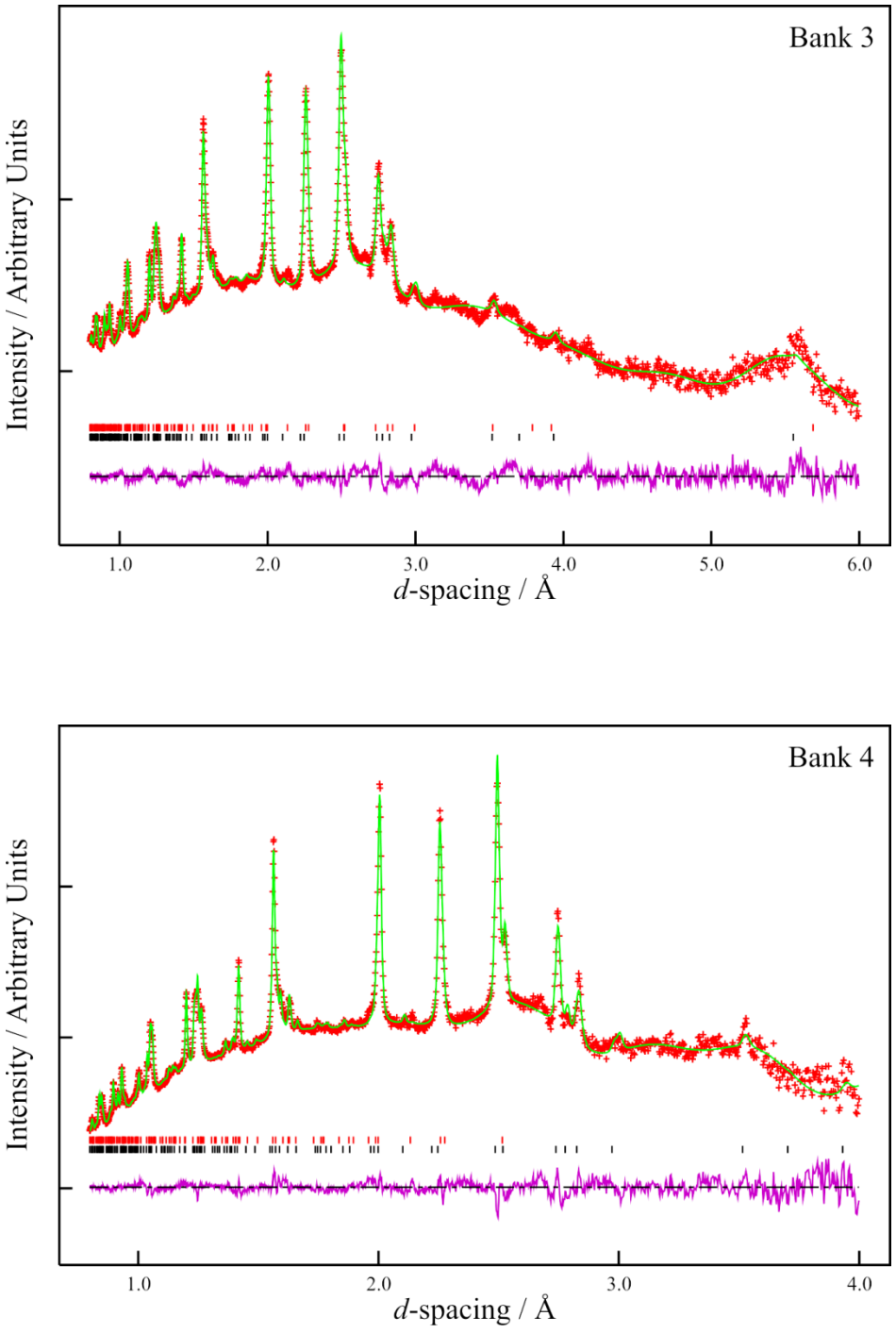

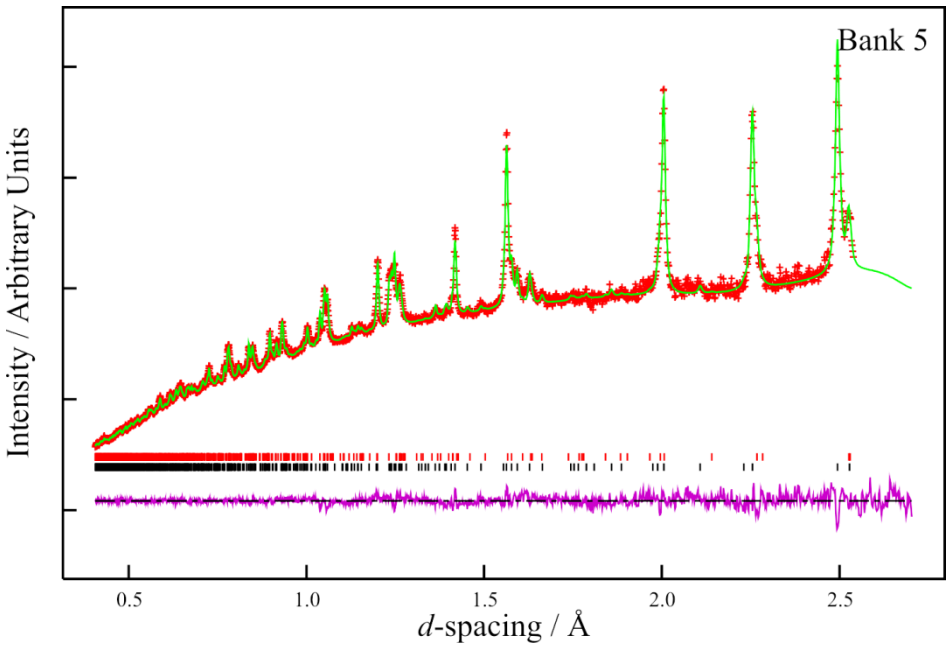

Figure 3.6: Observed, calculated, and difference plots for refinement of the structural model of $Sr_3Co_2O_4Cl_2$ at 298 K against neutron powder diffraction data collected using the POLARIS instrument. The upper set of tick marks corresponds to a ~ 10% by weight impurity of $Sr_3Co_2O_5Cl_2$.

Atom	Wyckoff Position	*x*	*y*	*z*	U_{iso} / Å^2
Sr(1)	2*a*	0	0	0	0.0033(7)
Sr(2)	4*e*	0	0	0.1526(1)	0.0038(5)
Co(1)	4*e*	0	0	0.4284(4)	0.0085(8)
O(1)	8*g*	1/2	0	0.0766(1)	0.0161(3)
Cl(1)	4*e*	0	0	0.2960(1)	0.0202(4)
$Sr_3Co_2O_4Cl_2$: space group *I*4/*mmm*; *a* = 4.007(1) Å and *c* = 22.282(1) Å; cell volume = 357.76(1) Å^3; weight fraction = 89.7%					
$Sr_3Co_2O_5Cl_2$: space group *I*4/*mmm*; *a* = 3.987(1) Å and *c* = 22.817(10) Å; cell volume = 362.70(1) Å^3; weight fraction = 10.3%					
χ^2 = 2.506, wRp = 0.64%, Rp = 0.90%					

Table 3.1: Refined structural parameters of $Sr_3Co_2O_4Cl_2$ at 298 K.

Cation	Anion	Bond Length / Å	Bond Valence Sum
Co(1)	O(1)	2.007(1) x 4	Co +1.79
	Cl(1)	2.950(2) x 1	
Sr(1)	O(1)	2.632(2) x 8	Sr +1.99
Sr(2)	O(1)	2.623(1) x 4	Sr +2.09
	Cl(1)	3.056(1) x 4	
	Cl(1)	3.195(3) x 1	
Co	Co	3.19(1)	

Table 3.2: Selected bond lengths and bond valence parameters from the refined structure of $Sr_3Co_2O_4Cl_2$ at 298 K.

3.3.2.3 Neutron Powder Diffraction at 5 K

Neutron powder diffraction data collected from $Sr_3Co_2O_4Cl_2$ at 5 K using the POLARIS instrument at ISIS exhibited a splitting of the diffraction peaks relative to the data collected at 298 K. This splitting was consistent with an orthorhombic distortion of the unit cell (Figure 3.8).

These data could be readily indexed on the basis of an orthorhombic unit cell with lattice parameters a = 3.9757(5) Å, b = 4.0294(5) Å, and c = 22.147(3) Å. An orthorhombic model (space group *Immm*) based on the structure of $Sr_3Co_2O_4Cl_2$ at 298 K was constructed and refined against the data to give a good statistical fit (χ^2 = 3.230). Observed, calculated, and difference plots are given in Appendix C. Full structural details of the refined structure are given in Table 3.3 and selected bond lengths are given in Table 3.4.

Atom	**Wyckoff Position**	***x***	***y***	***z***	U_{iso} / Å^2
Sr(1)	2*a*	0	0	0	0.0014(3)
Sr(2)	4*i*	0	0	0.1528(1)	0.0014(3)
Co(1)	4*i*	0	0	0.4276(3)	0.0090(5)
O(1)	4*j*	1/2	0	0.0749(4)	0.0094(5)
O(2)	4*j*	0	1/2	0.0773(4)	0.0094(5)
Cl(1)	4*i*	0	0	0.2952(1)	0.0110(5)
$Sr_3Co_2O_4Cl_2$: space group *Immm*; a = 3.9757(5) Å, b = 4.0294(5) Å, and c = 22.147(3) Å; cell volume = 357.76(1) Å^3; weight fraction = 89.7%					
$Sr_3Co_2O_5Cl_2$: space group *I*4/*mmm*; a = 3.983(1) Å and c = 22.720(10) Å; cell volume = 362.70(1) Å^3; weight fraction = 10.3%					
χ^2 = 3.230, wRp = 0.55%, Rp = 0.67%					

Table 3.3: Refined structural parameters of $Sr_3Co_2O_4Cl_2$ at 5 K.

Cation	**Anion**	**Bond Length / Å**	**Bond Valence Sum**
Co(1)	O(1)	2.015(1) x 2	Co +1.82
	O(2)	1.991(1) x 2	
	Cl(1)	2.932(7) x 1	
Sr(1)	O(1)	2.589(6) x 4	Sr +2.08
	O(2)	2.644(6) x 4	
Sr(2)	O(1)	2.632(6) x 2	Sr +2.10
	O(2)	2.618(6) x 2	
	Cl(1)	3.056(1) x 4	
	Cl(1)	3.154(3) x 1	
Co	Co	3.20(1)	

Table 3.4: Selected bond lengths and bond valence parameters from the refined structure of $Sr_3Co_2O_4Cl_2$ at 5 K.

These data showed additional features at large *d*-spacings consistent with the presence of a magnetic unit cell. Additional neutron powder diffraction data were collected from $Sr_3Co_2O_4Cl_2$ at 5 K using the D2b instrument, which provides increased sensitivity to large *d*-spacing features (Figure 3.7(a)).

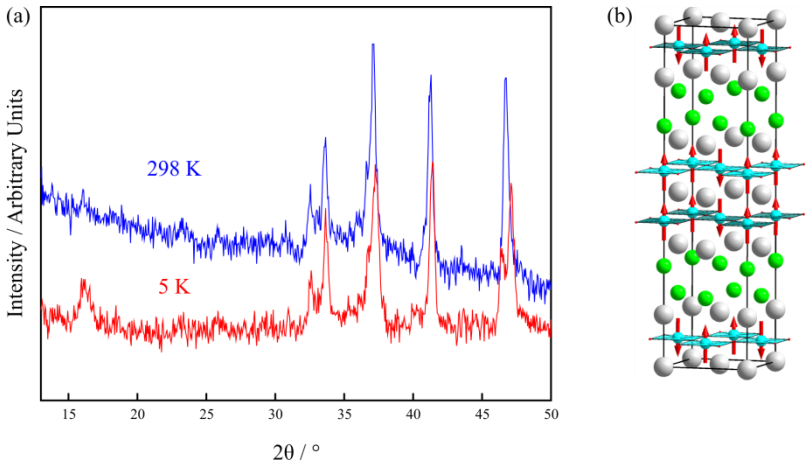

Figure 3.7: (a) Neutron powder diffraction data collected from $Sr_3Co_2O_4Cl_2$ at 298 K and 5 K using D2b. An additional peak at ~ 16 ° indicates long-range magnetic order. (b) The ordered model refined for $Sr_3Co_2O_4Cl_2$.

Additional features present in these diffraction data could be indexed on the basis of an expanded monoclinic unit cell with $a_{mag} \approx \sqrt{2}a_{cryst}$, $b_{mag} \approx \sqrt{2}b_{cryst}$, and $c_{mag} \approx c_{cryst}$. The data were best accounted for by a model in which the spins on neighbouring cobalt centres are aligned antiferromagnetically and adjacent sheets are aligned ferromagnetically. The spins on the cobalt centres are aligned parallel or antiparallel to the *z*-axis, with an ordered moment of 3.60(1) μ_B per cobalt centre (Figure 3.7(b)).

Full details of the magnetic refinement and fits to the data are given in Appendix C.

3.3.2.4 Variable Temperature Neutron Powder Diffraction

Neutron powder diffraction data were collected from $Sr_3Co_2O_4Cl_2$ as a function of temperature (Figure 3.8) in order to monitor the evolution of the structural distortion and magnetic ordering.

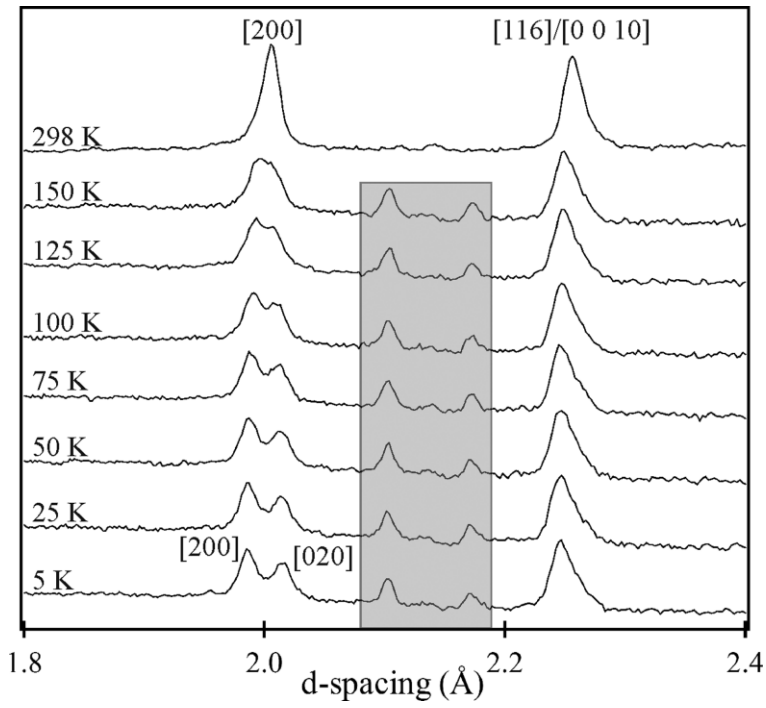

Figure 3.8: Neutron powder diffraction collected as a function of temperature from $Sr_3Co_2O_4Cl_2$ using the POLARIS instrument. Splitting of the [200] but not [116] or [0 0 10] indicates the presence of an orthorhombic distortion of the unit cell. Peaks in the shaded box correspond to contributions from the cryostat.

Structural and magnetic models were refined against these data to produce a plot of (b/a – 1) and the ordered moment per Co centre as a function of temperature, shown in Figure 3.9. These indicate that the orthorhombic distortion persists until T ~ 200 K, which is significantly higher than the magnetic ordering temperature (~ 50 K).

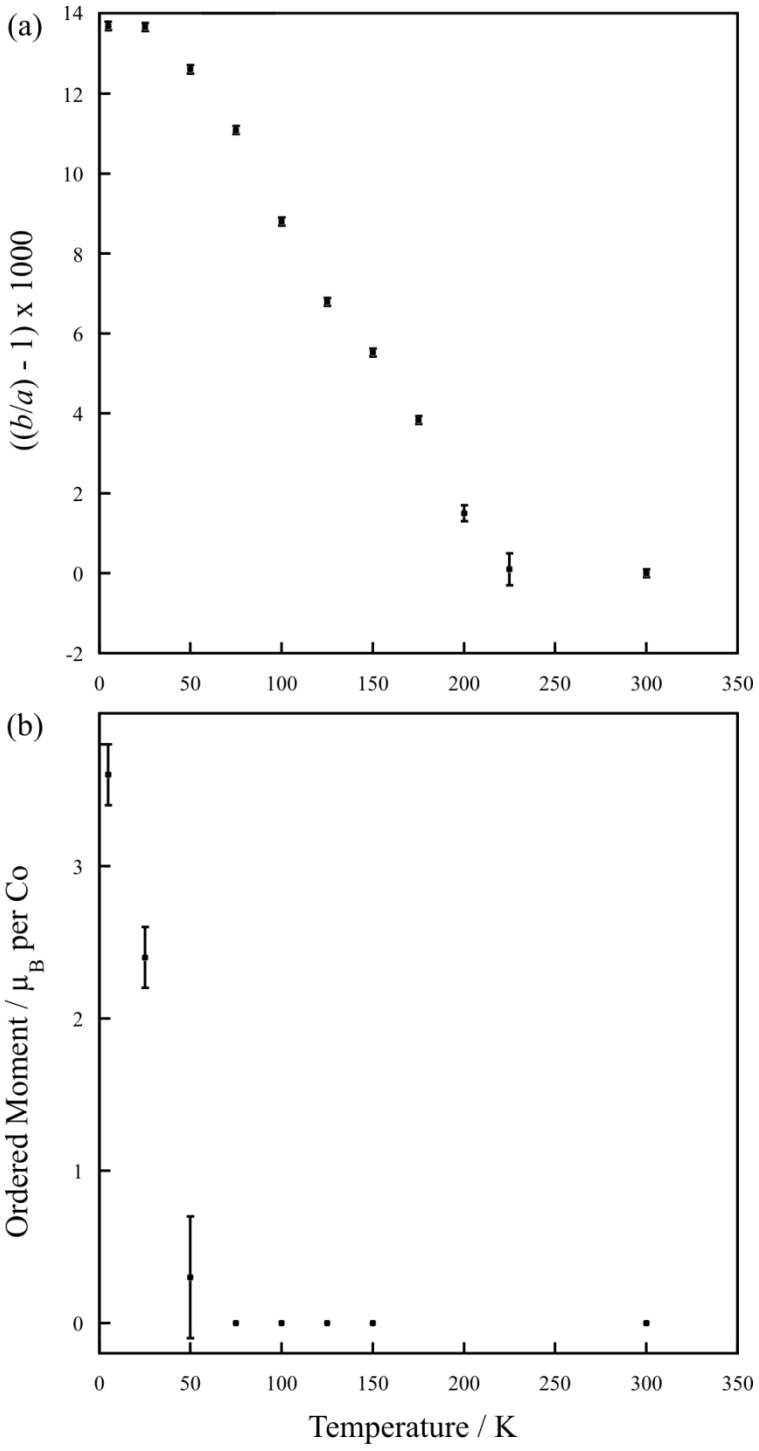

Figure 3.9: (a) A plot of (*b*/*a*) – 1 against temperature as a measure of the orthorhombic distortion of $Sr_3Co_2O_4Cl_2$. (b) The ordered antiferromagnetic moment of $Sr_3Co_2O_4Cl_2$ plotted as a function of temperature.

3.3.3 Magnetisation Measurements

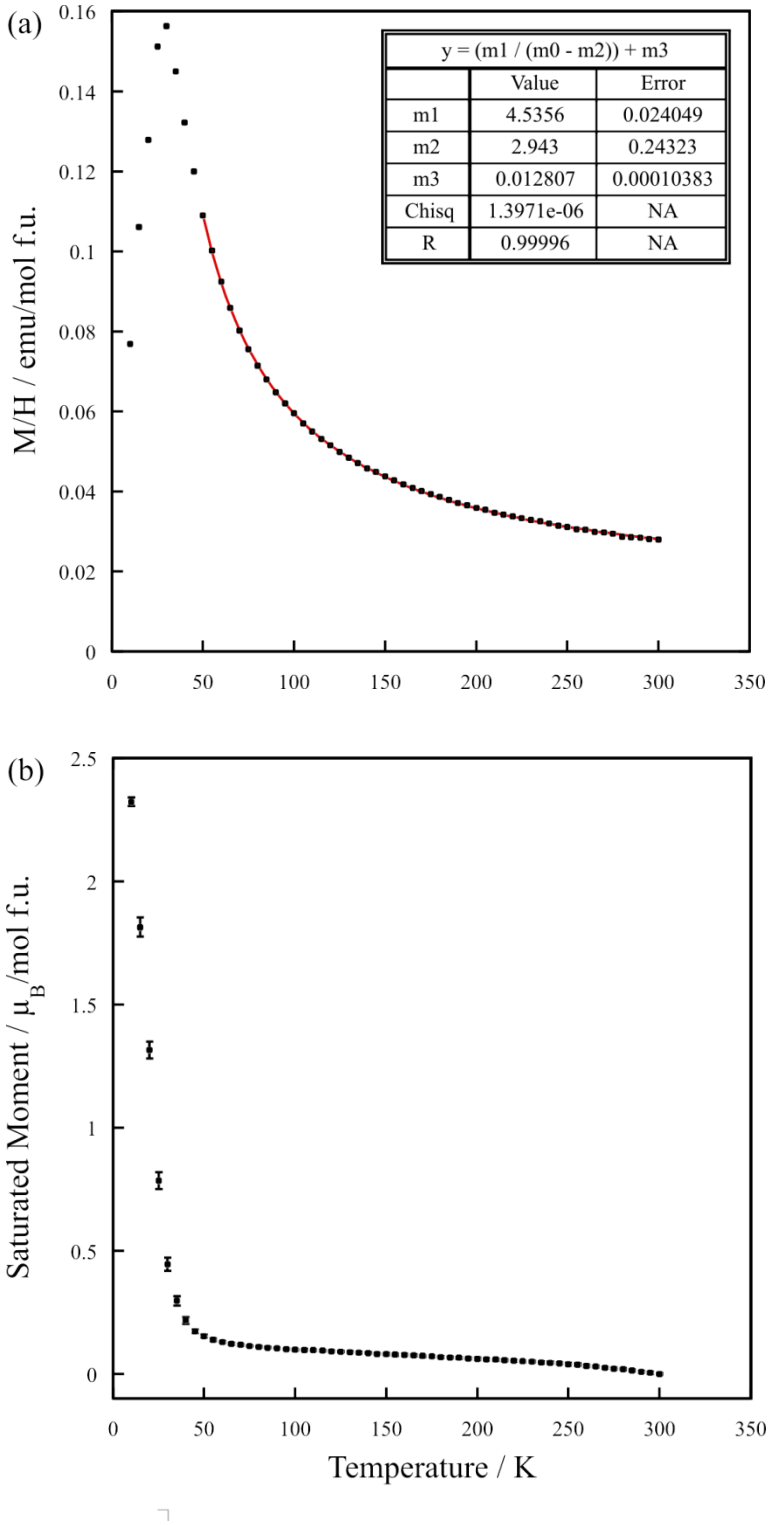

Figure 3.10: (a) The paramagnetic susceptibility of $Sr_3Co_2O_4Cl_2$ and fit to the Curie-Weiss law in the range $55 \leq T / K \leq 300$. (b) The saturated ferromagnetic moment.

Magnetisation data were collected from $Sr_3Co_2O_4Cl_2$ as a function of temperature using the ferromagnetic subtraction technique and are shown in Figure 3.10. These show a large

increase in the saturated ferromagnetic moment at T ~ 50 K, and a local maximum in the paramagnetic susceptibility at T ~ 35 K. These are consistent with the appearance of long range magnetic ordering observed in the low temperature neutron powder diffraction data. A fit of the paramagnetic susceptibility in the range $55 \leq T / K \leq 300$ to the Curie-Weiss law yields values of C = 4.53(3) cm^3 K mol^{-1} and θ = +2.94 K where mol^{-1} means per mole of formula units of $Sr_3Co_2O_4Cl_2$.

The observed Curie constant is much higher than would be expected for a spin-only Co^{II} system, even accounting for the 10% Co^{III} $Sr_3Co_2O_5Cl_2$ secondary phase (C_{exp} = 3.98 cm^3 K mol^{-1}).

The large increase in the saturated ferromagnetic moment (1.15 μ_B per Co centre at 5 K) indicates that there is a significant canting of the ordered cobalt spins. However, attempts to incorporate this into the magnetic refinements of low-temperature neutron powder diffraction were unsuccessful due to the low number of magnetic reflections.

A combination of the ordered moment at 5 K (3.60 μ_B) and the saturated ferromagnetic moment at 5 K (1.15 μ_B) as a vector sum yields a total value of 3.78 μ_B per Co centre. This value is also much larger than the 3 μ_B expected for a spin-only d^7, S = 3/2 Co^{II} system. This is consistent with a significant orbital contribution to the magnetism.

3.4 Discussion

3.4.1 Structural Selectivity

The reduction of $Sr_3Co_2O_5Cl_2$ proceeds in manner analogous to that of the $Sr_3(Fe_{1-x}Co_x)_2O_4Cl_2$ series of phases via removal of the central 'bridging' oxide ion to form a phase with composition $Sr_3Co_2O_4Cl_2$ containing double sheets of apex-linked $Co^{II}O_4$ square planes stacked with SrCl rocksalt layers.

The reduction of $Sr_3Fe_{2-x}Co_xO_5Cl_2$ results in phases where the B-cations adopt square-planar coordination environments for the entire $0 \leq x \leq 2$ range, and thus the electron count can be continuously varied from d^6 to d^7. In contrast, the reduction of $Sr(Fe_{1-x}M_x)O_3$ (M = Mn, Co) does not result in phases containing B-cations in square-planar environments when $x > 0.3$.[60] This suggests that in the latter case, the resulting d^6 electron configuration on reduction is important for the formation of square-planar arrays. The fact that the electron count for the $Sr_3Fe_{2-x}Co_xO_5Cl_2$ series of phases can be varied continuously over the entire range while displaying the same reduction behaviour suggests an additional component directing the selectivity of these reduction reactions. The high degree of selectivity in the reduction of $Sr_3Co_2O_5Cl_2$ can best be rationalised by considering the influence of the lattice itself rather than the identity of the B-cation on the formation energy of vacancies.

On reduction, the oxidation state of the B-cation will decrease, and thus the ideal geometry around it will contain fewer and/or longer anion contacts. However, the ideal geometry around the Sr centres will remain essentially unchanged. The most energetically favourable process is therefore the one that will maximise the change in the coordination environment of the B-cations while keeping that of the Sr-centres as unchanged as possible.

Bond valence sums have proved to be an effective tool in estimating the strength of various bonds in materials, and can therefore be used to estimate the most energetically favourable anion(s) to remove from a system on reduction. The anion for which BVS_B - BVS_{Sr} is most positive will result in the lowest vacancy formation energy. It should be noted that this approach assumes that, upon reduction, the system does not immediately relax into a more thermodynamically favourable configuration and that there are no electronic contributions (such as LFSE) that affect the strength of the interactions between cations and anions.

Contributions made by Co and Sr to the bond valence sums of the anions in $Sr_3Co_2O_5Cl_2$ are shown in Table 3.5.

	O(1)	**O(2)**	**Cl(1)**
Co(1)	0.916	1.696	0.069
Sr(1)	0.194	0.690	
Sr(2)	0.720		1.216
BVS_{Co} - BVS_{Sr}	0.002	**1.006**	-1.147

Table 3.5: Bond valence sums calculated for the anions of $Sr_3Co_2O_5Cl_2$.

From the table above, it can also be seen that the contribution of the chloride ions to the valence of the cobalt centres is minimal. In contrast, they account for more than half of the valence of Sr(2). Consequently, removal of the chloride ions from the structure would have a minimal impact on the coordination of the cobalt centres and result in extremely anion-deficient coordination about the Sr(2) centres. The equatorial oxide ion, O(1), contributes almost equally to the valence of the strontium and cobalt cations, while the bridging oxide O(2) contributes much more to the valence of cobalt than to that of strontium. The removal of the latter would therefore disturb the coordination of Sr the least while maximising the change to the coordination of Co. This prediction is in line with the observed selectivity. The selectivity of the reduction reaction of $Sr_3Co_2O_5Cl_2$ therefore appears to be directed by the substrate structure.

It can therefore be seen that it is possible to design a substrate such that the selectivity of topochemical reduction reactions can be controlled irrespective of the particular coordination preferences of the cations in the structure

3.4.2 Low-Temperature Structural Distortion

The structure of the sheets of apex-linked $Co^{II}O_4$ square planes present in $Sr_3Co_2O_4Cl_2$ is very similar to those observed in $Sr_2CoO_2Cl_2$ and $Ba_2CoO_2Cu_2S_2$ (Figure 3.11),[64,65] with very similar in-plane Co–O bond lengths for all three phases: 2.006(1) Å in $Sr_3Co_2O_4Cl_2$, 2.030 Å in $Sr_2CoO_2Cl_2$, and 2.032 Å in $Ba_2CoO_2Cu_2S_2$.

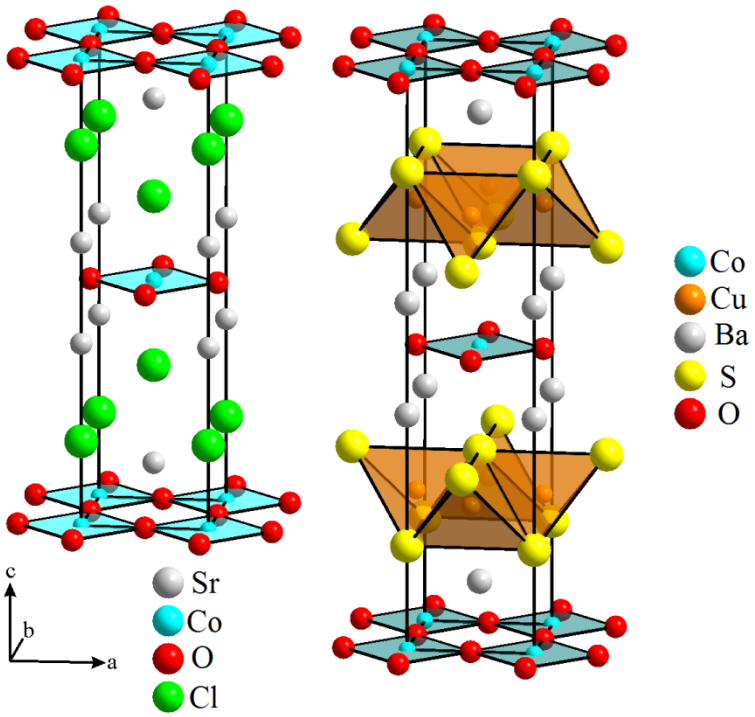

Figure 3.11: The structures of $Sr_2CoO_2Cl_2$ (left) and $Ba_2CoO_2Cu_2S_2$ (right).

On cooling below 200 K, $Sr_3Co_2O_4Cl_2$ undergoes a tetragonal to orthorhombic lattice distortion with a distortion ratio of $(b/a - 1) \sim 13.5 \times 10^{-3}$ at 5 K. In contrast, $Sr_2CoO_2Cl_2$ retains tetragonal symmetry down to the lowest temperature measured (20 K).[64] However, $Ba_2CoO_2Cu_2S_2$ undergoes a tetragonal to orthorhombic lattice distortion on cooling below 155 K, with a lattice distortion ratio of $(b/a - 1) \sim 3.5 \times 10^{-3}$ at 5 K.[65] Smura *et al.* proposed that this lattice distortion was due to magnetostriction.[65]

In $Ba_2CoO_2Cu_2S_2$, the magnetic moments are oriented mainly in the basal plane and point along one of the crystallographic axes, breaking the tetragonal symmetry of the structure (Figure 3.12). This type of ordering of magnetic moments that have an orbital component can lead to a structural distortion.[3] That magnetic ordering is responsible for the structural distortion in $Ba_2CoO_2Cu_2S_2$ is evidenced by the correlation between the orbital contribution to the magnetic moment and the size of the distortion.[65]

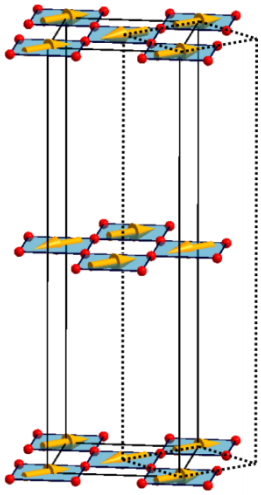

Figure 3.12: The magnetic structure adopted by $Ba_2CoO_2Cu_2S_2$.

The lattice in distortion in $Sr_3Co_2O_4Cl_2$, however, cannot be accounted for by magnetostriction for the following reasons:

1. The onset of the structural distortion occurs at a higher temperature than the magnetic ordering (T_{dist} ~ 200 K, T_N ~ 50 K). That is to say, the structural distortion is present in the absence of any long-range magnetic ordering (Figure 3.9).
2. Unlike in $(Sr_{1-x}Ba)_2CoO_2Cu_2S_2$, the ordered magnetic moments do not lie principally in the *ab* plane, but rather point mainly along *c* (Figure 3.7 (b)). Therefore any interaction that would lead to a breaking of the tetragonal symmetry would be comparatively weak. The small degree of canting of the spins in $Sr_3Co_2O_4Cl_2$ would produce a much smaller distortion than that seen in $(Sr_{1-x}Ba)_2CoO_2Cu_2S_2$.
3. The magnitude of the ordered moments in $Sr_3Co_2O_4Cl_2$ and $Sr_2CoO_2Cu_2S_2$ are almost equal (3.78 μ_B and 3.81 μ_B respectively), but the magnitude of the structural distortion in $Sr_3Co_2O_4Cl_2$ is ~ 30 times greater. As the fraction of barium increases in $(Sr_{1-x}Ba)_2CoO_2Cu_2S_2$, the orbital contribution to the magnetic moment (and thus the total ordered moment) increases, as does the magnitude of the structural distortion.

$Ba_2CoO_2Cu_2S_2$, which shows the largest orbital contribution to the magnetic moment, also has the largest structural distortion, but its magnitude remains ~ 4 times smaller than that present in $Sr_3Co_2O_4Cl_2$.[65]

The structural distortion observed in $Sr_3Co_2O_4Cl_2$ can be rationalised by considering the electronic structure of the Co^{II} centres. By analogy to the calculated electronic structure of Fe^{II} centres in $SrFeO_2$,[66] the local electronic structure of the Co^{II} centres in $Sr_3Co_2O_4Cl_2$ is shown in Figure 3.13.

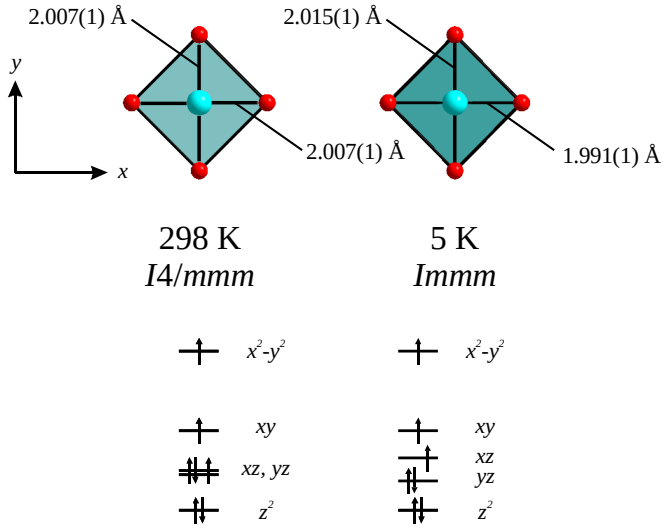

Figure 3.13: The local coordination geometry and electronic states of cobalt centers at 298 K (left) and 5 K (right).

The d^7, S = 3/2 system contains a pair of degenerate d_{xz} and d_{yz} orbitals occupied by three electrons, and is therefore unstable with respect to a Jahn-Teller structural distortion that lifts this degeneracy in order to lower the energy of the system. The structural distortion observed in $Sr_3Co_2O_4Cl_2$ is consistent with this lifting of degeneracy.

Jahn-Teller distortions are typically observed in oxide systems when octahedrally coordinated transition metal centres possess unevenly occupied degenerate e_g orbitals ($d_{x^2-y^2}$ and d_{z^2}). For

example, d^4 e_g^1 Cr^{2+} or Mn^{3+} or d^9 e_g^3 Cu^{2+} usually exhibit Jahn-Teller distortions in complex oxide phases (e.g. La_2CuO_4).[67]

Low spin Co^{2+} in octahedral environments (t_{2g}^6 e_g^1) is also susceptible to Jahn-Teller distortions, as observed in $A_2BCo(NO_2)_6$ (A = K, Rb; B = Sr, Ba). In these phases, the largest value obtained for the magnitude of the resulting structural distortion, observed in $Rb_2SrCo(NO_2)_6$ is (c/a – 1) ~ 31.6 x 10^{-3}, approximately twice that observed in $Sr_3Co_2O_4Cl_2$.[68]

Materials with unevenly occupied degenerate e_g orbitals generally display Jahn-Teller distortions due to the strong interactions between the e_g $d_{x^2-y^2}$ and d_{z^2} orbitals and the O 2*p* orbitals with *σ*-type symmetry, which makes breaking of the degeneracy particularly energetically favourable. Systems that possess uneven occupation of t_{2g} d_{xy}, d_{xz} and d_{yz} orbitals, in contrast, rarely show Jahn-Teller distortions. The much weaker interactions between these orbitals and the O 2*p* orbitals with π-symmetry means that any electronic stabilisation of the d-orbitals gained by distorting the symmetry is rarely enough to overcome the energy lost by distorting a high-symmetry structure.

In light of this, it is rather surprising that $Sr_3Co_2O_4Cl_2$ exhibits such a pronounced Jahn-Teller distortion from degenerate π-symmetry t_{2g} orbitals. Such distortions driven by degenerate t_{2g} orbitals usually rely on amplification of the stabilising effect by coupling to another electronic degree of freedom.

This is observed in, for example, $NaTiO_2$ and $NaVO_2$ (Ti^{3+} = d^1, t_{2g}^1; V^{3+} = d^2, t_{2g}^2) where the distortion not only lifts the degeneracy of the t_{2g} orbitals, but also relieves the strong magnetic frustration by distorting the triangular symmetry of the crystal structure (Figure 3.14).[69,70]

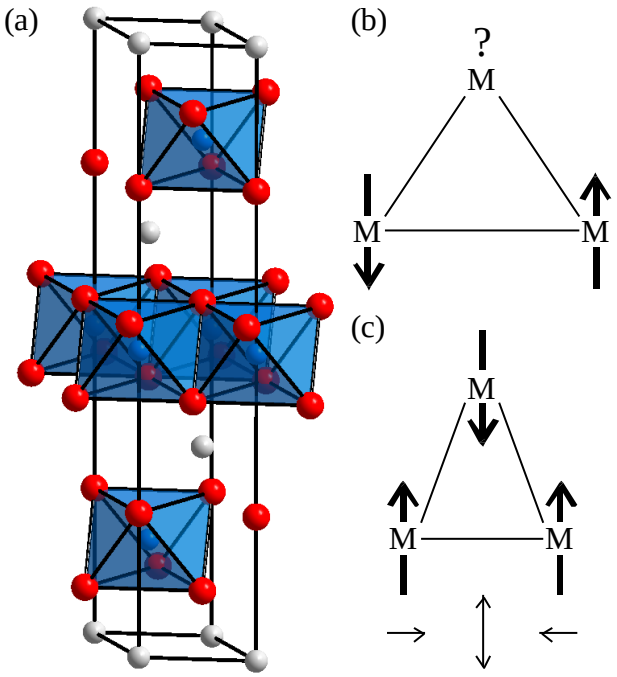

Figure 3.14: (a) The structure adopted by $NaMO_2$ (M = Ti, V). (b) The magnetic frustration resulting from a triangular lattice with all antiferromagnetic interactions. (c) Low temperature structural distortion causes a change in some interactions to ferromagnetic ordering, relieving the frustration.

Similarly, $LaTiO_3$ (t_{2g}^1) exhibits weak Jahn-Teller distortion at room temperature, which is increased by an order of magnitude at the onset of magnetic ordering (T_N = 150 K).[71]

It should be noted that other systems with square-planar Co^{II} centres, such as $Sr_2CoO_2Cl_2$ and $(Sr_{1-x}Ba)_2CoO_2Cu_2S_2$ are also susceptible to this type of structural distortion, as they have identical electronic states. That no such distortion is observed in these materials suggests that the elastic strain on the 'single-layer' phases is too great to allow lattice deformation.

Alternatively, interactions between the d_{xz} and d_{yz} orbitals of Co centres in adjacent layers could provide additional stabilisation on distorting from a tetragonal structure. The lack of such stabilising interactions in the single-layer materials could explain the differing behaviour.

3.4.3 Magnetic Behaviour

Both the low temperature ordered moment and the high temperature paramagnetic moment of $Sr_3Co_2O_4Cl_2$ are much higher than would be expected from a simple spin-only S = 3/2 Co^{II} system (Table 3.6). This suggests a significant orbital contribution to the magnetic behaviour.

	Expected	**Observed**
Ordered Moment	3 μ_B	3.78 μ_B
Paramagnetic Moment	3.98 cm^3 K mol^{-1}	4.53 cm^3 K mol^{-1}

Table 3.6: Expected and observed magnetic moments from $Sr_3Co_2O_4Cl_2$.

Clarke *et al.* have studied the orbital contribution to the magnetic moments of $Co^{II}O_4X_2$ (X = O, S, halogen) as a function of their coordination geometry and produced a plot of the ordered moment as a function of the ratio of the axial Co–X to the equatorial Co–O bond lengths.[65]

Using a ratio of Co–Cl/Co–O of 1.46 in $Sr_3Co_2O_4Cl_2$, an ordered moment of ~ 3.4 μ_B is predicted. The disagreement between this predicted value and the observed value of 3.78 μ_B is most likely due to the fact that the cobalt centres in $Sr_3Co_2O_4Cl_2$ do not find themselves in a $Co^{II}O_4X_2$ environment, but rather in a $Co^{II}O_4XCo$ environment (Co – Co = 3.20 Å). The interaction between adjacent cobalt cations perturbs the d-orbital energies of the cobalt centres, resulting in a modified orbital contribution to the magnetic moment.

In addition, $Sr_3Co_2O_4Cl_2$ displays a much lower magnetic ordering temperature (50 K) than the structurally related single-layer phases $Sr_2CoO_2Cl_2$ and $Ba_2CoO_2Cu_2S_2$ (T_N ~ 215 K and T_N ~ 210 K respectively).[64,65] This difference cannot be attributed to separation between the layers.

The ordering temperature of layered transition metal oxides depends strongly on the distance between the layers. For example, $LaSrMnO_{3.5}$ and $LaBaMnO_{3.5}$ order at 155 K and 135 K

respectively; the separation between the $MnO_{1.5}$ layers is 7.10 Å and 7.35 Å respectively.[72] Coupling between the layers in these phases proceeds via a through-space mechanism that is much weaker than M–O–M superexchange or M–M direct exchange. This also accounts for the much lower ordering temperature in $Sr_3Fe_2O_4Cl_2$ (T_N ~ 378 K), where double-sheets of $Fe^{II}O_4$ square-planes are separated by SrCl rocksalt layers, compared with the infinite layer $SrFeO_2$, where all interactions are M–O–M superexchange or M–M direct exchange (T_N ~ 473 K).[20,55]

However, the separation between the layers in $Sr_3Co_2O_4Cl_2$ is 7.727 Å, while that in $Sr_2CoO_2Cl_2$ is 7.559 Å and that in $Ba_2CoO_2Cu_2S_2$ is 9.383 Å.[64,65] The 3D ordering temperature of $Sr_3Co_2O_4Cl_2$ should therefore fall between that of $Sr_2CoO_2Cl_2$ and $Ba_2CoO_2Cu_2S_2$.

Furthermore, the analogous all-iron phase $Sr_3Fe_2O_4Cl_2$ adopts a G-type antiferromagnetic ordering (Figure 3.15), with antiferromagnetic coupling within and between the FeO_2 layers.[20] In contrast, $Sr_3Co_2O_4Cl_2$ still contains antiferromagnetically ordered sheets, but they couple to each other ferromagnetically. The competition between antiferromagnetic and ferromagnetic order between the sheets explains the glassy magnetic behaviour observed in the $Sr_3(Fe_{1-x}Co_x)_2O_4Cl_2$ series of phases.[21]

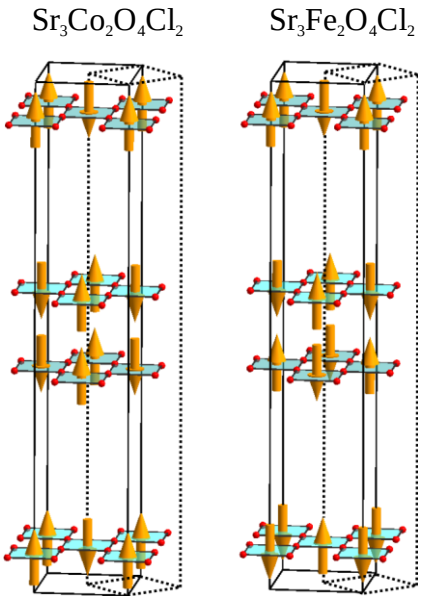

Figure 3.15: The magnetic structures of $Sr_3Co_2O_4Cl_2$ (left) and $Sr_3Fe_2O_4Cl_2$ (right).

The antiferromagnetic coupling between the layers in $Sr_3Fe_2O_4Cl_2$ arises from direct exchange between half-filled (d_{xz}, d_{yz}) orbitals.[20] The Goodenough-Kanamori rules predict interactions between full and half-full orbitals should lead to ferromagnetism.[3] In $Sr_3Co_2O_4Cl_2$, the d_{xz} and d_{yz} orbitals are half-full and full respectively, and therefore orbital ordering leading to interaction between d_{xz} and d_{yz} orbitals would lead to ferromagnetism. Such orbital ordering is incompatible with the observed low-temperature structural distortion: in order for a half-empty d_{xz} orbital to interact with a full d_{yz} orbital below it, the cobalt centres in adjacent layers must distort in orthogonal directions as shown in Figure 3.16. This arrangement would lead to a $\sqrt{2}a$ x $\sqrt{2}b$ x c expansion in the unit cell. This kind of antiferrodistortive ordering has been observed in $KCuF_3$ and K_2CuF_4.[73,74]

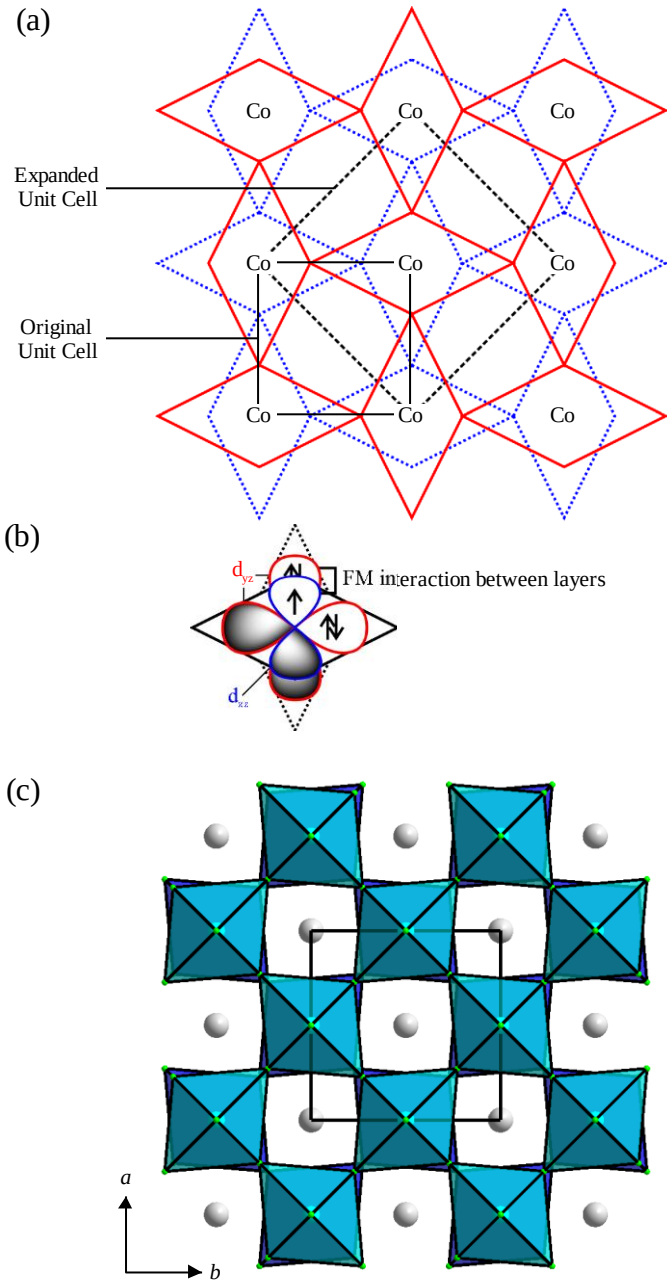

Figure 3.16: (a) Cartoon depiction of the expected distortion leading to ferromagnetic coupling between layers. The red and blue outlines correspond to different layers. (b) π-type exchange leading to ferromagnetism resulting from orbital ordering. (c) The structure of the distorted CuF_6 octahedra in $KCuF_3$.

The observed tetragonal to orthorhombic ferrodistortive ordering forces interactions between like orbitals, d_{xz} into d_{xz} and d_{yz} into d_{yz}. The cause of the ferromagnetic interaction is therefore somewhat of a mystery. It becomes apparent that the coupling between adjacent CoO_2 layers is responsible for behaviour that is markedly different from that of the isolated

single layers in $Sr_2CoO_2Cl_2$ and $Ba_2CoO_2Cu_2S_2$, leading to unexpected structural and electronic behaviour, such as the greatly reduced ordering temperature and the unexpected magnetic interaction between layers.

3.5 Conclusion

From the selectivity of the reduction reactions of the $Sr_3(Fe_{1-x}Co_x)_2O_4Cl_2$ series of phases, we can see that by carefully choosing the substrate material, we can exert a measure of control over the selectivity of topochemical reduction reactions. Such systems can in turn be used to tune the physical properties of materials by varying the *d*-electron count.

The controlled reaction of a carefully selected starting material has enabled the preparation of a material with a highly unusual electronic structure that exhibits strong coupling between the structural lattice and the electronic configuration. A similar synthesis strategy should enable the preparation of a large number of phases exhibiting complex correlated behaviour.

The research and findings in this chapter have been reported in a recent publication.[75]

Chapter 4 The Reduction of $Sr(Ru_{0.5}Fe_{0.5})O_3$

4.1 Introduction

Topochemical reduction of complex metal oxides with binary metal hydrides has enabled the preparation of a wide range of metastable phases containing low-valent metal centres such as square-planar Ni^{+}, Co^{+} and Fe^{2+} and octahedral Mn^{+}.[14-16,55] Reactions of this type are relatively well-studied for complex oxides of first row transition metals. However, analogous chemistry of complex oxides of second or third row transition metals has received comparatively little attention.

The topochemical reduction/oxidation of complex oxides of ruthenium is a particularly attractive prospect for a number of reasons:

- Ruthenium's position directly below iron in the periodic table would enable us to gain additional insight into the unexpected stability of Fe^{2+} in square-planar coordination environments. In addition, the reduction of $SrFeO_{3-\delta}$ and $Sr_3Fe_2O_6$ proceeds easily to form very stable products with high decomposition temperatures.[55] Exploitation of group trends in reactivity could lead to the formation of similarly stable products.
- Ruthenium oxides have been described as possessing 'schizophrenic' electrons.[26] That is to say, within a very narrow range of related structures, ruthenium oxides exhibit wildly different electronic and magnetic properties. For instance, $SrRuO_3$ is a ferromagnet with a transition temperature of $T_N \sim 160$ K while $CaRuO_3$ displays Curie-Weiss behaviour with a large negative Weiss temperature ($\theta \sim -200$ K). Similarly, Sr_2RuO_4 displays metallic behaviour with a transition to the only known *p*-wave superconducting state known at T = 1.5 K. In contrast, Ca_2RuO_4 is a Mott insulator. Small changes in the structure such as additional twisting of RuO_6 octahedra in the phases due to the smaller size of the Ca^{2+} cations lead to wildly

different properties and switching between localised and delocalised electrons.[26] Ruthenium oxides are therefore a promising area to search for both technologically useful materials as well as phases displaying esoteric properties.

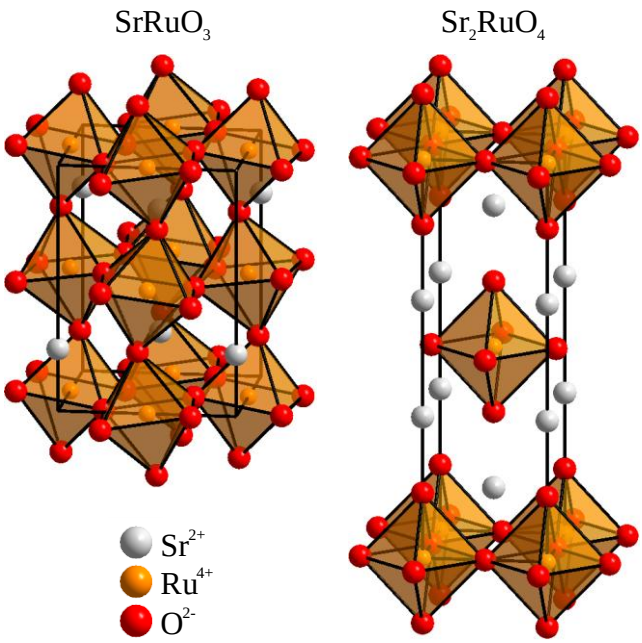

Figure 4.1: The structures of $SrRuO_3$ and Sr_2RuO_4.

The reduction of $SrRuO_3$, as well as that of the $Sr(Ru_{1-x}Fe_x)O_3$ solid solution would therefore prove to be an excellent starting point to begin exploring the topochemical reduction of second row transition metal oxides and ruthenium oxides in particular and their magnetic and electronic properties.

4.2 Experimental

4.2.1 Synthesis of $Sr(Ru_{0.5}Fe_{0.5})O_3$

Samples of $Sr(Ru_{0.5}Fe_{0.5})O_3$ were initially prepared via two different methods:

- The method previously described by Battle *et al*[76] via direct combination of $SrCO_3$ (Alfa Aesar 99.99%), Fe_2O_3 (Alfa Aesar 99.99%) and RuO_2 (from RuO_2 hydrate

(Alfa Aesar 99.99%) dried at 800 °C) ground together using an agate mortar and pestle. The resulting powders were placed in an alumina crucible and heated at 1 °C min^{-1} to 900 °C in air to decompose the carbonates. The powders were then reground, pressed into 13 mm diameter pellets and heated at 1300 °C for two periods of two days in air with one intermediate grinding.

- Use of a citrate gel precursor (see Section 2.3) from suitable stoichiometric quantities of $SrCO_3$, Fe metal (Alfa Aesar 99.99%) and RuO_2. The resulting powders were then treated in the same manner as above.

The resulting powders were observed to be phase-pure by laboratory X-ray powder diffraction, with lattice parameters a = 5.54(1) Å, b = 5.54(1) Å, and c = 7.87(1) Å, in good agreement with reported values (a = 5.54(1) Å, b = 5.54(1) Å, and c = 7.88(1) Å).[76] These data could be refined in $I2/c$ (No. 15) space group with only one Ru/Fe site. No evidence of ruthenium iron ordering was observed.

4.2.1 Synthesis of $SrRuO_3$

Samples of $SrRuO_3$ were prepared via the method previously described by Battle *et al.*[77] Suitable stoichiometric quantities of $SrCO_3$ and RuO_2 were ground together using an agate mortar and pestle. The resulting powder was calcined at 1000 °C for 24 hours before being pressed into pellets and heated at 1150 °C in air for two periods of two days.

The resulting powders were observed to be phase-pure by laboratory X-ray powder diffraction, with lattice parameters a = 5.57(1) Å, b = 5.54(1) Å, and c = 7.85(1) Å, in good agreement with reported values (a = 5.57(1) Å, b = 5.53(1) Å, and c = 7.84(1) Å).[77]

4.2.2 Synthesis of Other $Sr(Ru_{1-x}Fe_x)O_3$ Phases

Ru-rich phases with compositions $Sr(Ru_{0.6}Fe_{0.4})O_3$ and $Sr(Ru_{0.75}Fe_{0.25})O_3$ were synthesised from citrate gel precursors using the same route described above for the synthesis of

$Sr(Ru_{0.5}Fe_{0.5})O_3$. The resulting powders were observed to be phase pure by laboratory X-ray powder diffraction, with lattice parameters a = 5.56(1) Å, b = 5.54(1) Å, and c = 7.86(1) Å and a = 5.55(1) Å, b = 5.54(1) Å, and c = 7.85(1) Å respectively.

Attempts were made to synthesise the Fe-rich phases $Sr(Ru_{0.4}Fe_{0.6})O_3$ and $Sr(Ru_{0.25}Fe_{0.75})O_3$ via the methods described above for the synthesis of $Sr(Ru_{0.5}Fe_{0.5})O_3$. Laboratory X-ray powder diffraction data indicated that these compositions did not form a single phase, but rather a mixture of $Sr(Ru_{0.5}Fe_{0.5})O_3$ and $SrFeO_{3-\delta}$.

4.2.3 Reduction with Metal Hydrides

The reduction of $Sr(Ru_{1-x}Fe_x)O_3$ x = 0, 0.25, 0.4, 0.5, 0.6, and 0.75 was attempted with NaH, LiH and CaH_2 as solid-state reducing agents. In order to assess the reactivity of these materials, small samples (~ 200 mg) were ground together with a double (quadruple in the case of LiH) molar excess of each of the metal hydrides in an argon filled glovebox using an agate mortar and pestle. These mixtures were then sealed in Pyrex ampoules (or silica for reactions to be performed at temperatures above 400 °C) and heated at a series of temperatures in the range $200 \leq T / °C \leq 230$ when using NaH, $280 \leq T / °C \leq 350$ when using LiH, and $280 \leq T / °C \leq 450$ when using CaH_2 for periods of two days. Large samples suitable for neutron diffraction were prepared using two mole equivalents of CaH_2 in a pressure venting apparatus (Section 2.4.2) for two periods of two days. Reaction progress was monitored using X-ray powder diffraction.

Once a reaction was judged to be complete, the products were washed with 4 x 100 ml of a 0.1 M NH_4Cl solution in methanol, followed by 4 x 100 ml of clean methanol in order to remove unreacted metal hydrides and oxide/hydroxide reaction by-products. The samples were then dried under vacuum and returned to the glovebox.

4.3 Results

4.3.1 Reactivity

4.3.1.1 $Sr(Ru_{0.5}Fe_{0.5})O_3$

X-ray powder diffraction data collected from the washed products of reaction between $Sr(Ru_{0.5}Fe_{0.5})O_3$ and NaH revealed no reaction had taken place at any temperature below 230 °C. Reactions performed at 230 °C led to decomposition of the sample.

X-ray powder diffraction data collected from the washed products of reaction between $Sr(Ru_{0.5}Fe_{0.5})O_3$ and LiH or CaH_2 revealed that in both cases, no reaction occurred at temperatures below 300 °C. Reactions performed between 300 and 350 °C (LiH) and between 300 and 450 °C (CaH_2) led to a change in lattice parameters. Reactions performed at temperatures above 350 °C (LiH) and 450 °C (CaH_2) led to decomposition of the samples, as indicated by the presence of peaks corresponding to SrO and elemental Ru and Fe in the resulting X-ray powder diffraction data.

X-ray powder diffraction data collected from the washed products of the reduction of $Sr(Ru_{0.5}Fe_{0.5})O_3$ prepared via the ceramic method revealed incomplete reduction, even when the dwell time of the reaction was increased to 10 days (Figure 4.2). An extra peak can be observed at 33 °, consistent with some unreduced material. X-ray powder diffraction data collected from the washed products of the reduction of $Sr(Ru_{0.5}Fe_{0.5})O_3$ prepared via citrate gel methods, on the other hand, presented sharp diffraction peaks with no unaccounted-for features, after only 2 periods of 2 days. This indicates that thorough mixing of the transition metals is essential to produce a homogeneous product.

Peaks in the X-ray powder diffraction data of samples reduced with CaH_2 were sharper than those of samples reduced using LiH. Samples reduced using CaH_2 were therefore used in all subsequent measurements.

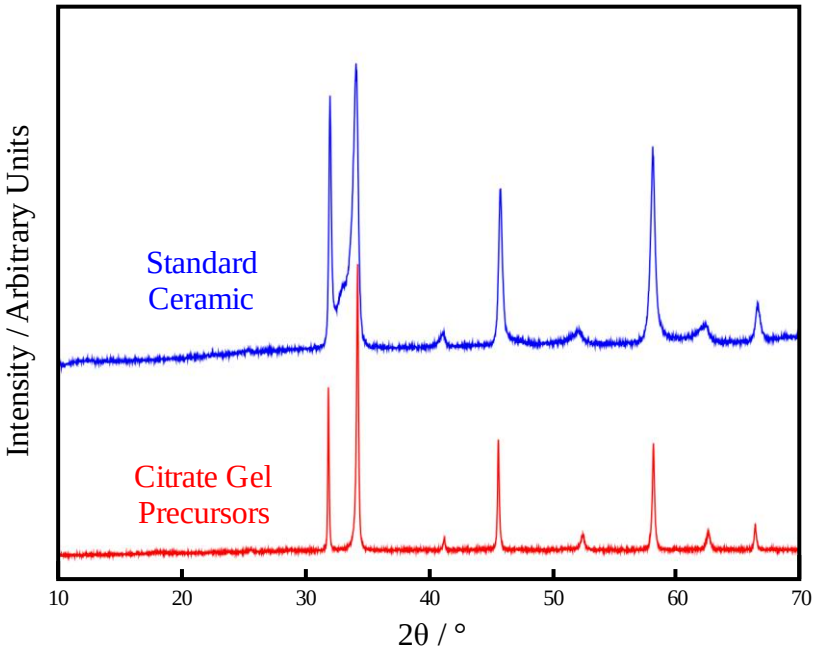

Figure 4.2: X-ray powder diffraction data collected from the washed products of reaction between CaH_2 and $Sr(Ru_{0.5}Fe_{0.5})O_3$ prepared via standard ceramic methods (top) and prepared via citrate gel methods (bottom).

4.3.1.2 $SrRuO_3$, $Sr(Ru_{0.6}Fe_{0.4})O_3$ and $Sr(Ru_{0.75}Fe_{0.25})O_3$

X-ray powder diffraction data collected from the washed products of reaction between $SrRuO_3$ and NaH revealed no reaction had taken place at any of the temperatures below 230 °C. Reactions performed at 230 °C led to decomposition of the sample to SrO and elemental Ru as shown by X-ray powder diffraction.

X-ray powder diffraction data collected from the washed products of reaction between $SrRuO_3$ and LiH or CaH_2 revealed that in both cases, no reaction occurred at temperatures below 325 °C. Reactions performed at temperatures above 325 °C led to decomposition of the samples to elemental ruthenium and SrO.

X-ray powder diffraction data collected from the washed products of reaction between $Sr(Ru_{0.6}Fe_{0.4})O_3$ or $Sr(Ru_{0.75}Fe_{0.25})O_3$ and CaH_2 indicate that their behaviour is analogous to

that of $SrRuO_3$ with no reaction taking place below 350 ° C and decomposition to SrO, elemental ruthenium and elemental iron for reactions carried out at 350 °C and above. This indicates that $Sr(Ru_{0.5}Fe_{0.5})O_3$ is the only member of the solid-solution that can be topochemically reduced.

4.3.2 X-ray Powder Diffraction

X-ray powder diffraction data collected from the washed products of the reduction of $Sr(Ru_{0.5}Fe_{0.5})O_3$ with CaH_2 could be indexed on the basis of a primitive tetragonal unit cell with lattice parameters a = 3.99(1) Å and c = 3.49(1) Å. These lattice parameters are very similar to those of the topochemically reduced phase $SrFeO_2$ (a = 3.99 Å and c = 3.47 Å),[55] and are therefore consistent with topochemical reduction to form $Sr(Ru_{0.5}Fe_{0.5})O_2$.

4.3.3 Thermogravimetric Analysis

Thermogravimetric analysis was performed by heating a small amount of the washed products of the reduction of $Sr(Ru_{0.5}Fe_{0.5})O_3$ with CaH_2 under a flow of oxygen to form $Sr(Ru_{0.5}Fe_{0.5})O_3$ (confirmed by X-ray powder diffraction). A mass gain of +8.4% is consistent with a composition of $Sr(Ru_{0.5}Fe_{0.5})O_{1.97(5)}$ for the reduced phase.

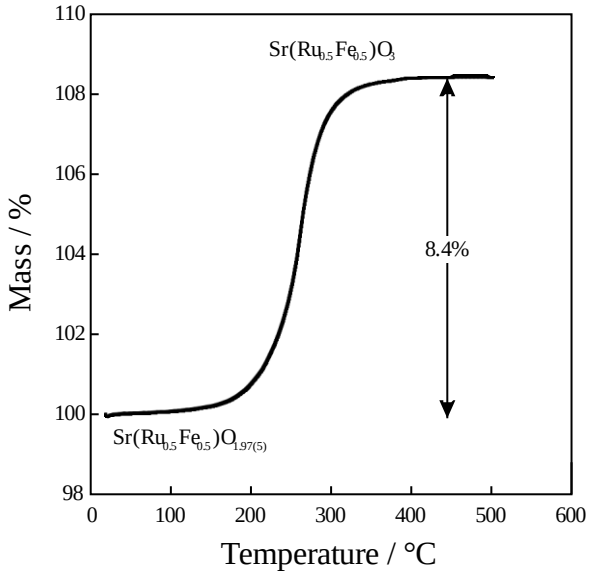

Figure 4.3: Thermogravimetric data collected during the reoxidation of $Sr(Ru_{0.5}Fe_{0.5})O_2$ to $Sr(Ru_{0.5}Fe_{0.5})O_3$.

4.3.4 Neutron Powder Diffraction

Neutron powder diffraction data were collected from $Sr(Ru_{0.5}Fe_{0.5})O_2$ at 298 K using the D2b instrument at the ILL (Section 2.6.2.1). Given the similarity between the lattice parameters of $Sr(Ru_{0.5}Fe_{0.5})O_2$ and $SrFeO_2$, a structural model based on the infinite-layer structure of $SrFeO_2$ with a 1:1 disordered mixture of iron and ruthenium on the B-site was refined against the neutron powder diffraction data.

The refinement converged readily to give a good statistical fit. Close inspection of the fit to the data revealed a number of additional weak diffraction features corresponding to a small amount (2.4(2)% by weight) of CaO not removed by the washing process. This was added to the structural model as a secondary phase to account for these features.

Observed, calculated, and difference plots are shown in Figure 4.4. Full details of the structural parameters are given in Table 4.1 and selected bond lengths are given in Table 4.2. As there is no published bond valence parameter for Ru^{II}, these calculations were performed using the value of 1.834 Å for Ru^{IV}–O, the only available bond valence sum parameter for ruthenium, explaining the anomalously high value obtained for ruthenium.[53]

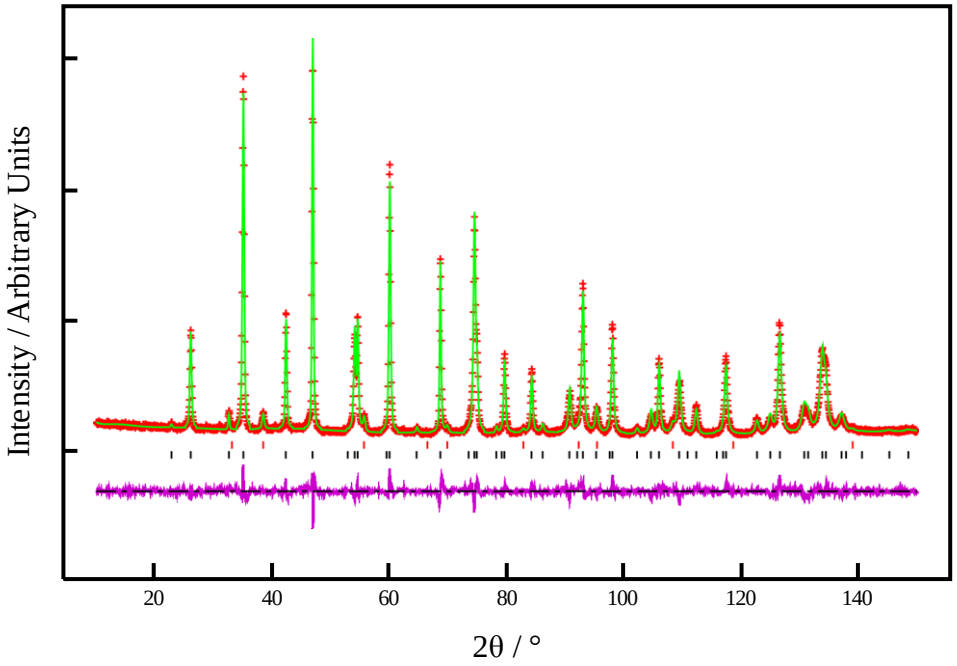

Figure 4.4: Observed, calculated, and difference plots for refinement of the structural model of $Sr(Ru_{0.5}Fe_{0.5})O_2$ at 298 K against neutron powder diffraction data collected using the D2b instrument. The upper set of tick marks corresponds to a ~ 2.4% by weight impurity of CaO.

Atom	Wyckoff Position	*x*	*y*	*z*	Fractional Occupancy	U_{iso} / Å^2
Sr	1*d*	1/2	1/2	1/2	1	0.0041(2)
Ru/Fe	1*a*	0	0	0	0.5/0.5	0.0040(1)
O	2*f*	1/2	0	0	1	0.0061(2)
$Sr(Ru_{0.5}Fe_{0.5})O_2$: space group *P*4/*mmm*; *a* = 3.9903(1) Å and *c* = 3.4978(1) Å; cell volume = 55.69(1) Å^3; weight fraction = 97.6(2)%						
CaO: space group *Fm*-3*m*; *a* = 4.8152(2) Å; cell volume = 111.65(1) Å^3; weight fraction = 2.4(2)%						
χ^2 = 2.63, wRp = 5.62%, Rp = 4.37%						

Table 4.1: Refined structural parameters for $Sr(Ru_{0.5}Fe_{0.5})O_2$ at 298 K.

Cation	Anion	Bond Length / Å	Bond Valence Sum
Sr	O	2.653(1) x 8	Sr +1.88
Ru/Fe	O	1.995(1) x 4	Ru +2.59
			Fe +1.98
Ru/Fe	Ru/Fe	3.498(1)	

Table 4.2: Selected bond lengths and bond valence parameters from the refined structure of $Sr(Ru_{0.5}Fe_{0.5})O_2$ at 298 K. Bond valence parameters for Ru^{IV} were used.

Neutron powder diffraction data collected from $Sr(Ru_{0.5}Fe_{0.5})O_2$ at 5 K did not display any additional features relative to data collected at 298 K indicative of long-range magnetic order.

4.3.5 X-ray Absorption Near Edge Spectroscopy

Thermogravimetric analysis defines the average transition metal oxidation state as M^{2+}, but does not define the individual oxidation states of the iron and ruthenium. In order to unambiguously determine the individual oxidation states of the transition metal cations in $Sr(Ru_{0.5}Fe_{0.5})O_2$, X-ray Absorption Near Edge Spectroscopy (XANES, Section 2.8) data were collected.

4.3.5.1 Experimental

Samples were prepared as described in Section 2.8. The same procedure was used to prepare pellets of $SrFeO_2$ and $Sr_2Fe_2O_5$ to act as Fe^{2+} and Fe^{3+} standards respectively. The syntheses of these phases are detailed in Appendix D.

The amount of sample in all cases was calculated to obtain an edge jump close to one. Data were collected from the Fe K-edge (ionisation from the 1*s* orbital) using the B18 instrument at Diamond Light Source.[51] The measurements and data handling were performed by Dr. Diego Gianolio and Dr. Giannantonio Cibin.

4.3.5.2 Results

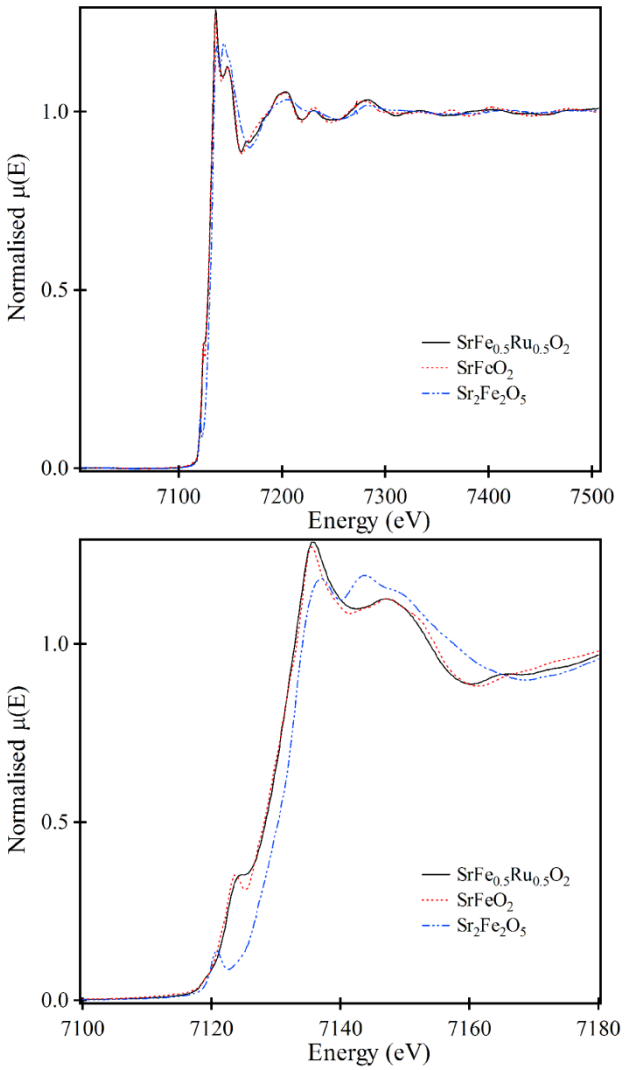

Figure 4.5: Fe K-edge absorption spectra collected from $Sr(Ru_{0.5}Fe_{0.5})O_2$, $SrFeO_2$ (Fe^{2+} standard), and $Sr_2Fe_2O_5$ (Fe^{3+} standard).

The Fe K-edge absorption data of $Sr(Ru_{0.5}Fe_{0.5})O_2$, $SrFeO_2$ and $Sr_2Fe_2O_5$ is shown in Figure 4.5. It can be seen that the absorption edges of $Sr(Ru_{0.5}Fe_{0.5})O_2$ and $SrFeO_2$ are almost identical, indicating that in both cases the Fe centres are in the same oxidation state and coordination environment (square-planar Fe^{2+}), and significantly displaced from that of $Sr_2Fe_2O_5$. By charge balancing, it can be seen that $Sr(Ru_{0.5}Fe_{0.5})O_2$ therefore contains Fe^{2+} and Ru^{2+}.

4.3.6 Magnetisation Measurements

Zero-field and field cooled magnetisation data collected from $Sr(Ru_{0.5}Fe_{0.5})O_2$ as a function of temperature in a field of 100 Oe are shown in Figure 4.6 (a). These show a weak divergence in the range $75 \leq T / K \leq 300$. A fit to the Curie-Weiss law in this temperature range yields values of C = 0.37(5) cm^3 K mol^{-1}, θ = -12.3(10) K and K = 0.00357(1) cm^3 where mol^{-1} means per mole of formula units of $Sr(Ru_{0.5}Fe_{0.5})O_2$.

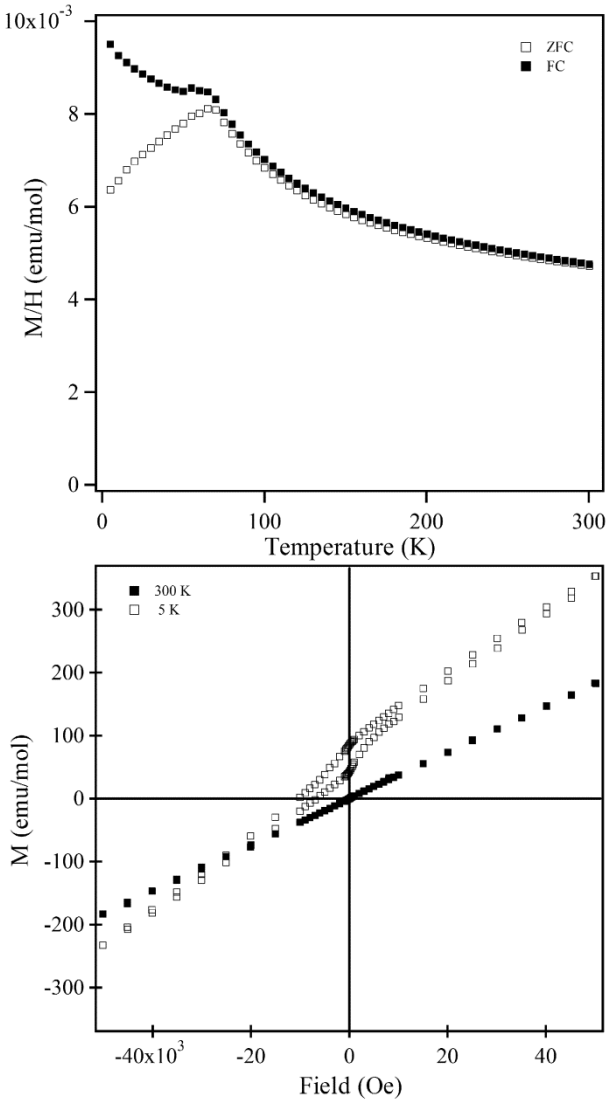

Figure 4.6: (a) Zero-field cooled and field cooled magnetisation data collected from $Sr(Ru_{0.5}Fe_{0.5})O_2$. (b) Magnetisation-field isotherms collected from $Sr(Ru_{0.5}Fe_{0.5})O_2$.

The low susceptibility, in conjunction with the weak divergence, suggests that there is strong coupling between magnetic centres even at high temperatures, preventing the deduction of the spin states of Fe^{2+} and Ru^{2+} from magnetisation data alone.

Below a local maximum in the zero-field cooled data at $T \sim 60$ K, the zero-field cooled and field cooled magnetisation data diverge much more strongly, indicating a magnetic transition.

Magnetisation-field isotherms were collected at 300 K and 5 K and are shown in Figure 4.6(b). The data collected from $Sr(Ru_{0.5}Fe_{0.5})O_2$ at 300 K are linear and pass through the origin, but the low-temperature data display weak hysteresis and are significantly displaced from the origin. This suggests that the transition at 60 K is due to the freezing of a spin glass.

4.3.7 Density Functional Theory Calculations

4.3.7.1 Introduction

In order to determine the spin states of Ru and Fe and the magnetic interactions present in $Sr(Ru_{0.5}Fe_{0.5})O_2$, Density Functional Theory (DFT) calculations were performed. DFT allows the computation of properties of many-electron systems through the use of functionals of the spatially dependent electron density. These calculations were performed by Dr. John McGrady.

4.3.7.2 Experimental

These calculations were performed with the Siesta 2.6.8-LDAU[78,79] package using a 6×6×10 k-point grid. The PBE functional[80] was used throughout with Hubbard U values of 4.0 and 3.0 eV for Fe and Ru, respectively. The unit cell parameters were optimized to a tolerance of 0.005 eV/Å. The basis sets were of double-ζ+polarization quality, with core electrons described by norm-conserving pseudopotentials.[81] Sr semi-core levels (4s, 4p) were included in the valence space. Magnetic couplings were computed by mapping the difference between

high-spin and broken-symmetry determinants onto the diagonal elements of Heisenberg-type spin Hamiltonians incorporating only nearest-neighbor interactions.

The electronic structure of $SrFeO_2$ has been described independently by both Xiang et al. and Pruneda et al., who showed that the Fe^{2+} centers adopt $S = 2$ configurations with the d_z^2 orbital being doubly occupied.[66,82] A parallel series of calculations was performed on $SrFe_{0.5}Ru_{0.5}O_2$ using a density functional approach (GGA+U), reproducing all the key features reported by Canadell and Whangbo (see 8.3Appendix 4.2).

X-ray and neutron powder diffraction data reveal that the iron and ruthenium cenres are completely disordered within the sample. In order to model the different possible interactions present in an ABO_2 framework, three distinct limiting Ru/Fe ordered configurations were considered: rocksalt, columnar, and planar (Figure 4.7) arranged within an $a' = \sqrt{2}a$, $c' = 2c$ expanded unit cell.

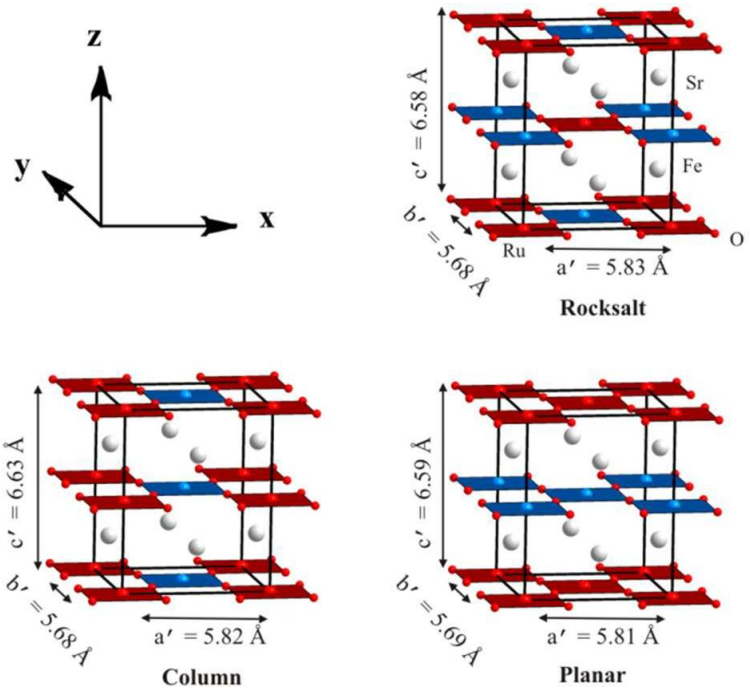

Figure 4.7: Optimized unit cells for the rock-salt, column, and planar configurations of $SrFe_{0.5}Ru_{0.5}O_2$.

While the disordered structure can be refined using a tetragonal unit cell (space group *P4*/*mmm*), Jahn-Teller instabilities at either Ru or Fe could induce orthorhombic distortions in the three limiting structures described here. As a result, no restrictions were placed on the lattice parameters (i.e. $a \neq b \neq c$) in the optimisation procedures.

4.3.7.3 Results

Of the three structures, the rocksalt is the most stable, although columnar and planar lie only 0.05 and 0.07 eV higher in energy. It should be noted that reduction does not cause the material to order in order to minimise the energy of the system as there is insufficient energy during the reduction reactions to overcome the energetic barriers to cation mobility. All the disorder in the cation lattice of the product is inherited from the disorder present in the starting $Sr(Ru_{0.5}Fe_{0.5})O_3$ substrate.

The local electronic structure at Ru and Fe proved independent of the cation ordering, so only the rocksalt configuration is described below. Details of the columnar and planar configurations can be found in Appendix 4.3 and Appendix 4.4.

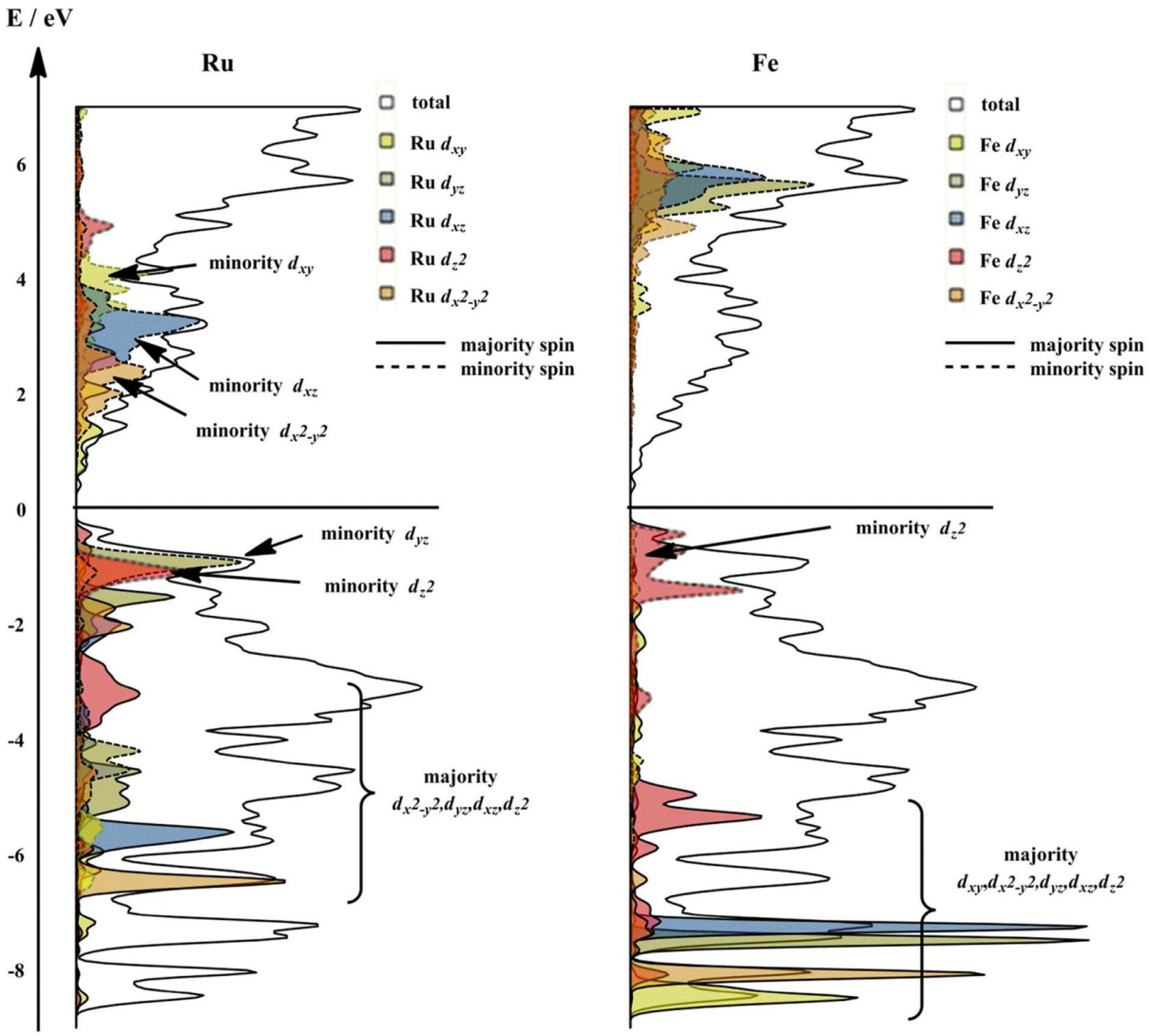

Figure 4.8: Computed partial density of states (PDOS) for the antiferromagnetic ground state of the rock-salt configuration of $SrFe_{0.5}Ru_{0.5}O_2$. Ru and Fe PDOS are shown on the left and right, respectively. Majority and minority-spin PDOS are shown as full and dashed lines, respectively.

The *x* and *y* axes were defined to lie along the unit cell vectors. Consequently, the d_{xy} orbital on each metal centre is strongly O–M–O antibonding, not the $d_{x^2-y^2}$ as in the axis system used by Pruneda *et al.*[82] In the most stable electronic state of the rock-salt structure the intralayer Fe–O–Ru coupling is ferromagnetic (J_1 = -2.39 meV), while the interlayer coupling is weakly antiferromagnetic (J_2 = 1.00 meV). The partial density of states (PDOS) for Ru shown in Figure 4.8 confirms that the majority-spin d_{z^2}, d_{xz}, d_{yz}, and $d_{x^2-y^2}$ levels (α on Ru1, β on Ru2) lie below the Fermi level, as do minority-spin d_{yz} and d_{z^2}. In contrast, minority-spin d_{xz} and

$d_{x^2-y^2}$, along with both spin components of d_{xy}, lie above the Fermi level. The local configuration at Ru^{2+} is therefore a triplet, $(d_{z^2})^2(d_{xz},d_{yz})^3(d_{x^2-y^2})^1(d_{xy})^0$, consistent with Mulliken spin densities of ±2.20 for Ru1 and Ru2, respectively. In the Fe manifold, in contrast, all five components of the majority-spin manifold (α on Fe1, β on Fe2), are occupied, along with the minority-spin d_{z^2}, giving a high-spin quintet configuration, $(d_{z^2})^2(d_{xz},d_{yz})^2(d_{x^2-y^2})^1(d_{xy})^1$ (Mulliken spin densities ±4.08), very similar to that in the parent $SrFeO_2$ phase.[66,82]

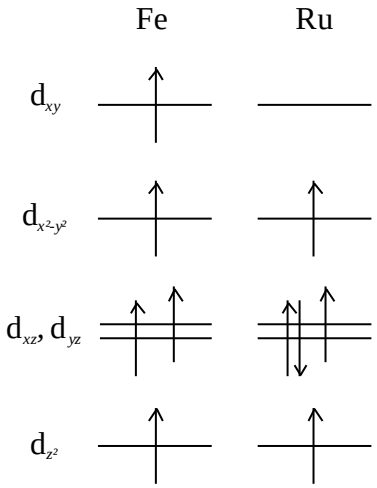

Figure 4.9: The electronic configurations of the Fe^{2+} and Ru^{2+} centres in $Sr(Ru_{0.5}Fe_{0.5})O_2$. NB the labelling of the $d_{x^2-y^2}$ and d_{xy} orbitals has been swapped to account for Jahn-Teller distortions during the calculations.

The $(d_{xz},d_{yz})^3$ configuration at ruthenium drives a small but distinct orthorhombic distortion (optimized lattice parameters: a' = 5.83 Å, b' = 5.68 Å, c'= 6.58 Å, a'/b' = 1.03), although the disorder in the crystal structure precludes the detection of such a small effect experimentally. The optimized cell parameters for the column and planar configurations are similar to those for the rock-salt analogue (a' = 5.82 Å, b' = 5.68 Å, c' = 6.63 Å and a' = 5.81 Å, b' = 5.69 Å, c' = 6.58 Å, respectively). The PDOS and Mulliken spin densities also confirm that the local electronic structure is independent of the precise arrangement of ions in the lattice: the S = 2 $(d_{z^2})^1(d_{xz},d_{yz})^2(d_{x^2-y^2})^1(d_{xy})^1$ and S = 1 $(d_{z^2})^2(d_{xz},d_{yz})^3(d_{x^2-y^2})^1(d_{xy})^0$ configurations are common to Fe and Ru, respectively, in all cases (see Appendix 4.3 and Appendix 4.4).

4.4 Discussion

4.4.1 Reduction Behaviour of $Sr(Ru_{1-x}Fe_x)O_3$

The reduction of $Sr(Ru_{0.5}Fe_{0.5})O_3$ with CaH_2 to form a phase with composition $Sr(Ru_{0.5}Fe_{0.5})O_2$ proceeds in a manner analogous to the reduction of $SrFeO_3$ to $SrFeO_2$.[55] The resulting phase adopts an infinite-layer structure with a disordered arrangement of Ru^{2+} and Fe^{2+} on the B-site. This is in direct contrast to the reduction behaviour of the Ru-rich phases, $SrRuO_3$, $Sr(Ru_{0.6}Fe_{0.4})O_3$, and $Sr(Ru_{0.75}Fe_{0.25})O_3$, which proceed directly to the formation of SrO, elemental ruthenium, and elemental iron.

This demonstrates the stabilisation of the low oxidation state of ruthenium by coupling the further reduction of Ru^{2+} centres to that of the Fe^{2+} centres. The robustness of the extended $SrFeO_2$-like oxide framework presents an energetic barrier to the further reduction of Ru^{2+}, which would be destroyed by reduction to elemental ruthenium. The endothermic reduction potential of iron can thus be used to restrict the otherwise facile reduction of ruthenium and enable the preparation of phases with transition metal centres adopting unusual low oxidation states.[83]

$$Fe^{2+}/Fe \qquad E° = -0.447V$$

$$Ru^{2+}/Ru \qquad E° = +0.455V$$

The inability to topochemically reduce $Sr(Ru_{0.6}Fe_{0.4})O_3$, and $Sr(Ru_{0.75}Fe_{0.25})O_3$ indicates that 50% is the minimal amount of iron needed to stabilise Ru^{2+}. This observation is consistent with the observed reduction behaviour of $Sr(Ru_{0.5}Fe_{0.5})O_3$ synthesised via convential ceramic methods compared with $Sr(Ru_{0.5}Fe_{0.5})O_3$ synthesised via citrate gel methods: standard ceramic synthesis results in potentially inhomogeneous samples due to the inherent limitations of mechanical grinding. Consequently, samples of $Sr(Ru_{0.5}Fe_{0.5})O_3$ synthesised

via conventional ceramic methods may contain Fe-rich and Ru-rich regions, which would not behave like homogeneous $Sr(Ru_{0.5}Fe_{0.5})O_3$.

The reduction behaviour of $Sr(Ru_{0.5}Fe_{0.5})O_3$ is also significantly different from that of other substituted $Sr(Fe_{1-x}M_x)O_3$ (M = Co, Mn) where $x > 0.3$, which are reduced to phases that do not adopt an infinite-layer structure.[60] This suggests that the introduction of ruthenium does not disrupt the selectivity of low-temperature reduction reactions, in turn reinforcing the idea that the formation of structures containing square-planar metal centres is favoured by a d^6 electronic configuration.

4.4.2 Square-Planar Ru^{2+}

Systems containing four coordinate Ru^{2+} centres such as those observed in $Sr(Ru_{0.5}Fe_{0.5})O_2$ are relatively rare, even in molecular complexes, due to the inherent stability of 6-coordinate S = 0 systems. The formation of four coordinate Ru^{2+} centres generally relies on the use of macrocyclic or chelating ligands. These compounds tend to adopt a distorted 'butterfly-shaped' configuration stabilised by the adoption of low-spin S = 0 configurations at the Ru centre.[84]

Bulky pincer-type ligands can be used to suppress this 'butterfly' distortion and produce square-planar complexes. These can adopt either S = 1 or S = 0 configurations depending on the π-donating properties of the ligands.[85]

The Ru^{2+} centres in $Sr(Ru_{0.5}Fe_{0.5})O_2$ are observed to be square-planar by diffraction, as defined by the *P*4/*mmm* space group symmetry (excepting any local symmetry-breaking distortions). The surrounding rigid Sr–Fe–O lattice inhibits the local 'butterfly' distortions of the Ru^{2+} centres.

The magnetic behaviour discussed below and the calculations described above indicate that the Ru^{2+} centres adopt an S = 1 intermediate spin state consistent with the modest π-donating ability of the oxide ligands.

4.4.3 Magnetic Behaviour of $Sr(Ru_{0.5}Fe_{0.5})O_2$

$SrFeO_2$ exhibits strong antiferromagnetic order below T_N = 473 K, attributed to strong superexchange within the Fe–O–Fe layers [$Fe(d_{xy})^1$–O(2p)–$Fe(d_{xy})^1$] and weaker direct exchange between layers [$Fe(d_{xz}, d_{yz})^2$–$Fe(d_{xz}, d_{yz})^2$] (note axis choice as described above).[55,82]

In the rocksalt ordered configuration of $Sr(Ru_{0.5}Fe_{0.5})O_2$, the in-plane Ru–O–Fe coupling is ferromagnetic (J_1 = -2.39 meV) due to the now-empty Ru d_{xy} orbital [$Ru(d_{xy})^0$–O(2p)–$Fe(d_{xy})^1$]. Coupling between the layers remains antiferromagnetic (J_2 = 1.00 meV) due to direct [$Ru(d_{xz}, d_{yz})^3$–$Fe(d_{xz}, d_{yz})^2$] exchange.

In the column configuration, there is also ferromagnetic coupling within the layers (J_1 = -2.75 meV). In the planar configuration, however, there is antiferromagnetic ordering (J_1' = 1.73 meV) within the Fe–O–Fe layers due to strong σ-type [$Fe(d_{xy})^1$–O(2p)–$Fe(d_{xy})^1$] superexchange, as in $SrFeO_2$. The Ru–O–Ru layers also order antiferromagnetically (J_1 = 4.77 meV), in this case due to π-type [$Ru(d_{xz})^1$–O(2p)–$Ru(d_{xz})^1$] superexchange along the a' lattice direction.

The combination of ferromagnetic Ru–O–Fe and antiferromagnetic Ru–O–Ru and Fe–O–Fe intraplanar couplings inevitably leads to magnetic frustration: any microdomain where an Ru–O–Fe unit lies above an Ru–O–Ru or Fe–O–Fe unit will be frustrated (Figure 4.10).

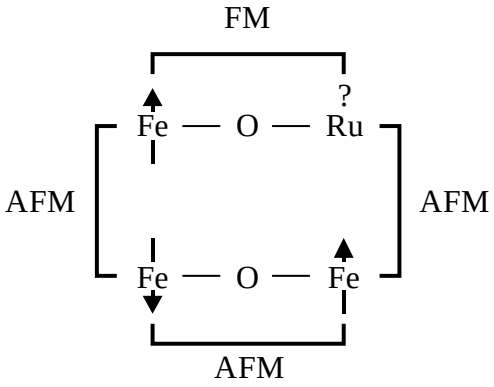

Figure 4.10: The frustrated magnetic interactions arising from an $RuFe_3$ microdomain in $Sr(Ru_{0.5}Fe_{0.5})O_2$.

Magnetisation data collected from $Sr(Ru_{0.5}Fe_{0.5})O_2$ show a strong divergence between the zero-field cooled and field cooled data below a local maximum at T ~ 60 K. The strongly displaced magnetisation-field isotherm collected at 5 K indicates that this corresponds to a spin-glass freezing transition. This behaviour arises as a natural consequence of the disorder present in $Sr(Ru_{0.5}Fe_{0.5})O_2$.

4.4.4 Ordered Sr_2RuFeO_6

Chang *et al.* recently reported the synthesis of artificially ordered Sr_2RuFeO_6 adopting rocksalt ordering via pulsed laser deposition.[86] Unlike $Sr(Ru_{0.5}Fe_{0.5})O_3$ prepared via conventional methods, which exhibits spin glass behaviour with a freezing temperature of T ~ 60 K,[76] this material possesses an ordering temperature of T ~ 390 K.

The calculations performed above suggest that, should the reduction of this phase be possible, Sr_2RuFeO_4 would contain ferromagnetic sheets aligned antiferromagnetically. Careful synthesis of ordered $Sr(Ru_{0.5}Fe_{0.5})O_3$ would therefore enable the preparation of phases displaying radically different magnetic behaviour from disordered $Sr(Ru_{0.5}Fe_{0.5})O_2$.

4.4.5 Synthesis of $Sr(Ru_{1-x}Fe_x)O_3$ $x > 0.5$

Single-phase products of the Fe-rich phases $Sr(Ru_{0.4}Fe_{0.6})O_3$ and $Sr(Ru_{0.25}Fe_{0.75})O_3$ could not be successfully synthesised, forming instead a mixture of $Sr(Ru_{0.5}Fe_{0.5})O_3$ and $SrFeO_{3-\delta}$. This suggests that the formation of $Sr(Ru_{0.5}Fe_{0.5})O_3$ is particularly favourable due to the presence of Ru^{5+}/Fe^{3+} charge ordering.[76] Segregation into two phases is understandable considering that, in order to form $Sr(Ru_{0.5-x}Fe_{0.5+x})O_3$, some of the iron would have to be in the +4 oxidation state. While the formation of Fe^{4+} itself is not impossible under these conditions (we are forming $SrFeO_{3-\delta}$ and not $SrFeO_{2.5}$), it appears that the separation into two phases is more favourable than the formation of a single phase owing to the particular stability of $Sr(Ru_{0.5}Fe_{0.5})O_3$.

4.5 Conclusion

The topochemical reduction of $Sr(Ru_{0.5}Fe_{0.5})O_3$ with CaH_2 was carried out to produce a phase with composition $Sr(Ru_{0.5}Fe_{0.5})O_2$, the first extended oxide phase containing Ru^{2+}. The robust Sr–Fe–O framework impedes the normally facile reduction of Ru^{2+}. Magnetisation data supported by calculations indicate that square-planar Ru^{2+} centres adopt an intermediate-spin S = 1 state, compared to an S = 2 spin state for the Fe^{2+} centres. This is consistent with the greater radial extent of 4d orbitals compared to 3d, and their consequently stronger interactions with the surrounding ligands. The use of a robust oxide framework to stabilise an unusual oxidation state of a 4d transition metal paves the way for the synthesis of a wide range of phases with other 4d transition metals in unusual oxidation states and coordination environments. The influence of disorder on the magnetic properties of the resulting phase is discussed.

Details of the reduction of $Sr(Ru_{0.5}Fe_{0.5})O_3$ has been the subject of a recent publication.[87]

The synthesis and reduction of other phases with composition $Sr(Ru_{1-x}Fe_x)O_3$ (x = 0, 0.25, 0.4, 0.6, and 0.75) was attempted. Single phase samples could not be prepared for the iron-rich (x = 0.6 and 0.75) compositions. The reduction of the ruthenium-rich samples (x = 0, 0.25, and 0.4) proceeded directly to SrO, elemental ruthenium, and elemental iron, indicating that the presence of a significant amount of iron is required to stabilise the low oxidation states of ruthenium.

Chapter 5 Reduction of $Sr_2(Ru_{0.5}Fe_{0.5})O_4$ and $Sr_3(Ru_{0.5}Fe_{0.5})_2O_7$

5.1 Introduction

While binary metal hydrides have been successfully used to prepare a number of topochemically reduced complex oxides 3*d* transition metals,[14-16] analogous chemistry on 4*d* transition metal based oxides has not been widely explored.

As described above, the topochemical reduction of $Sr(Ru_{0.5}Fe_{0.5})O_3$ to $Sr(Ru_{0.5}Fe_{0.5})O_2$ with CaH_2 resulted in the first reported example of Ru^{2+} in an extended transition metal oxide.[87] In this material, the presence of iron is necessary to prevent complete reduction of the ruthenium to the elemental metal by coupling this reduction to the destruction of an especially stable iron-oxide lattice.

Analogous chemistry on layered materials adopting Ruddlesden-Popper structures allows us to probe the reduction behaviour of ruthenium in extended transition metal oxides. The all-iron Sr_2FeO_3 and $Sr_3Fe_2O_5$ materials can be prepared via topochemical reduction with CaH_2 to form phases adopting structures containing extended networks of FeO_2 square planes.[19,88] These networks could also stabilise low oxidation states of ruthenium, and therefore doping these materials with Ru would enable the probing of the reduction behaviour of 4*d* transition-metal oxides in different environments.

5.2 Experimental

5.2.1 Synthesis of $Sr_2(Ru_{0.5}Fe_{0.5})O_4$ and $Sr_3(Ru_{0.5}Fe_{0.5})_2O_7$

Samples of $Sr_2(Ru_{0.5}Fe_{0.5})O_4$ and $Sr_3(Ru_{0.5}Fe_{0.5})_2O_7$ were synthesised via the route previously described by Battle *et al.*[89] Citrate gels (see Section 2.3) were prepared from suitable stoichiometric quantities of $SrCO_3$ (Alfa Aesar 99.99%), Fe metal (Alfa Aesar 99.99%) and RuO_2 (from RuO_2 hydrate (Alfa Aesar 99.99%) dried at 800 °C). The resulting powders were

placed in alumina crucibles and heated at 1 °C min^{-1} to 900 °C in air to decompose the carbonates. The powders were then reground and pressed into 13 mm diameter pellets. Samples of $Sr_2(Ru_{0.5}Fe_{0.5})O_4$ were heated at 1200 °C or for two periods of two days in air with one intermediate grinding. Samples of $Sr_3(Ru_{0.5}Fe_{0.5})_2O_7$ were heated at 1400 °C for two periods of two days in air with one intermediate grinding.

The resulting powders were observed to be phase-pure by laboratory X-ray powder diffraction, with lattice parameters a = 3.91(1) Å and c = 12.59(1) Å ($Sr_2(Ru_{0.5}Fe_{0.5})O_4$) and a = 3.92(1) Å and c = 20.40(1) Å ($Sr_3(Ru_{0.5}Fe_{0.5})_2O_7$), in good agreement with reported values (a = 3.91(1) Å, and c = 12.62(1) Å for $Sr_2(Ru_{0.5}Fe_{0.5})O_4$ and a = 3.92(1) Å, and c = 20.41(1) Å for $Sr_3(Ru_{0.5}Fe_{0.5})_2O_7$).[89]

5.2.2 Synthesis of Sr_2RuO_4 and $Sr_3Ru_2O_7$

Samples of Sr_2RuO_4 were synthesised using standard ceramic methods as described by Müller-Buschbaum and Wilkens.[90] Initial samples were prepared from suitable stoichiometric quantities of $SrCO_3$ (Alfa Aesar 99.99%) and RuO_2 (from RuO_2 hydrate (Alfa Aesar 99.99%) dried at 800 °C). The powders were intimately mixed using an agate mortar and pestle and subsequently placed in alumina crucibles and heated at 1 °C min^{-1} to 900 °C to decompose the carbonate. The powders were then reground and pressed into 13 mm diameter pellets. These were then heated at 1350 °C for two periods of two days with one intermediate grinding. The powders were observed to be phase-pure by laboratory X-ray powder diffraction data with lattice parameters a = 3.872(1) Å and c = 12.746(1) Å, in good agreement with reported values (a = 3.871(1) Å and c = 12.702(4) Å).[90]

Samples of $Sr_3Ru_2O_7$ were prepared using the method previously described by Cava *et al.*[91] Suitable stoichiometric amounts of RuO_2 and $SrCO_3$ were ground together using an agate mortar and pestle. The resulting powders were calcined at 1000 °C for 24 hours before being

pressed into pellets and heated to 1300 °C for two periods of two days. As a final step, the samples were quenched from high temperature into liquid nitrogen to prevent partial decomposition into $SrRuO_3$ and Sr_2RuO_4.[91] The resulting powders were observed to be phase pure by laboratory X-ray powder diffraction, with lattice parameters a = 3.88(1) Å and c = 20.66(1) Å, in good agreement with reported values (a = 3.89(1) Å and c = 20.55(1) Å).[90]

5.2.3 Reduction with Metal Hydrides

Reduction of the $SrO(Sr(Ru_{0.5}M_{0.5})O_3)_n$ (M = Ru, Fe) phases was attempted using CaH_2 as a solid-state reducing agents. In order to assess the reactivity of these materials, small samples (~ 200 mg) were ground together with a 2n molar excess of CaH_2 in an argon filled glovebox using an agate mortar and pestle. These mixtures were then sealed in Pyrex (or silica for reactions to be performed at temperatures above 400 °C) ampoules and heated at a series of temperatures in the range $280 \leq T / °C \leq 450$ for periods of two days. Large samples suitable for neutron diffraction were prepared using two mole equivalents of CaH_2 in a pressure venting apparatus (section 2.4.2) for two periods of two days with an intermediate grinding. Reaction progress was monitored using X-ray powder diffraction.

Once a reaction was judged to be complete, the products were washed with 4 x 100 ml of a 0.1 M NH_4Cl solution in methanol, followed by 4 x 100 ml of clean methanol in order to remove unreacted metal hydrides and reaction by-products. The samples were then dried under vacuum and returned to the glovebox.

5.3 Results

5.3.1 Reactivity

X-ray powder diffraction data were collected from the washed products of reaction between $Sr_2(Ru_{0.5}Fe_{0.5})O_4$ or $Sr_3(Ru_{0.5}Fe_{0.5})_2O_7$ and CaH_2. Reactions performed at temperatures between 375 °C and 430 °C resulted in a splitting of the 103 ($Sr_2(Ru_{0.5}Fe_{0.5})O_4$) or 105

($Sr_3(Ru_{0.5}Fe_{0.5})_2O_7$) peaks, consistent with a change from tetragonal to orthorhombic symmetry. Reactions performed above 430 °C led to decomposition of the samples to SrO, Fe and Ru.

X-ray powder diffraction data collected from the washed products of reaction between Sr_2RuO_4 or $Sr_3Ru_2O_7$ and CaH_2 revealed that at temperatures below 400 °C, no reaction occurred, while reactions performed at temperatures above 400 °C led to decomposition of the samples into SrO and Ru metal in a manner analogous to the reaction between $SrRuO_3$ and CaH_2 (Section 4.3.1.2).

5.3.2 X-ray Powder Diffraction

X-ray powder diffraction data collected from the washed products of reaction between $Sr_2(Ru_{0.5}Fe_{0.5})O_4$ and CaH_2 could be indexed on the basis of an orthorhombic unit cell (space group *Immm*) with lattice parameters a = 3.697(1) Å, b = 3.897(1) Å and c = 12.877(1) Å.

X-ray powder diffraction data collected from the washed products of reaction between $Sr_3(Ru_{0.5}Fe_{0.5})_2O_7$ and CaH_2 could be indexed on the basis of an orthorhombic unit cell (space group *Immm*) unit cell with lattice parameters a = 3.676(1) Å, b = 3.926(1) Å and c = 20.798(1) Å.

5.3.1 Thermogravimetric Analysis

Thermogravimetric analysis was performed by heating a small amount of the washed product of reaction between $Sr_2(Ru_{0.5}Fe_{0.5})O_4$ and CaH_2 under flowing oxygen to form $Sr_2(Ru_{0.5}Fe_{0.5})O_4$ (confirmed via X-ray powder diffraction), resulting in a mass change of +3.38% corresponding to an initial composition of $Sr_2(Ru_{0.5}Fe_{0.5})O_{3.35}$.

A similar analysis carried out on the washed product of reaction between $Sr_3(Ru_{0.5}Fe_{0.5})_2O_7$ and CaH_2 resulted in a mass change of +4.10%, corresponding to a composition of $Sr_3(Ru_{0.5}Fe_{0.5})_2O_{5.67}$.

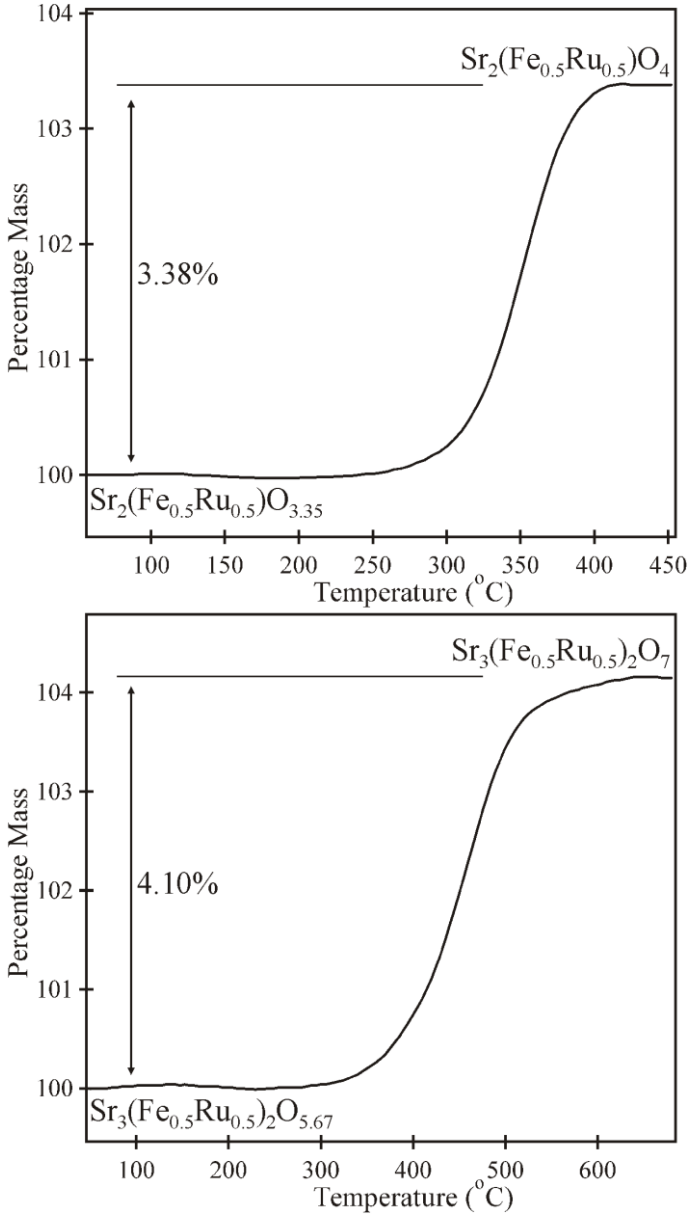

Figure 5.1: Thermogravimetric data collected during the reoxidation of $Sr_2(Ru_{0.5}Fe_{0.5})O_{3.35}$ and $Sr_3(Ru_{0.5}Fe_{0.5})_2O_{5.67}$.

5.3.1 Neutron Powder Diffraction

5.3.1.1 $Sr_2(Ru_{0.5}Fe_{0.5})O_{3.35}$

Neutron powder diffraction data were collected from the washed products of reaction between $Sr_2(Ru_{0.5}Fe_{0.5})O_4$ and CaH_2 at 298 K using the D2b diffractometer. These data could be indexed on the basis of a body-centred orthorhombic unit cell consistent with X-ray powder diffraction data. A model in space group *Immm* with a partially occupied anion site at (1/2, 0, 0) was refined against these data (Figure 5.2). When the fractional occupancies of the anion sites were refined, the apical site and the equatorial site at (0, 1/2, 0) remained fully occupied, while the equatorial site at (1/2, 0, 0) refined to ~35% occupancy.

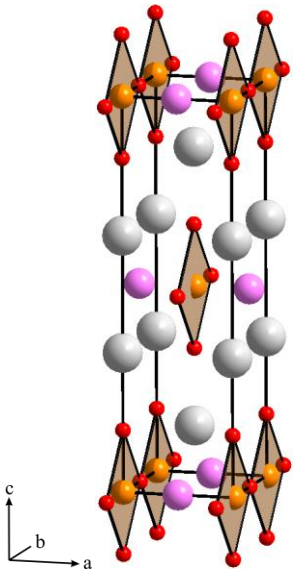

Figure 5.2: The *I4/mmm* model initially refined against neutron powder diffraction data collected from $Sr_2(Ru_{0.5}Fe_{0.5})O_{4-x}$. The large pink spheres represent partially occupied oxide sites.

While the model accounted for all the peaks, some reflections were too broad to be properly defined (Figure 5.3 (a) and Figure 5.4 (a)). An analysis of peak widths revealed that peaks with $h = 0$ were sharp, while peaks with $h \neq 0$ were unusually broad (Table 5.1).

hkl	2θ / °	FWHM
006	43.48	0.595
020	48.14	0.519
200	50.97	2.672
026	66.97	0.533
206	69.86	1.139
220	73.05	1.584

Table 5.1: Calculated full widths at half-maximum (FWHM) from neutron powder diffraction data collected from $Sr_2(Ru_{0.5}Fe_{0.5})O_{4-x}$ at 298 K.

Standard anisotropic peak broadening models led to an improvement in the fit to the data, but still did not fully describe the variation in peak shapes (Figure 5.3 (b) and Figure 5.4 (b)), suggesting the sample containing more than one phase.

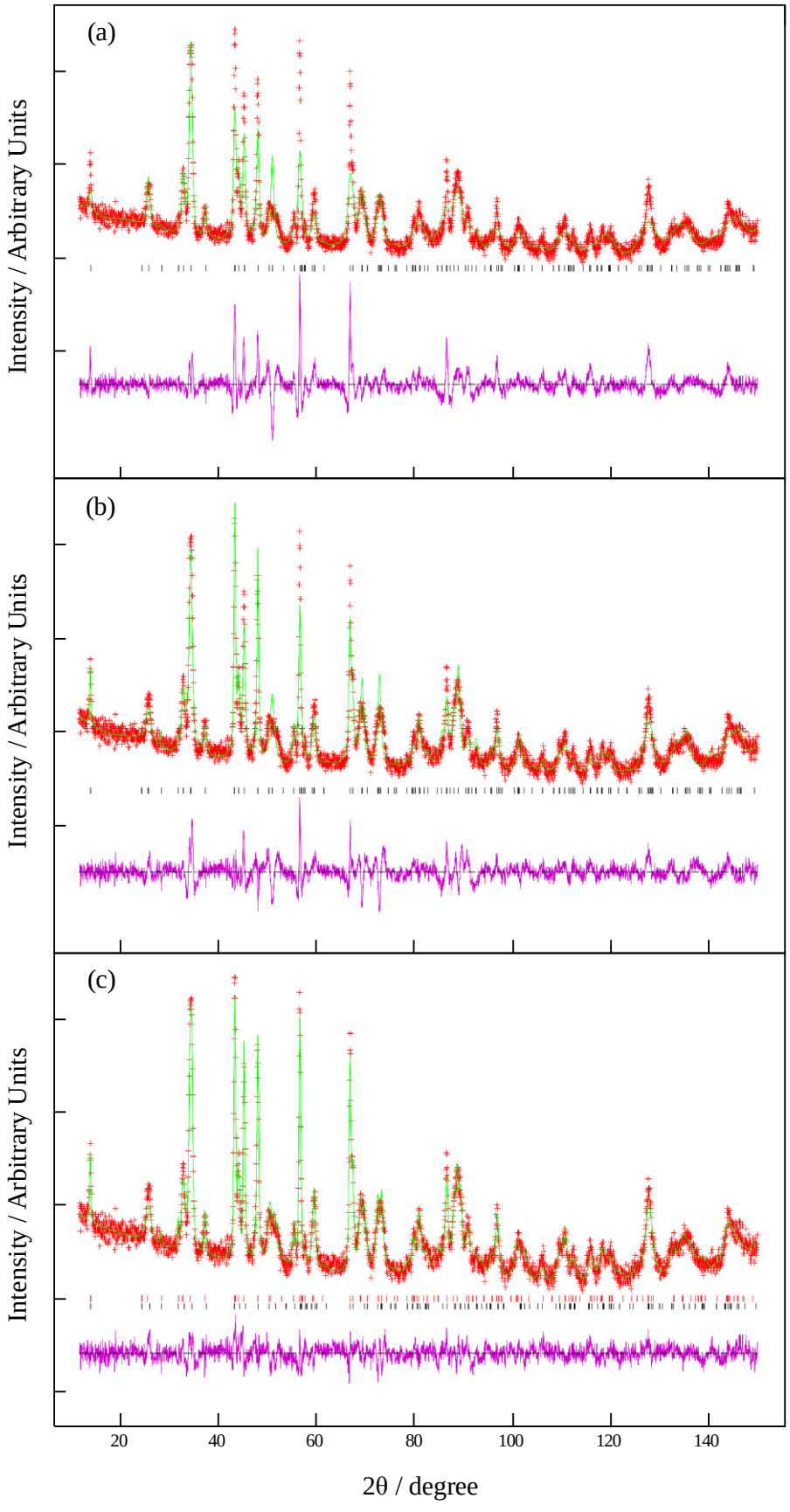

Figure 5.3: Observed calculated and difference plots from the refinement of (a) a single phase model, (b) a single phase model with *hkl* dependant peak broadening, (c) a two phase model against neutron diffraction data collected from $Sr_2(Ru_{0.5}Fe_{0.5})O_{3.35}$ at room temperature.

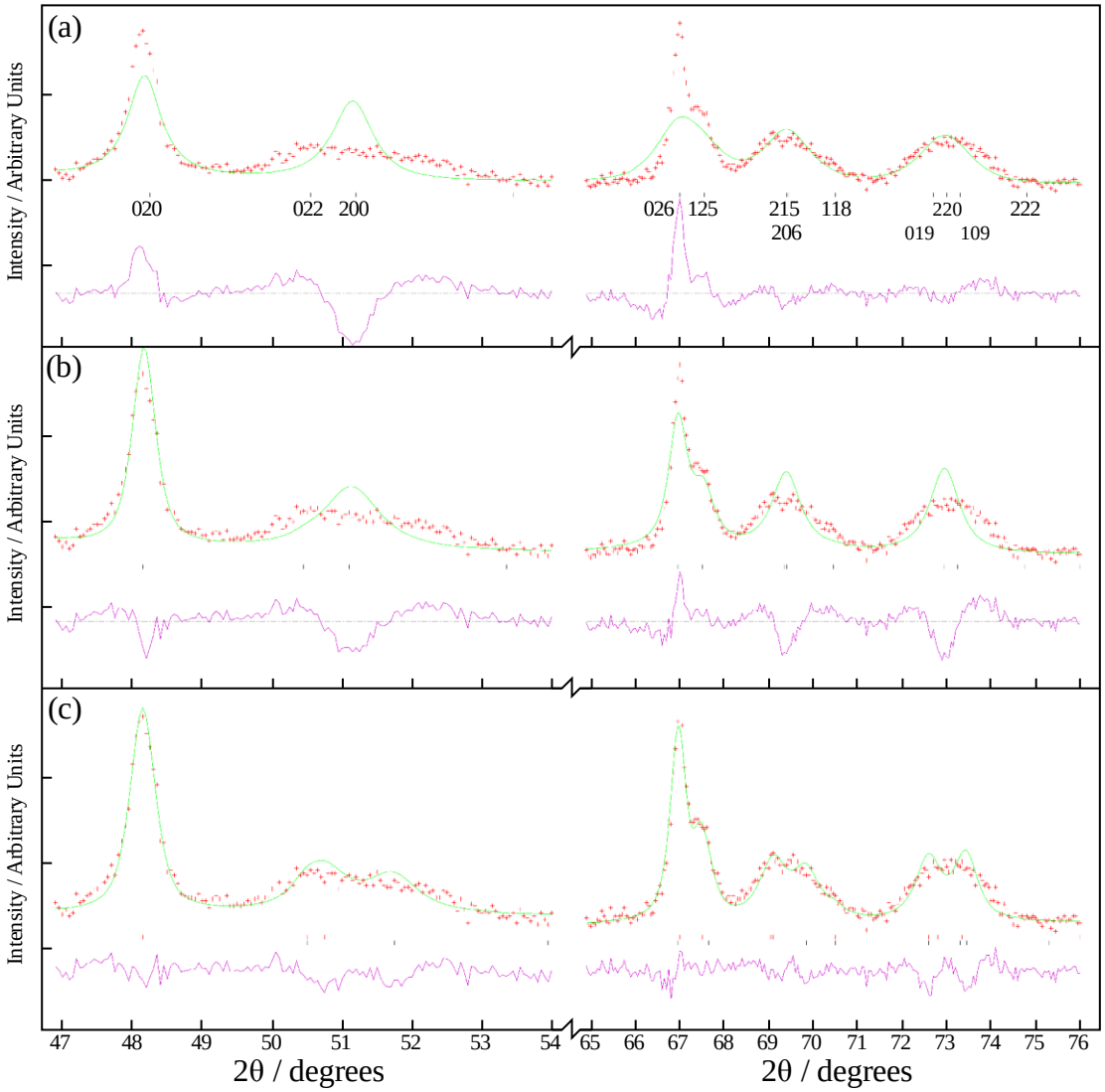

Figure 5.4: Expanded regions of the observed calculated and difference plots from the refinement of (a) a single phase model, (b) a single phase model with *hkl* dependent peak broadening, (c) a two phase model against neutron diffraction data collected from $Sr_2(Ru_{0.5}Fe_{0.5})O_{3.35}$ at room temperature.

A much improved fit to the data was achieved by using a two-phase model based on the same orthorhombically distorted n = 1 Ruddelsden-Popper structure. The lattice, structural, and anion occupancy parameters of the two phases were allowed to refine independently, but within each phase the thermal displacement parameters of the oxide ions were contrained to be identical to aid refinement stability. This two-phase model converged readily to give a

much improved statistical (χ^2 = 1.817) and visual fit to the data (Figure 5.3 (c) and Figure 5.4 (c)). Full details of the structural parameters are given in Table 5.2. Selected bond lengths are given in Table 5.3.

Phase 1					
Atom	***x***	***y***	***z***	**U_{iso} / Å^2**	**Fraction**
Sr(1)	0	0	0.3506(8)	0.004(1)	1
Ru/Fe(1)	0	0	0	0.011(1)	0.5/0.5
O(1)	0	0	0.1580(10)	0.006(2)	1
O(2)	0	1/2	0	0.012(2)	1
O(3)	1/2	0	0	0.012(2)	0.25(1)
$Sr_2(Ru_{0.5}Fe_{0.5})O_{3.25(1)}$: Space group *Immm* *a* = 3.6459(7) Å, *b* = 3.9028(7) Å, *c* = 12.898(2) Å. Weight fraction: 47.9(3) %					
Phase 2					
Atom	***x***	***y***	***z***	**U_{iso} / Å^2**	**Frac**
Sr(1)	0	0	0.3543(7)	0.004(1)	1
Ru/Fe(1)	0	0	0	0.011(1)	0.5/0.5
O(1)	0	0	0.1625(8)	0.004(1)	1
O(2)	0	1/2	0	0.011(3)	1
O(3)	1/2	0	0	0.011(3)	0.44(2)
$Sr_2(Ru_{0.5}Fe_{0.5})O_{3.44(2)}$: Space group *Immm* *a* = 3.7169(8) Å, *b* = 3.8939(6) Å, *c* = 12.856(2) Å. Weight fraction: 52.1(3) %					
χ^2 = 1.817; wRp = 4.78%; Rp = 3.85%					

Table 5.2: Refined structural parameters from the two-phase model of $Sr_2(Ru_{0.5}Fe_{0.5})O_{3.35}$ refined against neutron powder diffraction data collected at 298 K.

Cation	**Anion**	**Bond Distance (Å) Phase 1**	**Bond Distance (Å) Phase 2**
Sr(1)	O(1)	1 × 2.487(17)	1 × 2.454(14)
	O(1)	4 × 2.673(1)	4 × 2.699(1)
	O(2)	2 × 2.653(8)	2 × 2.647(6)
	O(3)	2 × 2.742(7)	2 × 2.710(6)
Ru/Fe	O(1)	2 × 2.038(13)	2 × 2.089(10)
	O(2)	2 × 1.951(1)	2 × 1.947(1)
	O(3)	2 × 1.823(1)	2 × 1.858(1)

Table 5.3: Selected bond lengths from the two-phase refinement of $Sr_2(Ru_{0.5}Fe_{0.5})O_{3.35}$. Bond multiplicities assume complete occupation of the O(3) anion site.

5.3.1.2 $Sr_3(Ru_{0.5}Fe_{0.5})_2O_{5.67}$

Neutron powder diffraction data collected from $Sr_3(Ru_{0.5}Fe_{0.5})_2O_{5.67}$ at 298K could be readily indexed using a body-centered orthorhombic cell. Close inspection of these data revealed the same unusual variation in diffraction peak width with *hkl* index as observed for

$Sr_2(Ru_{0.5}Fe_{0.5})O_{3.35}$, suggesting the $Sr_3(Ru_{0.5}Fe_{0.5})_2O_{5.67}$ sample also contained more than one phase. Therefore a structural model based on two orthorhombically distorted *n* = 2 Ruddlesden-Popper phases was refined against the data, in a manner directly analogous to that described above for $Sr_2(Ru_{0.5}Fe_{0.5})O_{3.35}$. Once again, a two-phase model was found to fit the data more effectively than a single phase model (χ^2 = 4.071 for two phases, compared with χ^2 = 7.298 for one. A comparison of single phase, *hkl* dependently broadened and two-phase refinements is given in Figure 5.6. Full details of the refined two-phasel model are given in Table 5.4. Selected bond lengths are given in Table 5.5.

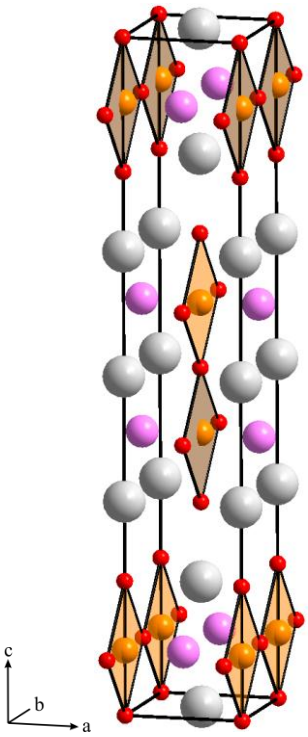

Figure 5.5: The *I*4/*mmm* model initially refined against neutron powder diffraction data collected from $Sr_3(Ru_{0.5}Fe_{0.5})_2O_{7-x}$. The large pink spheres represent partially occupied oxide sites.

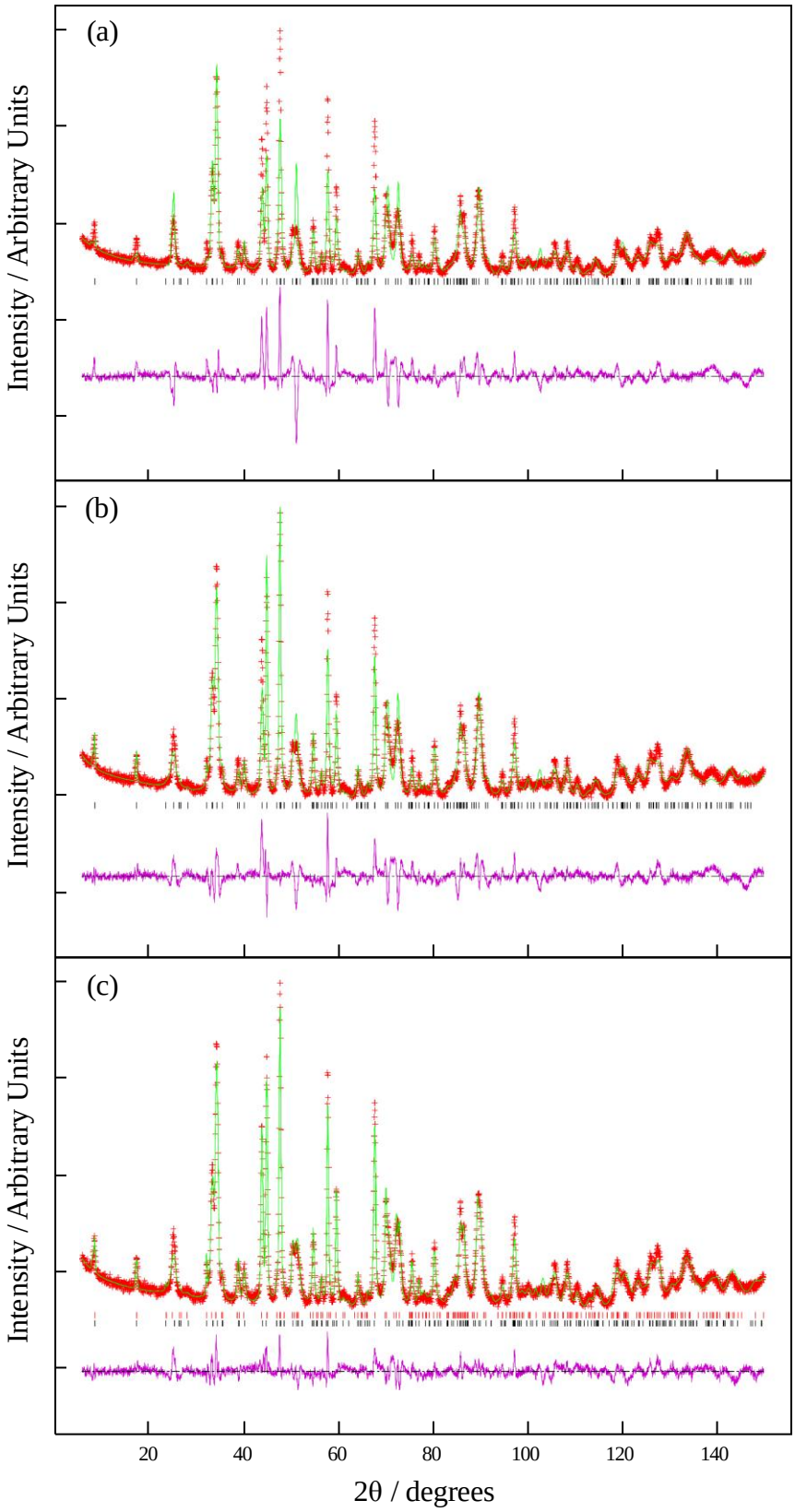

Figure 5.6: Observed calculated and difference plots from the refinement of (a) a single phase model, (b) a single phase model with *hkl* dependant peak broadening, (c) a two phase model against neutron diffraction data collected from $Sr_3(Ru_{0.5}Fe_{0.5})_2O_{5.67}$ at room temperature.

Phase 1					
Atom	***x***	***y***	***z***	**U_{iso} / Å^2**	**Occupancy**
Sr(1)	0	0	½	0.004(1)	1
Sr(2)	0	0	0.3163(3)	0.004(1)	1
Ru/Fe(1)	0	0	0.0968(3)	0.002(1)	0.5/0.5
O(1)	0	0	0.1948(3)	0.022(4)	1
O(2)	0	0	0	0.022(4)	1
O(3)	0	1/2	0.0972(4)	0.018(3)	1
O(4)	1/2	0	0.0972(4)	0.018(3)	0.25(1)
$Sr_3(Ru_{0.5}Fe_{0.5})_2O_{5.50(2)}$: Space group *Immm* *a* = 3.6553(5) Å, *b* = 3.9300(3) Å, *c* = 20.815(2) Å. Weight fraction: 49.8(15) %					
Phase 2					
Atom	***x***	***y***	***z***	**U_{iso} / Å^2**	**Occupancy**
Sr(1)	0	0	½	0.012(2)	1
Sr(2)	0	0	0.3129(4)	0.012(2)	1
Ru/Fe(1)	0	0	0.0991(6)	0.011(3)	0.5/0.5
O(1)	0	0	0.1961(6)	0.081(1)	1
O(2)	0	0	0	0.081(1)	1
O(3)	0	1/2	0.0898(6)	0.101(10)	1
O(4)	1/2	0	0.0898(6)	0.101(10)	0.43(3)
$Sr_3(Ru_{0.5}Fe_{0.5})_2O_{5.86(6)}$: Space group *Immm* *a* = 3.7164(5) Å, *b* = 3.9208(4) Å, *c* = 20.740(2) Å. Weight fraction: 50.2(15) %					
χ^2 = 4.01; wRp = 5.61%; Rp = 4.22%					

Table 5.4: Refined structural parameters from the two-phase model of $Sr_3(Ru_{0.5}Fe_{0.5})_2O_{5.67}$ refined against neutron powder diffraction data collected at 298 K.

Cation	Anion	Bond Distance (Å) Phase 1	Bond Distance (Å) Phase 2
Sr(1)	O(1)	4 × 2.684(1)	4 × 2.701(1)
	O(3)	4 × 2.726(6)	4 × 2.631(9)
	O(4)	4 × 2.820(6)	4 × 2.704(9)
Sr(2)	O(2)	1 × 2.529(9)	1 × 2.422(15)
	O(2)	4 × 2.693(1)	4 × 2.708(1)
	O(3)	2 × 2.566(7)	2 × 2.743(7)
	O(4)	2 × 2.665(7)	2 × 2.813(7)
Ru/Fe	O(1)	1 × 2.015(6)	1 × 2.055(12)
	O(2)	1 × 2.040(9)	1 × 2.012(18)
	O(3)	2 × 1.965(1)	2 × 1.970(2)
	O(4)	2 × 1.828(1)	2 × 1.868(2)

Table 5.5: Selected bond lengths from the two-phase refinement of $Sr_3(Ru_{0.5}Fe_{0.5})_2O_{5.67}$. Bond multiplicities assume complete occupation of the O(4) anion site.

5.3.2 X-ray Absorption Near Edge Spectroscopy

Thermogravimetric analysis only provides the average transition metal oxidation states. In order to determine the individual oxidation states of iron and ruthenium, X-ray Absorption Near Edge Spectroscopy data were collected.

5.3.2.1 Experimental

Samples suitable for characterisation by XANES were prepared as described in Section 4.3.5.1. Two sets of pellets were prepared: one suitable for determining the position of the absorption edge of iron and one for ruthenium. In addition, pellets of $Sr(Ru_{0.5}Fe_{0.5})O_2$ (Fe^{2+} and Ru^{2+}), $Sr_2Fe_2O_5$ (Fe^{3+}), and $SrRuO_3$ (Ru^{4+}; synthesis as described in Section 4.2.1) were prepared to serve as standards.

The amount of sample in all cases was calculated to obtain an edge jump close to one. Data were collected from the Fe K-edge (ionisation from the 1s orbital) using the B18 instrument at Diamond Light Source.[51] The measurements and data handling were performed by Dr. Diego Gianolio and Dr. Giannantonio Cibin.

5.3.2.2 Results

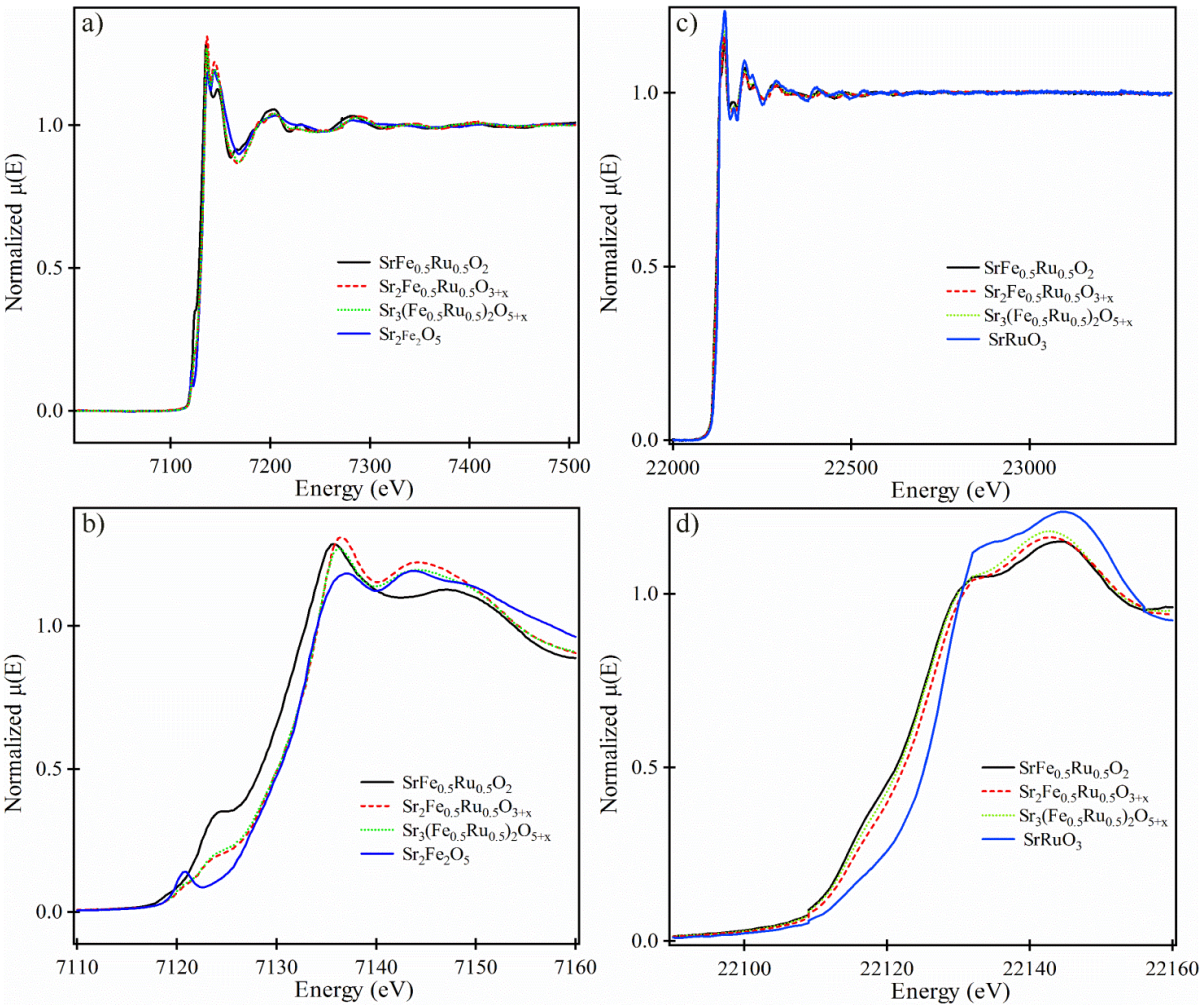

Figure 5.7: Fe K-edge ((a) and (b)) and Ru K-edge ((c) and (d)) absorption spectra collected from $Sr_2(Ru_{0.5}Fe_{0.5})O_{3.35}$, $Sr_3(Ru_{0.5}Fe_{0.5})_2O_{5.67}$, and selected standards.

The Fe K-edge adsorption data of $Sr_2(Ru_{0.5}Fe_{0.5})O_{3.35}$ and $Sr_3(Ru_{0.5}Fe_{0.5})_2O_{5.67}$ is shown in Figure 5.7 (a) and (b). It can be seen that, apart from pre-edge features relating to coordination environments, the absorption edges of $Sr_2(Ru_{0.5}Fe_{0.5})O_{3.35}$ and $Sr_3(Ru_{0.5}Fe_{0.5})_2O_{5.67}$ are a good match for those of $Sr_2Fe_2O_5$, the Fe^{3+} standard, and are significantly displaced from the position of the Fe^{2+} edge in $Sr(Ru_{0.5}Fe_{0.5})O_2$.

The presence of Fe^{3+} in both samples results in ruthenium oxidation states of +2.4 and +2.34 for the single and double layer phases respectively. This is consistent with the data observed

from the Ru K-edge: the edge position is displaced towards higher energy from $Sr(Ru_{0.5}Fe_{0.5})O_2$, consistent with these oxidation states.

5.3.3 ^{57}Fe Mössbauer Spectroscopy

^{57}Fe Mössbauer spectra collected from $Sr_2(Ru_{0.5}Fe_{0.5})O_{3.35}$ and $Sr_3(Ru_{0.5}Fe_{0.5})_2O_{5.67}$ are shown in Figure 5.8. Both spectra can be fitted by three overlapping doublets: a pair of doublets corresponding to Fe^{3+} centers (sites 1 and 2) which account for ~98% of the area of both spectra, and a further weak doublet (site 3) which corresponds to a low concentration of Fe^{4+} centers. Despite the small contribution of the Fe^{4+} sites to the spectra collected from both samples, the presence of this site is supported by a visually observed shoulder in the data, and the inclusion of this doublet significantly improves the fit to both spectra, as demonstrated by comparison of the χ^2 values associated with the two-doublet and three-doublet fits given in Table 5.6 and Table 5.7. Two-doublet fits to the spectra are shown in 8.3Appendix 5.1.

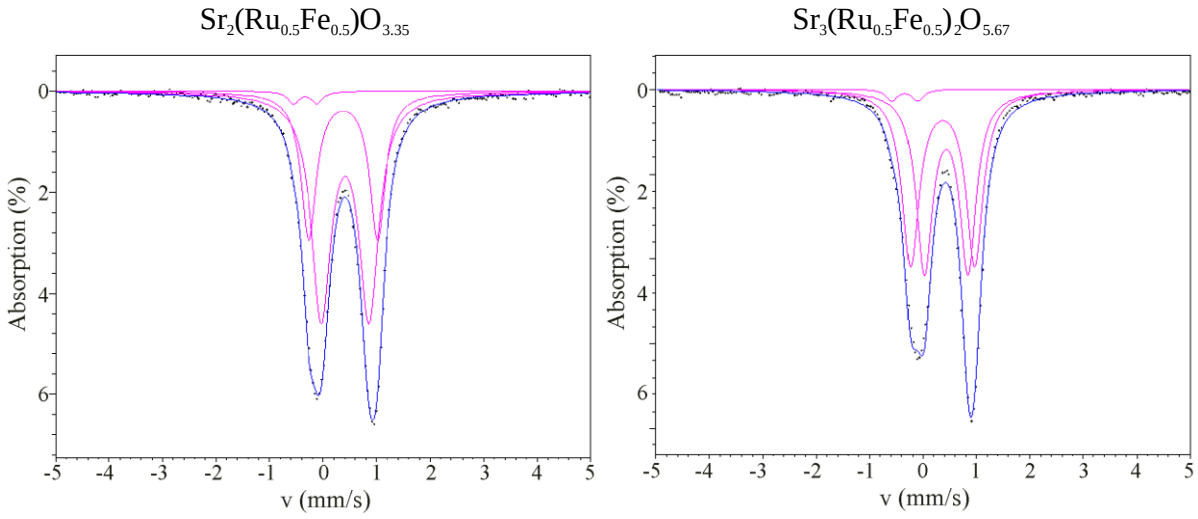

Figure 5.8: ^{57}Fe Mössbauer spectra collected from $Sr_2(Ru_{0.5}Fe_{0.5})O_{3.35}$ and $Sr_3(Ru_{0.5}Fe_{0.5})_2O_{5.67}$.

Doublet 1	**Fit 1**	**Fit 2**
Centre Shift / mm s^{-1}	0.406	0.411
Quadrupole Splitting / mm s^{-1}	0.912	0.892
Linewidth / mm s^{-1}	0.221	0.218
Area Fraction / %	67.9%	64.2%
Doublet 2		
Centre Shift / mm s^{-1}	0.373	0.375
Quadrupole Splitting / mm s^{-1}	1.298	1.285
Linewidth / mm s^{-1}	0.178	0.173
Area Fraction / %	32.1%	34.0%
Doublet 3	**-**	
Centre Shift / mm s^{-1}	-	-0.335
Quadrupole Splitting / mm s^{-1}	-	0.436
Linewidth / mm s^{-1}	-	0.12*
Area Fraction / %	-	1.86%
Reduced χ^2 for fit	1.45761	1.17749
# Data points	258	258
# Doublets in model	2	3
# Parameters in model	13	19
# Refined parameters	9	12

Table 5.6: A comparison of parameters extracted from 2-doublet and 3-doublet fits to the Mössbauer spectrum collected from $Sr_2(Ru_{0.5}Fe_{0.5})O_{3.35}$.

Doublet 1	**Fit 1**	**Fit 2**
Centre Shift / mm s^{-1}	0.429	0.433
Quadrupole Splitting / mm s^{-1}	0.835	0.818
Linewidth / mm s^{-1}	0.187	0.184
Area Fraction / %	50.1%	48.9%
Doublet 2		
Centre Shift / mm s^{-1}	0.365	0.367
Quadrupole Splitting / mm s^{-1}	1.204	1.202
Linewidth / mm s^{-1}	0.198	0.190
Area Fraction / %	49.9%	49.1%
Doublet 3		
Centre Shift / mm s^{-1}	-	-0.341
Quadrupole Splitting / mm s^{-1}	-	0.478
Linewidth / mm s^{-1}	-	0.12*
Area Fraction / %	-	2.05%
Reduced χ^2 for fit	3.82181	3.43853
# Data points	258	258
# Doublets in model	2	3
# Parameters in model	13	19
# Refined parameters	9	12

Table 5.7: A comparison of parameters extracted from 2-doublet and 3-doublet fits to the Mössbauer spectrum collected from $Sr_3(Ru_{0.5}Fe_{0.5})_2O_{5.67}$.

5.3.4 Magnetisation Measurements

Magnetisation data were collected as a function of temperature from $Sr_2(Ru_{0.5}Fe_{0.5})O_{3.35}$ in an applied field of 100 Oe. These reveal a divergence between the zero-field cooled and the field-cooled data at T ~ 260 K, and a local maximum in the zero-field cooled data at T ~ 20 K (Figure 5.9). Analogous magnetization data collected as a function of temperature from $Sr_3(Ru_{0.5}Fe_{0.5})_2O_{5.67}$ show a divergence at T ~ 20 K (Figure 5.9). Neither data set could be fitted to the Currie-Weiss law over any significant temperature range.

Magnetisation-field data collected at 5 K from both samples exhibit hysteresis and are displaced from the origin, suggesting spin-glass type behaviour (Figure 5.9). No evidence for long-range magnetic order was observed in neutron powder diffraction data collected at 5 K from either sample.

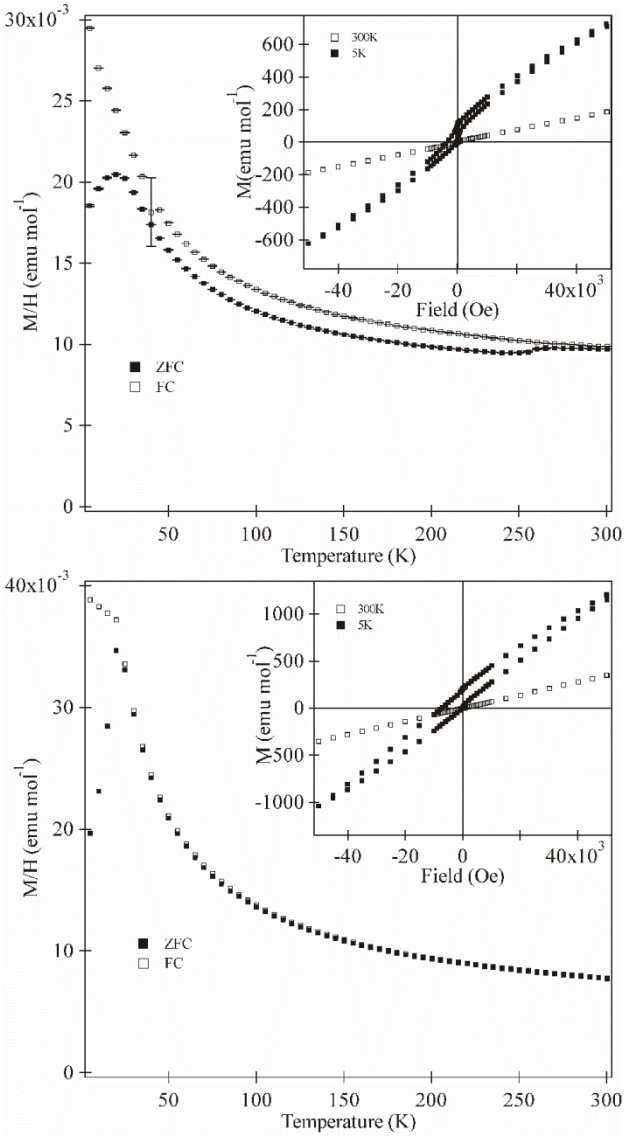

Figure 5.9: Zero-field cooled and field cooled magnetization data collected from $Sr_2(Ru_{0.5}Fe_{0.5})O_{3.35}$ (top) and $Sr_3(Ru_{0.5}Fe_{0.5})_2O_{5.67}$ (bottom). Insets show magnetization isotherms collected at 300K and 5K.

5.3.5 Two-Phase Reduction Behaviour

The separation of $Sr_2(Ru_{0.5}Fe_{0.5})O_4$ and $Sr_3(Ru_{0.5}Fe_{0.5})_2O_7$ into two distinct phases on reduction is rather unusual. In order to investigate this further, a series of test reactions were performed by heating 2:1 molar ratios of $Sr_2(Ru_{0.5}Fe_{0.5})O_4$ and CaH_2 in sealed silica ampoules at 375 °C for multiple periods of two days until the X-ray powder diffraction patters collected from the products no longer changed between heating periods. These

reactions utilised $Sr_2(Ru_{0.5}Fe_{0.5})O_4$ prepared in separate batches as described above, all of which were identical by diffraction.

X-ray powder diffraction data revealed that all test reactions produced two-phase mixtures of topochemically reduced $Sr_2(Ru_{0.5}Fe_{0.5})O_{4-x}$ phases. As shown in Table 5.8, the lattice parameters of the reduced product phases are very similar to those refined against neutron powder diffraction data collected from the large-scale sample, indicating that the same two phases are produced in all cases. However, the relative fractions of the two phases in the reduced products, while constant if the same batch of $Sr_2(Ru_{0.5}Fe_{0.5})O_4$ was used, varied between batches, indicating some subtle feature of the starting material was influencing the reduction behaviour.

	Phase 1			Phase ratio	Phase 2		
Batch	***a* (Å)**	***b* (Å)**	***c* (Å)**		***a* (Å)**	***b* (Å)**	***c* (Å)**
Neutron	3.645(1)	3.902(1)	12.898(2)	48:52	3.716(1)	3.893(1)	12.856(2)
X-ray 1	3.666(2)	3.889(3)	12.897(3)	42:58	3.723(4)	3.901(3)	12.865(6)
X-ray 2	3.633(2)	3.893(2)	12.905(3)	51:49	3.731(2)	3.906(2)	12.856(6)

Table 5.8: Lattice parameters and phase fractions extracted from the two phase samples prepared by the reaction of $Sr_2(Ru_{0.5}Fe_{0.5})O_4$ and CaH_2 at 375 °C.

5.4 Discussion

Reaction of the $n = 1$ and $n = 2$ Ruddlesden-Popper phases Sr_2RuO_4 and $Sr_3Ru_2O_7$ with CaH_2 leads to the decomposition of the extended oxide phases into a mixture of binary oxides and Ru metal in a manner analogous to that observed in the attempted reduction of $SrRuO_3$ (Chapter 4). However, substitution of 50% of the ruthenium with iron stabilises the extended metal-oxide lattice, enabling $Sr_2(Ru_{0.5}Fe_{0.5})O_4$ and $Sr_3(Ru_{0.5}Fe_{0.5})_2O_7$ to undergo topochemical reductive deintercalation of oxide ions from the $(Ru_{0.5}Fe_{0.5})O_2$ equatorial planes to yield materials with average compositions $Sr_2(Ru_{0.5}Fe_{0.5})O_{3.35}$ and $Sr_3(Ru_{0.5}Fe_{0.5})_2O_{5.67}$ respectively.

Powder diffraction data show that the reduced products formed from both starting materials are composed of two phases, which retain the cation lattice of the respective parent phases but with differing oxygen stoichiometries. Thus, the n = 1 product is a 47.9%:52.1% mixture of $Sr_2(Ru_{0.5}Fe_{0.5})O_{3.25}$ and $Sr_2(Ru_{0.5}Fe_{0.5})O_{44}$ and the n = 2 product is a 49.8%:50.2% mixture of $Sr_3(Ru_{0.5}Fe_{0.5})_2O_{5.50}$ and $Sr_3(Ru_{0.5}Fe_{0.5})_2O_{5.86}$.

5.4.1 Reactivity of $Sr_{n+1}(Ru_{0.5}Fe_{0.5})_nO_{3n+1}$ Phases

The relatively low level of reduction achieved (average transition metal oxidation states of +2.7 and +2.68 for n =1 and n = 2 respectively) and the separation into two phases on reaction with CaH_2 is quite unlike the behaviour observed in the reduction of the all-iron phases $SrFeO_{3-x}$ and $Sr_3Fe_2O_7$ and the iron/ruthenium perovskite $Sr(Ru_{0.5}Fe_{0.5})O_3$, all three of which form single-phase products with an average transition metal oxidation state of +2 (Chapter 4).[19,55,87] Given the similar reduction behaviour of both iron/ruthenium layered phases (an approximate 1:1 mixture of phases with composition $SrO(Sr(Ru_{0.5}Fe_{0.5})O_{2.25})_n$:$SrO(Sr(Ru_{0.5}Fe_{0.5})O_{2.43})_n$) it seems likely that there is a common explanation for the unusual reactivity of these materials.

Reviewing the reaction conditions necessary to effect the reduction of the all-iron phases, it is observed that $SrFeO_{3-x}$ is reduced at 280 °C, whereas $Sr_3Fe_2O_7$ is reduced at 350 °C.[19,55] This suggests that the n = 2 Ruddlesden-Popper phase presents a higher energetic barrier to oxide ion migration than the perovskite phase. Considering that the reduction of $Sr(Ru_{0.5}Fe_{0.5})O_3$ occurs at 400 °C, reduction of the layered iron/ruthenium phases would be expected to take place at a significantly higher temperature. However, reduction reactions of $Sr_2(Ru_{0.5}Fe_{0.5})O_4$ and $Sr_3(Ru_{0.5}Fe_{0.5})_2O_7$ attempted at temperatures above 430 °C resulted in decomposition of the starting materials to binary oxides and elemental metals. It is therefore proposed that the lower level of reduction achieved in the reactions between $Sr_2(Ru_{0.5}Fe_{0.5})O_4$ and $Sr_3(Ru_{0.5}Fe_{0.5})_2O_7$ and CaH_2 are due to the reduced anion mobility. That is to say, at the

temperatures required to have a suitably mobile anion lattice, the cation lattice is sufficiently mobile to inhibit topochemical reduction, resulting in non-topochemical, thermodynamic reaction products (SrO, Ru and Fe).

The separation of both $Sr_2(Ru_{0.5}Fe_{0.5})O_4$ and $Sr_3(Ru_{0.5}Fe_{0.5})_2O_7$ into two phases on reduction is unexpected, but not unprecedented. A number of other complex oxide phases have previously been observed to undergo phase separation on reduction, and this behaviour has been attributed to a number of different factors. For example, the n = 1 Ruddlesden-Popper phase $LaSrCoO_4$ forms two phases on reduction with dilute hydrogen gas: $LaSrCoO_{3.43}$ and $LaSrCoO_{3.57}$ due to incomplete reduction (compared with the analogous reaction with NaH) and inhomogeneous reaction conditions throughout the sample during reduction.[92]

In contrast, the two-phase behaviour observed during the reduction of the $Y_2Ti_2O_7$ pyrochlore phase can be explained on the basis of the existence of a compositional "phase gap" driven by the electronic structure of the material, such that materials with average compositions $Y_2Ti_2O_x$ ($6.50 < x < 5.90$) are two-phase mixtures of $Y_2Ti_2O_{6.50}$ and $Y_2Ti_2O_{5.90}$.[93]

However, neither situation offers a convincing explanation for the phase separation observed during the reduction of $Sr_2(Ru_{0.5}Fe_{0.5})O_4$ and $Sr_3(Ru_{0.5}Fe_{0.5})_2O_7$. As noted above, the molar ratio of the two phases produced in both cases does not evolve over time once established. This is unlike both the $LaSrCoO_{4-x}$ and $Y_2Ti_2O_{7-x}$ systems. In both cases, the reduction is still proceeding and single phases can be produced given enough time.

This leads to the conclusion that the observed two-phase behaviour of the $Sr_2(Ru_{0.5}Fe_{0.5})O_4$ and $Sr_3(Ru_{0.5}Fe_{0.5})_2O_7$ reduction products does not arise from incomplete reduction or electronically-driven phase separation, but is a result of different portions of the sample reacting with CaH_2 to different extents, despite being subject to the same reaction conditions. This in turn suggests that the observed behaviour is due to some inhomogeneity in the

starting materials which patterns the reduction behaviour. This is supported by the observation that the ratios of the two phases produced is constant within any one batch of starting material, but different batches yield different ratios (Table 5.8).

Close inspection of the diffraction data collected from the starting materials revealed no evidence of compositional inhomogeneity. In addition, the structural models refined against data collected from the reduced materials (Table 5.2 and Table 5.4) show no indication ruthenium/iron segregation between the product phases for either the $n = 1$ or $n = 2$ phases, indicating that, on the length scale probed by diffraction, both samples have homogeneous ruthenium/iron distributions.

The ^{57}Fe Mössbauer spectra collected, however, reveal that this is not the case over short length scales. Previous studies of the $SrO(Sr(Ru_{0.5}Fe_{0.5})O_3)_n$ series of phases indicate that the transition metals adopt a Ru^{5+}/Fe^{3+} oxidation state combination, as demonstrated by Mössbauer and magnetic data.[76,89,94] The observation of small, but clearly present Fe^{4+} signals in the Mössbauer data collected from the $SrO(Sr(Ru_{0.5}Fe_{0.5})O_{3-x})_n$ phases after reduction is therefore surprising. The most plausible explanation for their presence in the reduced material is that they were present in the starting material prior to reduction and were unaffected by reaction with CaH_2. The presence of Fe^{4+} in the starting material is consistent with the presence of very small ruthenium-rich and iron-rich regions which would contain some Ru^{4+} and Fe^{4+} centres respectively, rather than the Ru^{5+}/Fe^{3+} combination present in a totally homogeneous sample due to poor Ru/Fe mixing.

The phase separation of $SrO(Sr(Ru_{0.5}Fe_{0.5})O_3)_n$ on reduction can therefore be rationalised by observing that the introduction of ruthenium into $SrFeO_{3-x}$ raises the temperature required for anion deintercalation from 280 °C to 400 °C (Chapter 4) indicating a decline of anion

mobility.[55,87] Therefore, any local variation in the ruthenium:iron ratio is likely to lead to a significant change in the "reducibility," resulting in an inhomogeneous multiphase product.

5.4.2 Transition Metal Oxidation States and Coordination Geometries

The reduction of $SrO(Sr(Ru_{0.5}Fe_{0.5})O_3)_n$ phases occurs via the removal of oxide ions from the $(Ru_{0.5}Fe_{0.5})O_2$ sheets present in the starting material to form phases containing chains (n = 1) or double chains (n = 2) of apex-sharing $(Ru_{0.5}Fe_{0.5})O_4$ square planes running along the y-axis of the resulting orthorhombic phases. These chains are linked by oxide ions retained in the (1/2, 0, z) anion positions. As a result, the transition metal cations reside in both square-planar MO_4 and square-based pyramidal MO_5 coordination environments as shown in (Figure 5.10).

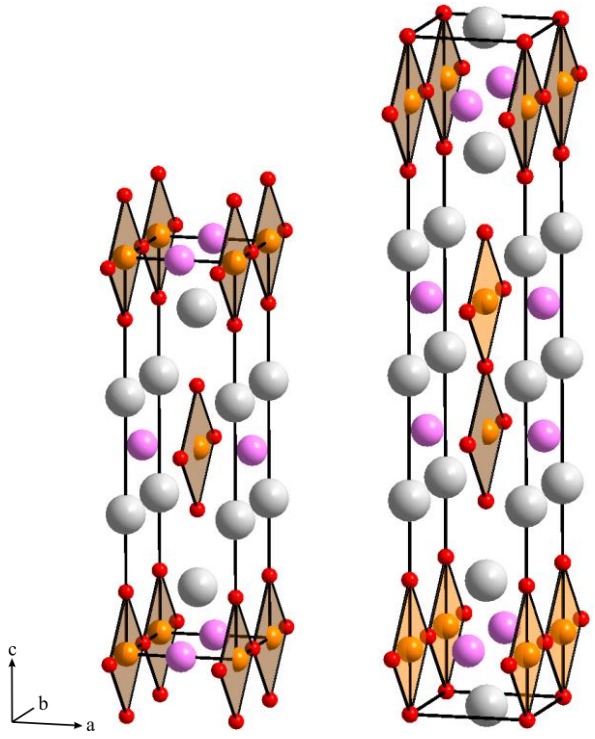

Figure 5.10: The structures of the reduced phases $Sr_2(Ru_{0.5}Fe_{0.5})O_{4-x}$ (left)and $Sr_3(Ru_{0.5}Fe_{0.5})_2O_{7-x}$ (right). Pink spheres represent partially occupied (1/2, 0, z) anion positions.

The primary difference between the $SrO(Sr(Ru_{0.5}Fe_{0.5})O_{2.25})_n$ phases and the $SrO(Sr(Ru_{0.5}Fe_{0.5})O_{2.43})_n$ phases produced on reduction is the concentration of oxide ions in the (1/2, 0, *z*) anion site. The $SrO(Sr(Ru_{0.5}Fe_{0.5})O_{2.25})_n$ phases have a 25% occupancy of the (1/2, 0, *z*) anion site, resulting in a 50:50 mixture of MO_4 and MO_5 transition metal coordination environments. The $SrO(Sr(Ru_{0.5}Fe_{0.5})O_{2.43})_n$ have a 43% occupancy of the (1/2, 0, *z*) anion site, resulting in a 14:86 mixture of MO_4 and MO_5 transition metal coordination environments.

It should be noted, however, that the absolute composition of the phases observed in neutron powder diffraction data cannot be determined solely from rietveld refinement. While the absolute composition is known from thermogravimetric data, the strong correlation between anion site occupancy and isotropic thermal displacement parameters means that the oxide content of the phases extracted in the refinement is an approximation and the true error bars on the values quoted are in reality much greater than estimated by the refinement.

XANES data collected from the iron K-edge of both reduced samples indicate that practically all of the iron centers are in the +3 oxidation state. Knowing the absolute overall oxygen content in the materials from thermogravimetric analysis, we can therefore know that the ruthenium centers are on average in oxidation states below 3. When combined with the oxygen stoichiometries extracted from neutron powder diffraction data, this yields oxidation state combinations of $Sr_2(Ru^{2+}_{0.5}Fe^{3+}_{0.5})O_{3.25}$ and $Sr_3(Ru^{2+}_{0.5}Fe^{3+}_{0.5})_2O_{5.5}$ for the $SrO(Sr(Ru_{0.5}Fe_{0.5})O_{2.25})_n$ phases and $Sr_2(Ru^{2.76+}_{0.5}Fe^{3+}_{0.5})O_{3.44}$ and $Sr_3(Ru^{2.72+}_{0.5}Fe^{3+}_{0.5})_2O_{5.86}$ for the $SrO(Sr(Ru_{0.5}Fe_{0.5})O_{2.43})_n$ phases. These phases thus join $Sr(Ru_{0.5}Fe_{0.5})O_2$ as the only examples of Ru^{2+} in extended oxide systems (Chapter 4).

The models refined against neutron powder diffraction data in both cases remain approximations, as it is more likely that the phases are composed of a continuous range of compositions rather than two discrete phases.

^{57}Fe Mössbauer spectroscopy data collected from both $Sr_2(Ru_{0.5}Fe_{0.5})O_{3.35}$ and $Sr_3(Ru_{0.5}Fe_{0.5})_2O_{5.67}$ indicate that 98% of the iron centres are in the +3 oxidation state, in agreement with the XANES data, with a small amount of the iron centres are in the +4 oxidation state (~2%, site 3). The relatively large values of the quadrupolar splitting of the Fe^{3+} sites are broadly consistent with FeO_5 and FeO_4 coordination sites obtained from the crystallographic analysis of both samples.

Furthermore, the 65.3%:34.6% area ration of sites 1 and 2 extracted from the spectrum collected from $Sr_2(Ru_{0.5}Fe_{0.5})O_{3.35}$ shows a good agreement with the 66%:34% ratio of FeO_5:FeO_4 predicted by the crystallographic data.

The area ratios obtained from the $Sr_3(Ru_{0.5}Fe_{0.5})_2O_{5.67}$ spectrum match the crystallographic predictions less well (49.9%:50.1% observed, 68%:32% predicted). This is most likely due to the correlation in parameters resulting from fitting broad smooth spectra to multiple overlapping doublets. With this in mind, it should be noted that while the fits to the Mössbauer spectra in Table 5.6 and Table 5.7 appear robust, it is possible that they may have significant errors associated with them. However, these caveats notwithstanding, the combination of crystallographic and Mössbauer data suggest that both $Sr_2(Ru_{0.5}Fe_{0.5})O_{3.35}$ and $Sr_3(Ru_{0.5}Fe_{0.5})_2O_{5.67}$ contain Fe^{3+} centres in square-planar coordination environments – a highly unusual occurrence in extended oxide phases. Square-planar Fe^{3+} has previously been observed in $YBa_2Cu_3O_x$ when doped with small (~0.1) amounts of iron.[95]

The Ru^{2+}/Fe^{3+} oxidation state combination observed in the $SrO(Sr(Ru_{0.5}Fe_{0.5})O_{2.25})_n$ phases is unexpected. Typically, 4*d* transition metals favour higher oxidation states than 3*d* transition

metals, as exemplified by the Ru^{5+}/Fe^{3+} oxidation state combination found in the $SrO(Sr(Ru_{0.5}Fe_{0.5})O_3)_n$ starting materials.[76,89,94] We would therefore expect to see the Ru^{3+}/Fe^{2+} oxidation state combination predicted by the standard reduction potentials of the two metals ($Ru^{3+}_{(aq)}/Ru^{2+}_{(aq)}$ = +0.248 V and $Fe^{3+}_{(aq)}/Fe^{2+}_{(aq)}$ = +0.77 V).[83]

However, the Ru^{3+}/Ru^{2+} and Fe^{3+}/Fe^{2+} redox couples exhibit a strong ligand dependence, such that in the presence of ligands high in the electrochemical series such as cyanide and 2, 2'-dipyridine (bipy), the Ru^{2+}/Fe^{3+} oxidation state combination is thermodynamically favourable ($Ru(CN)_6^{3-}/Ru(CN)_6^{4-}$ = +0.86 V, $Fe(CN)_6^{3-}/Fe(CN)_6^{4-}$ = +0.358 V; $Ru(bipy)_3^{3+}/Ru(bipy)_3^{2+}$ = +1.24 V; $Fe(bipy)_3^{3+}/Fe(bipy)_3^{2+}$ = +0.96 V).[96]

This suggests that the transition metal coordination sites in $SrO(Sr(Ru_{0.5}Fe_{0.5})O_x)_n$ reduced phases help to stabilise Ru in the +2 oxidation state in some way.

5.4.3 Magnetic Behaviour

Magnetisation data collected from the $SrO(Sr(Ru_{0.5}Fe_{0.5})O_x)_n$ reduced samples is indicative of spin-glass behaviour at low temperatures. This behaviour is similar to that observed in the cave of $Sr(Ru_{0.5}Fe_{0.5})O_2$ (Chapter 4) and consistent with the high levels of chemical and structural disorder in these materials and the consequent wide range of competing magnetic interactions.

5.5 Conclusion

Reaction of the n = 1 and n = 2 Ruddlesden-Popper phases $Sr_2(Ru_{0.5}Fe_{0.5})O_4$ and $Sr_3(Ru_{0.5}Fe_{0.5})_2O_7$ with calcium hydride results in the topochemical deintercalation of oxide ions and the resulting formation of phases with compositions $Sr_2(Ru_{0.5}Fe_{0.5})O_{3.35}$ and $Sr_3(Ru_{0.5}Fe_{0.5})_2O_{5.67}$ respectively.

Diffraction data reveal both materials undergo phase separation on reduction and consist of two-phase mixtures of topochemically reduced phases with slightly different oxygen stoichiometries. It is proposed that this phase separation is the result of short-range iron-ruthenium inhomogeneity in the starting materials.

The stoichiometries of the two $SrO(Sr(Ru_{0.5}Fe_{0.5})O_x)_n$ reduced materials yield average transition metal oxidation states of $M^{+2.70}$ and $M^{+2.67}$ for the n = 1 and n = 2 samples respectively. X-ray absorption spectra reveal these values are from a combination of Fe^{3+} and $Ru^{2+/3+}$. Considering the oxygen-stoichiometric $SrO(Sr(Ru_{0.5}Fe_{0.5})O_3)_n$ starting materials have Ru^{5+}/Fe^{3+} oxidation states,[76,89,94] this indicates that only the ruthenium centres are reduced during the oxygen deintercalation.

These findings have been reported in a recent publication.[97]

Chapter 6 Fluorination of $Sr_3(Ru_{0.5}M_{0.5})_2O_7$ (M = Ti, Mn, Fe)

6.1 Introduction

There are a large number of published examples of topochemical fluorination reactions resulting in the preparation of novel metastable phases containing correspondingly novel electronic states. For example, superconducting $La_2CuO_4F_\delta$ and $Sr_2CuO_3F_{2+\delta}$ can be prepared from semiconducting La_2CuO_4 and Sr_2CuO_3 by oxidative insertion of fluorine into vacant anion sites.[35,98]

Topochemical fluorination of Ruddlensden-Popper phases is particularly attractive as these phases contain an interstitial site within the rock salt layers that can accommodate insertion of fluoride anions. These sites are far from the transition metal centres. Fluorination therefore allows the transition metal oxidation state in these phases to be manipulated without altering their coordination environment.

For example, fluorination of $Sr_3Ru_2O_7$, a Ru^{4+} phase, results in the formation of $Sr_3Ru_2O_7F_2$ containing Ru^{5+}. This change is accompanied by a significant rise in the magnetic ordering temperature.[39]

The synthesis and fluorination of $Sr_3(Ru_{0.5}Ti_{0.5})_2O_7$ was performed in order to study the fluorination chemistry of oxidation states of ruthenium beyond +5. Additionally, the fluorination of $Sr_3(Ru_{0.5}M_{0.5})_2O_7$ (M = Fe, Mn) was performed in order to study the behaviour of these phases on changing oxidation states.

6.2 Experimental

6.2.1 Synthesis of $Sr_3(Ru_{0.5}M_{0.5})_2O_7$ (M = Fe, Mn)

Samples of $Sr_3(Ru_{0.5}Fe_{0.5})_2O_7$ were synthesised in the manner described in Section 5.2.1.

Samples of $Sr_3(Ru_{0.5}Mn_{0.5})_2O_7$ were synthesised via the route described by Battle *et al.*[99] using citrate gel precursors (see Section 2.3) from suitable stoichiometric quantities of $SrCO_3$ (Alfa Aesar 99.99%), RuO_2 (from RuO_2 hydrate (Alfa Aesar 99.99%) dried at 800 °C), and MnO_2 (Alfa Aesar 99.997%). The resulting powders were placed in an alumina crucible and heated at 1 °C min^{-1} to 1000 °C to decompose the carbonates. The powders were then reground, pressed into 13 mm diameter pellets and heated at 1000 °C, 1200 °C, 1300 °C, and 1350 °C for periods of two days at each temperature in air with one intermediate grinding at each temperature.

The resulting powders were observed to be phase-pure by laboratory X-ray powder diffraction, with lattice parameters a = 3.91(1) Å and c = 20.14(1) Å, in good agreement with reported values (a = 3.90(1) Å and c = 20.13(1) Å).[99] No additional peaks indicating B-cation order were observed.

6.2.2 Synthesis of $Sr_3(Ru_{0.5}Ti_{0.5})_2O_7$

As neither RuO_2 or TiO_2 dissolve easily, the synthesis of $Sr_3(Ru_{0.5}Ti_{0.5})_2O_7$ was carried out using standard ceramic techniques. Suitable stoichiometric quantities of $SrCO_3$, RuO_2, and TiO_2 (Alfa Aesar 99.995%) were ground together using an agate mortar and pestle. The resulting powders were placed in an alumina crucible and heated at 1 °C min^{-1} to 1000 °C to decompose the carbonate. The powders were then reground, pressed into 13 mm diameter pellets and heated at several temperatures between 1000 and 1400 °C for periods of two days at each temperature with intermediate grindings. Reaction progress was monitored using X-ray powder diffraction.

6.2.3 Fluorination of $Sr_3(Ru_{0.5}Fe_{0.5})_2O_7$ (M = Fe, Mn, Ti)

6.2.3.1 F_2 Gas

The fluorination of $Sr_3(Ru_{0.5}Fe_{0.5})_2O_7$ was attempted using a mixture of 10% F_2 in N_2. In order to assess the reactivity of this material, small samples (~ 200 mg) were placed in an alumina crucible, which was then placed in a quartz tube fitted with brass end caps (see Section 2.5.1). The tube was then purged with N_2 for an hour before being heated to the desired temperature. The flow was then switched to the mixture of 10% F_2 in N_2 for an appropriate length of time. The system was then again flushed with N_2 and allowed to cool.

6.2.3.2 CuF_2

The fluorination of $Sr_3(Ru_{0.5}Fe_{0.5})_2O_7$ was attempted using CuF_2 as a solid-state fluorinating agent. In order to assess the reactivity of these materials, small samples (~ 200 mg) were ground together with a suitable molar ratio of CuF_2 (anhydrous, Alfa Aesar 99.5%, kept under inert atmosphere). The powders were then placed in an alumina crucible and heated to suitable temperatures for an appropriate length of time.

Large samples suitable for neutron powder diffraction measurements were prepared by grinding $Sr_3(Ru_{0.5}M_{0.5})_2O_7$ (M = Fe, Mn, Ti) with two mole equivalents of CuF_2 using an agate mortar and pestle. The resulting powders were placed in an alumina crucible and heated to 250 °C under a flow of oxygen for periods of 12 hours. In order to ensure all CuF_2 had reacted to form CuO, heating cycles were repeated until no more CuF_2 was visible in X-ray powder diffraction data (three iterations were generally found to be sufficient).

6.2.4 Fluorination of $Sr_3(Ru_{0.5}M_{0.5})_2O_7$ (M = Mn, Ti)

The fluorination of $Sr_3(Ru_{0.5}M_{0.5})_2O_7$ (M = Mn, Ti) was performed using CuF_2. Samples were ground together with a double molar excess of CuF_2 using an agate mortar and pestle. The resulting powders were placed in an alumina crucible and heated to 250 °C under flowing

oxygen for periods of 12 hours. In order to ensure all CuF_2 had reacted to form CuO, heating cycles were repeated until no more CuF_2 was visible in X-ray powder diffraction data (three iterations were generally found to be sufficient).

6.3 Results

6.3.1 Synthesis and Structure of $Sr_3(Ru_{0.5}Ti_{0.5})_2O_7$

X-ray powder diffraction data from attempted syntheses of $Sr_3(Ru_{0.5}Ti_{0.5})_2O_7$ are shown in Figure 6.1.

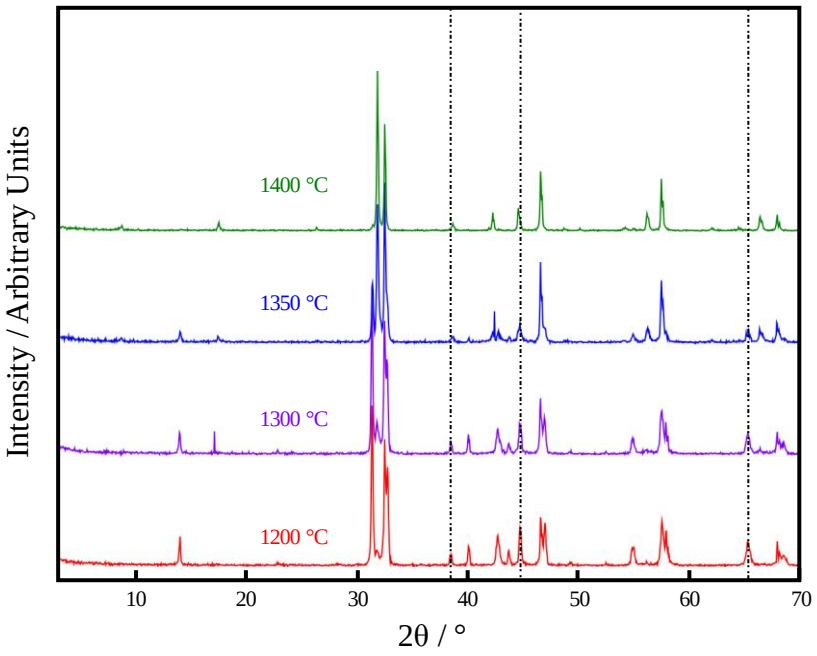

Figure 6.1: X-ray powder diffraction data collected from $Sr_3(Ru_{0.5}Ti_{0.5})_2O_7$ synthesised at different temperatures collected using the Philips PW1710 diffractometer. The indicated peaks are contributions from the aluminium sample holder.

Data collected from samples heated at 1200 °C were consistent with a mixture of a perovskite phase and an n = 1 Ruddlesden-Popper phase, with a small amount of an n = 2 phase.

As the reaction temperature was increased, the phase fractions of the pervoskite and n = 1 phase gradually decreased in favour of the n = 2. X-ray powder diffraction data collected

from samples heated to 1400 °C could be indexed on the basis of a body-centred tetragonal unit cell with lattice parameters a = 3.91(1) Å and c = 20.38(1) Å. A model based on the structure of an n = 2 Ruddlesden-Popper phase with a 1:1 disordered mixture of Ru and Ti on the B-site was constructed and refined against X-ray powder diffraction data collected using the X'Pert diffractometer to give a good statistical fit (χ^2 = 2.645). No evidence of multiple phases or Ru/Ti ordering was observed.

Observed, calculated and difference plots are shown in Figure 6.2. Full structural details of the refined structure are given in Table 6.1 and selected bond lengths are given in Table 6.2.

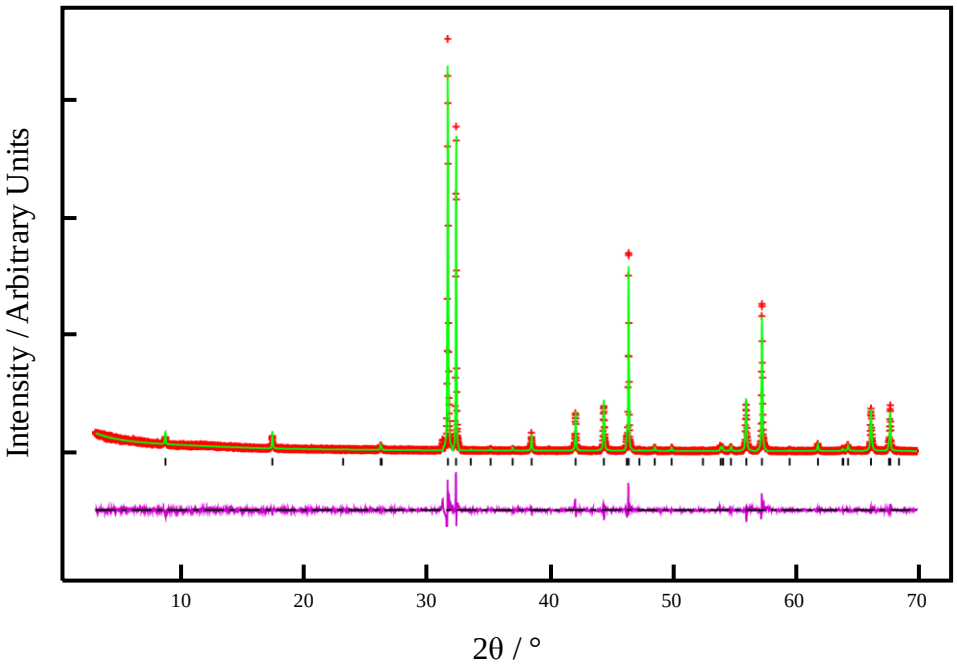

Figure 6.2: Observed, calculated, and difference plots for refinement of the structural model of $Sr_3(Ru_{0.5}Ti_{0.5})_2O_7$ against X-ray powder diffraction data collected using the X'Pert instrument.

Atom	Wyckoff Position	*x*	*y*	*z*	Fractional Occupancy	U_{iso} / Å^2
Sr(1)	2*b*	0	0	1/2	1	0.028(1)
Sr(2)	4*e*	0	0	0.3140(1)	1	0.032(1)
Ru/Ti(1)	4*e*	0	0	0.0990(1)	0.5/0.5	0.023(1)
O(1)	2*a*	0	0	0	1	0.066(7)
O(2)	4*e*	0	0	0.1993(5)	1	0.046(4)
O(3)	8*g*	0	1/2	0.0989(3)	1	0.065(3)
$Sr_3(Ru_{0.5}Ti_{0.5})_2O_7$: space group *I*4/*mmm*; *a* = 3.9078(1) Å and *c* = 20.3792(5) Å; cell volume = 311.21(1) Å^3; weight fraction = 100%						
χ^2 = 2.645, wRp = 0.17%, Rp = 0.12%						

Table 6.1: Refined structural parameters for $Sr_3(Ru_{0.5}Ti_{0.5})_2O_7$ at 298 K.

Cation	Anion	Bond Length / Å	Bond Valence Sum
Sr(1)	O(1)	2.763(1) x 4	Sr +1.95
	O(3)	2.806(4) x 8	
Sr(2)	O(2)	2.337(10) x 1	Sr +2.20
	O(2)	2.776(1) x 4	
	O(3)	2.641(4) x 4	
Ru/Ti	O(1)	2.018(2) x 1	Ru +4.07
	O(2)	2.044(10) x 1	Ti +3.86
	O(3)	1.954(1) x 4	

Table 6.2: Selected bond lengths and bond valence parameters from the refined structure of $Sr_3(Ru_{0.5}Ti_{0.5})_2O_7$ at 298 K.

6.3.2 Magnetic Properties of $Sr_3(Ru_{0.5}Ti_{0.5})_2O_7$

Zero-field and field cooled magnetisation data collected from $Sr_3(Ru_{0.5}Ti_{0.5})_2O_7$ as a function of temperature in a field of 100 Oe are shown in Figure 6.3. These could be fitted to the Curie-Weiss law in the temperature range $80 \leq T / K \leq 300$ to yield values of C = 1.62(2) cm^3 K mol^{-1}, θ = -27.7(3) K and K = 0.00008(4) cm^3 where mol^{-1} means per mole of formula units of $Sr_3(Ru_{0.5}Ti_{0.5})_2O_7$. Below T ~ 80 K, the zero-field cooled and field cooled data diverge, indicating a magnetic transition.

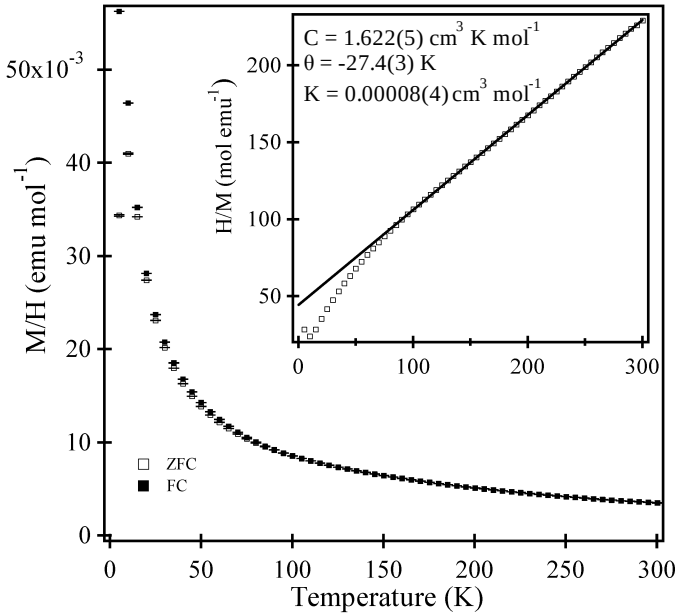

Figure 6.3: Zero-field cooled and field cooled magnetisation data collected from $Sr_3(Ru_{0.5}Ti_{0.5})_2O_7$.

6.3.3 Reactivity of $Sr_3(Ru_{0.5}Fe_{0.5})_2O_7$

6.3.3.1 F_2 Gas

Reactions performed below 140 °C showed no evidence of reaction. X-ray powder diffraction data collected from the products of reaction performed at higher temperatures are shown in Figure 6.4.

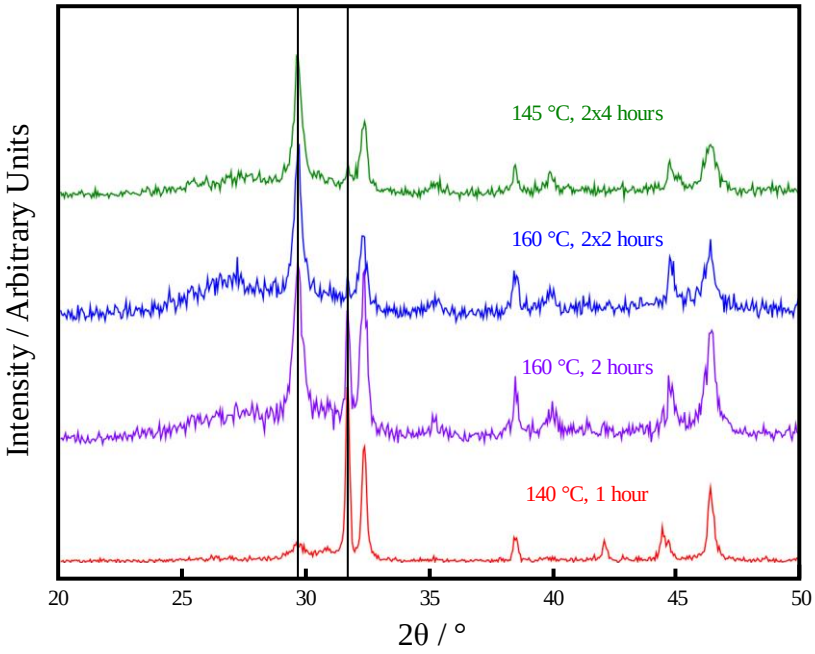

Figure 6.4: X-ray powder diffraction data from the products of reaction between $Sr_3(Ru_{0.5}Fe_{0.5})_2O_7$ and a mixture of 10% F_2 in N_2 collected using the Philips PW1710 diffractometer.

As shown in Figure 6.4, all reactions showed a decrease in the intensity of the 105 peak at 2θ ~ 31.5 ° and the appearance of a new peak at 2θ ~ 29.5 °, consistent with the intercalation of F_2 between the perovskite blocks as seen in the fluorination of $Sr_3Ru_2O_7$ to $Sr_3Ru_2O_7F_2$.[39] The broad lump at 2θ ~ 27.5 °, seen most prominently in the reactions performed at 160 °C, corresponds to the formation of SrF_2.

As the reaction clearly led to the formation of a new phase, but the use of F_2 gas resulted in poorly crystalline samples and the formation of SrF_2 under all reaction conditions attempted, the fluorination of $Sr_3(Ru_{0.5}Fe_{0.5})_2O_7$ was attempted using CuF_2.

6.3.3.2 CuF_2

X-ray powder diffraction data were collected from the products of reaction between $Sr_3(Ru_{0.5}Fe_{0.5})_2O_7$ and CuF_2 under a range of conditions, the results of which are summarised in Table 6.3.

Temp. / °C	Time / hours	Gas	Ratio CuF_2: $Sr_3(Ru_{0.5}Fe_{0.5})_2O_7$	Observations
220	12	Air	1:1	SrF_2 visible, some desired product
150	12	Air	1:1	Unreacted CuF_2 visible, some desired product
150	36	Air	1:1	SrF_2 visible, some desired product
250	1	O_2	1:1	~ 50% desired product, no SrF_2 visible
250	12	O_2	1:1	~ 50% desired product, no SrF_2 visible
250	12	O_2	2:1	No starting material or SrF_2 visible

Table 6.3: Results of reaction between $Sr_3(Ru_{0.5}Fe_{0.5})_2O_7$ and CuF_2 under a range of conditions.

As shown above, a flow of oxygen is essential to the formation of a single-phase product without decomposition. Reactions carried out under the same conditions but in static air resulted in a mixture of SrF_2, CuO and $Sr(Ru_{0.5}Fe_{0.5})O_3$, indicating that the oxidising agent is atmospheric O_2. Additionally, the presence of atmospheric water in air leads to the formation of HF:

$$CuF_2 + H_2O \rightarrow CuO + 2HF$$

The presence of HF subsequently leads to the formation of SrF_2 and the resulting decomposition of the starting material.

It was found that multiple heatings were required to ensure that all CuF_2 had reacted to form CuO, and would therefore not lead to additional uncertainty in subsequent measurements. Fluorination reactions performed with CuF_2 led to much more crystalline products than those performed with F_2 gas. No evidence for the formation of SrF_2 was detected in samples fluorinated under a flow of O_2.

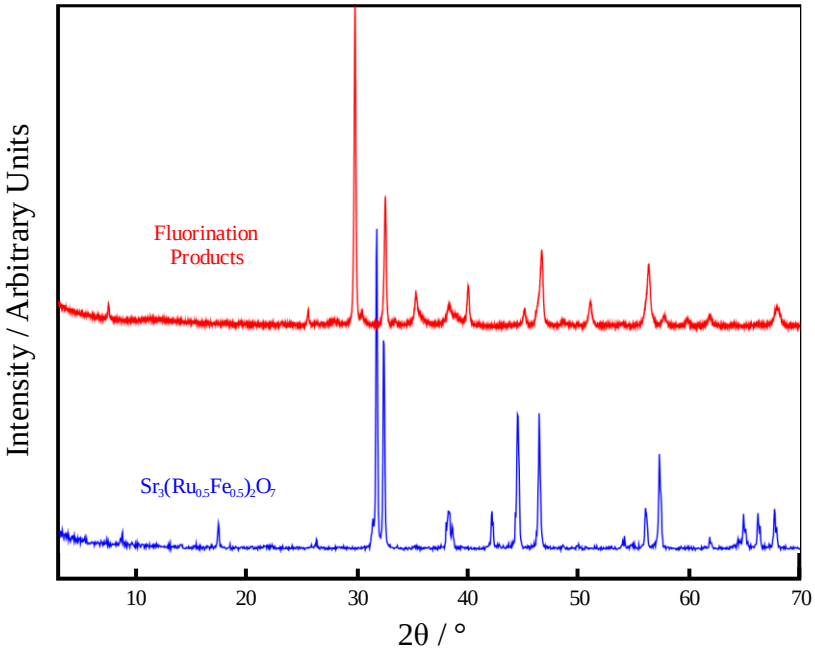

Figure 6.5: X-ray powder diffraction data collected from $Sr_3(Ru_{0.5}Fe_{0.5})_2O_7$ (bottom) and the products of fluorination with 2 mole equivalents of CuF_2 at 250 °C under a flow of oxygen for a total of 36 hours (top).

Attempts were made to carry out the reaction without mixing $Sr_3(Ru_{0.5}Fe_{0.5})_2O_7$ and CuF_2, either with both reagents placed in the same reaction vessel or a pellet of $Sr_3(Ru_{0.5}Fe_{0.5})_2O_7$ surrounded by CuF_2. These attempts resulted in negligible changes in the X-ray powder diffraction data, indicating that contact between $Sr_3(Ru_{0.5}Fe_{0.5})_2O_7$ and CuF_2 was necessary for the reaction to proceed.

X-ray powder diffraction data collected from the products of reaction between $Sr_3(Ru_{0.5}Fe_{0.5})_2O_7$ and 2 mole equivalents of CuF_2 under O_2 could be indexed on the basis of a body-centred tetragonal unit cell (space group *I*4/*mmm*) with lattice parameters a = 3.896(1) Å and c = 23.536(1) Å. These lattice parameters are very close to those of the topochemically fluorinated phase $Sr_3Ru_2O_7F_2$ (a = 3.830 Å and c = 24.26 Å)[39], and are thus consistent with the formation of a phase with composition $Sr_3(Ru_{0.5}Fe_{0.5})_2O_xF_y$.

6.3.4 Reactivity of $Sr_3(Ru_{0.5}M_{0.5})_2O_7$ (M = Mn, Ti)

X-ray powder diffraction data collected from the products of reaction between $Sr_3(Ru_{0.5}M_{0.5})_2O_7$ (M = Mn, Ti) and a double molar excess of CuF_2 at 250 °C under a flow of oxygen were consistent a similar lattice expansion to that observed in the fluorination of $Sr_3Ru_2O_7$ and $Sr_3(Ru_{0.5}Fe_{0.5})_2O_7$. These data could be indexed on the basis of a body-centred tetragonal unit cell (space group *I*4/*mmm*) with lattice parameters a = 3.818(1) Å and c = 23.891(1) Å (M = Mn) and a = 3.872(1) Å and c = 23.823(1) Å (M = Ti), and were therefore consistent with the formation of phases with composition $Sr_3(Ru_{0.5}M_{0.5})_2O_xF_y$ (M = Mn, Ti).

6.3.5 Structural Characterisation of $Sr_3(Ru_{0.5}Fe_{0.5})_2O_xF_y$

6.3.5.1 X-ray Powder Diffraction

X-ray powder diffraction data collected from the products of the reaction of $Sr_3(Ru_{0.5}Fe_{0.5})_2O_7$ with CuF_2 could be indexed on the basis of a body-centred tetragonal unit cell with lattice parameters a = 3.89(1) Å and c = 23.53(1) Å. These lattice parameters are very similar to those of the topochemically fluorinated phase $Sr_3Ru_2O_7F_2$ (a = 3.83 Å and c = 24.26 Å),[39] and therefore consistent with topochemical fluorination to form $Sr_3(Ru_{0.5}Fe_{0.5})_2O_xF_y$.

6.3.5.2 Neutron Powder Diffraction at 298 K

Neutron powder diffraction data were collected from the products of fluorination of $Sr_3(Ru_{0.5}Fe_{0.5})_2O_7$ at 298 K using the D2b diffractometer (Section 2.6.2.1).

A model in space group *I*4/*mmm* based on the structure of $Sr_3(Ru_{0.5}Fe_{0.5})_2O_7$, but with an additional anion site at (0, 1/2, 1/4), was initially refined against neutron powder diffraction data collected from $Sr_3(Ru_{0.5}Fe_{0.5})_2O_7$ (Figure 6.6). As the neutron scattering lengths of O and F are very similar (O = 5.803 fm; F = 5.645 fm),[43] no attempt was made to distinguish between them in refinements.

Close inspection of the fit to the data revealed additional features that could not be accounted for using this model. These could be accounted for using a $a' \sim \sqrt{2} \times a$, $b' \sim \sqrt{2} \times b$, and $c' = c$. An analogous expansion has previously been observed in the fluorinated phase $Sr_3Ru_2O_7F_2$.[39] A structural model based on the reported structure of $Sr_3Ru_2O_7F_2$ in space group *Pban* (No. 50) was therefore constructed and refined against the neutron powder diffraction data collected from $Sr_3(Ru_{0.5}Fe_{0.5})_2O_xF_y$ at 298K.

The cell expansion in $Sr_3Ru_2O_7F_2$ is attributed to disordered twisting of the RuO_6 octahedra, described using a pair of symmetry-related partially-occupied equatorial anion sites. On refinement of their occupancies, one of the sites refined to full occupancy and the other to zero indicating that, unlike in $Sr_3Ru_2O_7F_2$, the octahedra in $Sr_3(Ru_{0.5}Fe_{0.5})_2O_xF_y$ twist in an ordered manner. This enabled construction of a higher symmetry model in space group *Ccca* (No. 68) which gave a better statistical fit to the neutron powder diffraction data than the *Pban* model.

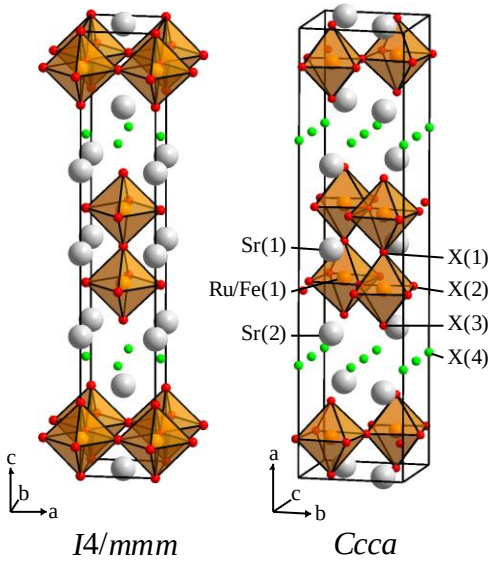

Figure 6.6: The initial model in space group *I4/mmm* (left) and final model in space group *Ccca* (right) refined against neutron powder diffraction data collected from the product of reaction between $Sr_3(Ru_{0.5}Fe_{0.5})_2O_7$ and CuF_2 at 298 K.

Considering the reaction conditions used to prepare $Sr_3(Ru_{0.5}Fe_{0.5})_2O_xF_y$, CuF_2 and CuO were added to the refinement as secondary phases. The phase fraction of CuF_2 rapidly refined to zero and was therefore removed from the refinement. The phase fraction of CuO rapidly refined to give a 2:1 molar ratio of CuO:$Sr_3(Ru_{0.5}Fe_{0.5})_2O_xF_y$, indicating that all CuF_2 had been converted to CuO. The refinement converged readily to give a good statistical fit. Refinement of the site occupancies of the anion sites gave no significant deviations from full occupancy.

Observed, calculated and difference plots are shown in Figure 6.7. Full structural details of the refined structure are given in Table 6.4 and selected bond lengths are given in Table 6.5.

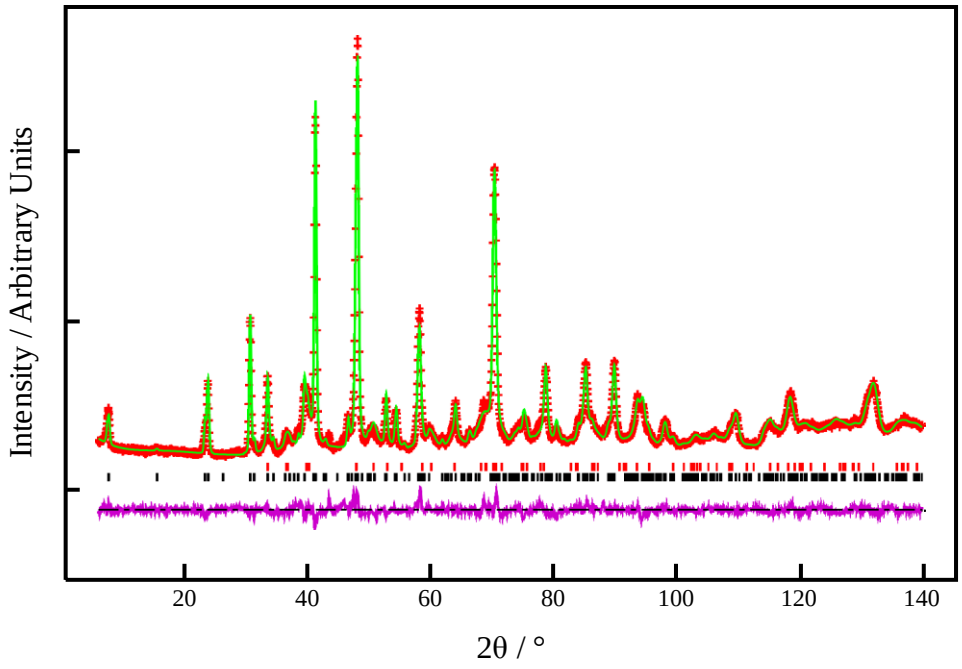

Figure 6.7: Observed, calculated, and difference plots for refinement of the structural model of $Sr_3(Ru_{0.5}Fe_{0.5})_2O_{5.5}F_{3.5}$ at 298 K against neutron powder diffraction data collected using the D2b instrument. The upper set of tick marks corresponds to the CuO secondary phase.

Atom	Wyckoff Position	*x*	*y*	*z*	Fractional Occupancy	U_{iso} / Å^2
Sr(1)	4*b*	0	1/4	3/4	1	0.009(1)
Sr(2)	8*e*	0.1864(1)	1/4	3/4	1	0.007(1)
Ru/Fe(1)	8*e*	0.0828(1)	3/4	3/4	0.5/0.5	0.007(1)
X(1)	4*a*	0	3/4	3/4	1	0.019(1)
X(2)	16*i*	0.0842(1)	0.5329(9)	0.4670(9)	1	0.016(1)
X(3)	8*e*	0.1645(2)	3/4	3/4	1	0.024(1)
X(4)	8*h*	1/4	0	0.0037(14)	1	0.014(1)
$Sr_3(Ru_{0.5}Mn_{0.5})_2O_7F_2$: space group *Ccca*; *a* = 23.522(1) Å, *b* = 5.509(1) Å, and *c* = 5.511(1) Å; cell volume = 714.13(1) Å^3; weight fraction = 77.8%						
CuO: space group *C*2/*c*; *a* = 4.676(1) Å, *b* = 3.430(1) Å, and *c* = 5.129(1) Å; β = 98.97(2) cell volume = 81.26(3) Å^3; weight fraction = 22.2%						
χ^2 = 7.220, wRp = 4.33%, Rp = 3.25%						

Table 6.4: Refined structural parameters for $Sr_3(Ru_{0.5}Fe_{0.5})_2O_{5.5}Fe_{3.5}$ at 298 K.

Cation	Anion	Bond Length / Å
Sr(1)	X(1)	2.756(1) x 2
	X(1)	2.755(1) x 2
	X(2)	2.924(4) x 4
	X(2)	2.605(5) x 4
Sr(2)	X(2)	2.939(4) x 2
	X(2)	3.262(4) x 2
	X(3)	2.802(1) x 2
	X(3)	2.803(1) x 2
	X(4)	2.456(6) x 2
	X(4)	2.457(5) x 2
Ru/Fe(1)	X(1)	1.948(2) x 1
	X(2)	1.965(5) x 2
	X(2)	1.966(6) x 2
	X(3)	1.922(5) x 1
Ru/Fe(1) – X(2) – Ru/Fe(1)		164.8(2) °
Ru/Fe(1) – X(1) – Ru/Fe(1)		179.9(2) °

Table 6.5: Selected bond lengths and bond angles from the refined structure of $Sr_3(Ru_{0.5}Fe_{0.5})_2O_{5.5}Fe_{3.5}$ at 298 K.

6.3.5.3 Thermogravimetric Analysis

Thermogravimetric analysis was performed by heating a small amount of the product of reaction between $Sr_3(Ru_{0.5}Fe_{0.5})_2O_7$ and CuF_2 under a flowing mixture of 25% H_2 in N_2 to form SrF_2, SrO, Fe, Ru, and Cu (confirmed via X-ray powder diffraction), resulting in a mass change of -13.69% corresponding to an initial composition of $Sr_3(Ru_{0.5}Fe_{0.5})_2O_{5.51(5)}F_{3.49(5)}$.

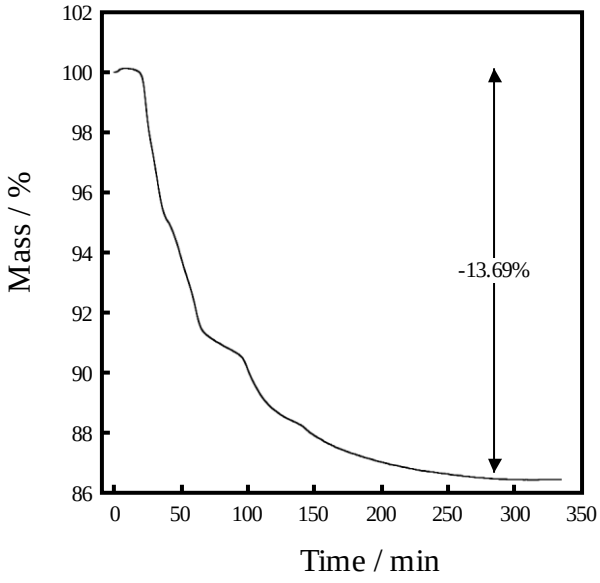

Figure 6.8: Thermogravimetric data collected during the reduction of $Sr_3(Ru_{0.5}Fe_{0.5})_2O_{5.5}F_{3.5}$ to SrF_2, SrO, Fe, Ru, and Cu.

6.3.5.4 ^{57}Fe Mössbauer Spectroscopy

^{57}Fe Mössbauer spectra were collected from $Sr_3(Ru_{0.5}Mn_{0.5})_2O_{5.5}F_{3.5}$ and are shown in Figure 6.9. These can be fitted to two lorentzian doublets as described in Table 6.6

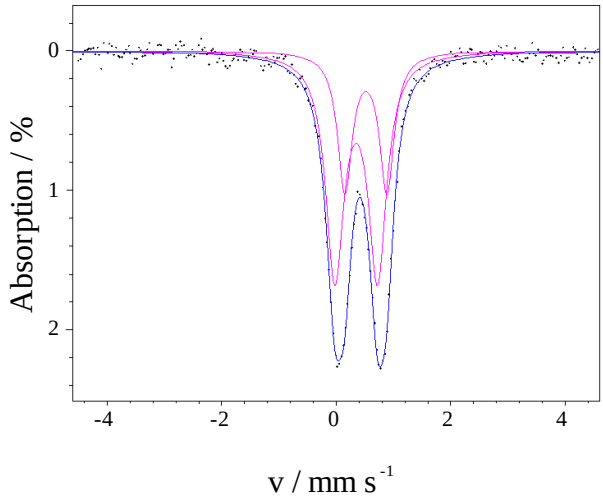

Figure 6.9: Fitted ^{57}Fe Mössbauer spectrum collected from $Sr_3(Ru_{0.5}Fe_{0.5})_2O_{5.5}F_{3.5}$ at 298 K.

	Site 1	Site 2
Centre Shift / mm s^{-1}	0.347	0.517
Quadrupole Splitting / mm s^{-1}	0.744	0.733
Linewidth / mm s^{-1}	0.192	0.154
Area Fraction / %	66.6%	33.4%

Table 6.6: Parameters extracted from fitting ^{57}Fe Mössbauer spectra. Centre shift and quadrupole splitting indicate both sites correspond to octahedral Fe^{3+}.

The centre shift and quadrupolar splitting parameters extracted from the fit to the data indicate that, within the sensitivity of the measurement, all the iron in the sample is in the +3 oxidation state and octahedrally coordinated. Additionally, the data indicate the presence of two sites in the sample with similar quadrupolar splitting values, indicating similar levels of site distortion from perfect cubic symmetry, occupied in a 2:1 ratio. These observations are consistent with 66.6% of the iron in $Sr_3(Ru_{0.5}Mn_{0.5})_2O_{5.5}F_{3.5}$ being located in $Fe^{3+}O_5F$ sites and 33.4% in $Fe^{3+}O_6$ sites.

6.3.6 Magnetic Characterisation of $Sr_3(Ru_{0.5}Fe_{0.5})_2O_{5.5}F_{3.5}$

6.3.6.1 Magnetisation Measurements

Zero-field and field cooled magnetisation data were collected from $Sr_3(Ru_{0.5}Fe_{0.5})_2O_{5.5}F_{3.5}$ as a function of temperature and are shown in Figure 6.10. These data can be fitted to the Curie-Weiss law in the range $140 \leq T$ / K ≤ 300 to yield values of C = 0.248(5) cm^3 K mol^{-1}, θ = 48.9(16) K and K = 0.0026(1) cm^3 where mol^{-1} means per mole of formula units of $Sr_3(Ru_{0.5}Fe_{0.5})_2O_{5.5}F_{3.5}$. Below T ~ 125 K, the zero-field cooled and field cooled data diverge, indicating a magnetic transition.

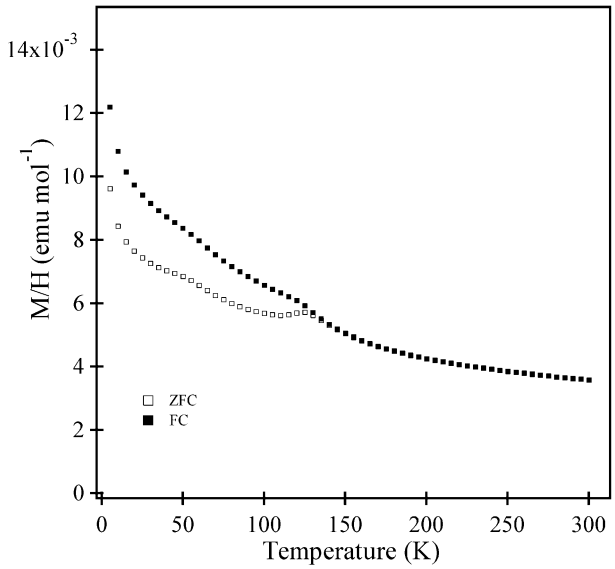

Figure 6.10: Zero-field and field cooled magnetisation data collected from $Sr_3(Ru_{0.5}Fe_{0.5})_2O_{5.5}F_{3.5}$ as a function of temperature.

Magnetisation-field isotherms (Figure 6.11) collected at 300 K are linear and pass through the origin. Analogous data collected at 5 K exhibit weak hysteresis and are displaced from the origin, indicating a glassy component to the magnetic behaviour.

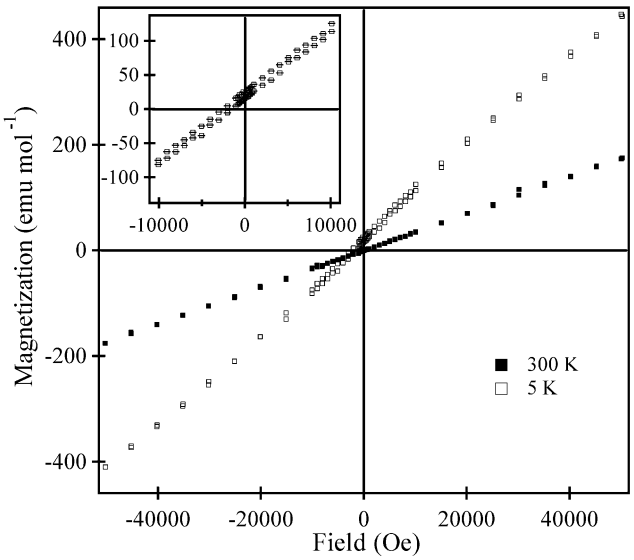

Figure 6.11: Magnetisation-field isotherms collected from $Sr_3(Ru_{0.5}Fe_{0.5})_2O_{5.5}F_{3.5}$ at 300 K and 5 K.

6.3.6.2 Neutron Powder Diffraction at 5 K

Neutron powder diffraction data collected from $Sr_3(Ru_{0.5}Fe_{0.5})_2O_{5.5}F_{3.5}$ at 5 K using the D2b diffractometer at the ILL exhibited additional diffraction features relative to analogous data collected at 298 K. These additional features could be indexed on the basis of a magnetic unit cell with the same dimensions as the crystallographic unit. The intensities of these reflections could best be accounted for using a G-type antiferromagnetically ordered model, with spins aligned parallel to the crystallographic *a*-axis (Figure 6.12).

The refinement converged readily to yield an ordered moment of 1.12(3) μ_B per transition metal centre. Observed, calculated and difference plots are shown in Figure 6.13. Full details of the magnetic structure are given in Appendix 8.3Appendix 6.

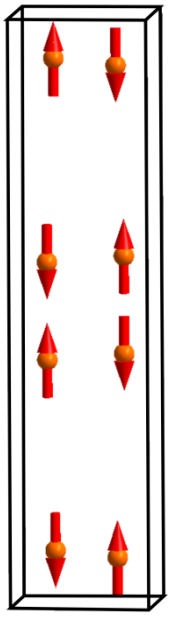

Figure 6.12: The refined magnetic structure of $Sr_3(Ru_{0.5}Fe_{0.5})_2O_{5.5}F_{3.5}$.

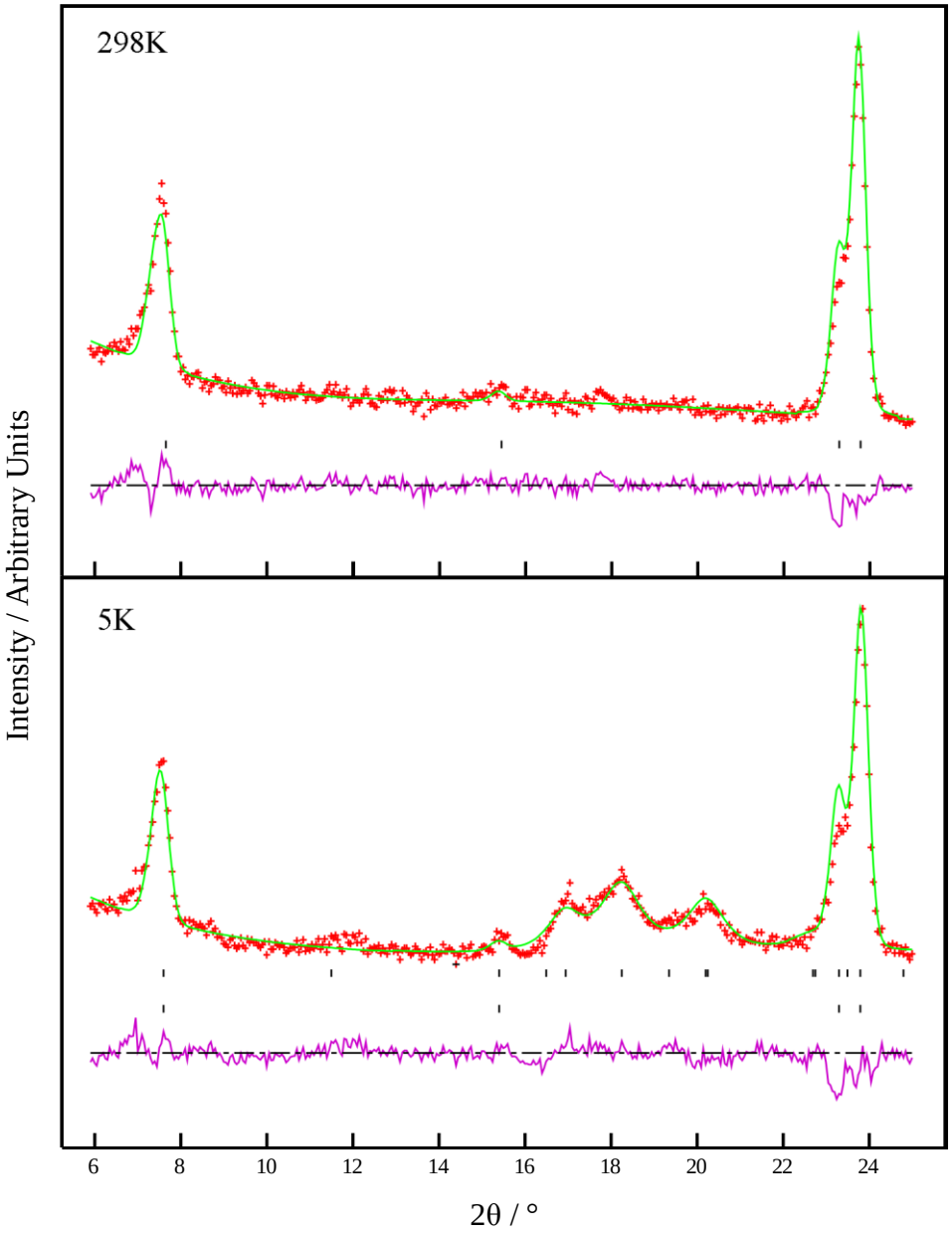

Figure 6.13: Observed, calculated, and difference plots for refinement of the structural and magnetic models of $Sr(Ru_{0.5}Fe_{0.5})_2O_{5.5}F_2$ at 298 K (top) and 5 K (bottom) against neutron powder diffraction data collected using the D2b instrument. The upper set of tick marks corresponds to the magnetic model.

6.3.7 Structural Characterisation of $Sr_3(Ru_{0.5}Mn_{0.5})_2O_xF_y$

6.3.7.1 X-ray Powder Diffraction

X-ray powder diffraction data collected from the products of the reaction of $Sr_3(Ru_{0.5}Mn_{0.5})_2O_7$ with CuF_2 could be indexed on the basis of a body-centred tetragonal unit cell with lattice parameters a = 3.81(1) Å and c = 23.89(1) Å. These lattice parameters are

very similar to those of the topochemically fluorinated phase $Sr_3Ru_2O_7F_2$ (a = 3.83 Å and c = 24.26 Å),[39] and therefore consistent with topochemical fluorination to form $Sr_3(Ru_{0.5}Mn_{0.5})_2O_xF_y$.

6.3.7.2 Neutron Powder Diffraction at 298 K

Neutron powder diffraction data collected from $Sr_3(Ru_{0.5}Mn_{0.5})_2O_xF_y$ at 298 K displayed analogous diffraction features to those collected from $Sr_3(Ru_{0.5}Fe_{0.5})_2O_xF_y$ which precluded the use of a model in space group *I*4/*mmm*.

An analogous model in space group *Ccca* was constructed and refined against the data. Again, CuF_2 and CuO were added as secondary phases, with the fraction of CuF_2 rapidly refining to zero and that of CuO rapidly refining to give a 2:1 molar ratio of $CuO:Sr_3(Ru_{0.5}Mn_{0.5})_2O_xF_y$. The refinement converged readily to give a good statistical fit. Refinement of the site occupancies of the anion sites gave no significant deviations from full occupancy.

Observed, calculated and difference plots are shown in Figure 6.14. Full structural details of the refined structure are given in Table 6.7 and selected bond lengths are given in Table 6.8.

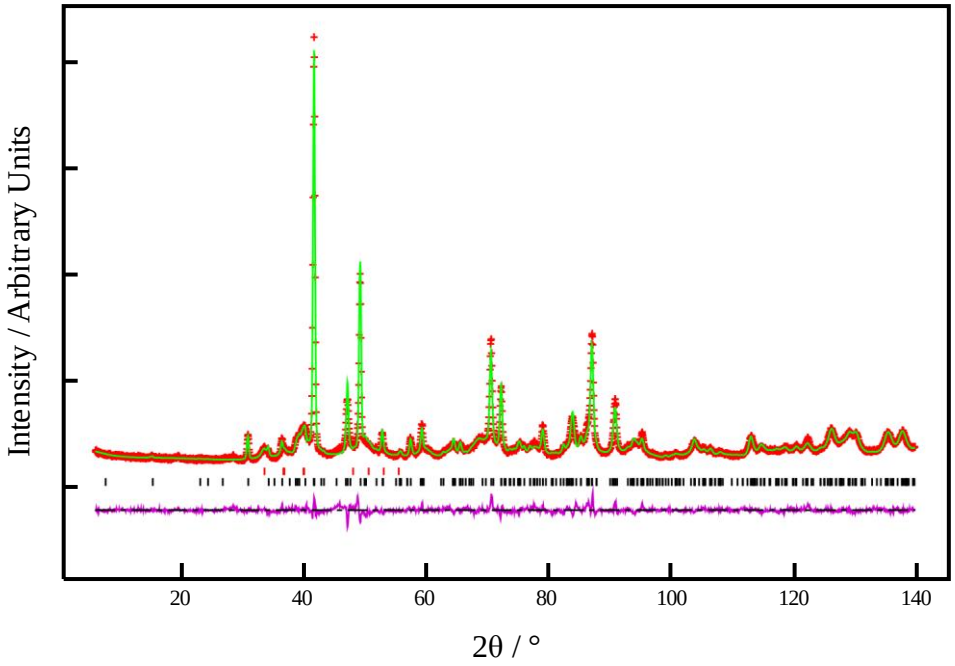

Figure 6.14: Observed, calculated, and difference plots for refinement of the structural model of $Sr_3(Ru_{0.5}Mn_{0.5})_2O_7F_2$ at 298 K against neutron powder diffraction data collected using the D2b instrument. The upper set of tick marks corresponds to the CuO secondary phase.

Atom	Wyckoff Position	*x*	*y*	*z*	Fractional Occupancy	U_{iso} / Å^2
Sr(1)	4*b*	0	1/4	3/4	1	0.012(1)
Sr(2)	8*e*	0.1856(1)	1/4	3/4	1	0.003(1)
Ru/Mn(1)	8*e*	0.0874(4)	3/4	3/4	0.5/0.5	0.007(1)
X(1)	4*a*	0	3/4	3/4	1	0.012(1)
X(2)	16*i*	0.0835(2)	0.5341(8)	0.4655(9)	1	0.014(1)
X(3)	8*e*	0.1644(2)	3/4	3/4	1	0.007(1)
X(4)	8*h*	1/4	0	0.0037(14)	1	0.014(1)
$Sr_3(Ru_{0.5}Mn_{0.5})_2O_7F_2$: space group *Ccca*; *a* = 23.867(1) Å, *b* = 5.4007(9) Å, and *c* = 5.4028(9) Å; cell volume = 696.41(1) Å^3; weight fraction = 77.6%						
CuO: space group *C*2/*c*; *a* = 4.676(1) Å, *b* = 3.430(1) Å, and *c* = 5.129(1) Å; β = 98.97(2) cell volume = 81.26(3) Å^3; weight fraction = 22.4%						
χ^2 = 7.260, wRp = 4.33%, Rp = 3.25%						

Table 6.7: Refined structural parameters for $Sr_3(Ru_{0.5}Mn_{0.5})_2O_7F_2$ at 298 K.

Cation	Anion	Bond Length / Å
Sr(1)	X(1)	2.700(1) x 2
	X(1)	2.700(1) x 2
	X(2)	2.948(5) x 4
	X(2)	2.586(5) x 4
Sr(2)	X(2)	2.942(5) x 2
	X(2)	3.264(5) x 2
	X(3)	2.747(1) x 2
	X(3)	2.748(1) x 2
	X(4)	2.460(3) x 2
	X(4)	2.443(3) x 2
Ru/Mn(1)	X(1)	2.086(10) x 1
	X(2)	1.928(5) x 2
	X(2)	1.932(5) x 2
	X(3)	1.938(11) x 1
Ru/Mn(1) – X(2) – Ru/Mn(1)		161.5(2) °
Ru/Mn(1) – X(1) – Ru/Mn(1)		180.0(2) °

Table 6.8: Selected bond lengths and bond angles from the refined structure of $Sr_3(Ru_{0.5}Mn_{0.5})_2O_7F_2$ at 298 K.

6.3.7.3 Thermogravimetric Analysis

Thermogravimetric analysis was performed by heating a small amount of the product of reaction between $Sr_3(Ru_{0.5}Mn_{0.5})_2O_7$ and CuF_2 under a flowing mixture of 25% H_2 in N_2 to form SrF_2, SrO, MnO, Ru, and Cu (confirmed via X-ray powder diffraction). A mass change of -13.25% corresponds to an initial composition of $Sr_3(Ru_{0.5}Mn_{0.5})_2O_{7.03(5)}F_{1.97(5)}$.

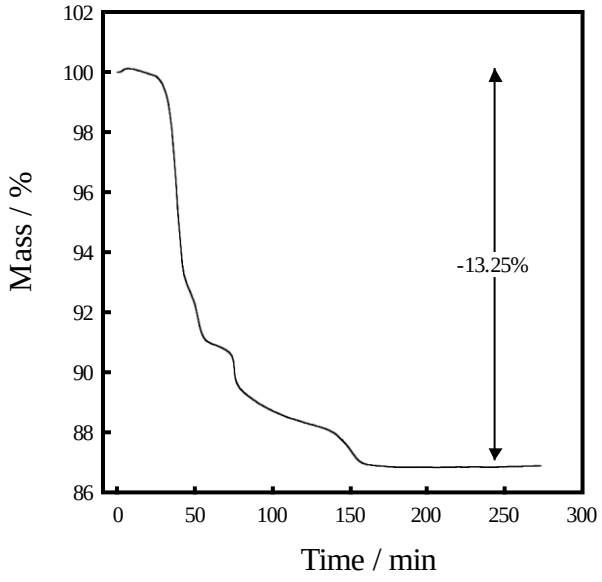

Figure 6.15: Thermogravimetric data collected during the reduction of $Sr_3(Ru_{0.5}Mn_{0.5})_2O_{5.5}F_{3.5}$ to SrF_2, SrO, MnO, Ru, and Cu.

6.3.8 Magnetic Characterisation of $Sr_3(Ru_{0.5}Mn_{0.5})_2O_7F_2$

6.3.8.1 Magnetisation Measurements

Zero-field and field cooled data as a function of temperature were collected from $Sr_3(Ru_{0.5}Mn_{0.5})_2O_7F_2$ and are shown in Figure 6.16. These data exhibit a local maximum at T ~ 190 K accompanied by a divergence between zero-field and field cooled data. The data could not be fitted to the Curie-Weiss law over any significant temperature range.

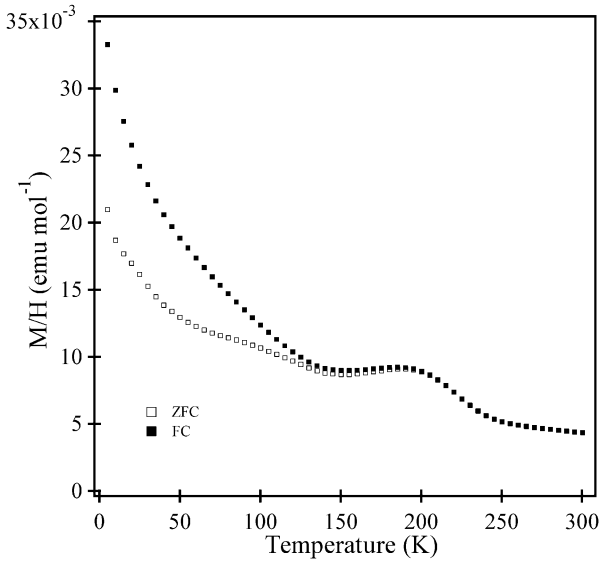

Figure 6.16: Zero-field and field cooled magnetisation data collected from $Sr_3(Ru_{0.5}Mn_{0.5})_2O_7F_2$ as a function of temperature.

Magnetisation-field data (shown in Appendix 8.3Appendix 6) were collected at 300 K and 5 K. Data collected at 300 K are linear and pass through the origin. Analogous data collected at 5 K exhibit weak hysteresis and are displaced from the origin, indicating a glassy component to the magnetic behaviour.

6.3.8.2 Neutron Powder Diffraction at 5 K

Neutron powder diffraction data collected from $Sr_3(Ru_{0.5}Mn_{0.5})_2O_7F_2$ at 5 K using the D2b diffractometer at the ILL exhibited additional diffraction features relative to analogous data

collected at 298 K. These additional features could be indexed on the basis of a magnetic unit cell with the same dimensions as the crystallographic unit, but their weak intensities did not allow for discrimination between possible magnetic models. Not attempt to determine the low-temperature magnetic structure of $Sr_3(Ru_{0.5}Mn_{0.5})_2O_7F_2$ was made.

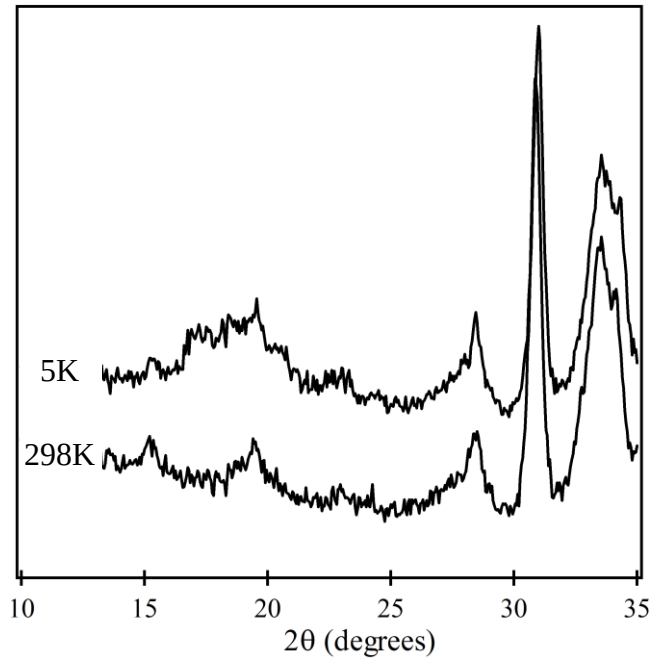

Figure 6.17: Neutron powder diffraction data collected from $Sr_3(Ru_{0.5}Mn_{0.5})_2O_7F_2$ at 298 K (bottom) and 5 K (top).

6.3.9 Structural Characterisation of $Sr_3(Ru_{0.5}Ti_{0.5})_2O_xF_y$

6.3.9.1 X-ray Powder Diffraction

X-ray powder diffraction data collected from the products of the reaction of $Sr_3(Ru_{0.5}Ti_{0.5})_2O_7$ with CuF_2 could be indexed on the basis of a body-centred tetragonal unit cell with lattice parameters a = 3.8740(1) Å and c = 23.827(1) Å. These lattice parameters are very similar to those of the topochemically fluorinated phase $Sr_3Ru_2O_7F_2$ (a = 3.83 Å and c = 24.26 Å),[39] and therefore consistent with topochemical fluorination to form $Sr_3(Ru_{0.5}Ti_{0.5})_2O_xF_y$. As oxide and fluoride are isoelectronic, and therefore indistinguishable via X-ray powder diffraction, no attempt was made to distinguish between them in the refinement.

A structural model in space group *I*4/*mmm*, based on the structure of $Sr_3(Ru_{0.5}Ti_{0.5})_2O_7$ but with an additional anion site at (1/2,0,1/4), was constructed and refined against data collected using the X'Pert diffractometer. Once again, CuO and CuF_2 were added as secondary phases. The phase fraction of CuF_2 rapidly refined to zero and that of CuO rapidly refining to give a 2:1 molar ratio of CuO:$Sr_3(Ru_{0.5}Ti_{0.5})_2O_xF_y$. The refinement converged rapidly to give a good statistical fit. An orthorhombic model in space group *Ccca*, analogous to that used to describe $Sr_3(Ru_{0.5}Mn_{0.5})_2O_xF_y$, was observed to give a worse statistical fit to the data that the *I*4/*mmm* model (*Ccca* $\chi^2 = 2.98$; *I*4/*mmm* $\chi^2 = 2.62$), and so the tetragonal model was retained.

Observed, calculated and difference plots are shown in Figure 6.18. Full structural details of the refined structure are given in Table 6.9 and selected bond lengths are given in Table 6.10.

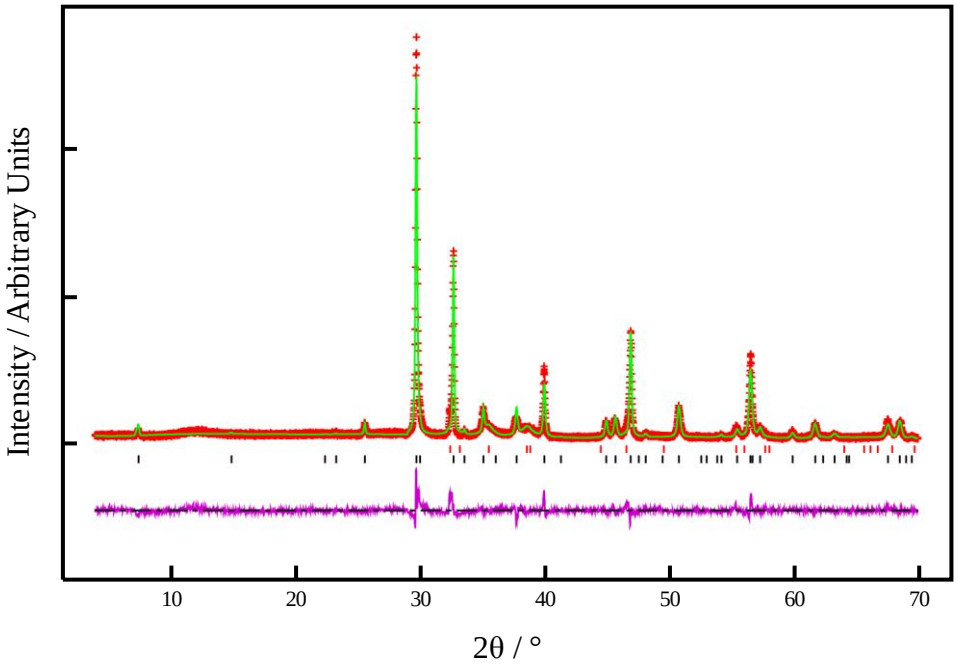

Figure 6.18: Observed, calculated, and difference plots for refinement of the structural model of $Sr_3(Ru_{0.5}Ti_{0.5})_2O_7F_2$ at 298 K against X-ray powder diffraction data collected using the X'Pert instrument. The upper set of tick marks corresponds to the CuO secondary phase.

Atom	Wyckoff Position	*x*	*y*	*z*	Fractional Occupancy	U_{iso} / Å^2
Sr(1)	2*b*	0	0	1/2	1	0.049(1)
Sr(2)	4*e*	0	0	0.3149(1)	1	0.037(1)
Ru/Ti(1)	4*e*	0	0	0.0871(1)	0.5/0.5	0.024(1)
X(1)	2*a*	0	0	0	1	0.035(1)
X(2)	8*g*	0	1/2	0.0830(4)	1	0.035(1)
X(3)	4*e*	0	0	0.1659(5)	1	0.035(1)
X(4)	4*d*	0	1/2	1/4	1	0.035(1)
$Sr_3(Ru_{0.5}Ti_{0.5})_2O_7F_2$: space group *I*4/*mmm*; *a* = 3.8740(1) Å, and *c* = 23.827(1) Å; cell volume = 357.59(1) Å^3; weight fraction = 82.1%						
CuO: space group *C*2/*c*; *a* = 4.673(1) Å, *b* = 3.432(1) Å, and *c* = 5.131(1) Å; β = 98.98(2) cell volume = 81.26(3) Å^3; weight fraction = 17.9%						
χ^2 = 3.542, wRp = 4.36%, Rp = 3.31%						

Table 6.9: Refined structural parameters for $Sr_3(Ru_{0.5}Ti_{0.5})_2O_7Fe_2$ at 298 K.

Cation	Anion	Bond Length / Å
Sr(1)	X(1)	2.739(1) x 4
	X(2)	2.768(7) x 8
Sr(2)	X(2)	3.110(8) x 4
	X(3)	2.777(2) x 4
	X(4)	2.479(1) x 4
Ru/Ti	X(1)	2.075(2) x 1
	X(2)	1.939(1) x 4
	X(3)	1.878(12) x 1
Ru/Ti(1) – X(2) – Ru/Ti(1)		180 °
Ru/Ti(1) – X(1) – Ru/Ti(1)		180 °

Table 6.10: Selected bond lengths and bond angles from the refined structure of $Sr_3(Ru_{0.5}Ti_{0.5})_2O_7Fe_2$ at 298 K.

6.3.9.2 Thermogravimetric Analysis

Thermogravimetric analysis was performed by heating a small amount of the product of reaction between $Sr_3(Ru_{0.5}Ti_{0.5})_2O_7$ and CuF_2 under a flowing mixture of 25% H_2 in N_2 to form SrF_2, SrO, TiO_2, Ru, and Cu (confirmed via X-ray powder diffraction). A mass change of -10.96% corresponds to an initial composition of $Sr_3(Ru_{0.5}Ti_{0.5})_2O_{6.92(5)}F_{2.08(5)}$.

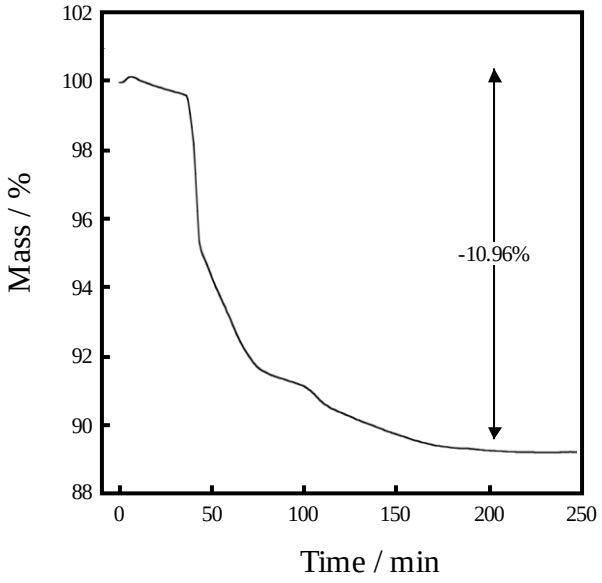

Figure 6.19 Thermogravimetric data collected during the reduction of $Sr_3(Ru_{0.5}Ti_{0.5})_2O_{5.5}F_{3.5}$ to SrF_2, SrO, TiO_2, Ru, and Cu.

6.3.10 Magnetic Characterisation of $Sr_3(Ru_{0.5}Ti_{0.5})_2O_7F_2$

6.3.10.1 Magnetisation Measurements

Zero-field and field cooled magnetisation data collected from $Sr_3(Ru_{0.5}Ti_{0.5})_2O_7$ as a function of temperature in a field of 100 Oe are shown in Figure 6.20. These data also exhibit a weak divergence between the zero-field cooled and field cooled data below 80 K, ascribed to a very small amount of unfluorinated $Sr_3(Ru_{0.5}Ti_{0.5})_2O_7$ present in the sample. Despite the presence of this impurity and CuO in the sample, the data could be fitted to the Curie-Weiss law in the temperature range $10 \leq T / K \leq 300$ yields values of $C = 0.232(2)$ cm^3 K mol^{-1}, $\theta = -12.1(2)$ K and $K = 0.00232(1)$ cm^3 where mol^{-1} means per mole of formula units of $Sr_3(Ru_{0.5}Ti_{0.5})_2O_7F_2$. Given the presence of two mole equivalents of CuO in the sample, these should be taken as maximal values.

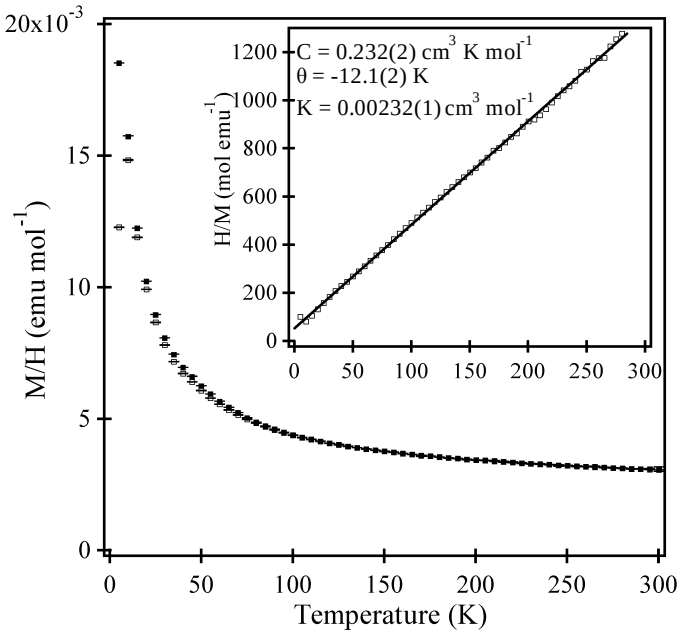

Figure 6.20: Zero-field cooled and field cooled magnetisation data collected from $Sr_3(Ru_{0.5}Ti_{0.5})_2O_7F_2$.

6.4 Discussion

6.4.1 Structure and Magnetism of $Sr_3(Ru_{0.5}Ti_{0.5})_2O_7$

Traditional high-temperature synthetic methods have enabled the preparation of the as-yet unreported phase $Sr_3(Ru_{0.5}Ti_{0.5})_2O_7$, adopting an n = 2 Ruddlesden-Popper structure with a disordered arrangement of Ru^{4+} and Ti^{4+} on the B-site.

$Sr_3(Ru_{0.5}Ti_{0.5})_2O_7$ exhibits Curie-Weiss behaviour above $T \sim 80$ K, below which temperature there is a transition to what is assumed to be an antiferromagntically ordered state. The observed Curie constant is much greater than would be expected for low-spin S = 1 ruthenium and S = 0 titanium ($C_{expected}$ = 1 cm^3 K mol^{-1}, $C_{observed}$ = 1.622(5) cm^3 K mol^{-1}). A similar anomalously large Curie constant has been observed in related Ru^{4+} double perovskites La_2MgRuO_6 and La_2ZnRuO_6.[100]

A detailed analysis of the low-temperature magnetic structure of $Sr_3(Ru_{0.5}Ti_{0.5})_2O_7$ was not performed.

6.4.2 Fluorination Behaviour of $Sr_3(Ru_{0.5}M_{0.5})_2O_7$ (M = Fe, Mn, Ti)

Low temperature reaction between $Sr_3(Ru_{0.5}M_{0.5})_2O_7$ (M = Fe, Mn, Ti) and CuF_2 leads to the formation of the novel phases $Sr_3(Ru_{0.5}M_{0.5})_2O_xF_y$. In the case of M = Mn and Ti, the process is simple oxidative insertion of fluorine between the rocksalt layers, resulting in $Sr_3(Ru_{0.5}Mn_{0.5})_2O_7F_2$ and $Sr_3(Ru_{0.5}Ti_{0.5})_2O_7F_2$ and an accompanying rise in average transition metal oxidation state from +4 to +5. In contrast, the fluorination of $Sr_3(Ru_{0.5}Fe_{0.5})_2O_7$ proceeded via a mixture of insertion and substitution, resulting in a phase with composition $Sr_3(Ru_{0.5}Fe_{0.5})_2O_{5.5}F_{3.5}$ which possesses an average transition metal oxidation state of +4.25.

6.4.3 Distribution of Oxide and Fluoride Ions

The crystal structures of the $Sr_3(Ru_{0.5}M_{0.5})_2O_xF_y$ series of phases contain an additional anion site in the SrX rocksalt layers compared to the $Sr_3(Ru_{0.5}M_{0.5})_2O_7$ starting materials, allowing for the increase in anion stoichiometry. As a result, the oxyfluoride phases contain four crystallographically distinct sites (Figure 6.21).

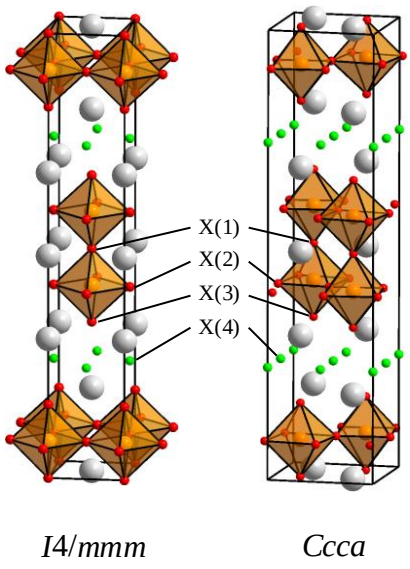

Figure 6.21: The anion sites present in the crystal structures of the $Sr_3(Ru_{0.5}M_{0.5})_2O_xF_y$ (M = Fe, Mn, Ti) series of phases.

As noted above, the X-ray and neutron scattering lengths of O^{2-} and F^- are so similar as to be indistinguishable by either diffraction technique.[43] This prevents direct determination of the distribution of oxide and fluoride anions in oxyfluorides via diffraction techniques.

However, it is possible to estimate the distribution of oxide and fluoride anions by detailed examination of the local bonding at anion sites through the use of bond valence sums (BVS).[53,101]

The bond valence sums calculated for the anion sites in all three oxyfluorides and their respective $Sr_3(Ru_{0.5}M_{0.5})_2O_7$ starting materials are given in Table 6.11. The values obtained from the oxyfluoride phases were calculated as if they were occupied by both oxide or fluoride anions.

$Sr_3(Ru_{0.5}Fe_{0.5})_2O_7$		**$Sr_3(Ru_{0.5}Fe_{0.5})_2O_{5.5}F_{3.5}$**		
Anion	**BVS (O)**	**Anion**	**BVS (O)**	**BVS (F)**
O(1)	1.911	X(1)	**2.184**	1.687
O(2)	2.225	X(2)	**1.924**	1.487
O(3)	1.751	X(3)	1.417	**1.092**
		X(4)	1.602	**1.226**
$Sr_3(Ru_{0.5}Mn_{0.5})_2O_7$		**$Sr_3(Ru_{0.5}Mn_{0.5})_2O_7F_2$**		
Anion	**BVS (O)**	**Anion**	**BVS (O)**	**BVS (F)**
O(1)	2.205	X(1)	**1.841**	1.419
O(2)	2.320	X(2)	**2.040**	1.578
O(3)	1.785	X(3)	**1.719**	1.320
		X(4)	1.647	**1.260**
$Sr_3(Ru_{0.5}Ti_{0.5})_2O_7$		**$Sr_3(Ru_{0.5}Ti_{0.5})_2O_7F_2$**		
Anion	**BVS (O)**	**Anion**	**BVS (O)**	**BVS (F)**
O(1)	1.855	X(1)	**1.789**	1.380
O(2)	1.996	X(2)	**2.196**	1.969
O(3)	1.764	X(3)	**1.538**	1.220
		X(4)	1.507	**1.153**

Table 6.11: Bond valence sums calculated for the anion sites of $Sr_3(Ru_{0.5}M_{0.5})_2O_7$ and $Sr_3(Ru_{0.5}M_{0.5})_2O_xF_y$ (M = Fe, Mn, Ti), with values for the latter calculated for occupation by both oxide and fluoride anions. All values calculated using the Ru^{4+} parameter for contributions from mixed Ru/M sites.

Examination of the values obtained from $Sr_3(Ru_{0.5}Mn_{0.5})_2O_7F_2$ reveal that the interstitial anion site (X(4)) possesses the lowest bond valence sum of all the sites in

$Sr_3(Ru_{0.5}Mn_{0.5})_2O_7F_2$, consistent with the occupation of this site by fluoride. Furthermore, the Sr(2)–X(4) bond length (2.45 Å) is very similar to the Sr–F bond length observed in SrF_2 (2.511 Å)[102] and those observed in $Sr_3Ru_2O_7F_2$ (2.32 – 2.56 Å),[39] providing additional evidence for the occupation of this site by fluoride anions. It is therefore possible to conclude that the fluorination of $Sr_3(Ru_{0.5}Mn_{0.5})_2O_7$ proceeds via the simple topochemical insertion of F into the interstitial anion sites of the host phase in a manner directly analogous to the fluorination of $Sr_3Ru_2O_7$ to $Sr_3Ru_2O_7F_2$.[39]

A similar situation is observed in the bond valence sums calculated for the anion sites in $Sr_3(Ru_{0.5}Ti_{0.5})_2O_7F_2$. The Sr(2)–X(4) bond length (2.48 Å) is once again very close to that observed in SrF_2 and $Sr_3Ru_2O_7F_2$. In this case, however, the poor X-ray scattering power of the light oxide ions in the presence of the heavier metal cations reduces the accuracy with which anion site positions (especially X(3)) can be known, and therefore introduce a degree of ambiguity in the result.

Bond valence sums calculated from $Sr_3(Ru_{0.5}Fe_{0.5})_2O_{5.5}F_{3.5}$ reveal a different picture. In common with $Sr_3(Ru_{0.5}Mn_{0.5})_2O_7F_2$ and $Sr_3(Ru_{0.5}Ti_{0.5})_2O_7F_2$, the X(4) anion site is a good match for occupation by fluoride. The Sr(2)–X(4) bond length (2.45 Å) is very close to that observed in $Sr_3(Ru_{0.5}Mn_{0.5})_2O_7F_2$ and $Sr_3(Ru_{0.5}Ti_{0.5})_2O_7F_2$ and once again very close to that observed in SrF_2 and $Sr_3Ru_2O_7F_2$. However, it can be seen in Table 6.11 that the X(3) anion site has declined significantly on fluorination, from +1.751 in $Sr_3(Ru_{0.5}Fe_{0.5})_2O_7$ to +1.417 in $Sr_3(Ru_{0.5}Fe_{0.5})_2O_{5.5}F_{3.5}$ (values calculated using the BVS parameter for oxide ions).[53] This suggests that this site is occupied by a significant concentration of fluoride ions.

Considering the chemical composition of $Sr_3(Ru_{0.5}Fe_{0.5})_2O_{5.5}F_{3.5}$, it is consistent with the observed data for the X(1) and X(2) sites to be fully occupied by oxide ions, the X(4) site by fluoride ions, and the X(3) site by a 3:1 disordered arrangement of fluoride and oxide.

A similar tendency to locate fluoride on the external anion sites of $n = 2$ Ruddlesden-Popper phases has previously been observed by Weller *et al.* during the fluorination of $Sr_3Fe_2O_6$ to $Sr_3Fe_2O_6F_{0.8}$ (Figure 6.22), where fluorination induces a rearrangement in the oxide anion lattice rather than simple insertion of fluoride into the vacant position.[101]

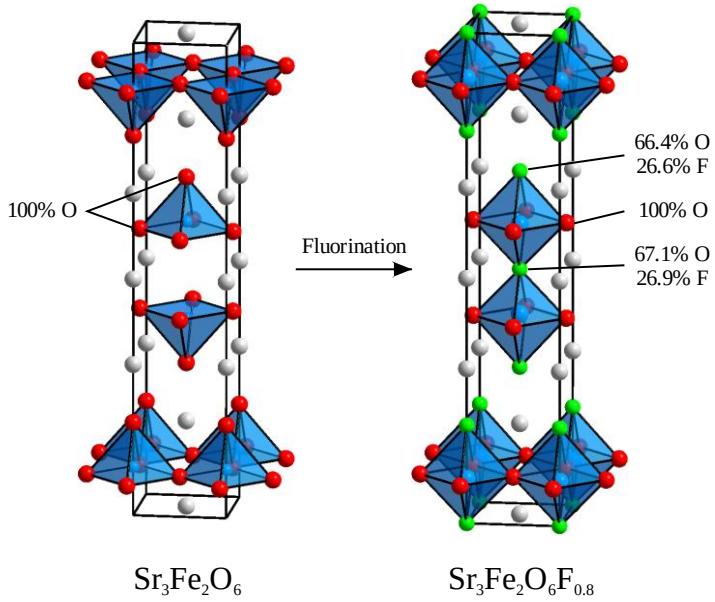

Figure 6.22: The structures of $Sr_3Fe_2O_6$ and its product of fluorination.[101]

This distribution of oxide and fluoride ions is also consistent with the ^{57}Fe Mössbauer data collected from $Sr_3(Ru_{0.5}Fe_{0.5})_2O_{5.5}F_{3.5}$. The two octahedral iron sites indicated by this data were assigned to FeO_5F and FeO_6 in which the fluoride ion is located in the X(3) site. The observed 2:1 ratio of FeO_5F:FeO_6 is slightly less than the expected 3:1 ratio from a statistical distribution of 75% F and 25% O. This suggests that, of all the available X(3) sites, subsititution preferentially occurs at X(3) sites coordinated to ruthenium, resulting in a 5:1 ratio of RuO_5F:RuO_6 (Figure 6.23).

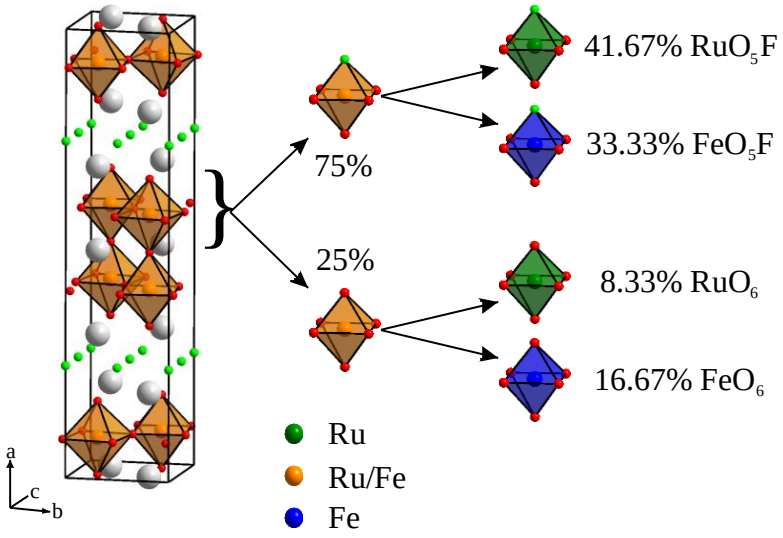

Figure 6.23: Final structure and local coordination environments in $Sr_3(Ru_{0.5}Fe_{0.5})_2O_{5.5}F_{3.5}$.

6.4.4 Transition Metal Oxidation States

6.4.4.1 $Sr_3(Ru_{0.5}Ti_{0.5})_2O_7F_2$

Oxidative insertion of fluorine into $Sr_3(Ru_{0.5}Ti_{0.5})_2O_7$ raises the average transition metal oxidation state from +4 to +5. Fluorination of the related phase Sr_2TiO_4 using 1 mole equivalent of CuF_2 at 250 °C results in a phase with composition $Sr_2TiO_3F_2$, where an oxide ion is substituted for two fluoride ions in a redox neutral proxess rather than oxidative intercalation (Figure 6.24).[103] Ti remains in the +4 oxidation state. Given the extreme thermodynamic unfavourability of oxidizing Ti^{4+}, a composition of $Sr_3(Ru_{0.5}Ti_{0.5})_2O_7$ implies an oxidation state combination of Ru^{6+} and Ti^{4+}. It can therefore be seen that ruthenium can be oxidised to Ru^{6+} under these 'soft' fluorination conditions.

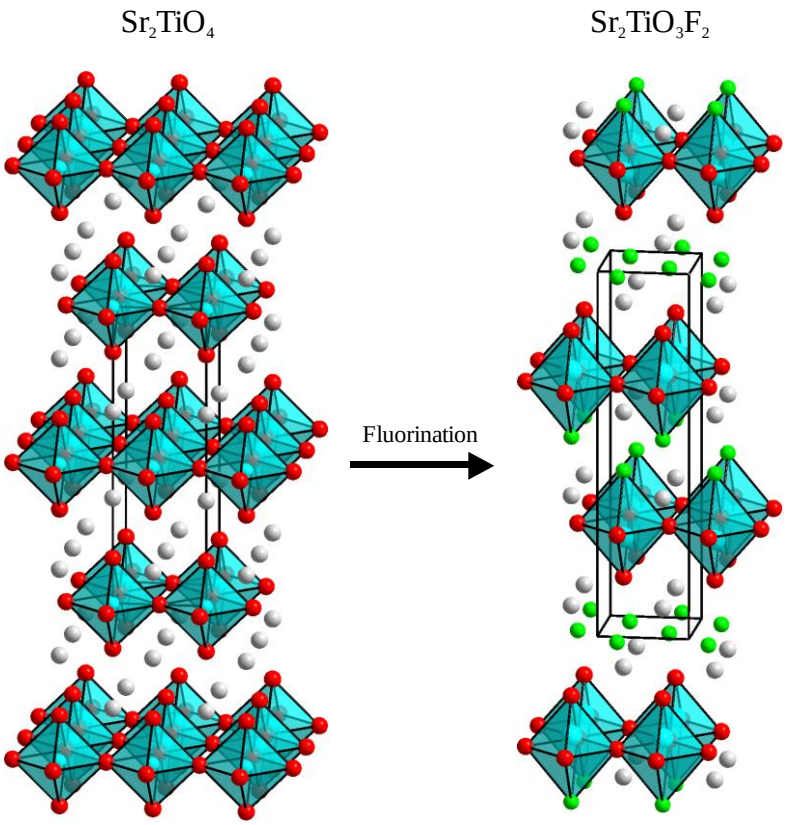

Figure 6.24: The fluorination of Sr_2TiO_4 to form $Sr_2TiO_3F_2$.

As described above, the oxidising 'power' of topochemical fluorination reactions using CuF_2 is provided by the oxygen atmosphere. CuF_2 acts as a source of fluorine, not an oxidant. This is exemplified by the difference in the products of the reaction between $Sr_3(Ru_{0.5}Fe_{0.5})_2O_7$ and CuF_2: reactions performed under flowing oxygen produced $Sr_3(Ru_{0.5}Fe_{0.5})_2O_{5.5}F_{3.5}$, while reactions performed under static air produced a mixture of SrF_2 and $Sr(Ru_{0.5}Fe_{0.5})O_3$, a redox-neutral process.

The formation of a phase containing Ru^{6+} under these conditions is therefore somewhat surprising, given that the stabilisation of high oxidation states of ruthenium typically requires the use of high pressures of oxygen. For example, the synthesis of $Sr_2Ru_3O_{10}$ requires ~ 0.2 GPa, while that of $Tl_2Ru_2O_7$ requires 1 GPa.[104,105]

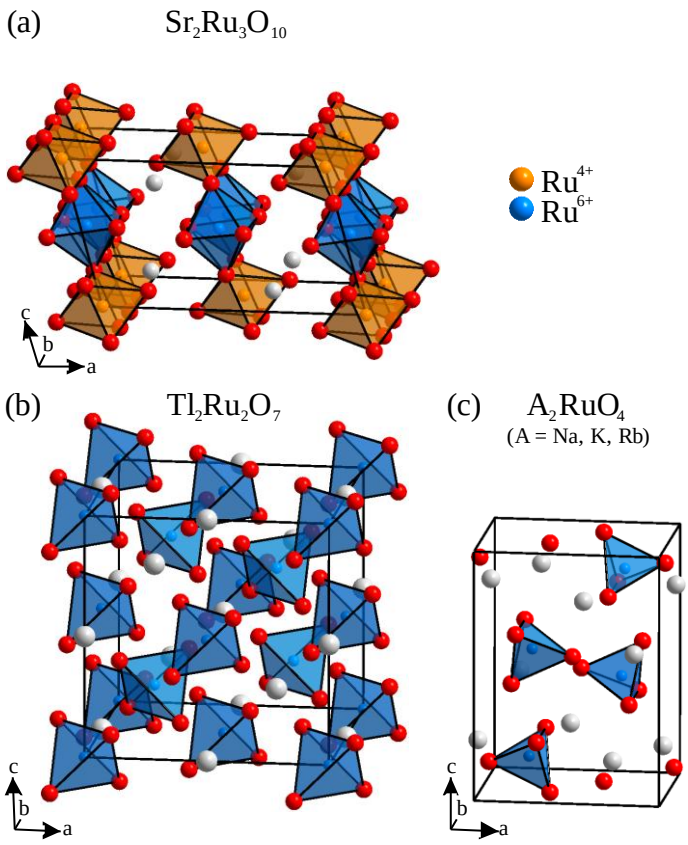

Figure 6.25: The structures of (a) $Sr_2Ru_3O_{10}$ (b) $Tl_2Ru_2O_7$ and (c) M_2RuO_4 (M = Na, K, Rb).

There are, however, examples in the literature of phases containing Ru^{6+} synthesised under ambient pressure, particularly when group 1 (Na, K, Rb) peroxides or superoxides are employed as reagents. For example, A_2RuO_4 (A = Na, K, Rb) phases can be prepared by heating the appropriate A_2O_2 peroxide with RuO_2 under a flow of oxygen at a modest temperature (T < 720 °C).[106,107]

These reactions are reminiscent of the use of metal hydroxide fluxes as strongly oxidising media to stabilise high transition metal oxidation states. For example, $A_2NaRu^{5+}O_6$ (A = La, Pr, Nd) can be synthesised from A_2O_3 and RuO_2 with the use of a NaOH flux in air at 600 °C.[106,107]

Molten hydroxide fluxes can react with oxygen to form peroxide and superoxide anions *in situ*. These anions, in combination with the relatively low synthesis temperatures, favour the formation of highly oxidised products.

A similar explanation can be used to rationalise the oxidising power of the CuF_2/O_2 system: low synthesis temperatures, in conjunction with the high gain in lattice energy upon insertion of the small fluoride anions, favours anion-rich oxidised phases, enabling the formation of highly oxidised products.

6.4.4.2 $Sr_3(Ru_{0.5}Mn_{0.5})_2O_7F_2$

Previous studies have shown that $Sr_3(Ru_{0.5}Mn_{0.5})_2O_7$ adopts a Ru^{4+} and Mn^{4+} combination.[99] Oxidative insertion of fluorine to form a phase with composition $Sr_3(Ru_{0.5}Mn_{0.5})_2O_7F_2$ raises the average transition metal oxidation state from +4 to +5. This is consistent with Ru^{6+}/Mn^{4+}, Ru^{5+}/Mn^{5+} or some combination thereof.

Oxide phases containing manganese in the +5 oxidation state are certainly known. For example, $Ba_3Mn_2O_8$ and $BaRbMnO_4$.[108,109] Oxyfluoride phases containing manganese in an oxidation state above +4 are also known, such as $Ba_5Mn_3O_{12}F$ synthesised at 850 °C.[110] Greaves *et al.* carried out oxidative fluorine insertion into $La_{1.2}Sr_{1.8}Mn_2O_7$ and $Sr_3Mn_2O_6$ to form $La_{1.2}Sr_{1.8}Mn_2O_7F_2$ and $Sr_3Mn_2O_6F_n$ (n = 1, 2, 3) using a flowing mixture of 10% F_2 in N_2, although the former was not fully characterised.[111,112]

However, it should be noted that CuF_2/O_2 is a less oxidising fluorinating agent than F_2 gas.[113] Furthermore, topochemical fluorination of $Ca_3Mn_2O_7$ (described in Appendix 8.3Appendix 6.3) using CuF_2 was unsuccessful. The topochemical oxidation of Mn^{4+} to Mn^{5+} using CuF_2 therefore seems to be, if not impossible under these soft conditions, at least highly unfavourable, while the oxidation of Ru^{4+} to Ru^{6+} is facile, as shown above. This supports $Sr_3(Ru_{0.5}Mn_{0.5})_2O_7F_2$ adopting a Ru^{6+}/Mn^{4+} combination.

6.4.4.3 $Sr_3(Ru_{0.5}Fe_{0.5})_2O_{5.5}F_{3.5}$

Previous studies have shown that $Sr_3(Ru_{0.5}Fe_{0.5})_2O_7$ adopts a Ru^{5+} and Fe^{3+} combination.[89] Fluorination to form a phase with composition $Sr_3(Ru_{0.5}Fe_{0.5})_2O_{5.5}F_{3.5}$ raises that average transition metal oxidation state from +4 to +4.25. ^{57}Fe Mössbauer spectroscopy indicates that all the iron centres are in the +3 oxidation state. The average ruthenium oxidation state is therefore +5.5. Once again, Ru^{6+} has been formed under 'soft' reaction conditions.

Similar substitutive behaviour can be seen in the fluorination of $LaSrFeO_4$ to form $LaSrFeO_3F_3$,[114] while the manganese analogue $LaSrMnO_4$ forms $LaSrMnO_4F_2$.[111] These reactions were performed using a mixture of 10% F_2 in N_2, a more oxidising fluorinating agent than CuF_2/O_2.[113]

The large substitutive component to the reaction of $Sr_3(Ru_{0.5}Fe_{0.5})_2O_7$ with CuF_2 indicates that the Ru/Fe transition metal combination is less readily oxidised than Ru/Ti. This difference can be principally attributed to the thermodynamic difficulty in oxidising Fe^{3+} to Fe^{4+}. For example, synthesis of stoichiometric $Sr_3Fe_2O_7$ requires annealing at 500 °C under 500 atmospheres of oxygen.[18] It is therefore not surprising that these 'soft' reaction conditions do not result in a phase containing Fe^{4+}.

However, the formation of a phase containing $Ru^{5.5+}$ rather than Ru^{6+} suggests that there are as-yet unknown factors that influence the degree of oxidation of ruthenium during this reaction.

6.4.5 Magnetic Behaviour of Fluorinated Phases

As noted above, the topochemical fluorination of $Sr_3(Ru_{0.5}M_{0.5})_2O_7$ (M = Ti, Mn, Fe) raises the oxidation state of the ruthenium centres while leaving that of the transition metal M-cations unchanged. Despite this common chemical feature, the fluorination reactions have a strikingly different effect on the magnetic behaviour of these materials:

6.4.5.1 $Sr_3(Ru_{0.5}Ti_{0.5})_2O_7F_2$

Fluorination of $Sr_3(Ru_{0.5}Ti_{0.5})_2O_7$ to form $Sr_3(Ru_{0.5}Ti_{0.5})_2O_7F_2$ leads to a suppression of the magnetic ordering transition, a drop in the observed Curie constant ($Sr_3(Ru_{0.5}Ti_{0.5})_2O_7$ = 1.622(5) cm^3 K mol^{-1}; $Sr_3(Ru_{0.5}Ti_{0.5})_2O_7F_2$ = 0.232(2) cm^3 K mol^{-1}) and a significant rise in the temperature-independent paramagnetic contribution to the magnetic response ($Sr_3(Ru_{0.5}Ti_{0.5})_2O_7$ = 0.8(4) x 10^{-4} cm^3 mol^{-1}; $Sr_3(Ru_{0.5}Ti_{0.5})_2O_7F_2$ = 23.2(1) x 10^{-4} cm^3 mol^{-1}). This is consistent with a shift towards metallic behaviour on fluorination.

Previous analysis by Goodenough provides some guidance as to the changes in magnetic coupling strength on changing transition metal oxidation states.[28] Figure 6.26 shows a simplified schematic phase diagram of the transfer energy *b*, which is a measure of the strength of the electronic interaction between like atoms, against temperature. As the size of *b* increases from some small value, materials will changed from localised electron insulators/semiconductors to itinerant electron metals at some critical value b_m. The change in the strength of the magnetic superexchange coupling between neighbouring atoms increases leading to a corresponding increase in the magnetic ordering temperature, T_N.

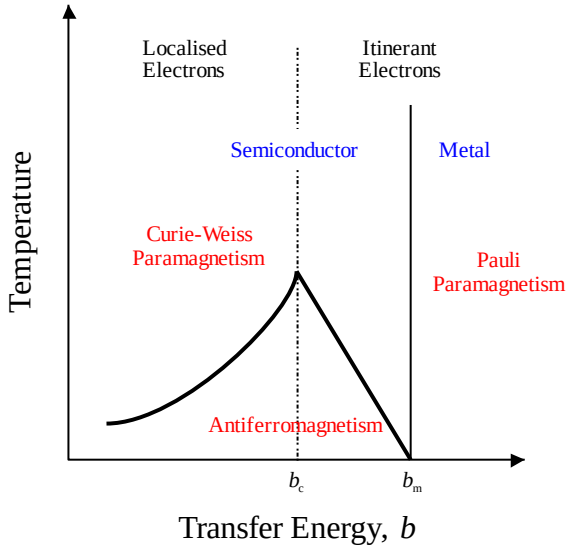

Figure 6.26: Simplified temperature-transfer energy integral phase diagram for a one-electron system.

However, at some critical value b_c, some of the localised electrons in the system become itinerant, screening the magnetic couplings between neighbouring atoms, weakening the magnetic superexchange coupling and leading to a decline in T_N with increasing b until metallic Pauli paramagnetism is observed at b_m. In this intermediate $b_c < b < b_m$ range, interactions between localised and itinerant electrons lead to strong deviations from simple Curie-Weiss paramagnetic behaviour, with observed Curie constants exceeding those calculated using the spin-only formula.

Previous studies by Goodenough and Battle suggest that ruthenium oxides with ruthenium oxidation states in the $Ru^{4+/5+}$ range reside in this intermediate $b_c < b < b_m$ regime.[115] It is no surprise therefore that $Sr_3(Ru_{0.5}Ti_{0.5})_2O_7$ exhibits an anomalously large Curie constant. Raising the oxidation state of a transition metal centre will tend to increase the transfer energy of the system, as oxidation lowers the energy of the metal orbitals, leading to a widening of the bands derived from metal d-orbitals (particularly π*-bands) due to stronger metal d – oxyen 2p interaction.

Thus, fluorination of $Sr_3(Ru_{0.5}Ti_{0.5})_2O_7$ to $Sr_3(Ru_{0.5}Ti_{0.5})_2O_7F_2$ would be expected to increase *b*, explaining the suppression of magnetic order, the decline in Curie constant, and the increase in temperature-independent paramagnetism as the oxyfluoride phase approaches itinerant metallic behaviour (Section 6.3.10).

6.4.5.2 $Sr_3(Ru_{0.5}Fe_{0.5})_2O_{5.5}F_{3.5}$ and $Sr_3(Ru_{0.5}Mn_{0.5})_2O_7F_2$

In contrast to $Sr_3(Ru_{0.5}Ti_{0.5})_2O_7$, $Sr_3(Ru_{0.5}Fe_{0.5})_2O_7$ and $Sr_3(Ru_{0.5}Mn_{0.5})_2O_7$ exhibit spin-glass behaviour at low temperatures.[89,99] Fluorination appears to relieve the magnetic frustration present in these phases, allowing the oxyfluorides to exhibit long-range magnetic ordering.

Battle *et al.* pointed out that, when considered simply, the magnetic couplings in $Sr_3(Ru_{0.5}Fe_{0.5})_2O_7$ should not be frustrated.[89] The Goodenough-Kanamori rules[3] indicate that

the 180 ° σ-type superexchange coupling between nearest neighbour Fe^{3+} ($t_{2g}^3e_g^2$) and Ru^{5+} (t_{2g}^3) should be as follows:

Fe–O–Fe	Antiferromagnetic	$J^{nn}_{Fe/Fe} < 0$
Fe–O–Ru	Ferromagnetic	$J^{nn}_{Fe/Ru} > 0$
Ru–O–Ru	Antiferromagnetic	$J^{nn}_{Ru/Ru} < 0$

These pair-wise magnetic couplings can be satisfied for all Ru/Fe arrangements. This can easily be seen by first considering an all-iron system in which the $J^{nn}_{Fe/Fe}$ coupling lead to G-type antiferromagnetic order in which the spin on each iron centre is antiparallel to that on all of its neighbours (Figure 6.27 (a)). Random substitution of half the iron sites with ruthenium to form the $Sr_3(Ru_{0.5}Fe_{0.5})_2O_7$ lattice can be performed while satisfying the magnetic couplings above by inverting the spin direction at each substituted site, such that the spins in the Fe and Ru sublattices are arranged antiparallel to each other (Figure 6.27 (b)). This arrangement would lead to an expected ordered moment on each site equal to the difference between the local iron and ruthenium moments divided by two, i.e. (5-3)/2 = 1μ_B. The fact that $Sr_3(Ru_{0.5}Fe_{0.5})_2O_7$ does not order antiferromagnetically, but rather displays spin glass behaviour indicates more complex behaviour.

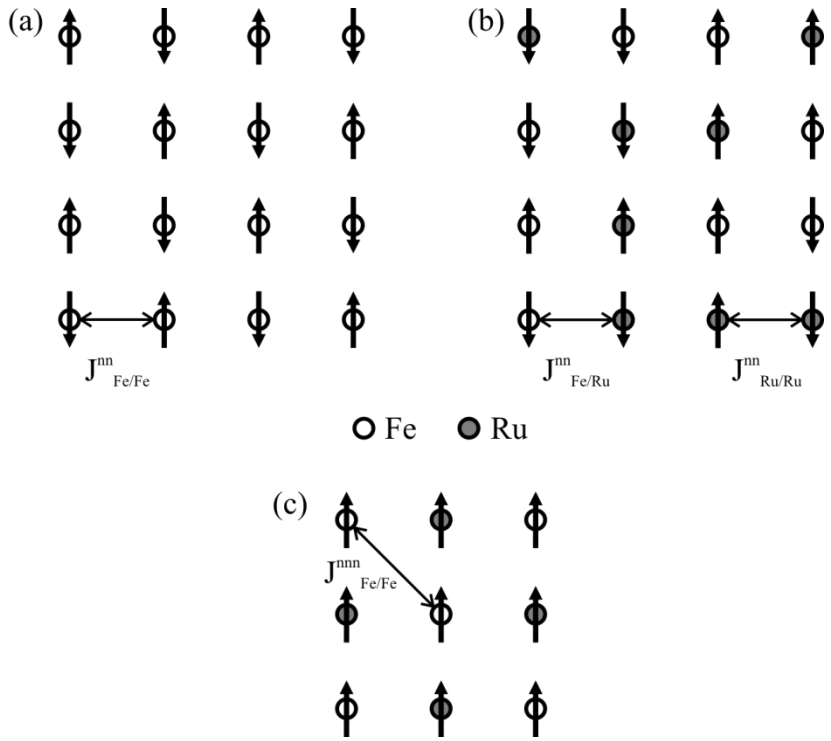

Figure 6.27: (a) The G-type antiferromagnetically ordered structure of a square lattice of Fe^{3+}. (b) The antiparallel arrangement of a disordered array of Fe^{3+} and Ru^{5+}. (c) Strong antiferromagnetic $J^{nnn}_{Fe/Fe}$ couplings lead to frustration in some Ru/Fe arrangements.

Battle *et al.* have suggested that the observed magnetic behaviour arises from a mismatch between the strong interactions of 3d iron centres compared to the relatively weak exchange interactions of 4d ruthenium centres.[89] As a result, $|J^{nn}_{Fe/Fe}| >> |J^{nn}_{Fe/Ru}| \sim |J^{nn}_{Ru/Ru}| \sim |J^{nnn}_{Fe/Fe}|$. That is to say, the next-nearest neighbour coupling between iron centres is comparable to any nearest neighbour interaction involving ruthenium. When these next-nearest neighbour interactions are taken into account, provided they are antiferromagnetic, some arrangements of iron and ruthenium become frustrated, as shown in Figure 6.27 (c), explaining the observed spin glass behaviour.

The adoption of an antiferromagnetically ordered state by $Sr_3(Ru_{0.5}Fe_{0.5})_2O_{5.5}F_{3.5}$ below $T \sim$ 125 K indicates that fluorination of $Sr_3(Ru_{0.5}Fe_{0.5})_2O_7$ lifts the magnetic frustration of the Ru/Fe lattice. Given that the iron centres remain in the +3 oxidation state and their

coordination is essentially unchanged on fluorination, the only way the frustration can be lifted is by strengthening the ruthenium nearest-neighbour interactions relative to the iron-iron next-nearest neighbour interactions, as the σ-type superexchange couplings of Ru^{6+} are predicted to be of the same sign as those of Ru^{5+}. This would result in an antiferromagnetic arrangement of ruthenium and iron spins as shown in Figure 6.27 (b) with an average ordered moment of 1.25 μ_B per transition metal centre, consistent with the observed antiferromagnetic behaviour of $Sr_3(Ru_{0.5}Fe_{0.5})_2O_{5.5}F_{3.5}$ (observed ordered moment = 1.12(3) μ_B).

Such a strengthening of the ruthenium superexchange interactions appears to contradict the argument presented above, where an increase in oxidation state results in an increase in *b* and thus a *decrease* in the strength of the ruthenium superexchange. However, the change in ruthenium oxidation state is not the only factor determining the magnitude of *b*. As noted in Section 6.3.5.2, the fluorination of $Sr_3(Ru_{0.5}Fe_{0.5})_2O_7$ results in a lowering of the crystallographic symmetry due to a change in the (Ru/Fe)–O–(Ru/Fe) bond angle from 180 ° to 164.8(2) °. This tightening of the bond angle will lead to a narrowing of the bands derived from the ruthenium d-orbitals, leading to a decrease in *b* and the observed strengthening of the ruthenium superexchange interactions.

This view is supported by the observation that the all ruthenium phase, $Sr_3Ru_2O_7F_2$, has both the highest ordering temperature (T_N ~ 185 K) and the tightest Ru–O–Ru bond angles (158.1 °, 154.1 °) of all the ruthenium-containing oxyfluoride phases studied, despite containing exclusively Ru^{5+}.[39]

The Ru/Mn phases appear to adopt the same behaviour as the Ru/Fe. On fluorination, the (Ru/Mn)–O–(Ru/Mn) bond angles contract to 161.5 °, strengthening the ruthenium superexchange couplings and lifting the magnetic frustration on fluorination. A disordered arrangement of Mn^{4+} (d^3) and Ru^{6+} (d^2) would yield an antiferromagnetic state with an

average ordered moment of (3-2)/2 = 0.5 μ_B per transition metal centre, hence the weak diffraction peaks observed for this phase at low temperature (Figure 6.17).

Magnetisation-field data collected from both $Sr_3(Ru_{0.5}Fe_{0.5})_2O_{5.5}F_{3.5}$ and $Sr_3(Ru_{0.5}Mn_{0.5})_2O_7F_2$ show that a small glassy component to the magnetisation remains, indicating that although the majority of the frustration has been lifted, some M/Ru configurations remain frustrated. This suggests that the strengthening of the ruthenium superexchange interactions on fluorination is not sufficient to completely remove the influence of the $J^{nnn}_{M/M}$ interactions in these materials.

6.5 Conclusion

Reaction of $Sr_3(Ru_{0.5}M_{0.5})_2O_7$ (M = Ti, Mn, Fe) with CuF_2 under flowing oxygen leads to topochemical insertion in the case of M = Ti, Mn, forming phases with composition $Sr_3(Ru_{0.5}M_{0.5})_2O_7F_2$; and topochemical insertion and substitution in the case of M = Fe, forming a phase with composition $Sr_3(Ru_{0.5}Fe_{0.5})_2O_{5.5}F_{3.5}$. In all three cases, 'soft' conditions enable the preparation of phases containing Ru^{6+}, allowing the complex magnetic coupling interactions present in the parent phase to be tuned by a combination of electronic and structural interactions.

It is reasonable to think that these same synthetic methods could be applied to a wide variety of materials, allowing for the preparation of phases containing highly oxidised 4d and 5d transition metal cations in unusual coordination environments.

These findings have been reported in a recent publication.[116]

Chapter 7 The Reduction of $SrO(SrVO_3)_n$ ($n = 1, 2, \infty$)

7.1 Introduction

Topochemical reduction using binary metal hydrides has enabled the preparation of a wide range of metastable materials with novel combinations of oxidation states and coordination environments.[14-16,87] However, the bulk of the work done so far has focussed on reduction of complex oxides of the late 3*d* transition metals: Mn, Fe, Co, and Ni. Comparatively little attention has been paid to early 3*d* transition metal oxides. Sc, Ti, and V are highly electropositive, and the group oxidation state tends to be particularly stable.[83] Consequently, analogous chemistry performed on early 3*d* transition metal oxides requires much more extreme conditions than for late 3*d* transition metal oxides.

There is nevertheless a wealth of interesting electronic behaviour among early 3*d* complex oxides, such as the ferroelectric behaviour of $BaTiO_3$ or the cooperative orbital ordering behaviour of $LaVO_3$ that results in a reversing of the ferromagnetic component.[28] Early 3*d* complex oxides also display excellent tunability. For instance, $LaTiO_3$ adopts a G-type antiferromagnetic order with an ordering temperature of approximately 140 K, whereas isoelectronic and isostructural $SrVO_3$ remains metallic at all temperatures measured.[28] Similarly, while stoichiometric $CaVO_3$ behaves like $SrVO_3$, slight deviations in the oxygen content render it antiferromagnetic like $LaTiO_3$.[117]

Vanadium oxides such as $LiVO_2$ and LiV_2O_5 have found use as lithium battery materials indicating that redox chemistry on these materials is sufficiently facile to allow practical use.[118] Similarly, the recent report of the formation of $BaTiO_{3-x}H_x$ from reaction between $BaTiO_3$ and CaH_2 suggests that reduction of early transition metal oxides using binary metal hydrides can enable the preparation of novel materials with interesting and technologically useful properties.[119]

In order to investigate the reduction behaviour of complex vanadium oxides, the reaction between the $SrO(SrVO_3)_n$ (n = 1, 2, ∞) series of phases and CaH_2 was investigated. Tuning the reduction behaviour via La or Ca A-site substitution was also attempted.

7.2 Experimental

7.2.1 Synthesis of $SrO(SrVO_3)_n$ (n = 1, 2, ∞)

Samples of $SrO(SrVO_3)_n$ were prepared using the method previously described by Rey *et al.*[120] Suitable stoichiometric amounts of $SrCO_3$ (Alfa Aesar 99.99%) and V_2O_5 (Alfa Aesar 99.99%) were ground together using an agate mortar and pestle. The resulting powders were then placed in an alumina crucible and heated to 900 °C for 12 hours in order to decompose the carbonate and form the appropriate precursor V^{5+} complex oxide, $Sr_2V_2O_7$ (n = ∞), $Sr_3V_2O_8$ (n = 2), and a mixture of $Sr_3V_2O_8$ and SrO (n = 1), as indicated by X-ray powder diffraction measurements.

The powders were then heated at 1000 °C (1100 °C to form $Sr_3V_2O_7$) under flowing H_2 for periods of 12 hours with intermediate grindings. Reaction progress was monitored via X-ray powder diffraction.

7.2.1.1 $SrVO_3$ (n = ∞)

After 7 periods of 12 hours at 1000 °C under flowing H_2, samples of $SrVO_3$ were observed to be phase pure by laboratory X-ray powder diffraction, with lattice parameter a = 3.85(1) Å, in good agreement with literature values for (a = 3.846 Å).[120]

7.2.1.2 Sr_2VO_4 (n = 1)

After 10 periods of 12 hours at 1000 °C under flowing H_2, no further change could be observed in sequential X-ray powder diffraction data. X-ray powder diffraction data collected from samples of Sr_2VO_4 contained an additional peak at 2θ ~ 32 °, corresponding to an

approximately 10% by weight impurity of $Sr_3V_2O_7$ from loss of SrO at high temperatures. Attempts to produce a pure sample of Sr_2VO_4 by varying the synthesis temperature and amount of $SrCO_3$ did not have a measurable impact on the amount of $Sr_3V_2O_7$ present. This impurity was also present in samples prepared by Rey *et al*, although incorrectly assigned to the formation of $Sr(OH)_2 \bullet H_2O$.[120]

X-ray powder diffraction data were consistent with the majority phase having lattice parameters a = 3.83(1) Å and c = 12.56(1) Å, in good agreement with literature values (a = 3.837 Å and c = 12.576 Å).[120]

7.2.1.3 $Sr_3V_2O_7$ (n = 2)

After 14 periods of 12 hours at 1100 °C under flowing H_2, samples of $Sr_3V_2O_7$ were observed to be phase pure by laboratory X-ray powder diffraction, with lattice parameter a = 3.85(1) Å and c = 20.26(1) Å, in good agreement with literature values (a = 3.833 Å and c = 20.246 Å).[121]

7.2.2 Synthesis of $CaVO_3$

$CaVO_3$ was synthesised using the method described by Garcia-Jaca *et al*.[122] Suitable stoichiometric amounts of $CaCO_3$ (Alfa Aesar 99.99%) and V_2O_5 (Alfa Aesar 99.99%) were ground together using an agate mortar and pestle. The resulting powders were then placed in an alumina crucible and heated to 900 °C for 12 hours in order to decompose the carbonate and form the appropriate V^{5+} complex oxide $Ca_2V_2O_7$ as indicated by X-ray powder diffraction measurements.

The powders were then heated at 800 °C under flowing H_2 for periods of 12 hours with intermediate grindings. Reaction progress was monitored via X-ray powder diffraction. Samples of $CaVO_3$ were observed to be phase-pure by laboratory X-ray powder diffraction

measurements with lattice parameters a = 5.33(1) Å, b = 5.36(1) Å, and c = 7.59(1) Å, in good agreement with literature values (a = 5.317 Å, b = 5.340 Å, and c = 7.542 Å).[122]

7.2.3 Synthesis of $La_xSr_{1-x}VO_3$

Samples of $La_xSr_{1-x}VO_3$ (x = 0.1, 0.2, 0.3, 0.5, 0.7, 1.0) were synthesised using the method described by Mahajan *et al.*[123] Suitable stoichiometric quantities of SrO (from $SrCO_3$, Alfa Aesar 99.99% heated at 900 °C for 24 hours in air followed by 1000 °C and 1100 °C under dynamic vacuum for 24 hours at each temperature), La_2O_3 (Alfa Aesar 99.999%, predried at 900 °C), and V_2O_3 (Alfa Aesar, 99.7%) were ground together using an agate mortar and pestle in an argon-filled glovebox. The resulting mixtures were then pressed into a pellet without exposing to the air. The pellets were then transferred to an arc furnace and arc melted a total of four times as described in Section 2.2. The pellets were flipped between each firing to expose potentially unreacted material. Reaction progress was monitored by X-ray powder diffraction.

All samples of the La-doped materials except $LaVO_3$ showed evidence of peak splitting in high resolution X-ray powder diffraction data indicative of the presence of multiple phases. All phases could be indexed on the basis of cubic cells.

7.2.4 Reduction with Metal Hydrides

7.2.4.1 $SrO(SrVO_3)_n$ (n = 1, 2, ∞)

The reduction of $SrO(SrVO_3)_n$ (n = 1, 2, ∞) phases was attempted using CaH_2 as a solid-state reducing agent. In order to assess the reactivity of these materials, small samples (~ 200 mg) were ground together with a double molar excess of calcium hydride in an argon filled glovebox using an agate mortar and pestle. These mixtures were then sealed in silica ampoules and heated at a series of temperatures in the range $300 \leq T / °C \leq 700$ for periods of two days. At temperatures above 630 °C CaH_2 was found to react with the silica ampoule.

Reactions performed above this temperature were carried out by placing the reagents inside a niobium sleeve which was then sealed into a silica ampoule under vacuum. Reaction progress was monitored using X-ray powder diffraction. No reaction was observed at reaction temperatures below 600 °C. At temperatures above 600 °C, additional peaks were evident in the X-ray powder diffraction data, indicative of the formation of new phases. At temperatures above 650 °C, the reactions were observed to lead to decomposition to SrO, CaO, V_2O_3 and lower vanadium oxides.

In order to enable full structural characterisation of the new materials, large samples were required for neutron powder diffraction measurements. It was found that, at the elevated reaction temperatures needed to effect the reduction of these phases, the pressure-venting system described in Section 2.4.2 was insufficiently airtight as indicated by the formation of CaO (observed by X-ray powder diffraction measurements) with no visible to change to the lattice parameters of the vanadium containing phases. The pressure bomb described in Section 2.4.3 could not be used to prepare large samples as it has a maximum operating temperature of 500 °C.

Samples suitable for neutron powder diffraction experiments were synthesised in sealed silica ampoules. Approximately 2.5g of $SrO(SrVO_3)_n$ (n = 1, 2, ∞) were ground together with 0.5g of CaH_2 in an argon filled glovebox using an agate mortar and pestle. These mixtures were then sealed in silica ampoules and heated at 600 °C (n = 1), 610 °C (n = 2) or 630 °C ($n = \infty$) for periods of two days. The ampoules were subsequently returned to the glovebox, scored with a glass knife and opened. The samples were then ground with an additional 0.5g of CaH_2 and reheated. This process was repeated as necessary until no further change was observed via X-ray powder diffraction measurements.

Once a reaction was judged to be complete, the products were washed with 4 x 100 ml of a 0.1 M NH_4Cl solution in methanol, followed by 4 x 100 ml of clean methanol in order to remove unreacted metal hydrides and reaction by-products. The samples were then dried under vacuum and returned to the glovebox.

7.2.4.2 $CaVO_3$

The reduction of $CaVO_3$ was attempted using CaH_2 as a solid-state reducing agent. In order to assess its reactivity, small samples (~ 200 mg) were ground together with a double molar excess of calcium hydride in an argon filled glovebox using an agate mortar and pestle. The mixtures were then sealed in silica ampoules and heated at a series of temperatures in the range and $300 \leq T / °C \leq 500$ for periods of two days. Reaction progress was monitored using X-ray powder diffraction.

Once a reaction was judged to be complete, the products were washed with 4 x 100 ml of a 0.1 M NH_4Cl solution in methanol, followed by 4 x 100 ml of clean methanol in order to remove unreacted metal hydrides and reaction by-products. The samples were then dried under vacuum and returned to the glovebox.

7.2.4.3 $La_xSr_{1-x}VO_3$

The reduction of the $La_xSr_{1-x}VO_3$ (x = 0.1, 0.2, 0.3, 0.5, 0.7, 1.0) was attempted in the same manner as described above for samples of $SrVO_3$.

7.3 Results

7.3.1 Synthesis of $La_xSr_{1-x}VO_3$

High resolution laboratory X-ray powder diffraction data collected from as-synthesised samples of $La_xSr_{1-x}VO_3$ (x = 0.1, 0.2, 0.3, 0.5, 0.7) revealed the presence of multiple phases within the sample, all of which could be indexed on the basis of cubic structures.

High resolution laboratory X-ray powder diffraction data was collected from a sample with average composition $La_{0.1}Sr_{0.9}VO_3$. A model containing two phases based on the room-temperature structure of $SrVO_3$ with a 0.1 occupancy of the A-site by lanthanum was refined against this data. Lattice parameters were allowed to refine independently. Thermal parameters were constrained to be same for analogous atoms in both phases, and their peak shapes were also constrained to be identical. The refinement converged readily to a good statistical fit to the data ($\chi^2 = 2.534$). The two phases were refined to have lattice parameters *a* = 3.8660(1) Å and *a* = 3.8466(1) Å present in a 72.5(2)% to 27.5(2)% ratio by weight.

The fractional occupancies of the two phases were constrained to always have full A-site occupancy and maintain an overall sample composition of $La_{0.1}Sr_{0.9}VO_3$. Refinement of the fractional occupancies of the A-site resulted in a slight improvement in the statistical fit to the data ($\chi^2 = 2.446$). The majority phase refined to a composition $La_{0.15(1)}Sr_{0.85(1)}VO_3$ and the minority refined to a composition of $La_{0.00(1)}Sr_{1.00(1)}VO_3$. Details of the refined structural parameters are given in Table 7.1. It should be noted that the peak splitting was only evident in high resolution X-ray powder diffraction data. Data collected using the Philips diffractometer with a lower resolution show single broad peaks.

Atom	**Wyckoff Position**	***x***	***y***	***z***	**U_{iso} / Å^2**	**Frac. Phase 1**	**Frac. Phase 2**
Sr	1*a*	0	0	0	0.017(1)	0.85(1)	0.15(1)
La	1*a*	0	0	0	0.017(1)	1.00(1)	0.00(1)
V	1*b*	1/2	1/2	1/2	0.012(1)	1	1
O	3*c*	1/2	1/2	0	0.017(1)	1	1
Phase 1: $La_xSr_{1-x}VO$: space group *Pm*-3*m*; *a* = 3.8661(1) Å cell volume = 57.78(1) Å^3; weight fraction = 71.5(2)%							
Phase 2: $La_xSr_{1-x}VO$: space group *Pm*-3*m*; *a* = 3.8467(1) Å cell volume = 56.92(1) Å^3; weight fraction = 28.5(2)%							
$\chi^2 = 2.454$, wRp = 1.36%, Rp = 0.92%							

Table 7.1: Refined structural parameters for $La_{0.1}Sr_{0.9}VO_3$ against laboratory X-ray powder diffraction data.

Other samples along the compositional range $La_xSr_{1-x}VO_3$ could be refined using a similar two-phase model as described above. A further discussion can be found in Section 7.4.1.2.

7.3.2 Reactivity

7.3.2.1 $SrO(SrVO_3)_n$ (n = 1, 2, ∞)

X-ray powder diffraction data collected from the washed products of reaction between $SrO(SrVO_3)_n$ (n = 1, 2, ∞) and CaH_2 revealed that no reaction took place at temperatures below 600 °C. Reactions performed between 600 °C and 630 °C produced phases as detailed below. Reactions performed above 630 °C led to decomposition of the samples into binary oxides (CaO, SrO, V_2O_3, and lower vanadium oxides).

7.3.2.2 $SrVO_3$ (n = ∞)

X-ray powder diffraction data collected from the washed products of reaction between $SrVO_3$ and CaH_2 could be indexed on the basis of a primitive tetragonal unit cell with lattice parameters a = 3.93(1) Å and c = 3.67(1) Å. A model based on the infinite-layer structure of $LaNiO_2$ was constructed and refined against the data, accounting for the majority of the peaks. Additional peaks were evident in the X-ray powder diffraction data corresponding to some unreduced cubic $SrVO_{3-x}$. Multiple attempts to produce a pure sample of the tetragonal material were unsuccessful: increasing the reaction time did not result in any measurable decrease in the fraction of the cubic phase, and increasing the reaction temperature above 630 °C resulted in decomposition of the sample to binary oxides (CaO, SrO, V_2O_3, and lower vanadium oxides). The best sample used for all subsequent measurements was refined against X-ray powder diffraction data to give a mixture of 81(1)% of the tetragonal material (taken to have composition $SrVO_2$) and 19(1)% of the cubic material by weight.

7.3.2.3 Sr_2VO_4 (n = 1)

X-ray powder diffraction data collected from the washed products of reaction between Sr_2VO_4 and CaH_2 could be indexed on the basis of a body centred orthorhombic unit cell with lattice parameters a = 3.67(1) Å, b = 3.89(1) Å and c = 12.78(1) Å. The 10% by weight impurity of $Sr_3V_2O_7$ present in the starting material produced a phase as detailed below under these reaction conditions.

7.3.2.4 $Sr_3V_2O_7$ (n = 2)

X-ray powder diffraction data collected from the washed products of reaction between $Sr_3V_2O_7$ and CaH_2 could be indexed on the basis of a body centred orthorhombic unit cell with lattice parameters a = 3.67(1) Å, b = 3.91(1) Å and c = 20.62(1) Å.

7.3.2.5 $La_xSr_{1-x}VO_3$

X-ray powder diffraction data collected from the washed products of reaction between $LaVO_3$ and CaH_2 showed no reaction occurred at temperatures below 700 °C. At 700 °C, the sample decomposed into La_2O_3, CaO, V_2O_3 and lower oxides of vanadium.

X-ray powder diffraction data collected from the washed products of reaction between a sample of $La_{0.1}Sr_{0.9}VO_3$ showed that at temperatures below 600 °C, no reaction occurred. Reactions performed at temperatures between 600 °C and 630 °C led to the formation of a phase that could be indexed on the basis of a tetragonal unit cell with lattice parameters a = 3.93(1) Å and c = 3.67(1) Å. However, a significant amount of cubic material remained in the sample. In order to gauge the extent of reduction, a model containing one phase with a structure of the tetragonal material with composition $La_{0.1}Sr_{0.9}VO_2$ and a secondary phase based on the structure of the cubic material with composition $La_{0.1}Sr_{0.9}VO_3$ was refined against the data to give a ratio of 33.3:66.6 in favour of the cubic phase. Addition of extra

CaH_2, hotter reaction temperatures, and longer reaction times did not lead to an observable increase in the amount of tetragonal material present in the sample.

Attempted reduction of phases with greater lanthanum content led to similar observed reduction behaviour, with separation into a tetragonal phase and a large amount of apparently unreacted cubic material. The phase fraction of the tetragonal material decreased monotonically with increasing lanthanum content until $x = 0.5$, which behaved like $LaVO_3$, i.e. no change in the X-ray powder data until reduction/decomposition to binary oxides.

In summary, attempts at A-site substitution of $SrVO_3$ result in non-topochemical reduction behaviour, even for small amounts of La-doping.

7.3.3 Neutron Powder Diffraction at 298 K

Neutron powder diffraction data from all three reduced phases derived from $SrO(SrVO_3)_n$ ($n = 1, 2, \infty$) at 298 K were collected using the POLARIS diffractometer.

7.3.3.1 Reduced $SrVO_3$ ($n = \infty$)

Neutron powder diffraction data collected from the washed products of reaction between $SrVO_3$ and CaH_2 could be indexed on the basis of a primitive tetragonal unit cell with lattice parameters $a = 3.93(1)$ Å and $c = 3.67(1)$ Å.

A model based on the room-temperature structure of $LaNiO_2$[14] was refined against neutron powder diffraction data collected from the washed products of reaction between $SrVO_3$ and CaH_2 at 298 K. While the pattern could be indexed on the basis of this model, the fit to the diffraction intensities was poor. An oxide anion was introduced at the (0, 0, 1/2) position. Refinement of the fractional occupancy of this site quickly led to a large negative value suggesting the presence of hydrogen on this site (neutron scattering lengths O = 5.803 fm,

H = -3.739 fm).[43] Replacement of the oxide anion for a hydride at the (0, 0, 1/2) position led to a much better fit of the model to the data.

Given the very small neutron scattering length of vanadium (-0.3824),[43] their thermal displacement parameters were fixed at 0.002 $Å^2$ and not refined.

In order to account for the unreacted $SrVO_{3-x}$ in the sample, a secondary phase corresponding so $SrVO_{3-x}$ was added to the model. Given the small weight fraction of this phase and correlation between fractional occupancy and thermal factors, no attempt was made to refine the oxide content of this phase.

Inspection of the resulting fit to the data revealed additional features at large *d*-spacing that could be indexed using a unit cell based on an $a' \approx \sqrt{2}a$, $b' \approx \sqrt{2}b$, and $c' \approx 2c$ expansion of the reduced $SrVO_3$ tetragonal unit cell, indicative of magnetic order. The intensities of these additional diffraction peaks were best accounted for by a model in which all spins are aligned antiferromagnetically to each other and parallel to the *z*-axis, with an ordered moment of 1.45(4) μ_B per vanadium centre (Figure 7.1).

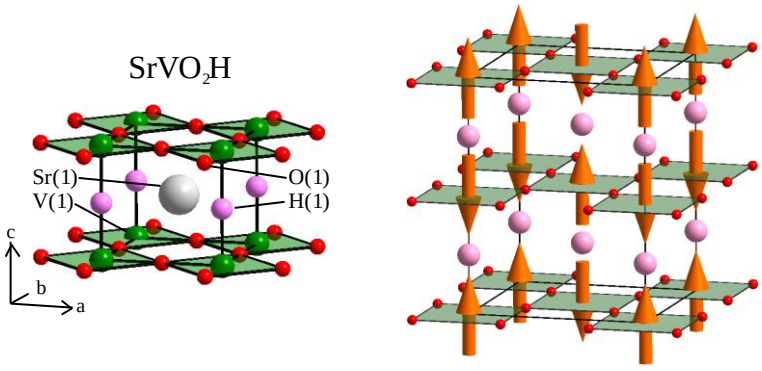

Figure 7.1: The refined atomic and magnetic structures of $SrVO_2H$ at 298 K.

The hydride anion occupancies in the model were found to correlate strongly with the thermal factors and were therefore set to unity. The composition of $SrVO_2H$ was confirmed by

chemical titration as described in Section 7.3.4. The refinement converged readily to a good statistical fit (χ^2 = 2.888). Observed, calculated, and difference plots are given in Figure 7.2. Full details of the structural and magnetic parameters are given in Table 7.2 and Table 7.3 and selected bond lengths are given in Table 7.4.

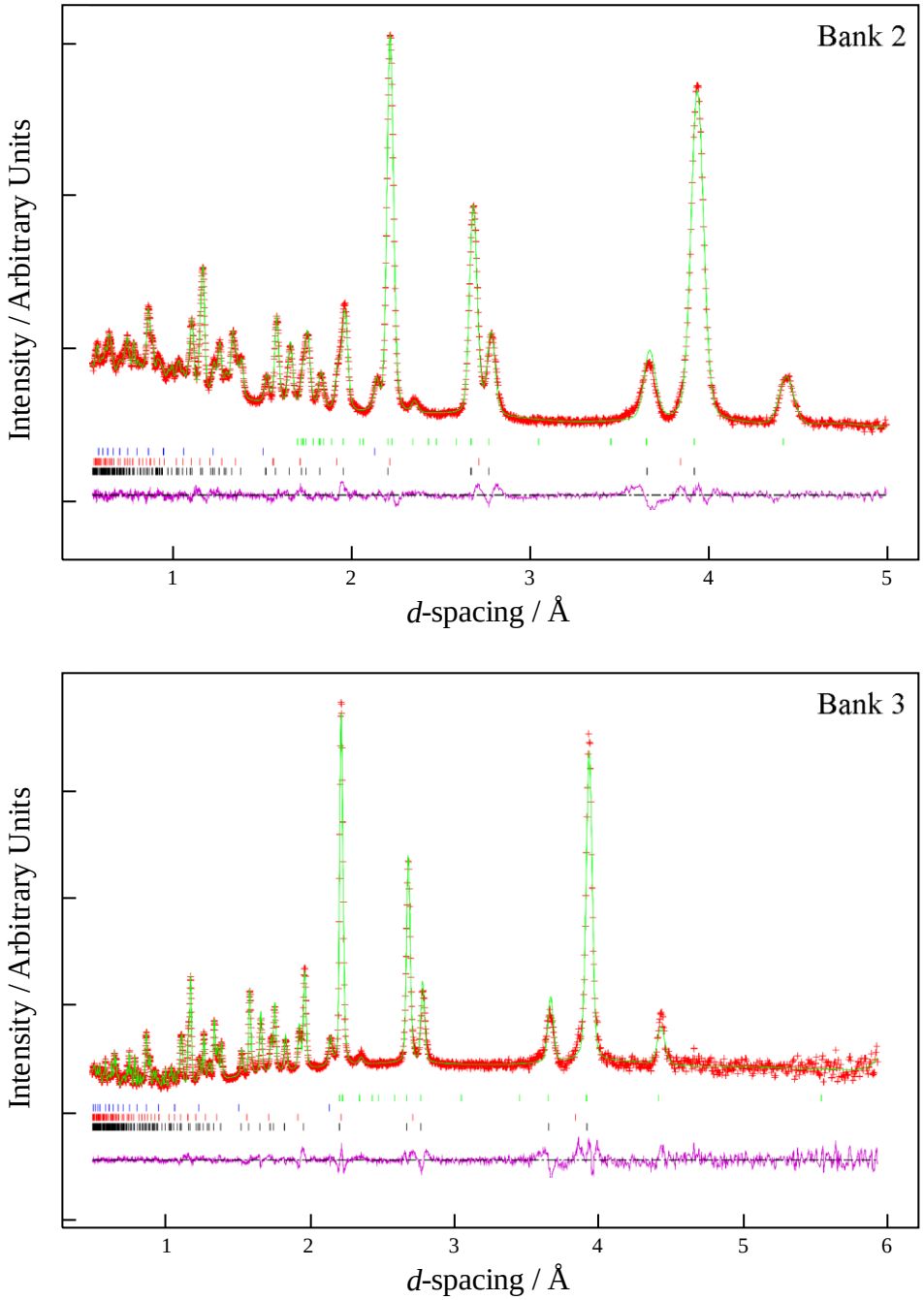

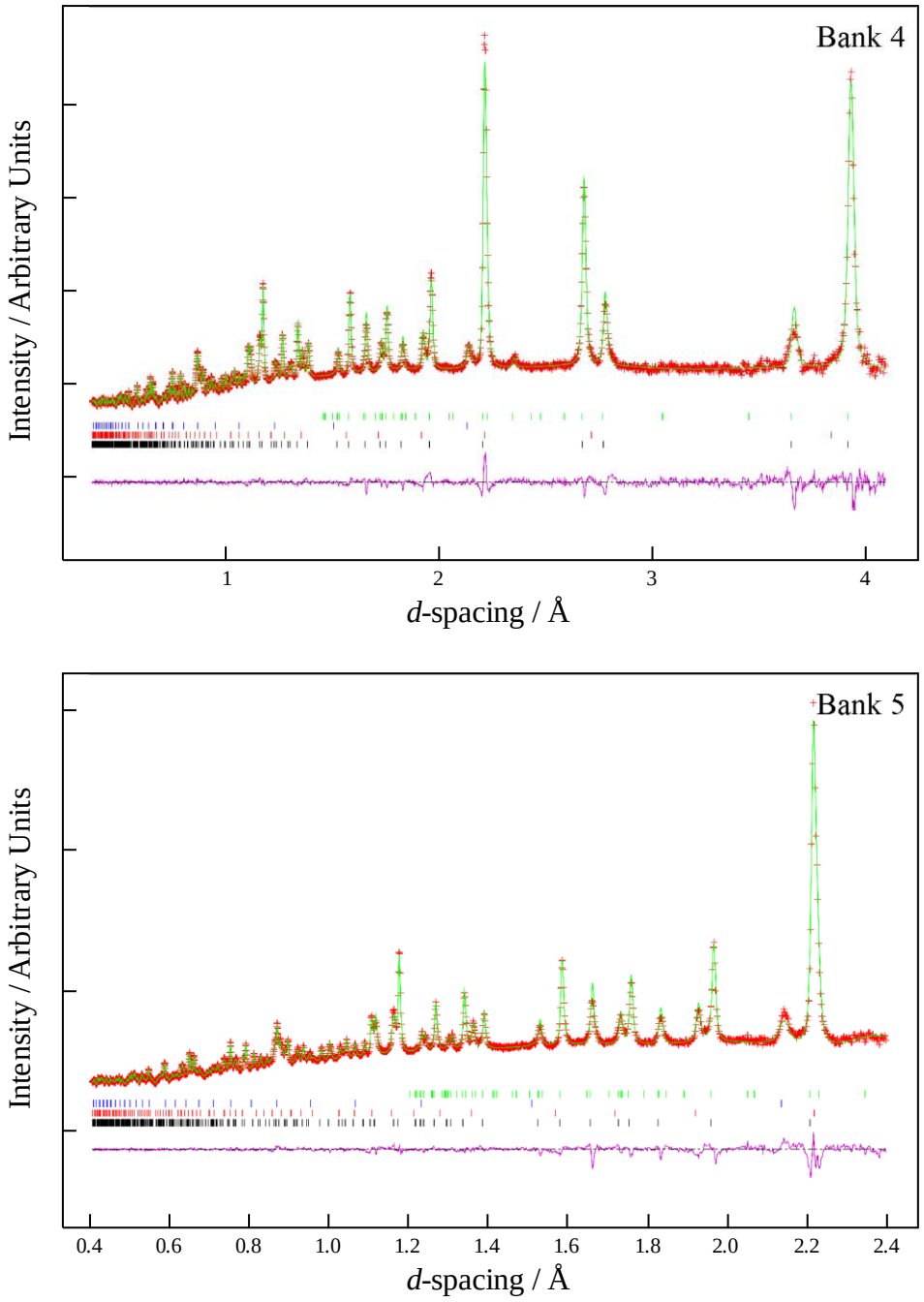

Figure 7.2: Observed, calculated, and difference plots for refinement of the structural model of $SrVO_2H$ at 298 K against neutron powder diffraction data collected using the POLARIS instrument. Red tick marks correspond to a 13.5(3)% by weight impurity of $SrVO_{3-x}$. Blue tick marks correspond to contributions from the vanadium sample holder. Green tick marks correspond to the magnetic reflections.

Atom	Wyckoff Position	*x*	*y*	*z*	U_{iso} / Å^2	U_{11}	U_{22}	U_{33}
Sr(1)	4*i*	1/2	1/2	1/2	0.003(1)			
V(1)	2*a*	0	0	0	0.002			
O(1)	4*i*	0	1/2	0		0.0038(2)	0.0009(2)	0.0080(2)
H(1)	2*b*	0	0	1/2		0.0336(5)	0.0336(5)	0.00121(7)
$SrVO_2H$: space group *P*4/*mmm*; *a* = 3.9332(4) Å and *c* = 3.6671(4) Å; cell volume = 56.73(2) Å^3; weight fraction = 86.8(3)%								
Sr(1)	1*b*	1/2	1/2	1/2	0.003(1)			
V(1)	1*a*	0	0	0	0.002			
O(1)	3*d*	0	1/2	0	0.008(1)			
$SrVO_{3-x}$: space group *Pm*-3*m*; *a* = 3.8556(4) Å cell volume = 57.32(2) Å^3; weight fraction = 13.2(3)%								
χ^2 = 2.888, wRp = 1.33%, Rp = 1.83%								

Table 7.2: Refined structural parameters for $SrVO_2H$ at 298 K.

Magnetic Model				
Atom	***x***	***y***	***z***	***Mz*** / μ_B
V(1)	0	0	0	1.49(2)
V(2)	1/2	1/2	0	-1.49(2)
V(3)	0	0	1/2	-1.49(2)
V(4)	1/2	1/2	1/2	1.49(2)
Space group *P*1 *a* = 5.56(1) Å, *b* = 5.56(1) Å, *c* = 7.32(1) Å				

Table 7.3: Refined magnetic parameters for $SrVO_2H$ at 298 K.

Cation	Anion	Bond Length / Å	Bond Valence Sum
Sr(1)	O(1)	2.689(1) x 8	Sr +2.20
	H(1)	2.781(1) x 4	
V	O(1)	1.967(1) x 4	V +3.19
	H(1)	1.834(1) x 2	

Table 7.4: Selected bond lengths and bond valence parameters from the refined structure of $SrVO_2H$ at 298 K.

7.3.3.2 Reduced Sr_2VO_4 (*n* = 1)

A body-centred model based on the *Immm* structure of Sr_2CuO_3[124] containing square-planar VO_4 units was refined against neutron powder diffraction data collected (Figure 7.3). The fit to the data was poor (χ^2 = 173). Once again, addition of a hydride ion at (1/2, 0, 0) greatly improved the observed and statistical fits (χ^2 = 4.523). $Sr_3V_2O_5H_2$, described below, was included as a second phase to account for the additional peaks from the reduction of the $Sr_3V_2O_7$ impurity present in the starting material.

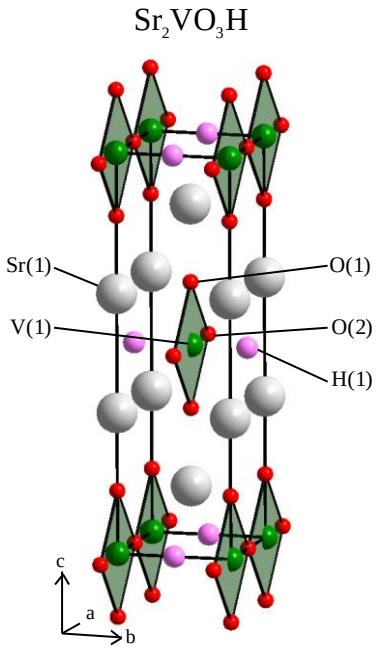

Figure 7.3: Final refined structure of Sr_2VO_3H at 298 K.

Observed, calculated and difference plots are given in Appendix 7. Full details of the structural parameters are given in Table 7.5 and selected bond lengths are given in Table 7.6.

Atom	**Wyckoff Position**	***x***	***y***	***z***	**U_{iso} / Å^2**	**U_{11}**	**U_{22}**	**U_{33}**
Sr(1)	4*i*	0	0	0.3519(1)	0.003(1)			
V(1)	2*a*	0	0	0	0.002			
O(1)	4*i*	0	0	0.1575(1)		0.0029(3)	0.0108(4)	0.0011(3)
O(2)	2*b*	1/2	0	0		0.0009(5)	0.0077(7)	0.0071(6)
H(1)	2*d*	0	1/2	0		0.0331(19)	0.0051(14)	0.0733(3)
Sr_2VO_3H: space group *Immm*; *a* = 3.8878(6) Å, *b* = 3.6666(6) Å, and *c* = 12.7746(19) Å; cell volume = 182.10(8) Å^3; weight fraction = 73.1(4)%								
Sr(1)	2*c*	0	0	1/2	0.009(1)			
Sr(2)	4*i*	0	0	0.3174(3)	0.009(1)			
V(1)	4*i*	0	0	0.0911(37)	0.002			
O(1)	2*a*	0	0	0	0.004(1)			
O(2)	4*i*	0	0	0.1975(3)	0.004(1)			
O(3)	4*j*	1/2	0	0.0916(3)	0.004(1)			
H(1)	4*j*	0	1/2	0.1141(10)	0.004(1)			
$Sr_3V_2O_5H_2$: space group *Immm*; *a* = 3.8955(9) Å, *b* = 3.6803(8) Å, and *c* = 20.5936(47) Å; cell volume = 295.24(14) Å^3; weight fraction = 26.9(4)%								
χ^2 = 4.523, wRp = 1.74%, Rp = 2.18%								

Table 7.5: Refined structural parameters for Sr_2VO_3H at 298 K.

Cation	Anion	Bond Length / Å	Bond Valence Sum
Sr(1)	O(1)	2.483(2) x 1	Sr +2.06
	O(1)	2.675(1) x 4	
	O(2)	2.634(1) x 2	
	H(1)	2.713(1) x 2	
V	O(1)	2.012(1) x 2	V +3.13
	O(2)	1.944(1) x 2	
	H(1)	1.833(1) x 2	

Table 7.6: Selected bond lengths and bond valence parameters from the refined structure of Sr_2VO_3H at 298 K.

7.3.3.3 Reduced $Sr_3V_2O_7$ (n = 2)

A model based on the room-temperature structure of $Sr_3Fe_2O_5$[19] (space group *Immm*) but with an additional hydride anion at (1/2, 0, *z*) was refined against neutron powder diffraction data collected (Figure 7.4). Close inspection of the fit to the data revealed a number of diffraction features that could not be accounted for using this model. These could be accounted for by a small impurity of $SrVO_2H$. The refinement converged readily to give a good statistical fit (χ^2 = 2.797).

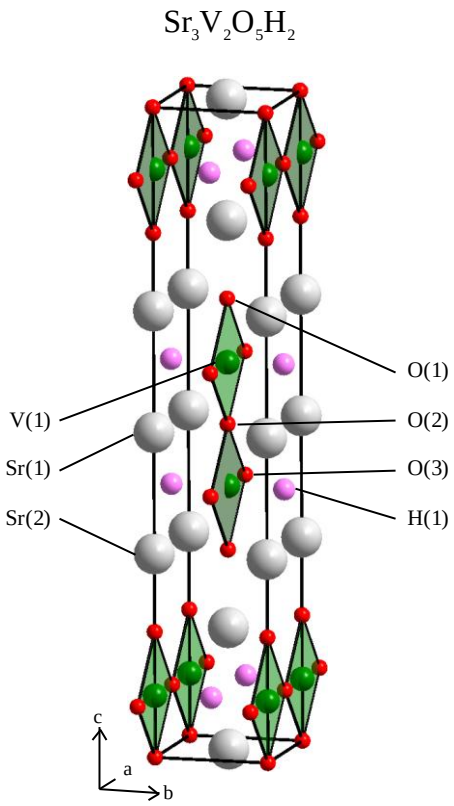

Figure 7.4: Final refined structure of $Sr_3V_2O_5H_2$ at 298 K.

Observed, calculated and difference plots are given in Appendix 7. Full details of the structural parameters are given in Table 7.7 and selected bond lengths are given in Table 7.8.

Atom	Wyckoff Position	*x*	*y*	*z*	U_{iso} / Å^2	U_{11}	U_{22}	U_{33}
Sr(1)	2*c*	0	0	1/2	0.004(1)			
Sr(2)	4*i*	0	0	0.3132(1)	0.004(1)			
V(1)	4*i*	0	0	0.0954(1)	0.002			
O(1)	2*a*	0	0	0	0.004(1)			
O(2)	4*i*	0	0	0.1929(1)	0.005(1)			
O(3)	4*j*	1/2	0	0.0954(1)		0.0014(4)	0.0098(6)	0.0048(4)
H(1)	4*j*	0	1/2	0.0967(2)		0.0355(14)	0.0033(8)	0.0350(17)
$Sr_3V_2O_5H_2$: space group *Immm*; *a* = 3.9157(7) Å, *b* = 3.6680(6) Å, and *c* = 20.6342(36) Å; cell volume = 293.36(15) Å^3; weight fraction = 89.4(3)%								
Sr(1)	4*i*	1/2	1/2	1/2	0.003(1)			
V(1)	2*a*	0	0	0	0.002			
O(1)	4*i*	0	1/2	0	0.003(1)			
H(1)	2*b*	0	0	1/2	0.075(9)			
$SrVO_2H$: space group *P*4/*mmm*; *a* = 3.9209(13) Å and *c* = 3.6920(20) Å; cell volume = 56.76(4) Å^3; weight fraction = 10.6(3)%								
χ^2 = 2.797, wRp = 1.34%, Rp = 1.67%								

Table 7.7: Refined structural parameters for $Sr_3V_2O_5H_2$ at 298 K.

Cation	Anion	Bond Length / Å	Bond Valence Sum
Sr(1)	O(1)	2.683(1) x 4	Sr +2.20
	O(3)	2.690(2) x 4	
	H(1)	2.795(3) x 4	
Sr(2)	O(2)	2.482(3) x 1	Sr +2.04
	O(2)	2.686(1) x 4	
	O(3)	2.631(2) x 2	
	H(1)	2.700(3) x 2	
V	O(1)	1.969(2) x 1	V +3.15
	O(2)	2.012(3) x 1	
	O(3)	1.958(1) x 2	
	H(1)	1.834(1) x 2	

Table 7.8: Selected bond lengths and bond valence parameters from the refined structure of $Sr_3V_2O_5H_2$ at 298 K.

7.3.4 Manganometric Titration

7.3.4.1 Introduction

The vanadium oxidation states in the washed products of reaction were determined via titration with $KMnO_4$ using the method described by Niwa and Murakami.[125] Samples containing vanadium were dissolved in 4.5 M sulfuric acid and the resulting solution was titrated against a $KMnO_4$ solution of known concentration, determined by calibration using sodium oxalate solution.[126]

Reduced vanadium ions in solution are oxidised by $KMnO_4$ to V^{5+} as follows:

$$MnO_4^- + 8H^+ + 5e^- \rightarrow Mn^{2+} + 4H_2O$$

$$V_{(aq)}^{(5-x)+} \rightarrow V_{(aq)}^{5+} + x \cdot e^-$$

7.3.4.2 Experimental Methods

Approximately 50mg of sample were accurately weighed out in an argon-filled glovebox and placed into a three-necked round bottom flask which was then sealed with suba seals. The flask was then removed from the glovebox and flushed with argon. The titrations were carried out under an argon atmosphere in order to prevent aerial oxidation of the vanadium ions.

Titrations were carried out using an approximately 0.0025M solution of $KMnO_4$. The exact concentration was determined by titrating against a known volume of 0.0125M sodium oxalate solution.

The solution was stirred using a magnetic stirrer bar. The end point was indicated by the persistence of a pink colour for at least 30 seconds.

7.3.4.3 Results

Results of these titrations are given in Table 7.9.

Sample	Average Vanadium Oxidation State	Standard Deviation	Material Composition (by weight)
$SrVO_2H_x$	+3.18	0.02	86.8(3)% $SrVO_2H$ 13.2(3)% $SrVO_3$
$Sr_2VO_3H_x$	+3.08	0.02	73.1(4)% Sr_2VO_3H 26.9(4)% $Sr_3V_2O_5H_2$
$Sr_3V_2O_5H_{2x}$	+3.12	0.06	89.4(3)% $Sr_3V_2O_5H_2$ 10.6(3)% $SrVO_2H$

Table 7.9: Average vanadium oxidation states obtained via manganometric titration.

These values are calculated using the weight fractions refined against neutron powder diffraction data and are consistent with values of $x = 1$ in all three cases. In the case of the

$SrVO_2H_x$ sample, the average vanadium oxidation state is in good agreement with the refined weight fractions.

In all three cases, the vanadium oxidation state is slightly above +3. While there are complex transition metal oxyhydrides such as $Sr_3Co_2O_{4.33}H_{0.84}$ and $BaTiO_{3-x}H_x$ in which oxide and hydride anions share a site, these sites are generally much more like oxide anion sites and therefore much larger than those observed in the vanadium oxyhydrides.[119,127] Furthermore, their occupancy fractions generally skew in the direction of the oxide, suggesting that while an oxide anion site can be partially occupied by a hydride anion, the reverse may not be true.

The slightly high oxidation state in these materials is therefore attributed to the presence of some amorphous SrO or $Sr(OH)_2$ in the sample, which would decrease the amount of $KMnO_4$ needed to oxidise a given amount of sample, and would therefore lead to a higher apparent oxidation state.

In all three cases, the oxidation states are consistent with full occupancy of the hydride anion site.

7.3.5 Magnetic Characterisation

7.3.5.1 Magnetisation Measurements

Zero-field and field cooled magnetisation data were collected from $SrVO_2H$ as a function of temperature in the range $5 \leq T / K \leq 300$ and are shown in Figure 7.5. The data diverge over the entire range.

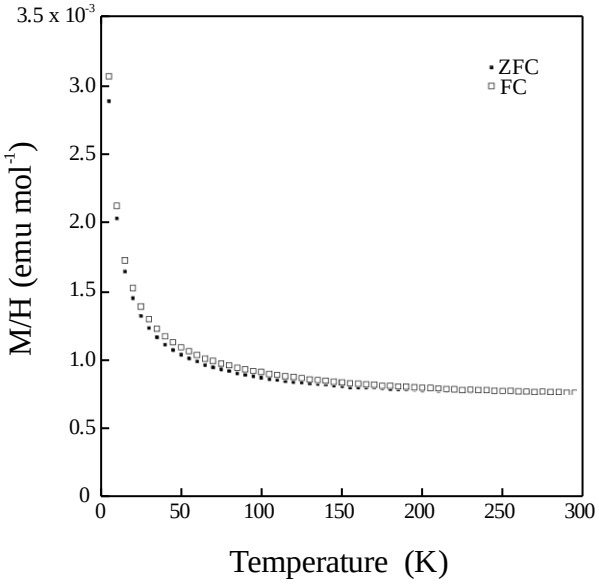

Figure 7.5: Zero-field and field cooled magnetisation data collected from $SrVO_2H$ as a function of temperature.

The zero-field cooled data can be approximately fitted to the Curie-Weiss law in the range $5 \leq T / K \leq 300$ to yield values of C = 0.0175(1) cm^3 K mol^{-1}, θ = -3.07(7) K, and K = 6.97(7) x 10^{-4} cm^3 where mol^{-1} means per mole of formula unit of $SrVO_2H$. The observed moment corresponds to approximately 1.75 % of the expected moment for one d^2 V^{3+} centre per formula unit ($C_{expected}$ = 1 cm^3 K mol^{-1})

Zero-field and field cooled magnetisation data were collected from Sr_2VO_3H and $Sr_3VO_5H_2$ as a function of temperature in the range $5 \leq T / K \leq 300$ and are shown in Figure 7.6 and Figure 7.7. In both cases, these data diverge over the entire range.

Data collected from Sr_2VO_3H show a small event at T ~ 65 K. The zero-field cooled data can be approximately fitted to the Curie-Weiss law in the range $80 \leq T / K \leq 300$ to yield values of C = 0.120(8) cm^3 K mol^{-1}, θ = -68.7(71) K, and K = 0.00262(2) cm^3 where mol^{-1} means per mole of formula unit of Sr_2VO_3H.

Zero-field cooled data collected from $Sr_3V_2O_5H_2$ can be approximately fitted to the Curie-Weiss law in the range $15 \leq T / K \leq 300$ to yield values of $C = 0.0415(1)$ cm^3 K mol^{-1}, $\theta = -4.6(2)$ K, and $K = 0.00261(1)$ cm^3 where mol^{-1} means per mole of formula unit of $Sr_3V_2O_5H_2$.

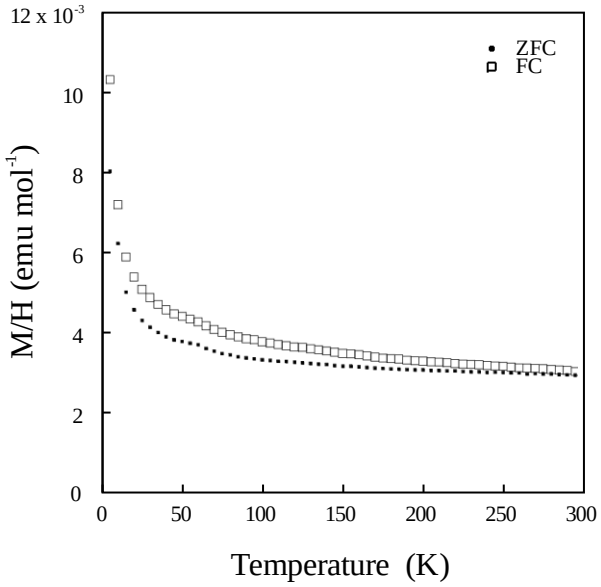

Figure 7.6: Zero-field and field cooled magnetisation data collected from Sr_2VO_3H as a function of temperature.

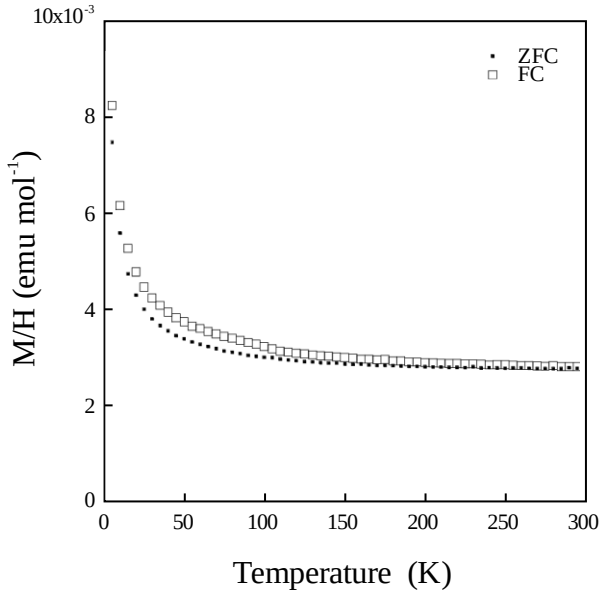

Figure 7.7: Zero-field and field cooled magnetisation data collected from $Sr_3V_2O_5H_2$ as a function of temperature.

For d^2 V^{3+} centres, $C_{expected}$ = 1 cm^3 K mol^{-1} for Sr_2VO_3H and $C_{expected}$ = 2 cm^3 K mol^{-1} for $Sr_3V_2O_5H_2$. The observed moments correspond to approximately 12% and 2% of the expected moment respectively.

7.3.5.2 Neutron Powder Diffraction at 4 K

Neutron powder diffraction data were collected from $SrVO_2H$ at 4 K. Structural and magnetic models based on the room-temperature structural and magnetic models were refined against these data. The refinement converged readily to give a good statistical fit (χ^2 = 1.950). The refined ordered moment at 4 K was 1.56(2) μ_B. No additional features were observed relative to the data collected from $SrVO_2H$ at 298 K. Full observed, calculated, and difference plots as well as full details of the magnetic refinements are given in Appendix 7.

Neutron powder diffraction data collected from Sr_2VO_3H and $Sr_3V_2O_5H_2$ at 4 K using the POLARIS diffractometer at ISIS exhibited additional diffraction features relative to analogous data collected at 298 K (Figure 7.9 and Figure 7.10). In both cases, these could be accounted for using magnetic unit cells related to the crystallographic unit cell by $a_{mag} = \sqrt{2}a_{cryst}$, $b_{mag} = \sqrt{2}b_{cryst}$, $c_{mag} = c_{cryst}$ expansions of the crystallographic unit cells.

The intensities of these reflections could best be accounted for by G-type antiferromagnetic ordering, with the spins aligned parallel to the *c* axis in the case of Sr_2VO_3H and within the *ab* plane, aligned along the V–H–V bonds in the case of $Sr_3V_2O_5H_2$.

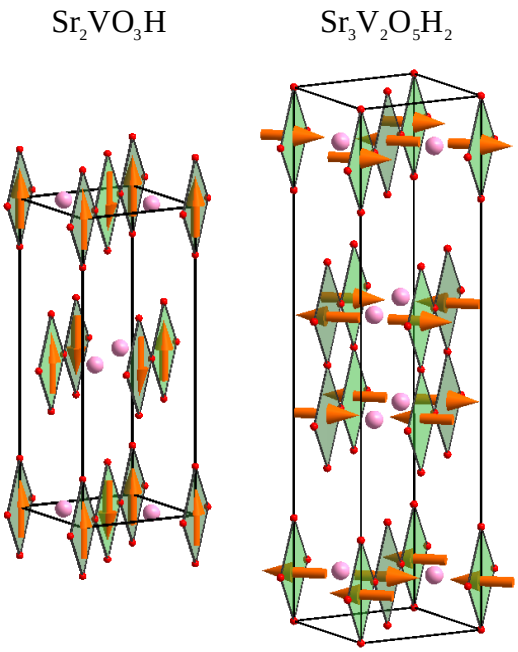

Figure 7.8: Refined magnetic structures of Sr_2VO_3H (left) and $Sr_3V_2O_5H_2$ (right).

Refinements converged readily to give good statistical fits (χ^2 = 3.654 and χ^2 = 2.168) and yielded ordered moments of 1.48(7) in the case of Sr_2VO_3H and 1.35(20) μ_B in the case of $Sr_3V_2O_5H_2$. Full observed, calculated, and difference plots as well as full details of the magnetic refinements are given in Appendix 7.

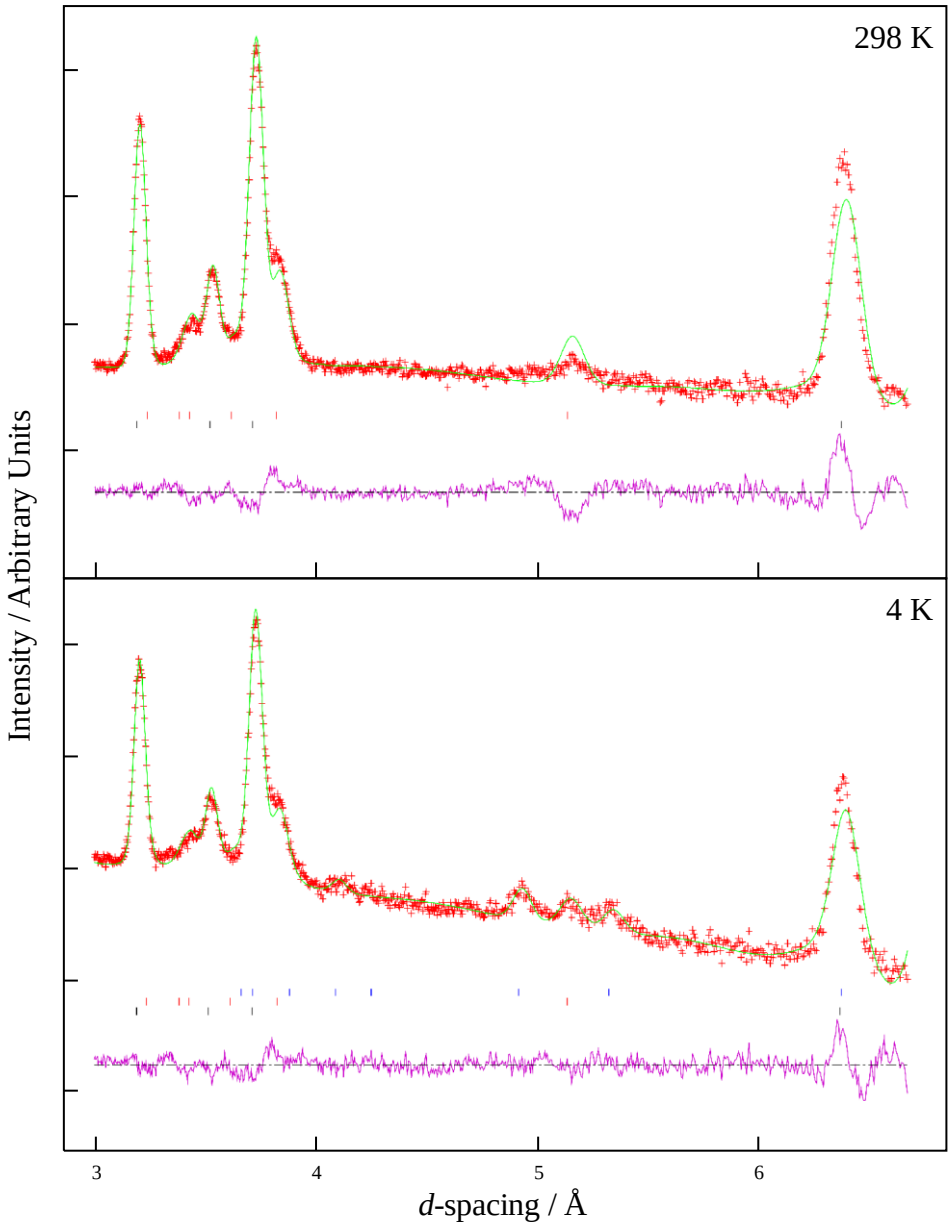

Figure 7.9: Observed, calculated, and difference plots for refinement of the structural and magnetic models of Sr_2VO_3H at 298 K (top) and 4 K (bottom) against neutron powder diffraction data collected using the POLARIS diffractometer. Red tick marks correspond to the ~28.4(4)% by weight impurity of $Sr_3V_2O_5H_2$. Blue tick marks correspond to the magnetic model.

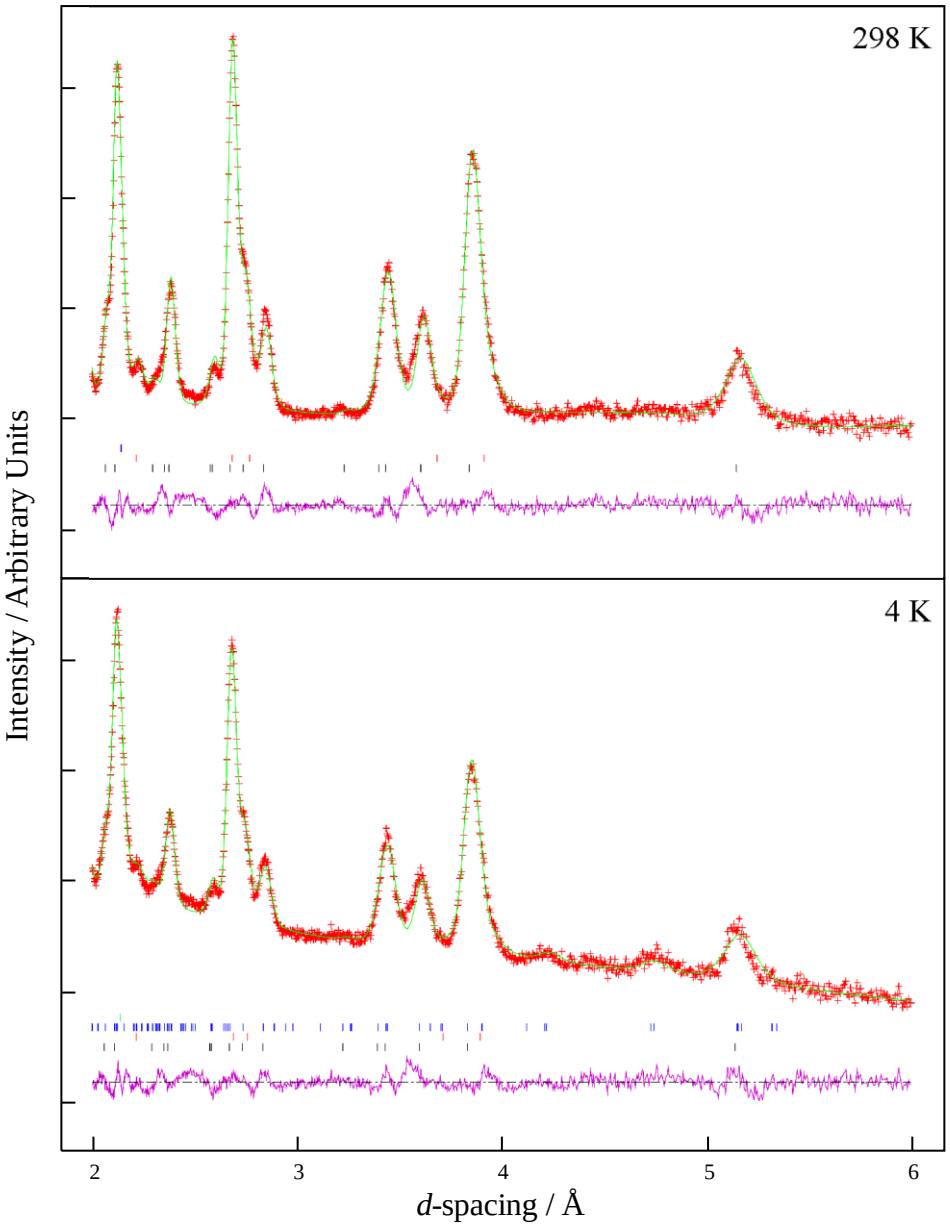

Figure 7.10: Observed, calculated, and difference plots for refinement of the structural and magnetic models of $Sr_3V_2O_5H_2$ at 298 K (top) and 4 K (bottom) against neutron powder diffraction data collected using the POLARIS diffractometer. Red tick marks correspond to the ~10.8(3)% by weight impurity of $SrVO_2H$. Blue tick marks correspond to the magnetic model. Green marks correspond to contributions from the vanadium sample holder.

7.3.5.3 Variable Temperature Neutron Powder Diffraction

Neutron powder diffraction data were collected from Sr_2VO_3H at various temperatures in order to monitor the evolution of the magnetic order. Structural and magnetic models were refined against these data to produce a plot of the ordered moment as a function of temperature, shown in Figure 7.11.

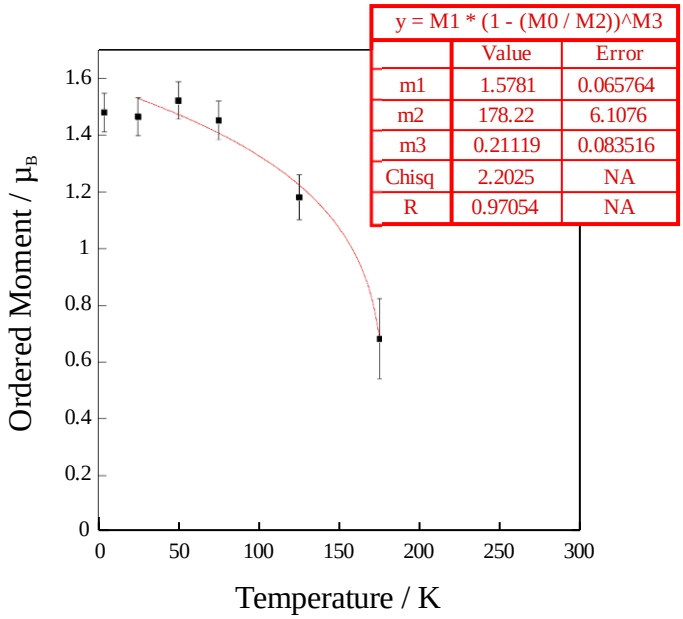

Figure 7.11: Ordered magnetic moments extracted from refinements of Sr_2VO_3H at various temperatures and their fit to a power law.

These data can be fitted to a power law of the form $I = A(1 - \frac{T}{T_N})^{\beta}$ to give the following parameters: T_N = 178(6) K, β = 0.21(8), and A = 1.58(7) μ_B.

T_N extracted from this fit matches the temperature at which the static field disappears in the μSR data (see below).

7.3.5.4 Muon-Spin Relaxation (μSR) Spectroscopy

μSR spectroscopy was collected from all three reduced $SrO(SrVO_2H)_n$ (n = 1, 2, ∞) samples contained within silver foil envelopes (thickness 25 μm) using the GPS instrument at the Swiss Muon Source, Paul Scherrer Institut, Switzerland.

All three samples exhibited oscillations in the asymmetry between forward (F) and backwards (B) detectors at low temperatures, indicating long-range magnetic order through the bulk of the sample.

Data collected from Sr_2VO_3H showed clear oscillations at low temperatures (Figure 7.12). These could be well described by

$$A(t) = A_1 \exp\left(\frac{-\sigma^2 t^2}{2}\right)\cos(2\pi\nu t) + A_2 \exp(-\lambda_2 t) + A_{nr}$$

Where the first term is due to the muons experiencing a static magnetic field B and hence oscillate at a frequency $\nu = \gamma_\mu B$ ($\gamma_\mu = 2\pi$ x 135.5 MHz / T is the muon gyromagnetic ratio), the Gaussian envelope results from the finite width of fields experienced by the muon. The second term is due to muons that experience a field distribution that is so wide that it does not give rise to oscillations (λ < 0.3 MHz and increases at lower temperatures). The third term is a non-relaxing term due to the fraction of muons polarised parallel to the local magnetic field (expected to be 1/3 in a randomly oriented powder sample) as well as due to muons stopped in the sample holder or cryostat.

Figure 7.12 shows data taken above and below T_N = 171(1) K. The rise in the non-relaxing background is evident and indicative of a breaking of symmetry. An additional oscillation in the data collected from the sample above T_N = 171(1) K is consistent with a small impurity of $Sr_3VO_5H_2$. Temperature evolution of the oscillation frequency (and thus the strength of the local magnetic field) is a good match for the size of the ordered moment extracted from variable-temperature neutron powder diffraction data (Figure 7.11).

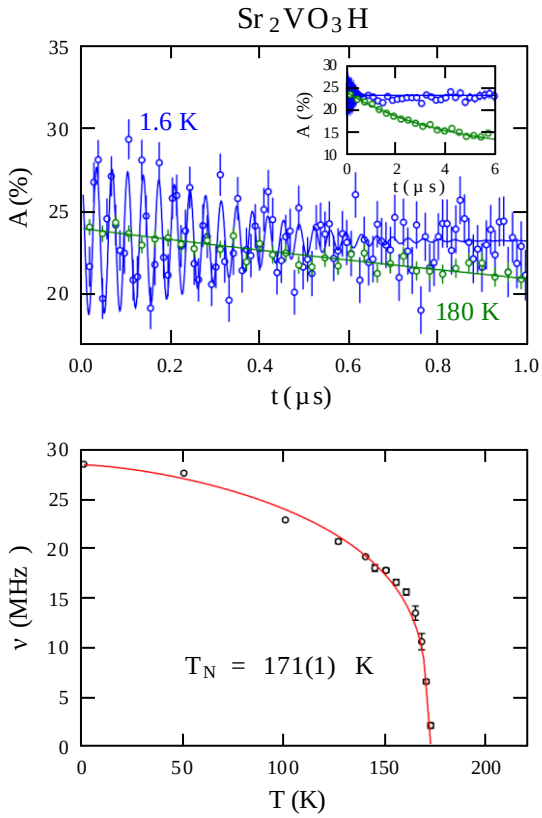

Figure 7.12: μSR asymmetry data collected from Sr_2VO_3H at 1.6 K and 180 K (top) and temperature evolution of the oscillation frequency *ν* (bottom).

Data collected from $Sr_3VO_5H_2$ and $SrVO_2H$ at low temperatures (Figure 7.13 and Figure 7.14) could be well-described by:

$$A(t) = A_1 \exp\left(\frac{-\sigma_1^2 t^2}{2}\right)\cos(2\pi\nu t) + A_2 \exp\left(\frac{-\sigma_2^2 t^2}{2}\right) + A_3 \exp\left(\frac{-\sigma_3^2 t^2}{2}\right) + A_{nr}$$

Where $\sigma_2 \leq 0.5$ MHz and $\sigma_3 >> \sigma_2$. In data collected from magnetically ordered $Sr_3VO_5H_2$, a considerable amount of asymmetry is missing, indicative of muon sites where the muon experiences a field so large that it depolarises too rapidly to be observed. The missing asymmetry is recovered on warming through T_N = 240(1) K. The fast feature seen in the data collected at 240 K is most likely due to the presence of muonium.

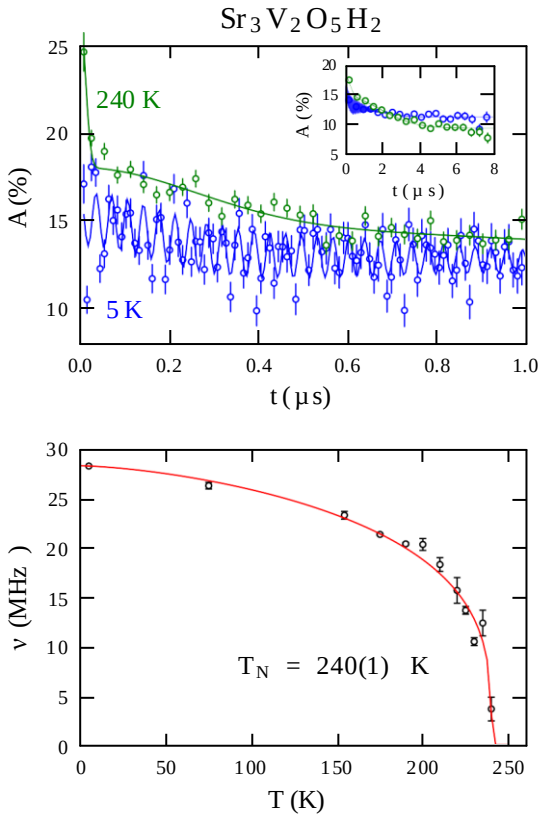

Figure 7.13: μSR asymmetry data collected from $Sr_3V_2O_5H_2$ at 5 K and 180 K (top) and temperature evolution of the oscillation frequency *ν* (bottom).

The signal observed in data collected from $SrVO_2H$ is unusual. At low temperatures oscillations are observed at slightly higher frequency than in Sr_2VO_3H and $Sr_3VO_5H_2$. These oscillations disappear sharply just below T = 80 K, despite only a minor reduction in the oscillation frequency. Furthermore, there is only a slight rise in the non-relaxing background between 5 and 100 K despite the large oscillating signal.

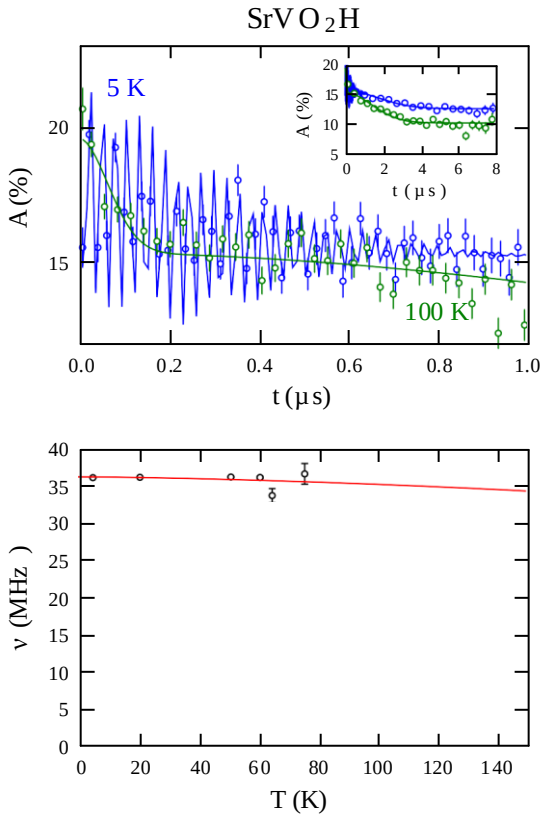

Figure 7.14: µSR asymmetry data collected from $SrVO_2H$ at 1.6 K and 180 K (top) and temperature evolution of the oscillation frequency *ν* (bottom).

7.4 Discussion

7.4.1 Synthesis of the Starting Materials

7.4.1.1 $SrO(SrVO_3)_n$ (n = 1, 2, ∞)

The formation of some $Sr_3V_2O_7$ during the high-temperature synthesis of Sr_2VO_4 is indicative of loss of SrO during the reaction. $SrVO_2H$ present in the large sample of $Sr_3V_2O_5H_2$ would result from reduction of $SrVO_3$ in the starting material, although the coincidence of peaks makes its detection difficult. A refinement of X-ray powder diffraction data collected from $Sr_3V_2O_7$ incorporating $SrVO_3$ as a secondary phase gave a fit that was statistically no better than a single phase refinement, despite the clear presence of $SrVO_2H$ following reduction.

During the synthesis of the starting materials, high temperature reaction with under flowing H_2 causes loss of some SrO leading to the formation of phases that are effectively strontium deficient.

It is only in the case of the perovskite where loss of SrO cannot be compensated by the formation of a different phase. In this case, SrO loss would result in an A-cation deficient perovskite, which would show different reduction behaviour and could account for the different reduction behaviour throughout the sample leading to the observed two-phase behaviour on reduction. The expected loss is very small, approximately 5% by weight of SrO, and thus difficult to detect via X-ray powder diffraction data.

Similar A-site deficient perovskites have been reported in the $La_{1-x}TiO_3$ system which exist for the full range $0 \leq x \leq 0.33$.[128] In this system, A-site deficiency is accompanied by oxidation of the titanium cations. Similarly, the formation of $Sr_{1-x}VO_3$ would result in the oxidation of vanadium cations.

As shown in Table 7.10, the single layer Sr_2VO_4 contains the greatest amount of secondary phase by weight. This can be accounted for by considering the synthesis conditions: prior to heating under hydrogen gas, the corresponding V^{5+} oxides are formed for the $n = 2$ and ∞ materials, but heating 2 equivalents of SrO with half an equivalent of V_2O_5 under air produces a mixture of $Sr_3V_2O_8$ and SrO. The unincorporated SrO will be more volatile than that from extended vanadium oxides, resulting in a greater loss of SrO from this sample. This observation also accounts for the inability to produce single phase materials by addition of excess $SrCO_3$, which will result in unincorporated SrO and volatilise before forming the appropriate materials.

Sample	Material Composition (by weight)
$SrVO_2H_x$	86.8(3)% $SrVO_2H$ 13.2(3)% $SrVO_3$
$Sr_2VO_3H_x$	73.1(4)% Sr_2VO_3H 26.9(4)% $Sr_3V_2O_5H_2$
$Sr_3V_2O_5H_{2x}$	89.4(3)% $Sr_3V_2O_5H_2$ 10.6(3)% $SrVO_2H$

Table 7.10: Compositions of the three vanadium oxyhydride samples from refinement against neutron powder diffraction data.

7.4.1.2 $La_{1-x}Sr_xVO_3$

Attempts to synthesise phases with composition $La_{1-x}Sr_xVO_3$ (x = 0.1, 0.2, 0.3, 0.5, 0.7) produced materials that could be indexed on the basis of multiple phases. A two-phase model refined against high-resolution laboratory X-ray powder diffraction data collected from a sample with nominal composition $La_{0.1}Sr_{0.9}VO_3$ converged to phases with composition $La_{0.15(1)}Sr_{0.85(1)}VO_3$ and $La_{0.00(1)}Sr_{1.00(1)}VO_3$.

The segregation of these materials into multiple phases indicates that a true solid solution cannot be formed for these materials. There have been previous reports by Mahajan *et al.* of the synthesis of single phase materials with composition $La_{1-x}Sr_xVO_3$ over the entire $0 \leq x \leq 1$ range.[123] However, close inspection of their data reveal broad peaks such as those observed when diffraction data was collected on a low-resolution diffractometer. Given the similarity between the lattice parameters of the phases that the materials segregate into, peak splitting is only observable in high-resolution data, and it is therefore possible that Mahajan *et al*. did not have data of sufficient quality to notice this.

In light of the segregation into multiple phases, it is not surprising that these materials show reduction behaviour that appears to be a mixture of that of $SrVO_3$ and $LaVO_3$, with the formation of a phase adopting a tetragonal structure corresponding to the strontium rich portion of the materials and a phase behaving like $LaVO_3$ corresponding to the lanthanum-rich.

7.4.2 Reduction Behaviour of $SrO(SrVO_3)_n$ (n = 1, 2, ∞)

The reduction of $SrO(SrVO_3)_n$ (n = 1, 2, ∞) with CaH_2 proceeds to form oxyhydrides with the general formula $SrO(SrVO_2H)_n$ (n = 1, 2, ∞). These adopt structures in which the vanadium atoms are in VO_4H_2 six-coordinate environments in which the hydride anions are *trans* to each other. The V–O bond lengths (1.958(1)–2.025(3) Å) in all three reduced materials are of similar lengths to those found in $LaVO_3$ (2.001–2.004 Å).[129]

In contrast to the reduction behaviour of the $SrO(SrFeO_{3-\delta})_n$ (n = 1, 2, ∞) series of phases, there appears to be no reduction to form materials containing transition metal oxidation states below 3+. In both acidic and basic solutions, V^{3+} is the most stable oxidation state.[130] It is quite possible that in all three reduced vanadium phases, the formation of an oxyhydride is due to the thermodynamic barrier to further reduction of the vanadium centres.

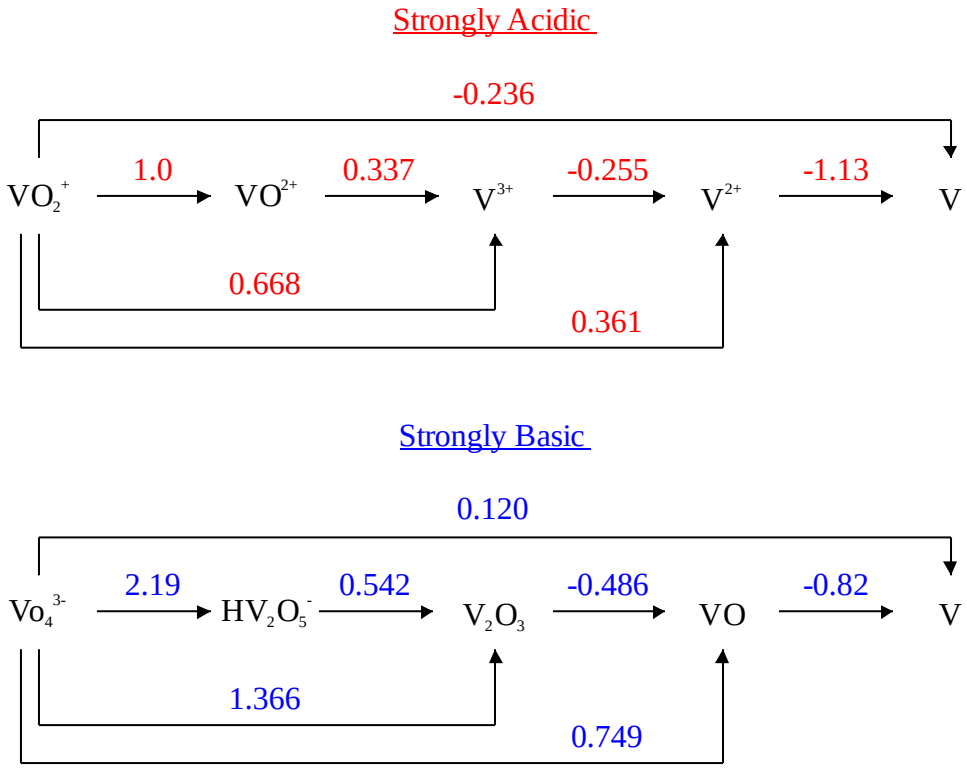

Figure 7.15: Reduction potentials of vanadium ions in solution.

To the best of our knowledge, no known extended oxides exist with vanadium oxidation states below +3 other than binary V_xO_y such as VO, indicative of the difficulty in stabilising low oxidation states of vanadium. V^{2+} has been observed in extended complex fluorides with the general formula AVF_3 (A = Na, K, Rb) and their synthesis requires highly reducing conditions: heating a mixture of VF_2 and AF at 800 °C for 30 days in vanadium-lined molybdenum tubes sealed under vacuum.[131]

Given then the apparent stability of V^{3+} it is not surprising that $LaVO_3$ cannot be topochemically reduced.

7.4.3 Comparison with other Oxyhydrides

The layered cobalt-based phases $LnSrCoO_4$ (Ln = La, Pr, Nd) can be reacted with CaH_2 at various temperatures and $Sr_3Co_2O_{7-x}$ can be reacted with CaH_2 at temperatures between 240 °C and 255 °C to form oxyhydrides.[127,132,133]

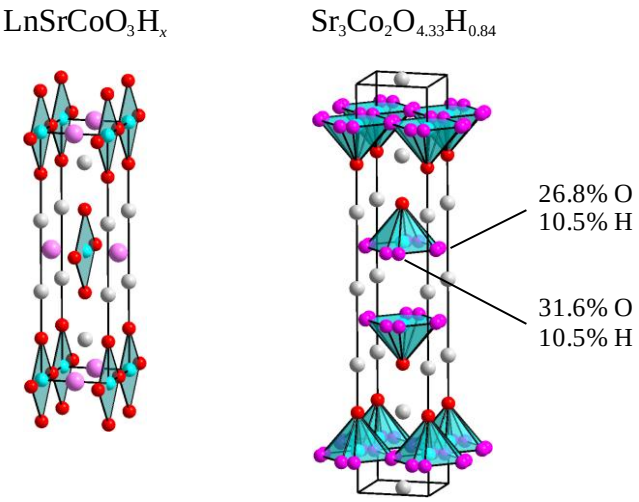

Figure 7.16: The structures of $LnSrCoO_3H_x$ (left) and $Sr_3Co_2O_{4.33}H_{0.84}$ (right).

The hydride content of the $LnSrCoO_3H_x$ series of phases can be varied by changing the nature of the Ln cation and the synthesis temperature: x = 0.80 for Ln = Nd reacted at 140 °C, x = 0.58 for Ln = Nd reacted at 100 °C, and x = 0.68 for Ln = Pr reacted at 175 °C.[132] In these

phases, the hydride anion site is partially occupied and vacancies are disordered throughout the structure.[132]

In contrast to the behaviour of the cobalt materials, the perovskite $BaTiO_3$ can be reacted with CaH_2 at temperatures $550 \leq T/\,°C \leq 580$ to form phases with composition $BaTiO_{3-x}H_x$ ($0 \leq x \leq 0.6$) in which the hydride anions are disordered throughout the structure (Figure 7.17).[119] Here too, variation of the synthesis conditions leads to materials with different compositions, although the anion sites remain fully occupied.

Unlike the cobalt-based oxyhydrides previously reported which are antiferromagnetic insulators,[127,133,134] $BaTiO_{3-x}H_x$ is a good electronic conductor (10^{-4} S cm^{-1}).[119]

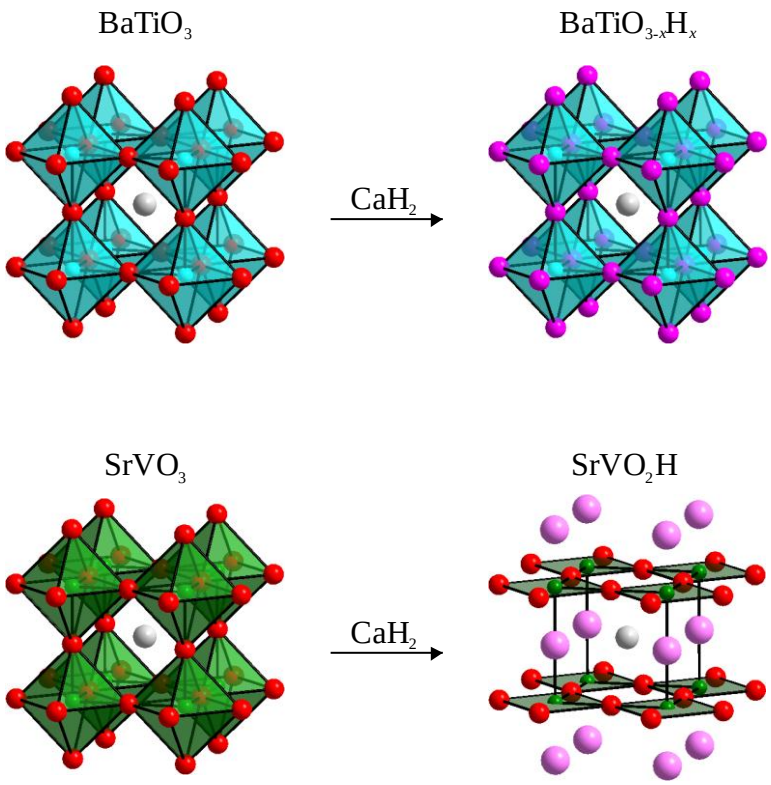

Figure 7.17: The structures of titanium and vanadium based oxyhydrides.

In contrast, the $SrO(SrVO_2H)_n$ (n = 1, 2, ∞) series of phases show no evidence of similar tunability, resulting in direct formation of a well ordered stoichiometric oxyhydride with no

indication of anion vacancies. This material represents the first example of complete substitution of an oxide anion for a hydride on one site via topochemical methods. This series represents the first example of stoichiometric oxyhydrides.

The titanium-based oxyhydrides are alone in being good electronic conductors; both $SrO(SrVO_2H)_n$ (n = 1, 2, ∞) and the cobalt-based oxychlorides show strong magnetic interactions. Both $SrVO_2H$ and $LaSrCoO_3H_{0.7}$ show long-range magnetic order in neutron powder diffraction data collected at room temperature, and the layered vanadium-based oxyhydrides reported here are coupled at room temperature despite not being fully ordered.[133]

Attempts to lanthanum-dope $SrVO_3$ were largely unsuccessful and the reduction of $CaVO_3$ is non-topochemical and does not form an extended oxyhydride. $BaVO_3$ adopts a hexagonal pervoskite structure.[135] The $SrO(SrVO_2H)_n$ (n = 1, 2, ∞) series of phases may therefore stand as singular exceptions rather than rule of vanadium reductions.

While there are a plethora of known molecular vanadium complexes with V–H bonds,[136-139] this represents the first example of an extended vanadium oxyhydride prepared by solid-state synthesis routes.

The V–H distances in $SrO(SrVO_2H)_n$ (n = 1, 2, ∞) are consistent across all three phases: 1.833(1) – 1.835(1) Å. This distance is shorter than any V–O bond distances (1.958(1)–2.025(3) Å) and the sum of the ionic radii of V^{3+} and H^- (0.78 Å and 1.46 Å respectively, sum = 2.24 Å) indicative of significant covalent character.[140,141] V^{3+} hydride complexes such as $(V[(Me_3Si)N(CH_2\text{-}CH_2N[SiMe_3])_2])_2(H)_2$ show almost identical bond lengths: 1.83(3) – 1.85(3) Å.[142] In this case, bulky chelating ligands are required to stabilise the V–H bonds.

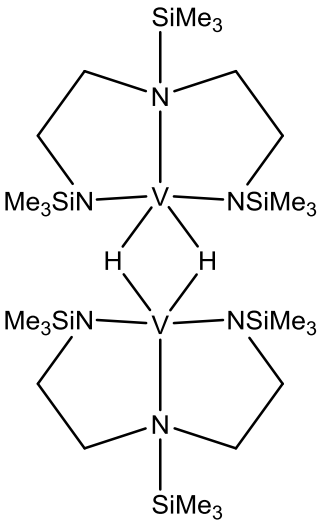

Figure 7.18: The structure of $(V[(Me_3Si)N(CH_2\text{-}CH_2N[SiMe_3])_2])_2(H)_2$.

A similarly short M–H bond distance has been previously observed in other oxyhydrides $LaSrCoO_3H_{0.7}$ (1.80174(2) Å)[133] and $Sr_3Co_2O_{4.33}H_{0.84}$ (1.901(1) Å and 1.925(1) Å)[127]. The latter contains a mixed O/H anion site, accounting for the longer bond length.[127] The short M–H distance in these compounds is owed to the large polarisability of the hydride anion.[143]

The mechanism proposed for the formation of $LaSrCoO_3H_{0.7}$ goes via the formation of a $LaSrCoO_{3.5+\delta}$ intermediate which then undergoes an essentially redox-neutral anion exchange reaction with CaH_2 to form the oxyhydride. The degree of anion exchange in this step is dependent on the pressure of hydrogen gas over the sample, allowing the composition to be tuned by varying this parameter.[132-134]

Similarly, the formation of $SrO(SrVO_2H)_n$ from $SrO(SrVO_3)_n$ is expected to proceed via a $SrO(SrVO_{2.5})_n$ intermediate containing V^{3+} cations. In the cobalt-based oxyhydrides, however, hydride anions do not fill all available anion sites, and the occupancy can be turned by varying the hydrogen pressure above the sample during synthesis.[132,134] In the

$SrO(SrVO_2H)_n$ series of phases, all anion sites are fully occupied. In these phases, V^{3+} appears to be the lowest accessible oxidation state.

7.4.4 Magnetism

All three vanadium oxyhydrides synthesised are magnetically coupled at room temperature as indicated by the very low observed magnetisation, with the layered materials undergoing transitions from 2D to 3D magnetic order at 170 K (n = 1) and 240 K (n = 2) as determined by μSR. This is in contrast to $LaVO_3$, which undergoes ordering at 140 K. A partial explanation for the unusually high ordering temperatures of the oxyhydrides can be attributed to the V–O–V angle in these phases (180° in $SrO(SrVO_2H)_n$ compared to 156.97–157.05 in $LaVO_3$).[129] The twisting present in $LaVO_3$ will serve to lower the overlap, and consequently decrease the strength of the superexchange interactions.[3]

It should be noted, however, that the V^{3+} cations in an octahedral environment will adopt a degenerate t_{2g}^2 configuration. In the absence of orbital ordering, the Goodenough-Kanamori rules[3] predict magnetic frustration arising from competing interactions; interactions between half-filled orbitals will lead to antiferromagnetism, while interactions between half-filled and empty orbitals will lead to ferromagnetism. While magnetic interactions in $LaVO_3$ are strong (θ = -665 K)[144], order only sets in in the presence of cooperative orbital ordering that lifts the degeneracy. In a D_{4h} configuration as found in $SrVO_2H$, the degeneracy is not present, and the system is consequently not frustrated allowing strong magnetic interactions a consequently high T_N.

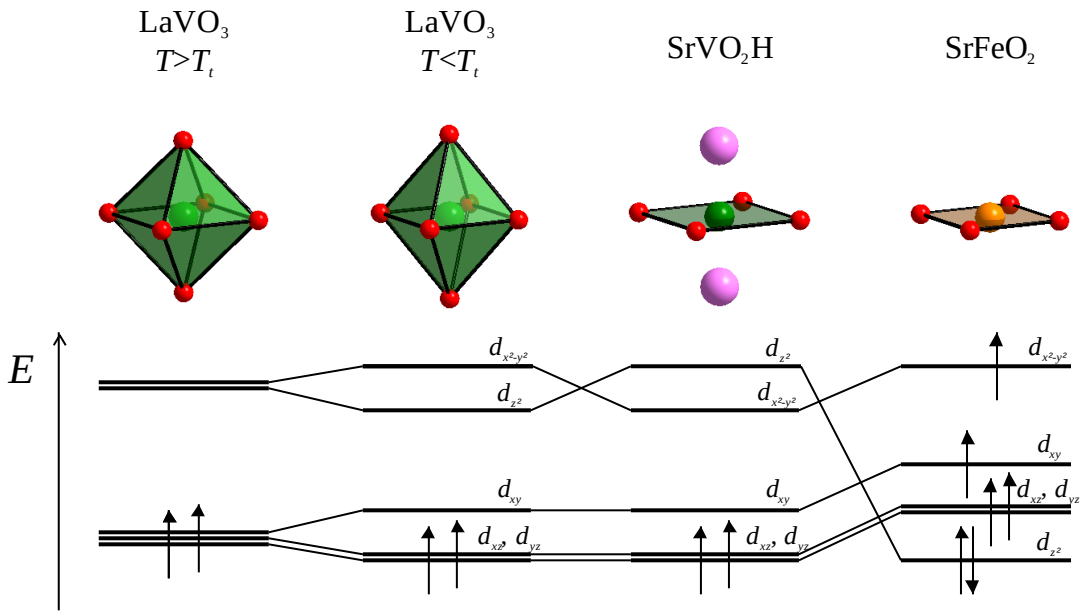

Figure 7.19: Local coordination environments and electronic structure of V^{3+} cations in $LaVO_3$ and $SrVO_2H$ and Fe^{2+} cations in $SrFeO_2$.

Magnetic interactions within the VO_2 planes can therefore be understood simply on the basis of antiferromagnetic π-type interactions mediated by V d_{xz} or d_{yz} and O 2*p* orbitals.

Previously synthesised oxyhydrides with the general formula $LnSrCoO_{3+x}H_y$ (Ln = La, Nd, Pr) display high magnetic ordering temperatures (380 K < T_N < 445 K).[132-134] In these materials, DFT calculations indicate that the hydride-mediated σ-superexchange is comparable in strength to the strongest metal-oxide superexchange interaction.[134]

However, it is hard to rationalise the involvement of hydride ions in the out-of-plane interactions present in $SrVO_2H$. There are no occupied vanadium orbitals with the correct symmetry to interact with the H 1*s* orbital. Interactions between empty orbitals are expected to be antiferromagnetic, but weakly so, and would not account for the high ordering temperature observed in the vanadium oxyhydrides.[3]

The electronic structure of the vanadium cations can be likened to that of iron cations in $SrFeO_2$ in that both species contain $(d_{xz}, d_{yz})^2$ orbitals. In $SrFeO_2$, direct interactions between

these half-occupied orbitals is responsible the strong out of plane magnetic interactions that lead to the high ordering temperature (T_N = 473 K).[55,82]

The high ordering temperature of the vanadium oxyhydrides can therefore be rationalised as arising from similar direct interactions between vanadium d_{xz} and d_{yz} orbitals. In these materials, the hydride anions are likely to play a very minor role in the magnetic properties as there no occupied orbitals of the appropriate symmetry to interact with.

The strong damping at ~80 K in the oscillations observed in μSR data collected from $SrVO_2H$ cannot be readily explained. A number of structural models with expanded unit cells could be used to account for the position of the extra diffraction features in the neutron powder diffraction data, but none could account for both the intensity and the observed composition from chemical titration. Only a magnetic unit cell can be used to account for both. In addition, there are no noticeable differences between the diffraction intensities of these extra features in data collected from a sample at 298 K and one at 4 K. If the onset of magnetic order was indeed at 80 K, additional features or intensity due to magnetic scattering would be apparent in the low temperature diffraction data. Additionally, no event is seen in the magnetisation data collected as a function of temperature.

Sample integrity was confirmed via X-ray powder diffraction data collected after the μSR experiment, ruling out the possibility of reoxidation. The observed oscillations are also inconsistent with implantation solely in the minority phase. The source of the damping therefore remains somewhat of a mystery. One possible explanation is a small reorientation of the electronic spins, which may be sufficient to cause enough broadening to obscure the oscillations in the asymmetry. Investigation of this transition will require additional investigation. The similar oscillation frequency observed in all three samples is, however,

consistent with muon implantation in similar sites and experiencing similar internal fields in all three samples.

In the layered materials (n = 1, 2), the onset of 3-dimensional antiferromagnetic ordering occurs at a lower temperature compared to the $n = \infty$ phase. Above 170 K (n = 1) or 240 K (n = 2), the materials are expected to show strong coupling between the magnetic centres as evidenced by the low magnetisation. Ordering within the layers occurs via the same superexchange interactions as in the $n = \infty$ material and are therefore expected to be of similar strength. However, the introduction of non-magnetic SrO layers means that ordering between the layers must occur via some other mechanism. The lack of features indicative of long-range magnetic order in neutron powder diffraction data collected from samples at 298 K suggests that at these temperatures, there is ordering within each layer but not between layers.

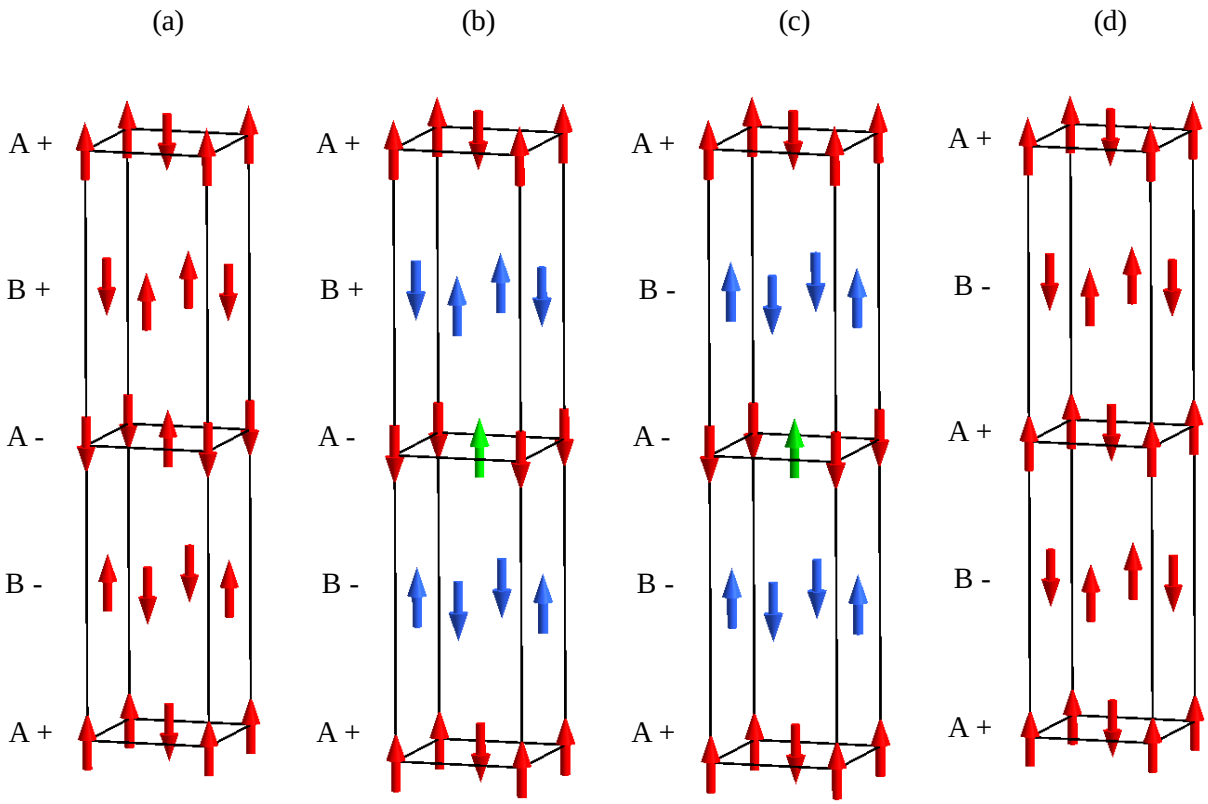

Figure 7.20: The possible orientations of the magnetic moments in Sr_2VO_3H.

Ruddlesden-Popper phases have two types of layers related by a (0, 1/2, 1/2) translation. If each layer is antiferromagnetically ordered, it can adopt one of two possible configurations (Figure 7.20 (a)). The orientation of each layer can be disordered despite all the moments within each layer being antiferromagnetically ordered, which would lead to a lack of features in neutron-powder diffraction data and a low observed moment. The two possible orientations of any one layer can be related by a (1/2, 1/2, 0) translation.

An additional complication arises from the fact that adjacent layers present the same 'coordination environment' regardless of whether or not they are ordered: as shown in Figure 7.20 (b) and (c), the green arrow is surrounded by four 'up' and four 'down' moments (the blue arrows) from the layers above, regardless of whether those layers are parallel or antiparallel to each other or whether all blue spins are flipped. Adjacent layers cannot direct

each other's orientations as they are fundamentally indistinguishable. In order for long range magnetic order to set in, A layers need to couple to other A layers, the next nearest ones. In Figure 7.20 (d), the observed magnetic structure would be identical if all spins were flipped, or all spins on one type of layer only were flipped.

The observed onset of 3-dimensional ordering is consistent with the decrease in dimensionality in these materials. This view is consistent with the decrease in T_N for the analogous reduced iron-containing materials $SrFeO_2$ ($n = \infty$, $T_N = 473$ K), $Sr_3Fe_2O_4Cl_2$ ($n = 2$, $T_N = 378$ K), and Sr_2FeO_3 ($n = 1$, $T_N = 190$ K).[20,55,88]

7.5 Conclusion

The topochemical reduction of the $SrO(SrVO_3)_n$ ($n = 1, 2, \infty$) series of phases was carried out using CaH_2 as a solid state reducing agent to produce novel oxyhydrides with composition $SrO(SrVO_2H)_n$ ($n = 1, 2, \infty$). In these materials, the vanadium cations are in an octahedral coordination environment with hydride ions *trans* to each other. Oxidative titration was used to determine the vanadium cations are in the +3 oxidation state, and thefore the hydride positions are fully occupied. These phases represent the first example of topochemically prepared vanadium-based oxyhydrides.

In these materials, strong interactions between the half-occupied d_{xz} and d_{yz} orbitals leads to high antiferromagnetic ordering temperatures in a manner similar to the iron-based $SrO(SrFeO_2)_n$ ($n = 1, 2, \infty$) series of phases.

Chapter 8 Conclusions

8.1 Summary

The work presented herein concerns the topochemical synthesis of novel complex transition metal oxides, oxyhalides, and oxyhydrides:

NaH can be used as a solid-state reducing agent to effect the reduction of $Sr_3Co_2O_5Cl_2$ and form $Sr_3Co_2O_4Cl_2$. This was an extension of previous work performed on the reduction of the $Sr_3(Fe_{1-x}Co_x)_2O_5Cl_2$ series of phases. This demonstrates the ability of heteroanions to direct topochemical reduction reactions.

$Sr_3Co_2O_4Cl_2$ displays unusual electronic and magnetic properties, such as Jahn-Teller distortion from non-bonding degenerate orbitals, and ferromagnetic coupling between adjacent CoO_2 square-planar sheets that cannot be readily explained. This demonstrates the ability of topochemical reduction reactions can be used to prepare phases where unusual combinations of oxidation states and coordination environments give rise to unusual properties.

The reduction of $Sr(Ru_xFe_{1-x})O_3$, $Sr_2(Ru_{0.5}Fe_{0.5})O_4$, and $Sr_3(Ru_{0.5}Fe_{0.5})_2O_7$ using CaH_2 extends previous work on reduction using binary metal hydrides into 4*d* transition metal oxides, a previously unexplored area. This work demonstrates not only the ability to prepare previously unobserved oxidation state and coordination environment combinations (square-planar Ru^{2+} in an extended oxide), but also the ability to stabilise low-valent ruthenium centres through coupling to a robust framework.

Low-temperature oxidation using CuF_2 as a solid state fluoride source was performed on materials with composition $Sr_3(Ru_{0.5}M_{0.5})_2O_7$ (M = Ti, Mn, Fe). In the case of M = Mn and Ti, materials with composition $Sr_3(Ru_{0.5}M_{0.5})_2O_7F_2$ are produced in which the ruthenium

centres are oxidised to Ru^{6+}. In combination with the aforementioned reduction of ruthenium-based complex oxides, this demonstrates the rich redox chemistry of ruthenium oxides, particularly in combination with other transition metals which can stabilise certain oxidation states.

Reaction of the $SrO(SrVO_3)_n$ (n = 1, 2, ∞) series of phases with CaH_2 results in the formation of phases with composition $SrO(SrVO_2H)_n$ (n = 1, 2, ∞). Formation of the oxyhydrides is not unprecedented,[119,127,133] but these phases represent the first example of a 1:1 substitution of O^{2-} for H^- in extended oxides. The high magnetic ordering temperature arises from strong interactions between (d_{xy}, d_{yz}) orbitals in a manner analogous to the reduced iron-containing phases $SrO(SrFeO_2)_n$.

Previous topochemical chemistry of this type had been focussed on Mn-Ni-based complex transition metal oxides. The successful topochemical modification of ruthenium-based and vanadium-based complex transition metal oxides indicates that these techniques can be extended to a wider range of materials to produce phases that display a wide array of interesting electronic and magnetic properties.

8.2 Reduction vs. Oxyhydride Formation

One of the key factors required for the successful development of synthesis by rational design is the ability to predict the end products of a given reaction with a degree of accuracy. So far, reduction of complex transition metal oxides with sodium hydride has solely led to the formation of oxygen-deficient phases,[14,16,92] whereas reduction with calcium hydride has led both to oxygen deintercalation[42,87] (as observed in the reduction of $Sr(Ru_xFe_{1-x})O_3$) and the formation of oxyhydride materials[127,134] (as observed in the reduction of $SrO(SrVO_3)_n$ (n = 1, 2, ∞)).

The effect of differing reducing agents on the nature of the final products can be illustrated by the reduction of $LaSrCoO_4$, which forms $LaSrCoO_{3.5+x}$ on reduction with NaH, and $LaSrCoO_3H_{0.7}$ on reduction with CaH_2.[92,133]

Examples of transition metal oxyhydrides are relatively rare in the literature, and as such a full understanding of the factors affecting their formation as opposed to simple oxygen deintercalation remains elusive. However, they can mostly be broken down into two groups: early transition metal oxyhydrides and cobalt-based oxyhydrides.

The formation of early transition metal oxyhydrides, such as $BaTiO_{3-x}H_x$ and $SrO(SrVO_3)_n$ (n = 1, 2, ∞) can be rationalised by noting that early transition metals are fairly electropositive. As such, low oxidation states are energetically difficult to attain, and formation of an oxyhydride is preferable to further reduction.

There are a number of Co-based oxyhydrides known.[127,133] Co(I) has been previously observed in extended complex metal oxides.[16] Additionally, the reduction of cobalt to the elemental metal is facile, as observed during reductive thermogravimetry under a 5% H_2 / N_2 mixture. The formation of oxyhydrides cannot be rationalised using the same arguments as for the early transition metals. Mn, Fe, and Ni-based complex transition metal oxides have not been previously observed to form oxyhydrides, only oxygen-deficient phases on reduction. Cobalt appears to be unique among the late transition metals in this regard.

H_2 gas alone is not enough to form oxyhydrides, as evidenced by the formation of $SrO(SrVO_3)_n$ (n = 1, 2, ∞) phases under pure H_2 at temperatures greater than 1000 °C rather than the oxyhydride. However, gas phase H_2 must play some role as reduction under conditions where the H_2 evolved is allowed to flow into a stream of argon does not produce the oxyhydride.

A ready mechanism to explain the formation of an oxyhydride rather than just oxide deintercalation does not yet exist, but the formation of the $SrO(SrVO_2H)_n$ (n = 1, 2, ∞) series of phases suggests that other early transition metal oxides should show similar behaviour, and would therefore be worthy of investigation.

8.3 Future Work

The work described in this thesis suggests a number of future avenues of research:

1. The presence of heteroatoms in the reduction of $Sr_3Co_2O_5Cl_2$ has directed the deintercalation of certain oxide anions and led to the formation of a phase with an unusual arrangement of cobalt centres. The nature of the interaction between the square-planar CoO_2 layers that leads to the structural distortion and observed magnetic behaviour is not well understood and worthy of further study. In addition, heteroatoms can be used to direct reduction and prepare materials with previously unreported oxidation state and coordination combinations.
2. The reductions of $Sr(Ru_xFe_{1-x})O_3$, $Sr_2(Ru_{0.5}Fe_{0.5})O_4$, and $Sr_3(Ru_{0.5}Fe_{0.5})_2O_7$ are the first reported examples of topochemical reduction of 4*d* transition metals using binary metals hydrides. While the reduction of the all-Ru phases $SrRuO_3$ and its layered analogues was unsuccessful, the work presented here shows that unusual low-valent oxidation states are accessible via these methods when suitably stabilised. Substituting other elements for iron in the starting materials and their effect on the reaction products would be worthy of investigation, as would analogous work on other 4*d* and 5*d* transition metal oxides.
3. The vanadium based oxyhydrides are not only the first examples of stoichiometric oxyhydrides, but also the first square-planar d^2 systems in extended transition metal oxides. Study of the reaction mechanism could shed light on the formation of the

other known oxyhydrides. Additionally, the successful reduction of $SrO(SrVO_3)_n$ (n = 1, 2, ∞) phases shows that binary metal hydrides can be used to prepare novel oxides of even very electropositive elements, paving the way for future work on the reduction of early transition metal oxides.

Appendix 1 – Table of Figures

Appendix 2 – Bibliography

(1) Cox, P. A. *Transition Metal Oxides: An Introduction to Their Electronic Structure and Properties*; OUP Oxford, 2010.

(2) Rao, C. N. R.; Raveau, B. *Transition Metal Oxides: Structure, Properties, and Synthesis of Ceramic Oxides*; Wiley, 1998.

(3) Goodenough, J. B. *Magnetism and the Chemical Bond*; Wiley, 1948.

(4) Pena, M.; Fierro, J. *Chemical Reviews* **2001**, *101*, 1981.

(5) Ishihara, T. *Perovskite Oxide for Solid Oxide Fuel Cells*; Springer London, Limited, 2009.

(6) Dawber, M.; Rabe, K.; Scott, J. *Reviews of modern physics* **2005**, *77*, 1083.

(7) Tomaszewski, P. *Wroclaw* **2002**, *1*, 1.

(8) Goldschmidt, V. *Berichte der deutschen chemischen Gesellschaft (A and B Series)* **1927**, *60*, 1263.

(9) Goldschmidt, V. M. *Naturwissenschaften* **1926**, *14*, 477.

(10) Woodward, P. *Acta Crystallographica Section B* **1997**, *53*, 32.

(11) Cox, P. A. *The Electronic Structure and Chemistry of Solids*; Oxford University Press, 1987.

(12) Moruzzi, V. L.; Marcus, P. M.; Schwarz, K.; Mohn, P. *Physical Review B* **1986**, *34*, 1784.

(13) Norman, M. R.; Pépin, C. *Reports on Progress in Physics* **2003**, *66*, 1547.

(14) Hayward, M. A.; Green, M. A.; Rosseinsky, M. J.; Sloan, J. *J. Am. Chem. Soc.* **1999**, *121*, 8843.

(15) Dixon, E.; Hadermann, J.; Ramos, S.; Goodwin, A. L.; Hayward, M. A. *J. Am. Chem. Soc.* **2011**, *133*, 18397.

(16) Seddon, J.; Suard, E.; Hayward, M. A. *J. Am. Chem. Soc.* **2010**, *132*, 2802.

(17) Gillie, L. J.; Wright, A. J.; Hadermann, J.; Van Tendeloo, G.; Greaves, C. *Journal of Solid State Chemistry* **2003**, *175*, 188.

(18) Dann, S. E.; Weller, M. T.; Currie, D. B. *Journal of Solid State Chemistry* **1992**, *97*, 179.

(19) Kageyama, H.; Watanabe, T.; Tsujimoto, Y.; Kitada, A.; Sumida, Y.; Kanamori, K.; Yoshimura, K.; Hayashi, N.; Muranaka, S.; Takano, M.; Ceretti, M.; Paulus, W.; Ritter, C.; André, G. *Angewandte Chemie International Edition* **2008**, *47*, 5740.

(20) Dixon, E.; Hayward, M. A. *Inorganic Chemistry* **2010**, *49*, 9649.

(21) Dixon, E.; Hayward, M. A. *Inorganic Chemistry* **2011**, *50*, 7250.

(22) Hubbard, J. *Proceedings of the Royal Society of London. Series A. Mathematical and Physical Sciences* **1963**, *276*, 238.
(23) Wollan, E. O.; Koehler, W. C. *Physical Review* **1955**, *100*, 545.
(24) Poeppelmeier, K. R.; Leonowicz, M. E.; Longo, J. M. *Journal of Solid State Chemistry* **1982**, *44*, 89.
(25) Tokura, Y. *Colossal Magnetoresistive Oxides*; Gordon and Breach Science Publishers, 2000.
(26) Cava, R. J. *Dalton Transactions* **2004**, *0*, 2979.
(27) Wold, A.; Dwight, K. In *Solid State Chemistry*; Springer Netherlands: 1993, p 90.
(28) Goodenough, J. B. *Progress in Solid State Chemistry* **1971**, *5*, 145.
(29) Maeno, Y.; Rice, T. M.; Sigrist, M. *Physics Today* **2001**, *54*, 42.
(30) Huang, Q.; Soubeyroux, J. L.; Chmaissem, O.; Sora, I. N.; Santoro, A.; Cava, R. J.; Krajewski, J. J.; Peck Jr, W. F. *Journal of Solid State Chemistry* **1994**, *112*, 355.
(31) Nakatsuji, S.; Maeno, Y. *Physical Review Letters* **2000**, *84*, 2666.
(32) Cao, G.; Bolivar, J.; McCall, S.; Crow, J. E.; Guertin, R. P. *Physical Review B* **1998**, *57*, R11039.
(33) Cava, R. J.; Batlogg, B.; Kiyono, K.; Takagi, H.; Krajewski, J. J.; Peck, W. F., Jr.; Rupp, L. W., Jr.; Chen, C. H. *Physical Review B* **1994**, *49*, 11890.
(34) Greaves, C.; Francesconi, M. G. *Current Opinion in Solid State and Materials Science* **1998**, *3*, 132.
(35) Almamouri, M.; Edwards, P. P.; Greaves, C.; Slaski, M. *Nature* **1994**, *369*, 382.
(36) Slater, P. R.; Hodges, J. P.; Francesconi, M. G.; Edwards, P. P.; Greaves, C.; Gameson, I.; Slaski, M. *Physica C: Superconductivity* **1995**, *253*, 16.
(37) Slater, P. R.; Hodges, J. P.; Francesconi, M. G.; Edwards, P. P.; Greaves, C.; Gameson, I.; Slaski, M. *Physica C* **1995**, *253*, 16.
(38) Slater, P. R.; Edwards, P. P.; Greaves, C.; Gameson, I.; Francesconi, M. G.; Hodges, J. P.; Almamouri, M.; Slaski, M. *Physica C* **1995**, *241*, 151.
(39) Li, R. K.; Greaves, C. *Physical Review B* **2000**, *62*, 3811.
(40) Pechini, M. P. *US Patent* **1967**.
(41) Adkin, J. J.; Hayward, M. A. *Inorganic Chemistry* **2008**, *47*, 10959.
(42) O'Malley, M.; Lockett, M. A.; Hayward, M. A. *Journal of Solid State Chemistry* **2007**, *180*, 2851.
(43) Sears, V. F. *Neutron News* **1992**, *3*, 26.
(44) *http://www.ill.eu/instruments-support/instruments-groups/instruments/d2b/*.
(45) *http://www.isis.stfc.ac.uk/about-isis/how-isis-works6313.html*.

(46) http://www.isis.stfc.ac.uk/instruments/polaris/polaris4643.html.
(47) Rietveld, H. *Journal of Applied Crystallography* **1969**, *2*, 65.
(48) Larson, A. C.; Von Dreele, R. B. *Los Alamos National Laboratory Report LAUR* **1994**, 86.
(49) Young, R. A. *The Rietveld Method* **1995**.
(50) Thompson, P.; Cox, D. E.; Hastings, J. B. *Journal of Applied Crystallography* **1987**, *20*, 79.
(51) Dent, A. J.; Cibin, G.; Ramos, S.; Smith, A. D.; Scott, S. M.; Varandas, L.; Pearson, M. R.; Krumpa, N. A.; Jones, C. P.; Robbins, P. E. *Journal of Physics: Conference Series* **2009**, *190*, 012039.
(52) Walker, L. R.; Wertheim, G. K.; Jaccarino, V. *Physical Review Letters* **1961**, *6*, 98.
(53) Brese, N. E.; Okeeffe, M. *Acta Crystallogr. Sect. B-Struct. Commun.* **1991**, *47*, 192.
(54) Brown, I. D.; Altermatt, D. *Acta Crystallogr. Sect. B-Struct. Commun.* **1985**, *41*, 244.
(55) Tsujimoto, Y.; Tassel, C.; Hayashi, N.; Watanabe, T.; Kageyama, H.; Yoshimura, K.; Takano, M.; Ceretti, M.; Ritter, C.; Paulus, W. *Nature* **2007**, *450*, 1062.
(56) Bréard, Y.; Michel, C.; Hervieu, M.; Studer, F.; Maignan, A.; Raveau, B. B. *Chemistry of Materials* **2002**, *14*, 3128.
(57) Dann, S. E.; Weller, M. T. *Journal of Solid State Chemistry* **1995**, *115*, 499.
(58) Veith, G. M.; Chen, R. J.; Popov, G.; Croft, M.; Shokh, Y.; Nowik, I.; Greenblatt, M. *Journal of Solid State Chemistry* **2002**, *166*, 292.
(59) Viciu, L.; Zandbergen, H. W.; Xu, Q.; Huang, Q.; Lee, M.; Cava, R. J. *Journal of Solid State Chemistry* **2006**, *179*, 500.
(60) Seinberg, L.; Yamamoto, T.; Tassel, C. d.; Kobayashi, Y.; Hayashi, N.; Kitada, A.; Sumida, Y.; Watanabe, T.; Nishi, M.; Ohoyama, K.; Yoshimura, K.; Takano, M.; Paulus, W.; Kageyama, H. *Inorganic Chemistry* **2011**, *50*, 3988.
(61) Grenier, J.-C.; Ghodbane, S.; Demazeau, G.; Pouchard, M.; Hagenmuller, P. *Materials Research Bulletin* **1979**, *14*, 831.
(62) Knee, C. S.; Field, M. A. L.; Weller, M. T. *Solid State Sciences* **2004**, *6*, 443.
(63) McGlothlin, N.; Ho, D.; Cava, R. J. *Materials Research Bulletin* **2000**, *35*, 1035.
(64) Knee, C. S.; Weller, M. T. *Physical Review B* **2004**, *70*, 144406.
(65) Smura, C. F.; Parker, D. R.; Zbiri, M.; Johnson, M. R.; Gál, Z. A.; Clarke, S. J. *J. Am. Chem. Soc.* **2011**, *133*, 2691.
(66) Xiang, H. J.; Wei, S.-H.; Whangbo, M. H. *Physical Review Letters* **2008**, *100*, 167207.

(67) Longo, J. M.; Raccah, P. M. *Journal of Solid State Chemistry* **1973**, *6*, 526.

(68) Backes, G.; Reinen, D. *Zeitschrift für anorganische und allgemeine Chemie* **1975**, *418*, 217.

(69) Clarke, S. J.; Fowkes, A. J.; Harrison, A.; Ibberson, R. M.; Rosseinsky, M. J. *Chemistry of Materials* **1998**, *10*, 372.

(70) McQueen, T. M.; Stephens, P. W.; Huang, Q.; Klimczuk, T.; Ronning, F.; Cava, R. J. *Physical Review Letters* **2008**, *101*, 166402.

(71) Cwik, M.; Lorenz, T.; Baier, J.; Müller, R.; André, G.; Bourée, F.; Lichtenberg, F.; Freimuth, A.; Schmitz, R.; Müller-Hartmann, E.; Braden, M. *Physical Review B* **2003**, *68*, 060401.

(72) Kitchen, H. J.; Saratovsky, I.; Hayward, M. A. *Dalton Transactions* **2010**, *39*, 6098.

(73) Zhou, J. S.; Alonso, J. A.; Han, J. T.; Fernández-Díaz, M. T.; Cheng, J. G.; Goodenough, J. B. *Journal of Fluorine Chemistry* **2011**, *132*, 1117.

(74) Herdtweck, E.; Babel, D. *Zeitschrift für anorganische und allgemeine Chemie* **1981**, *474*, 113.

(75) Denis Romero, F.; Coyle, L.; Hayward, M. A. *J. Am. Chem. Soc.* **2012**, *134*, 15946.

(76) Battle, P. D.; Gibb, T. C.; Jones, C. W.; Studer, F. *Journal of Solid State Chemistry* **1989**, *78*, 281.

(77) Jones, C. W.; Battle, P. D.; Lightfoot, P.; Harrison, W. T. A. *Acta Crystallographica Section C* **1989**, *45*, 365.

(78) Ordejón, P.; Artacho, E.; Soler, J. M. *Physical Review B* **1996**, *53*, R10441.

(79) Emilio, A.; Anglada, E.; Diéguez, O.; Gale, J. D.; García, A.; Junquera, J.; Martin, R. M.; Ordejón, P.; Pruneda, J. M.; Sánchez-Portal, D.; Soler, J. M. *Journal of Physics: Condensed Matter* **2008**, *20*, 064208.

(80) Perdew, J. P.; Burke, K.; Ernzerhof, M. *Physical Review Letters* **1996**, *77*, 3865.

(81) Troullier, N.; Martins, J. L. *Physical Review B* **1991**, *43*, 1993.

(82) Pruneda, J. M.; Iniguez, J.; Canadell, E.; Kageyama, H.; Takano, M. *Physical Review B* **2008**, *78*.

(83) Greenwood, N. N.; Earnshaw, A.; Elsevier: 1998.

(84) Lee, J. P.; Ke, Z. F.; Ramirez, M. A.; Gunnoe, T. B.; Cundari, T. R.; Boyle, P. D.; Petersen, J. L. *Organometallics* **2009**, *28*, 1758.

(85) Askevold, B.; Khusniyarov, M. M.; Herdtweck, E.; Meyer, K.; Schneider, S. *Angew. Chem.-Int. Edit.* **2010**, *49*, 7566.

(86) Chang, J.; Lee, K.; Jung, M. H.; Kwon, J.-H.; Kim, M.; Kim, S.-K. *Chemistry of Materials* **2011**, *23*, 2693.

(87) Denis Romero, F.; Burr, S.; McGrady, J. E.; Gianolio, D.; Cibin, G.; Hayward, M. A. *J. Am. Chem. Soc.* **2013**, *135*, 1838.

(88) Tassel, C.; Seinberg, L.; Hayashi, N.; Ganesanpotti, S.; Ajiro, Y.; Kobayashi, Y.; Kageyama, H. *Inorganic Chemistry* **2013**, *52*, 6096.

(89) Battle, P. D.; Bollen, S. K.; Powell, A. V. *Journal of Solid State Chemistry* **1992**, *99*, 267.

(90) Müller-Buschbaum, H.; Wilkens, J. *Zeitschrift für anorganische und allgemeine Chemie* **1990**, *591*, 161.

(91) Huang, Q.; Lynn, J. W.; Erwin, R. W.; Jarupatrakorn, J.; Cava, R. J. *Physical Review B* **1998**, *58*, 8515.

(92) Hayward, M. A.; Rosseinsky, M. J. *Chemistry of Materials* **2000**, *12*, 2182.

(93) Hayward, M. A. *Chemistry of Materials* **2005**, *17*, 670.

(94) Greatrex, R.; Greenwood, N. N.; Lal, M. *Materials Research Bulletin* **1980**, *15*, 113.

(95) Zhou, X. Z.; Raudsepp, M.; Pankhurst, Q. A.; Morrish, A. H.; Luo, Y. L.; Maartense, I. *Physical Review B* **1987**, *36*, 7230.

(96) Haynes, W. M.; Lide, D. R.; Bruno, T. J. *CRC Handbook of Chemistry and Physics 2012-2013*; CRC Press, 2012.

(97) Denis Romero, F.; Gianolio, D.; Cibin, G.; Bingham, P. A.; d'Hollander, J.-C.; Forder, S. D.; Hayward, M. A. *Inorganic Chemistry* **2013**, *52*, 10920.

(98) Chevalier, B.; Tressaud, A.; Lepine, B.; Amine, K.; Dance, J. M.; Lozano, L.; Hickey, E.; Etourneau, J. *Physica C* **1990**, *167*, 97.

(99) Gallon, D. J.; Battle, P. D.; Blundell, S. J.; Burley, J. C.; Coldea, A. I.; Cussen, E. J.; Rosseinsky, M. J.; Steer, C. *Chemistry of Materials* **2002**, *14*, 3976.

(100) Dass, R. I.; Yan, J. Q.; Goodenough, J. B. *Physical Review B* **2004**, *69*, 094416.

(101) Simon Case, G.; L. Hector, A.; Levason, W.; L. Needs, R.; F. Thomas, M.; T. Weller, M. *Journal of Materials Chemistry* **1999**, *9*, 2821.

(102) Greis, O.; Petzel, T. *Zeitschrift für anorganische und allgemeine Chemie* **1974**, *403*, 1.

(103) Slater, P. R.; Gover, R. K. B. *Journal of Materials Chemistry* **2002**, *12*, 291.

(104) Renard, C.; Daviero-Minaud, S.; Abraham, F. *Journal of Solid State Chemistry* **1999**, *143*, 266.

(105) Takeda, T.; Nagata, M.; Kobayashi, H.; Kanno, R.; Kawamoto, Y.; Takano, M.; Kamiyama, T.; Izumi, F.; Sleight, A. W. *Journal of Solid State Chemistry* **1998**, *140*, 182.

(106) Fischer, D.; Hoppe, R.; Mogare, K. M.; Jansen, M. *Zeitschrift fuer Naturforschung, Teil B. Anorganische Chemie, Organische Chemie* **2005**, *60*, 1113.

(107) Shikano, M.; Kremer, R. K.; Ahrens, M.; Koo, H. J.; Whangbo, M. H.; Darriet, J. *Inorganic Chemistry* **2003**, *43*, 5.

(108) Fischer, D.; Hoppe, R. *Journal of Solid State Chemistry* **1992**, *96*, 7.

(109) Weller, M. T.; Skinner, S. J. *Acta Crystallographica Section C* **1999**, *55*, 154.

(110) Knyazev, A. V.; Chernorukov, N. G.; Bulanov, E. N. *Materials Chemistry and Physics* **2012**, *132*, 773.

(111) Aikens, L. D.; Gillie, L. J.; Li, R. K.; Greaves, C. *Journal of Materials Chemistry* **2002**, *12*, 264.

(112) Sullivan, E.; Gillie, L. J.; Hadermann, J.; Greaves, C. *Materials Research Bulletin*.

(113) Slater, P. R.; Hodges, J. P.; Francesconi, M. G.; Greaves, C.; Slaski, M. *Journal of Materials Chemistry* **1997**, *7*, 2077.

(114) McCabe, E. E.; Greaves, C. *Journal of Fluorine Chemistry* **2007**, *128*, 448.

(115) Battle, P. D.; Goodenough, J. B.; Price, R. *Journal of Solid State Chemistry* **1983**, *46*, 234.

(116) Denis Romero, F.; Bingham, P. A.; Forder, S. D.; Hayward, M. A. *Inorganic Chemistry* **2013**, *52*, 3388.

(117) Iga, F.; Nishihara, Y. *Journal of the Physical Society of Japan* **1992**, *61*, 1867.

(118) Nazri, G.-A.; Pistoia, G. *Lithium batteries: science and technology*; Springer, 2004.

(119) Kobayashi, Y.; Hernandez, O. J.; Sakaguchi, T.; Yajima, T.; Roisnel, T.; Tsujimoto, Y.; Morita, M.; Noda, Y.; Mogami, Y.; Kitada, A.; Ohkura, M.; Hosokawa, S.; Li, Z.; Hayashi, K.; Kusano, Y.; Kim, J. e.; Tsuji, N.; Fujiwara, A.; Matsushita, Y.; Yoshimura, K.; Takegoshi, K.; Inoue, M.; Takano, M.; Kageyama, H. *Nat Mater* **2012**, *11*, 507.

(120) Rey, M. J.; Dehaudt, P.; Joubert, J. C.; Lambert Andron, B.; Cyrot, M.; Cyrot-Lackmann, F. *Journal of Solid State Chemistry* **1990**, *86*, 101.

(121) Suzuki, N.; Noritake, T.; Yamamoto, N.; Hioki, T. *Materials Research Bulletin* **1991**, *26*, 1.

(122) Garcia-Jaca, J.; Larramendi, J. I. R.; Insausti, M.; Arriortua, M. I.; Rojo, T. *Journal of Materials Chemistry* **1995**, *5*, 1995.

(123) Mahajan, A.; Johnston, D.; Torgeson, D.; Borsa, F. *Physical Review B* **1992**, *46*, 10973.

(124) Teske, C. L.; Müller-Buschbaum, H. *Zeitschrift für anorganische und allgemeine Chemie* **1969**, *371*, 325.

(125) Niwa, M.; Murakami, Y. *Journal of Catalysis* **1982**, *76*, 9.

(126) Vogel, A. I.; Bassett, J. *Vogel's textbook of quantitative inorganic analysis, including elementary instrumental analysis*; Longman, 1978.

(127) Helps, R. M.; Rees, N. H.; Hayward, M. A. *Inorganic Chemistry* **2010**, *49*, 11062.

(128) MacEachern, M. J.; Dabkowska, H.; Garrett, J. D.; Amow, G.; Gong, W.; Liu, G.; Greedan, J. E. *Chemistry of Materials* **1994**, *6*, 2092.

(129) Bordet, P.; Chaillout, C.; Marezio, M.; Huang, Q.; Santoro, A.; Cheong, S. W.; Takagi, H.; Oglesby, C. S.; Batlogg, B. *Journal of Solid State Chemistry* **1993**, *106*, 253.

(130) Bard, A. J.; Parsons, R.; Jordan, J. *Standard potentials in aqueous solutions*; CRC press, 1985; Vol. 6.

(131) Williamson, R. F.; Boo, W. O. J. *Inorganic Chemistry* **1977**, *16*, 646.

(132) Bowman, A.; Claridge, J. B.; Rosseinsky, M. J. *Chemistry of Materials* **2006**, *18*, 3046.

(133) Hayward, M. A.; Cussen, E. J.; Claridge, J. B.; Bieringer, M.; Rosseinsky, M. J.; Kiely, C. J.; Blundell, S. J.; Marshall, I. M.; Pratt, F. L. *Science* **2002**, *295*, 1882.

(134) Bridges, C. A.; Darling, G. R.; Hayward, M. A.; Rosseinsky, M. J. *J. Am. Chem. Soc.* **2005**, *127*, 5996.

(135) Liu, G.; Greedan, J. E. *Journal of Solid State Chemistry* **1994**, *110*, 274.

(136) Bansemer, R. L.; Huffman, J. C.; Caulton, K. G. *J. Am. Chem. Soc.* **1983**, *105*, 6163.

(137) Greiser, T.; Puttfarcken, U.; Rehder, D. *Transition Met Chem* **1979**, *4*, 168.

(138) Hessen, B.; Van Bolhuis, F.; Teuben, J. H.; Petersen, J. L. *J. Am. Chem. Soc.* **1988**, *110*, 295.

(139) Jonas, K.; Wiskamp, V.; Tsay, Y. H.; Krueger, C. *J. Am. Chem. Soc.* **1983**, *105*, 5480.

(140) Shannon, R. *Acta Crystallographica Section A* **1976**, *32*, 751.

(141) Wells, A. F. *Structural Inorganic Chemistry, by A. F. Wells*; Clarendon Press, 1945.

(142) P. Clancy, G.; C. S. Clark, H.; K. B. Clentsmith, G.; Geoffrey N. Cloke, F.; B. Hitchcock, P. *Journal of the Chemical Society, Dalton Transactions* **1999**, 3345.

(143) Pauling, L. *Proceedings of the Royal Society of London. Series A* **1927**, *114*, 181.

(144) Zubkov, V. G.; Bazuev, G. V.; Perelyae.Va; Shveikin, G. P. *Fizika Tverdogo Tela* **1973**, *15*, 1610.

(145) Schmidt, M.; Campbell, S. J. *Journal of Solid State Chemistry* **2001**, *156*, 292.

(146) Fawcett, I. D.; Sunstrom; Greenblatt, M.; Croft, M.; Ramanujachary, K. V. *Chemistry of Materials* **1998**, *10*, 3643.

Appendix 3 – Additional Data for Chapter 3

Appendix 3.1 5 K Neutron Data (POLARIS)

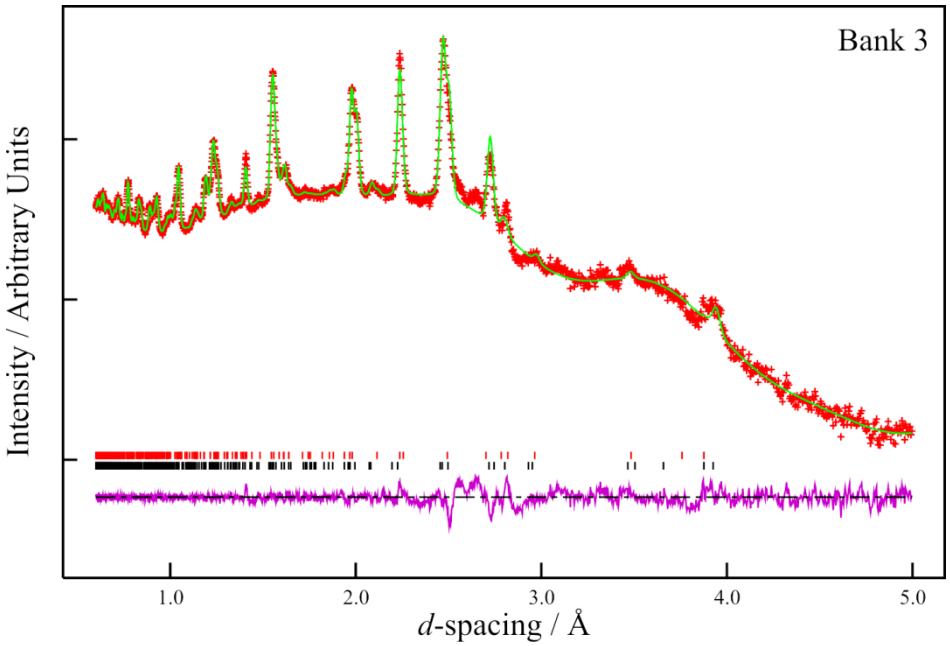

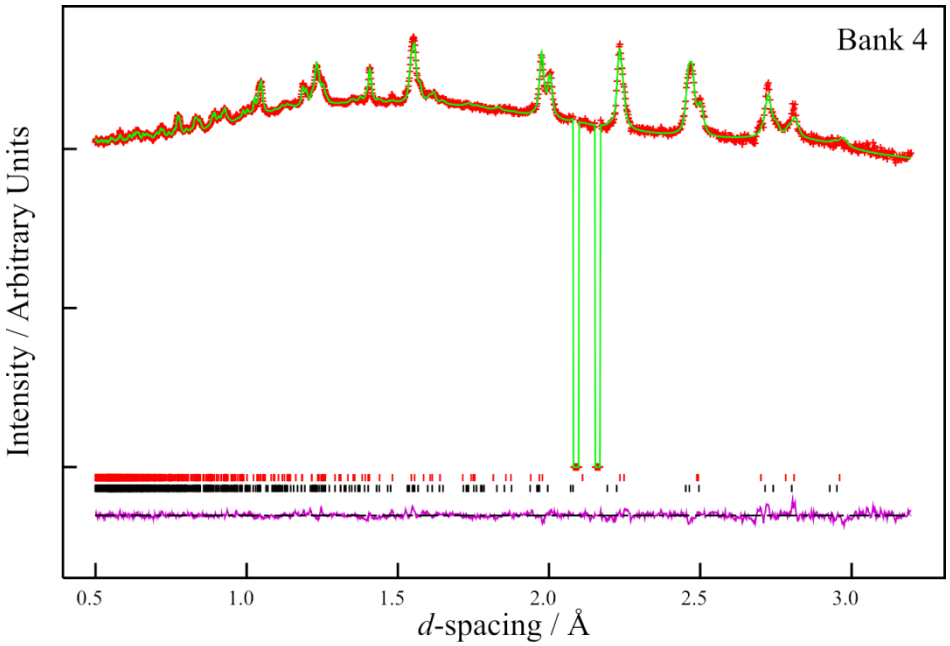

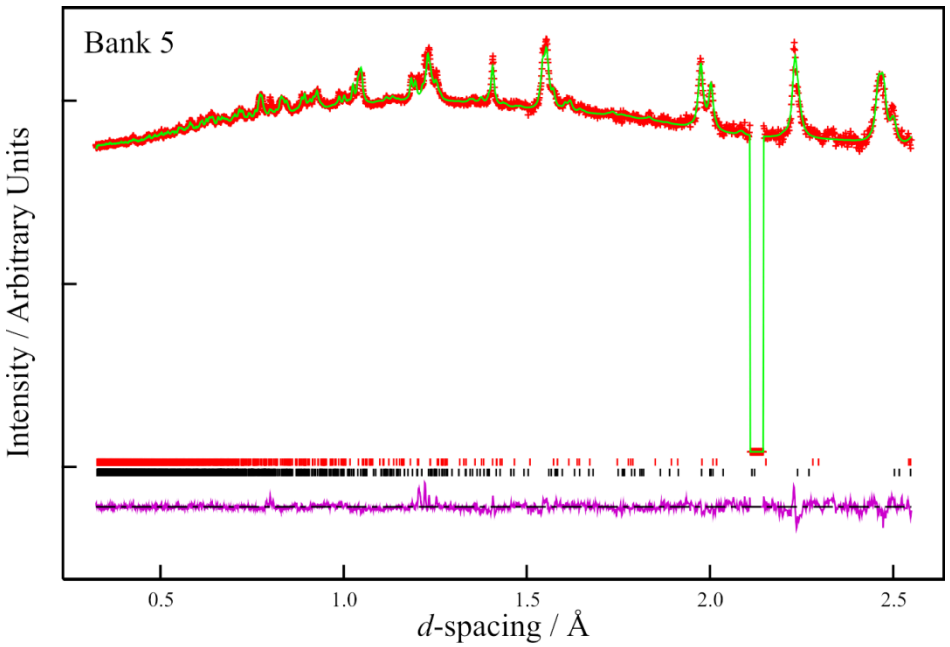

Figure 3.1: Observed, calculated, and difference plots for refinement of the structural model of $Sr_3Co_2O_4Cl_2$ at 5 K against neutron powder diffraction data collected using the POLARIS instrument. The upper set of tick marks correspond to a ~ 10% by weight impurity of $Sr_3Co_2O_5Cl_2$. Excluded regions correspond to contributions from the cryostat.

Appendix 3.2 5 K Neutron Data (D2b)

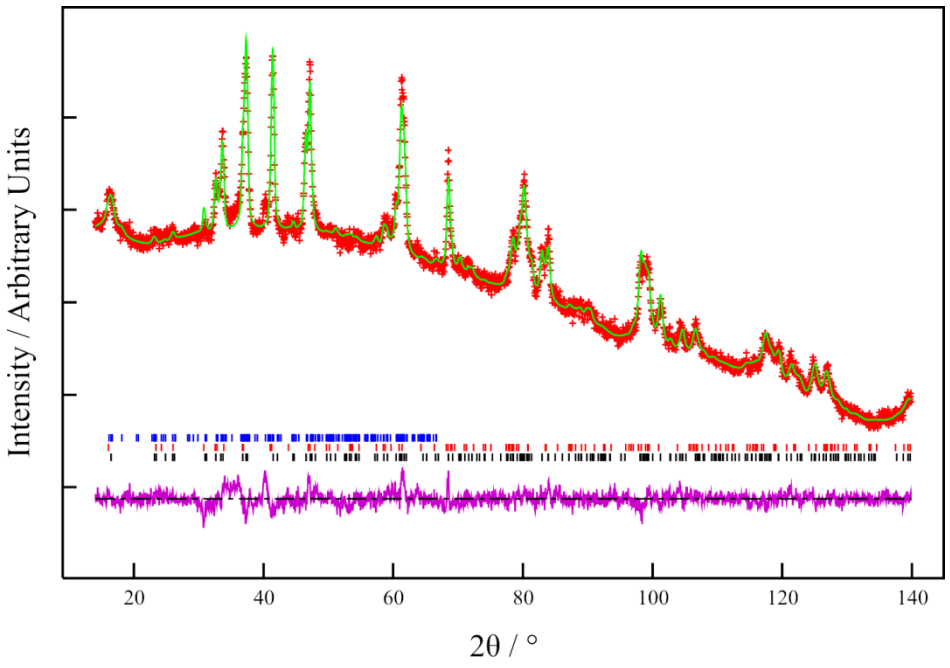

Figure 3.2: Observed, calculated and, difference plots for refinement of the structural model of $Sr_3Co_2O_4Cl_2$ at 5 K against neutron powder diffraction data collected using the POLARIS instrument. The middle set of tick marks correspond to a ~ 10% by weight impurity of $Sr_3Co_2O_5Cl_2$.

Appendix 3.3 Details of the Magnetic Structure of $Sr_3Co_2O_4Cl_2$

Atom	***x***	***y***	***z***	$\mathbf{m_x / \mu_B}$	$\mathbf{m_y / \mu_B}$	$\mathbf{m_z / \mu_B}$
Co(1)	0	0	0.428	0	0	3.60(1)
Co(2)	1/2	1/2	0.428	0	0	-3.60(1)
Co(3)	1/2	0	0.072	0	0	3.60(1)
Co(4)	0	1/2	0.072	0	0	-3.60(1)
Co(5)	0	0	0.572	0	0	3.60(1)
Co(6)	1/2	1/2	0.572	0	0	-3.60(1)
Co(7)	1/2	0	0.928	0	0	3.60(1)
Co(8)	0	1/2	0.928	0	0	-3.60(1)
Space group: *P*1; a = 5.660 Å, b = 5.660 Å, and c = 22.147 Å, γ = 90.75 °						

Table 3.1: The magnetic structure of $Sr_3Co_2O_4Cl_2$ at 5 K refined against neutron powder diffraction collected using D2b.

Appendix 4 – Additional Data for Chapter 4

Appendix 4.1 The Synthesis of $Sr_2Fe_2O_5$ and $SrFeO_2$

Samples of $Sr_2Fe_2O_5$ were synthesised via the route previously described by Schmidt and Campbell.[145] Suitable stoichiometric quantities of $SrCO_3$ and Fe_2O_3 were ground together using an agate mortar and pestle. The resulting powders were placed in an alumina crucible and heated in air to 1000 °C for 24 hours to decompose the carbonates. The powders were then pressed into pellets and heated in air at 1300 °C for two periods of two days with an intermediate grinding. The powders were then annealed at 1200 °C under a flow of argon for two days in order to obtain a phase with the correct oxygen stoichiometry. The resulting powders were observed to be phase-pure by laboratory X-ray powder diffraction, with lattice parameters a = 5.67(1) Å, b = 15.58(1) Å, and c = 5.52(1) Å, in good agreement with reported values (a = 5.67(1) Å, b = 15.58(1) Å, and c = 5.53(1) Å). Oxygen stoichiometry was confirmed via thermogravimetric analysis performed under a mixture of 5% H_2 in N_2.

Samples of $SrFeO_2$ were prepared via the route previously described by Tsujimoto *et al.*[55] Samples of as-synthesised $Sr_2Fe_2O_5$ were ground together with a double molar excess of CaH_2 in an argon-filled glovebox and then sealed under vacuum in silica ampoules. These were then heated to 300 °C for two periods of two days with an intermediate grinding. The reaction products were washed with 4 x 100 ml of a 0.1 M solution of NH_4Cl in methanol followed by 4 x 100 ml of clean methanol before being dried under vacuum and returned to the glovebox. The resulting powders were observed to be phase-pure by laboratory X-ray powder diffraction, with lattice parameters a = 3.99(1) Å, and c = 3.49(1) Å, in good agreement with reported values (a = 3.99(1) Å, c = 3.47(1) Å).[55] Oxygen stoichiometry was confirmed via thermogravimetric analysis performed under a mixture of 5% H_2 in N_2.

Appendix 4.2 Electronic Structure of $SrFeO_2$

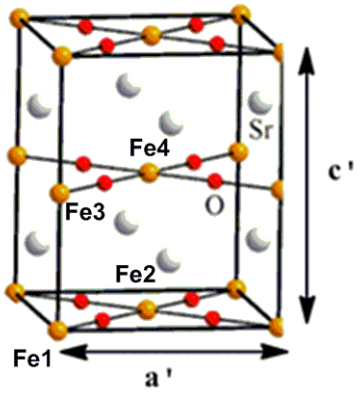

a′ = b′ = 5.73 Å c′ =6.52 Å

Ground-state Mulliken spin densities ρ(Fe1)= ρ(Fe4)= -ρ(Fe2)= -ρ(Fe3□)= 4.11 electrons

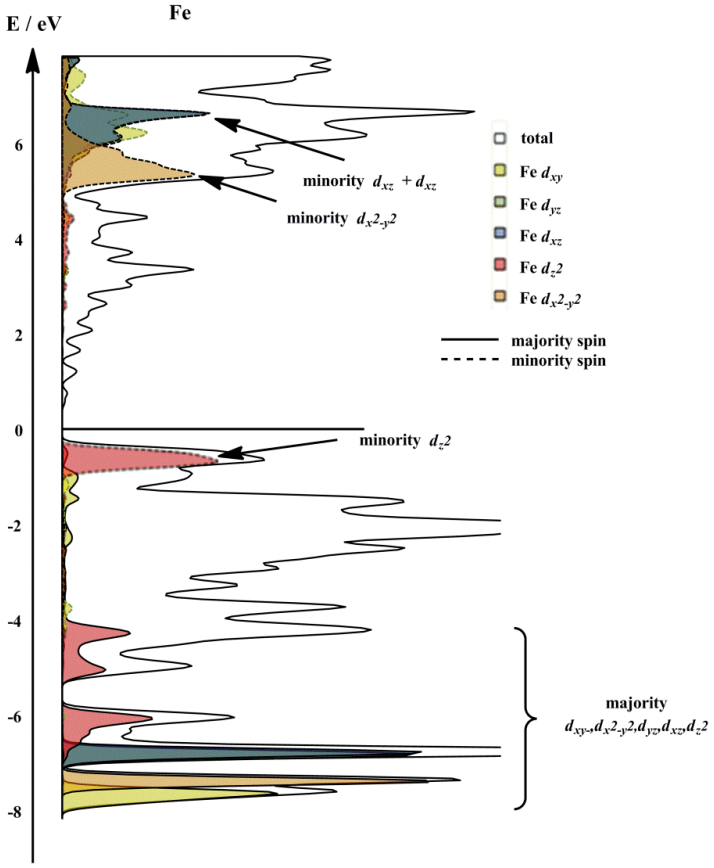

Figure 4.1: Density of states (full line = total, dotted line = Fe PDOS).

Appendix 4.3 Electronic Structure of $Sr(Ru_{0.5}Fe_{0.5})O_2$ (columnar)

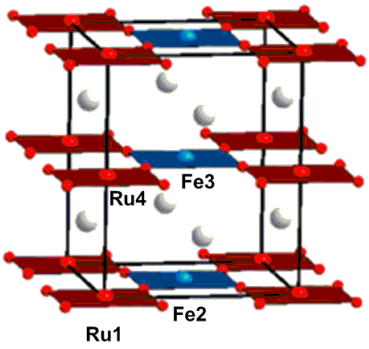

a′ = 5.82 Å b′ = 5.68 Å c′ =6.63 Å

Ground-state Mulliken spin densities ρ(Ru1)= -ρ(Ru4)□= 2.12, ρ(Fe2)= -ρ(Fe3□)= 4.09 electrons

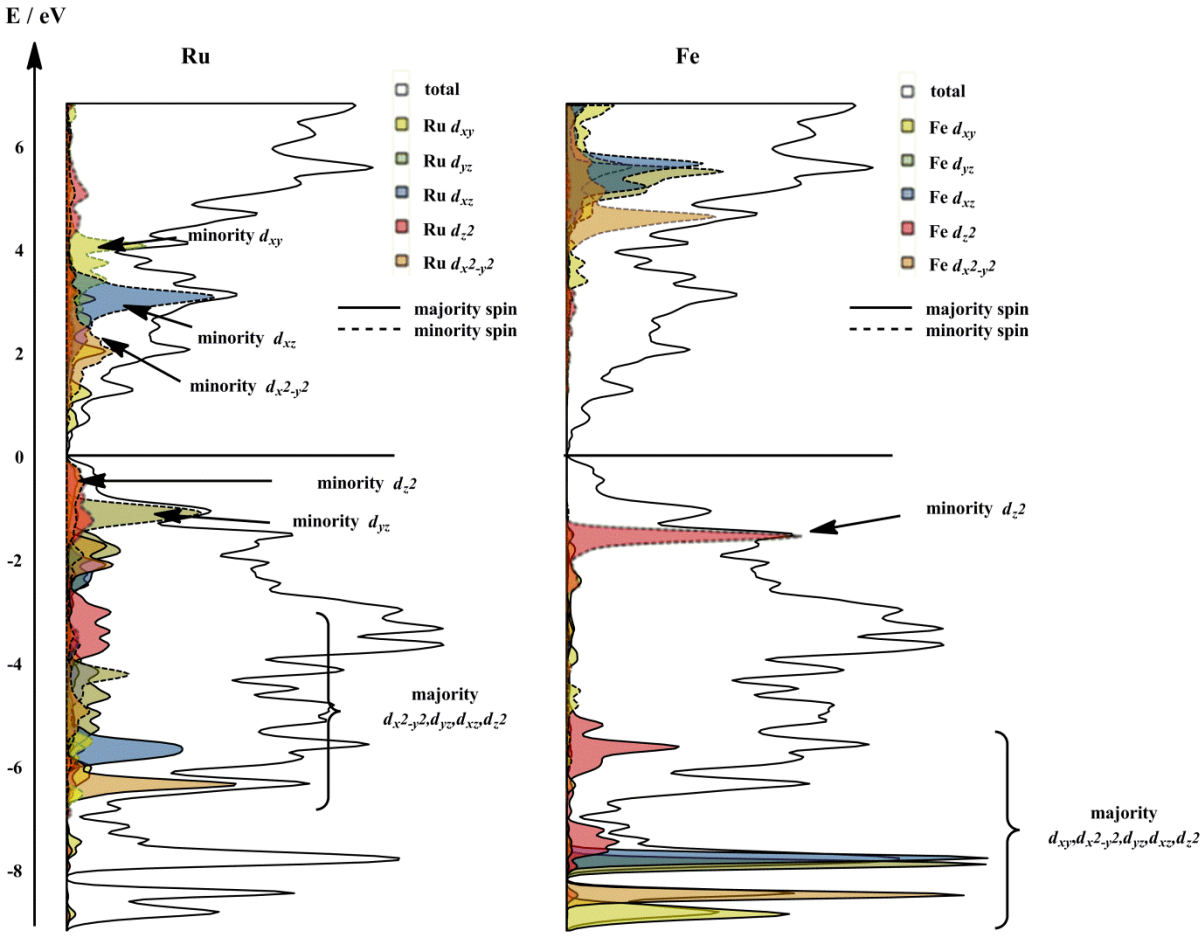

Figure 4.2: Density of states for the column configuration of $SrFe_{0.5}Ru_{0.5}O_2$ (left: Ru PDOS, right: Fe PDOS, full and dashed lines indicate majority- and minority spins, respectively).

Appendix 4.4 Electronic Structure of $Sr(Ru_{0.5}Fe_{0.5})O_2$ (planar)

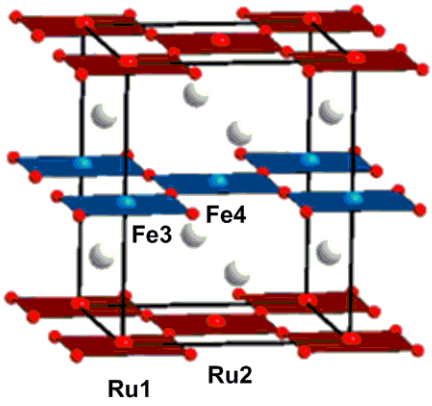

a′ = 5.81 Å b′ = 5.69 Å c′ =6.58 Å

Ground-state Mulliken spin densities ρ(Ru1)= -ρ(Ru4)= 1.86, ρ(Fe2)= -ρ(Fe3)= 4.03 electrons

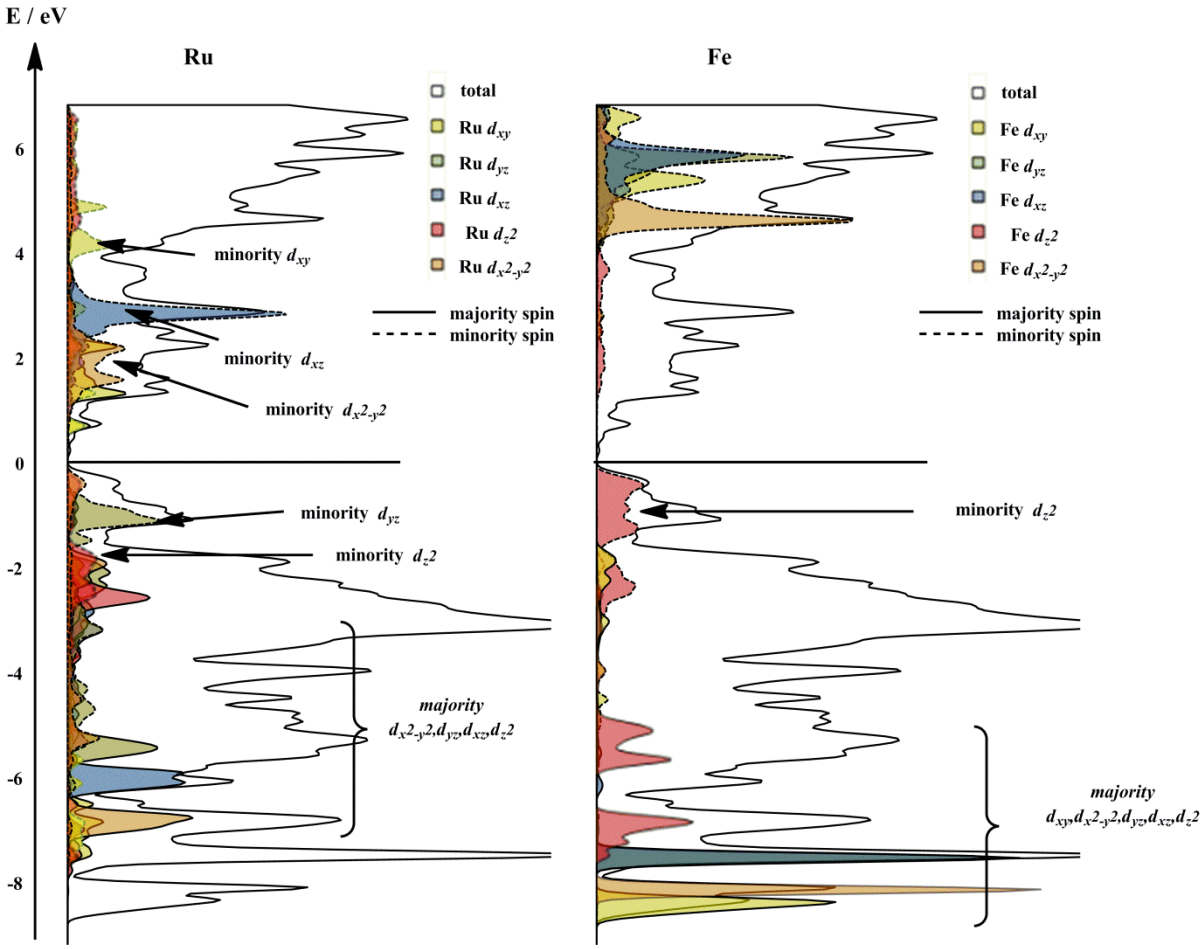

Figure 4.3: Density of states for the planar configuration of $SrFe_{0.5}Ru_{0.5}O_2$ (left: Ru PDOS, right: Fe PDOS, full and dashed lines indicate majority- and minority spins, respectively).

Appendix 4.5 Heisenberg Exchange Parameters

In all cases, the Heisenberg exchange parameters were obtained from a least squares fit of the differences between computed single-determinant energies and the corresponding diagonal elements of the Heisenberg spin Hamiltonian. Six distinct single-determinant states were computed, corresponding to the spin arrangements αααα, ααββ, αββα, αβαβ, αααβ and ααβα, in each case using the geometry of the most stable configuration. The numbering of the atoms in the configurations noted above (ααβα etc) and the coupling constants are defined in Figure 4.4 below.

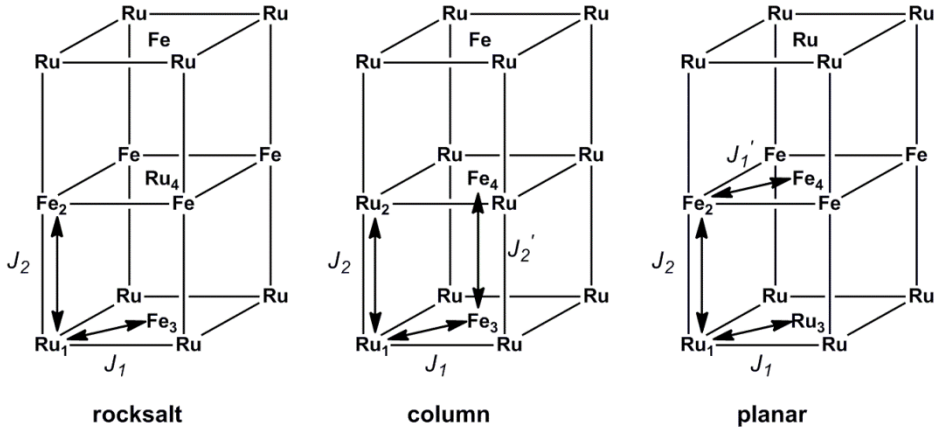

Figure 4.4: Definition of Heisenberg exchange constants used in Equations S1-S3 below. The numbering scheme adopted for the atoms is also shown.

$$H(\text{rocksalt})^{HDVV} = -\sum_{i,j} J_{ij}\left(\mathbf{S}_i \cdot \mathbf{S}_j\right) = -8J_1\left(\mathbf{S}_{Ru} \cdot \mathbf{S}_{Fe}\right) - 4J_2\left(\mathbf{S}_{Ru} \cdot \mathbf{S}_{Fe}\right)$$

$$J_1 = 2.39meV \qquad J_2 = -1.00meV$$

$$H(\text{column})^{HDVV} = -\sum_{i,j} J_{ij}\left(\mathbf{S}_i \cdot \mathbf{S}_j\right) = -8J_1\left(\mathbf{S}_{Ru} \cdot \mathbf{S}_{Fe}\right) - 2J_2\left(\mathbf{S}_{Ru} \cdot \mathbf{S}_{Ru}\right) - 2J_2'\left(\mathbf{S}_{Fe} \cdot \mathbf{S}_{Fe}\right)$$

$$J_1 = 2.75meV \qquad J_2 = -28.15meV \qquad J_2' = -2.70meV$$

The strong antiferromagnetic J_2 arises from the $(d_{z^2})^1$ configuration at each centre

$$H(\text{planar})^{HDVV} = -\sum_{i,j} J_{ij}\left(\mathbf{S}_i \cdot \mathbf{S}_j\right) = -4J_1\left(\mathbf{S}_{Ru} \cdot \mathbf{S}_{Ru}\right) - 4J_1'\left(\mathbf{S}_{Fe} \cdot \mathbf{S}_{Fe}\right) - 4J_2\left(\mathbf{S}_{Fe} \cdot \mathbf{S}_{Ru}\right)$$

$J_1 = -4.77meV$ $J_1' = -1.73meV$ $J_2 = 2.98meV$

Appendix 4.6 Recipe for the Perfect Mojito

Two limes were quartered and ground together with a table spoon of brown sugar and a generous helping of mint leaves using a wooden mortar and pestle. The result was transferred into a Collins glass containing 3 – 5 ice cubes. 60 ml of dark rum were added and the solution made up using lemonade.

Appendix 5 Additional Data for Chapter 5

Appendix 5.1 ^{57}Fe Mössbauer Spectroscopy Data

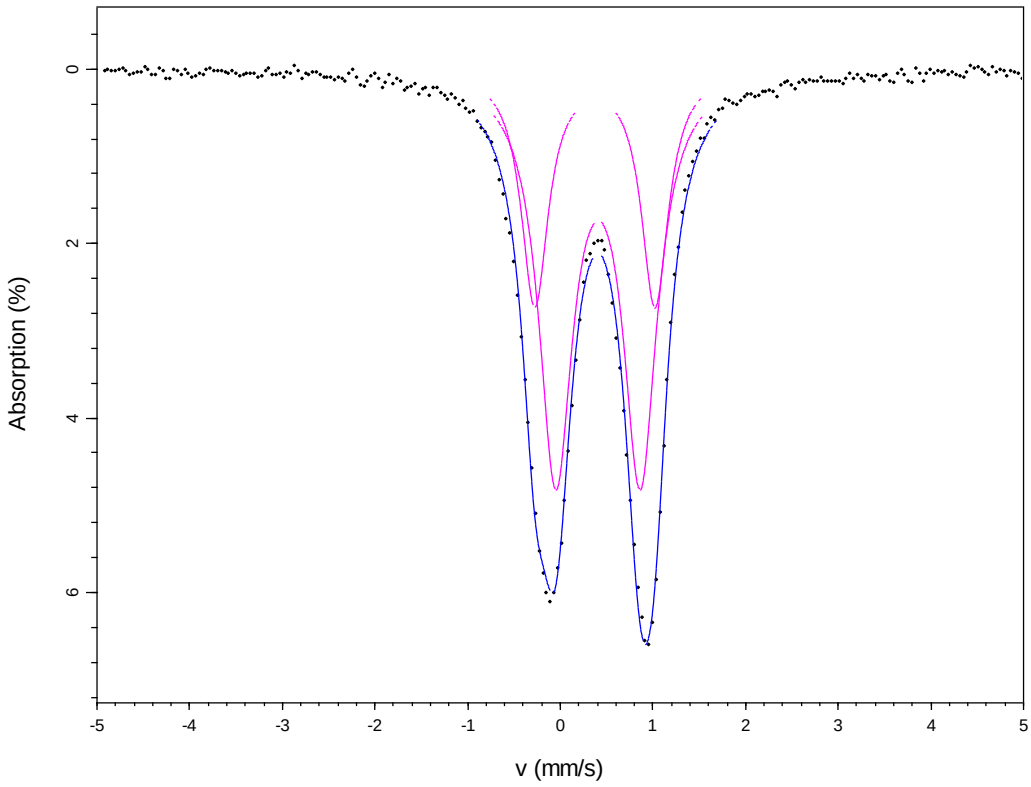

Figure 5.1: ^{57}Fe Mössbauer spectrum collected from $Sr_2(Ru_{0.5}Fe_{0.5})O_{3.35}$ at room temperature, fitted to two doublets.

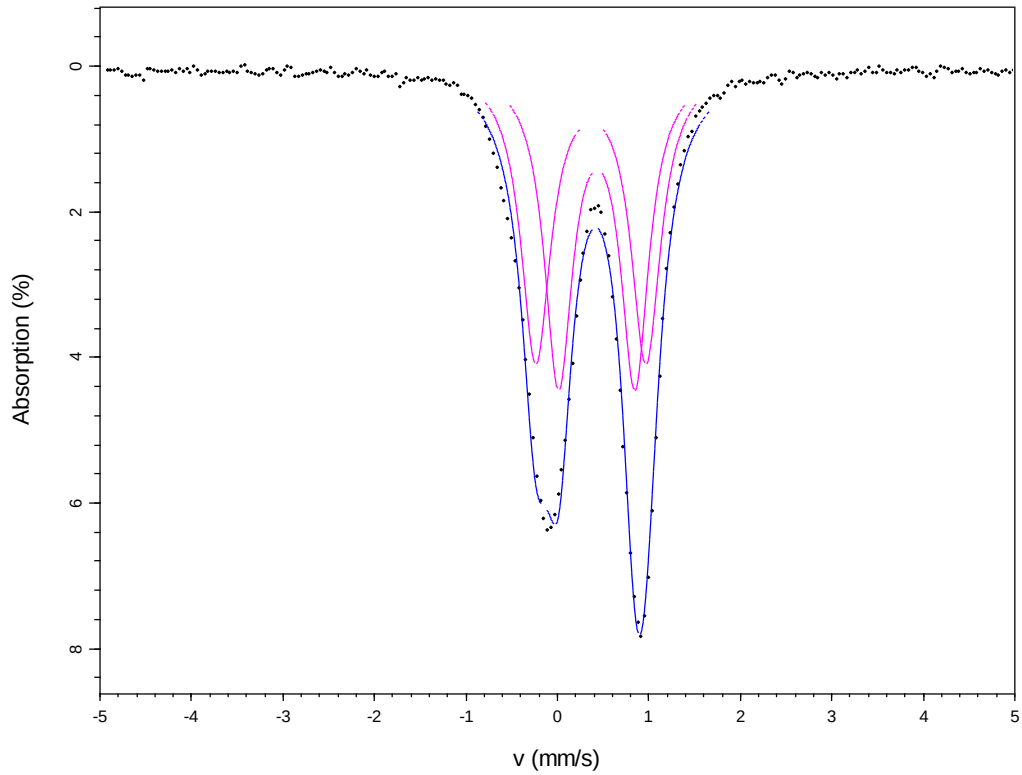

Figure 5.2: ^{57}Fe Mössbauer spectrum collected from $Sr_3(Ru_{0.5}Fe_{0.5})_2O_{5.67}$ at room temperature, fitted to two doublets.

Appendix 6 Additional Data for Chapter 6

Appendix 6.1 Magnetic Structure of $Sr_3(Ru_{0.5}Fe_{0.5})_2O_{5.5}F_{3.5}$

Atom	***x***	***y***	***z***	**Fractional Occupancy**	**U_{iso} / Å^2**
Sr(1)	0	¼	¾	1	0.002(1)
Sr(2)	0.1871(1)	¼	¾	1	0.005(1)
Ru/Fe(1)	0.0830(1)	¾	¾	0.5/0.5	0.006(1)
X(1)	0	¾	¾	1	0.015(1)
X(2)	0.0844(1)	0.536(1)	0.463(1)	1	0.007(1)
X(3)	0.1643(2)	¾	¾	1	0.020(1)
X(4)	¼	0	0.000(1)	1	0.010(1)
$Sr_3(Ru_{0.5}Fe_{0.5})_2O_{5.5}F_{3.5}$: Space group *Ccca* a = 23.491(1) Å, b = 5.487(1) Å, c = 5.493(1) Å. Weight fraction: 77.8%					
CuO: Space group *C*2/*c* a = 4.656(1) Å, b = 3.410(1) Å, c = 5.089(1) Å, β = 98.98(2)°. Weight fraction: 22.2%					
Magnetic model					
Atom	***x***	***y***	***z***	**Fractional Occupancy**	***Mz* / μ_B**
Ru/Fe(1)	0.0830	¾	¾	0.5/0.5	1.12(3)
Ru/Fe(2)	0.0830	¼	¼	0.5/0.5	-1.12(3)
Ru/Fe(3)	0.4170	¾	¼	0.5/0.5	1.12(3)
Ru/Fe(4)	0.4170	¼	¾	0.5/0.5	-1.12(3)
Ru/Fe(5)	0.5830	¾	¼	0.5/0.5	-1.12(3)
Ru/Fe(6)	0.5830	¼	¾	0.5/0.5	1.12(3)
Ru/Fe(7)	0.9170	¾	¾	0.5/0.5	-1.12(3)
Ru/Fe(8)	0.9170	¼	¼	0.5/0.5	1.12(3)
Space group *P*1 a = 23.491(1) Å, b = 5.487(1) Å, c = 5.493(1) Å					
χ^2 = 8.12; wRp = 4.35%; Rp = 3.31%					

Figure 6.1: Refined structural and magnetic parameters of $Sr_3(Ru_{0.5}Fe_{0.5})_2O_{5.5}F_{3.5}$ at 5 K refined against neutron powder diffraction collected using D2b.

Appendix 6.2 Magnetisation-field Isotherms Collected from $Sr_3(Ru_{0.5}Mn_{0.5})_2O_7F_2$

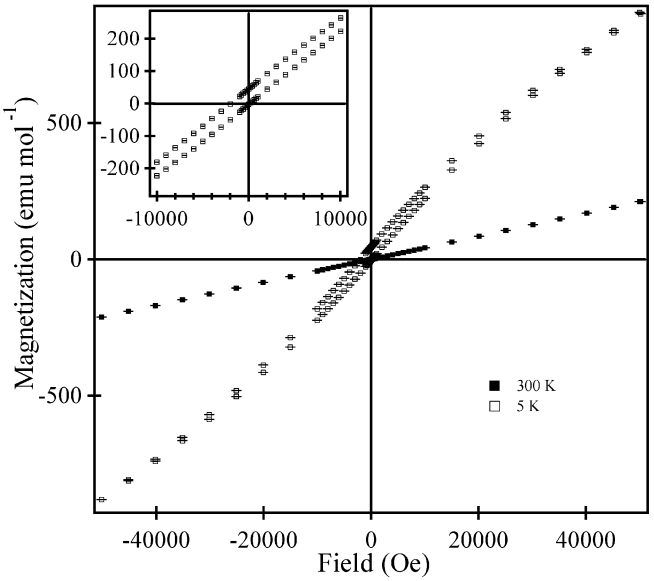

Figure 6.2: Magnetisation-field isotherms collected from $Sr_3(Ru_{0.5}Mn_{0.5})_2O_7F_2$ at 300 K and 5 K.

Appendix 6.3 Synthesis and Fluorination of $Ca_3Mn_2O_7$

Samples of $Ca_3Mn_2O_7$ were prepared via citrate gel methods from suitable stoichiometric quantities of $CaCO_3$ (Alfa Aesar, 99.997%) and MnO_2 (Alfa Aesar, 99.997%). The resulting powders were placed into alumina crucibles and heated at 1 °C min^{-1} to 1000 °C for 12 hours before being pressed into pellets. These were then heated under flowing O_2 at 1250 °C for two periods of two days with one intermediate grinding. The resulting powders were phase pure by laboratory X-ray powder diffraction with lattice parameters a = 3.70(1) Å and c = 19.40(1) Å in good agreement with literature values (a = 3.68(1) Å and c = 19.50(1) Å).[146]

The fluorination was attempted in the same manner as that of $Sr_3(Ru_{0.5}Mn_{0.5})O_7$, using a double excess of CuF_2 under flowing O_2 at 250 °C for 12 hours. X-ray powder diffraction data collected from the products were consistent with a mixture of CuO and unfluorinated

$Ca_3Mn_2O_7$. Attempts to increase the reaction temperature produced the same results, as CuF_2 decomposes to CuO in the presence of oxygen at $T \sim 250$ °C.

Appendix 7 Additional Data for Chapter 8

Appendix 7.1 Sr_2VO_3H 298 K Neutron Data

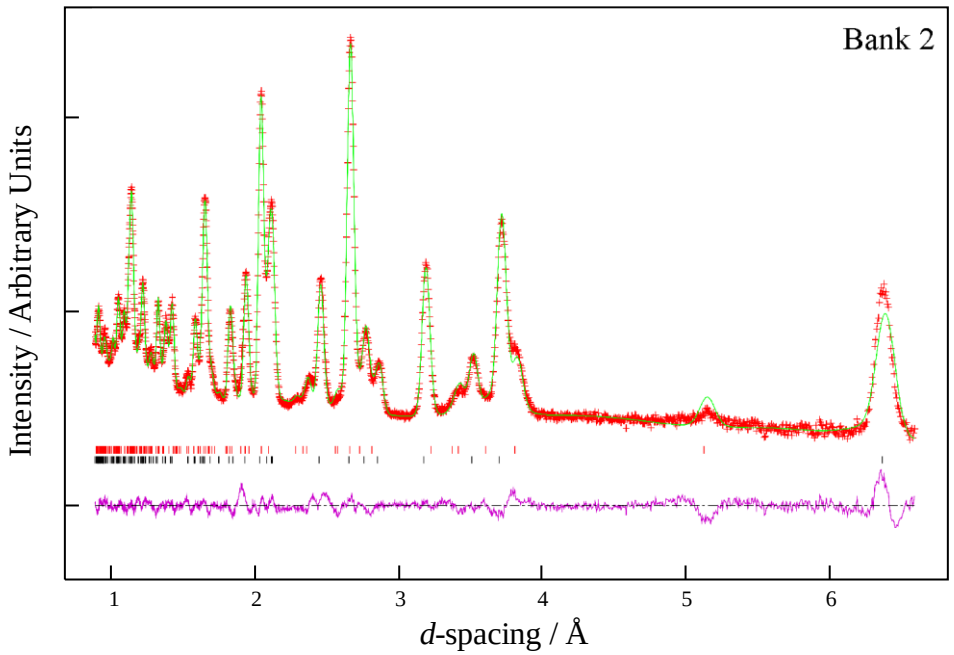

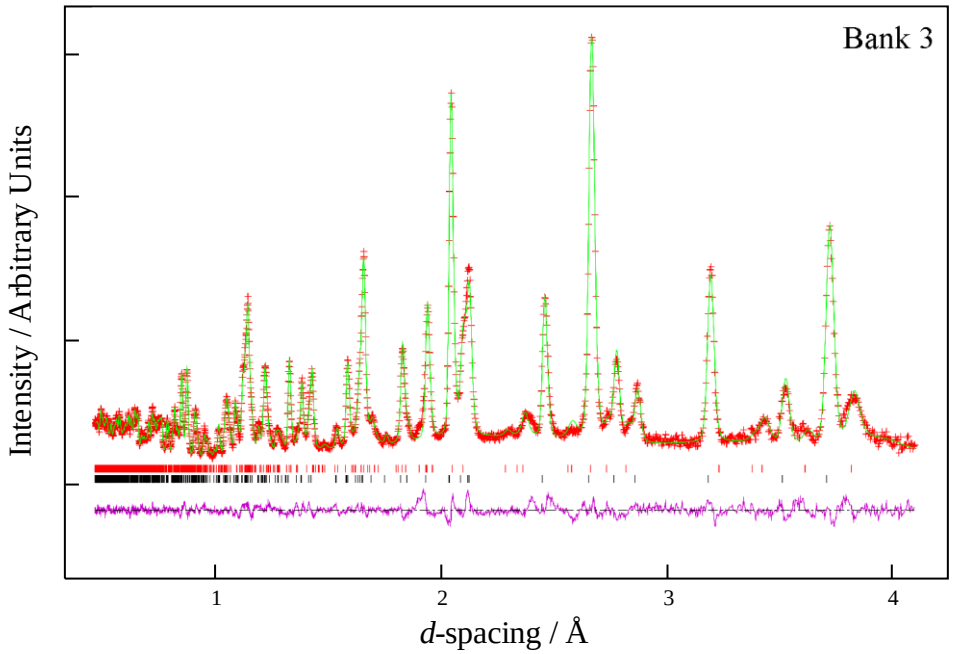

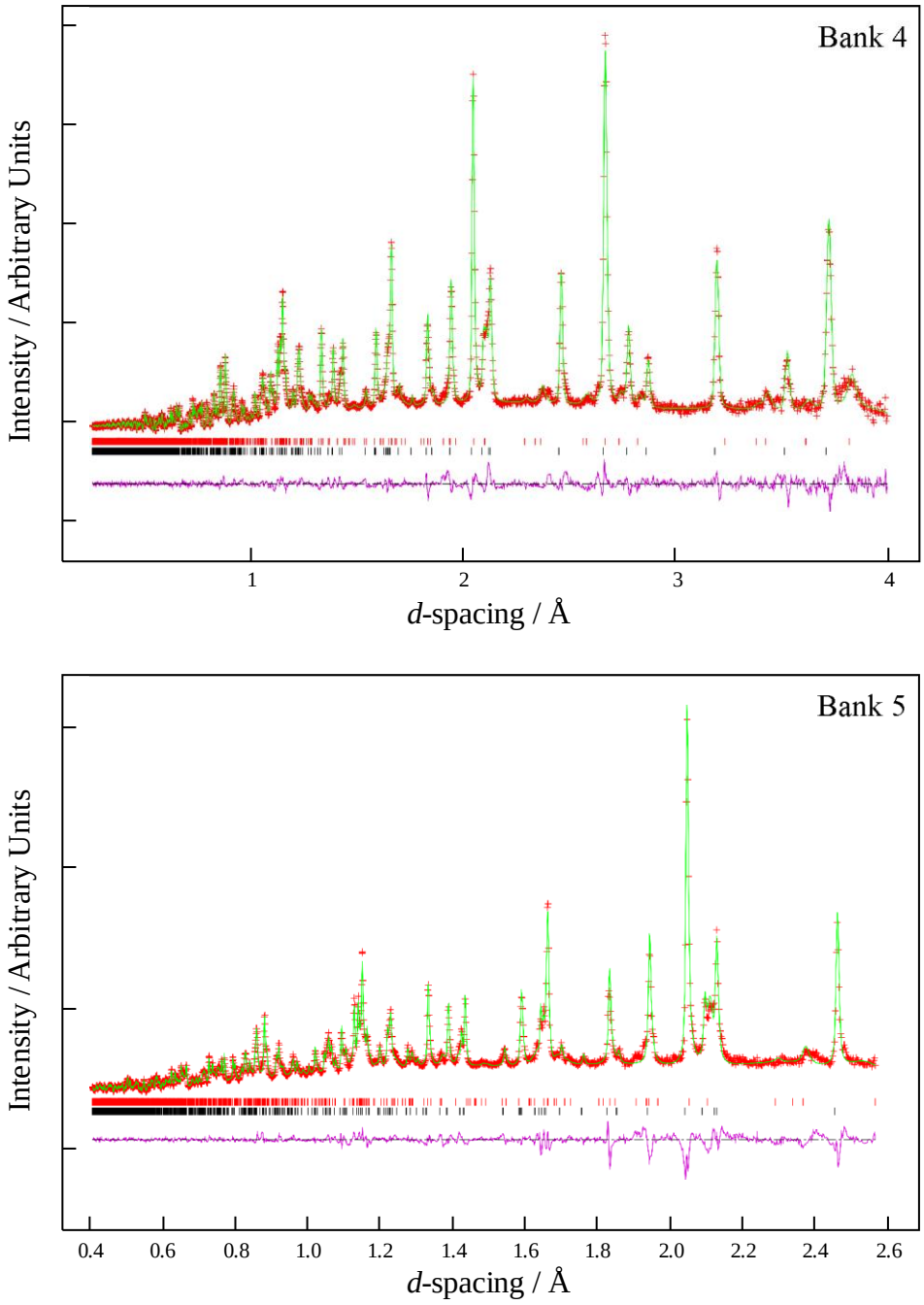

Figure 7.1: Observed, calculated, and difference plots for refinement of the structural model of Sr_2VO_3H at 298 K against neutron powder diffraction data collected using the POLARIS instrument. The upper set of tick marks correspond to a 28.4(4)% by weight impurity of $Sr_3V_2O_5H_2$.

Appendix 7.2 $Sr_3V_2O_5H_2$ 298 K Neutron Data

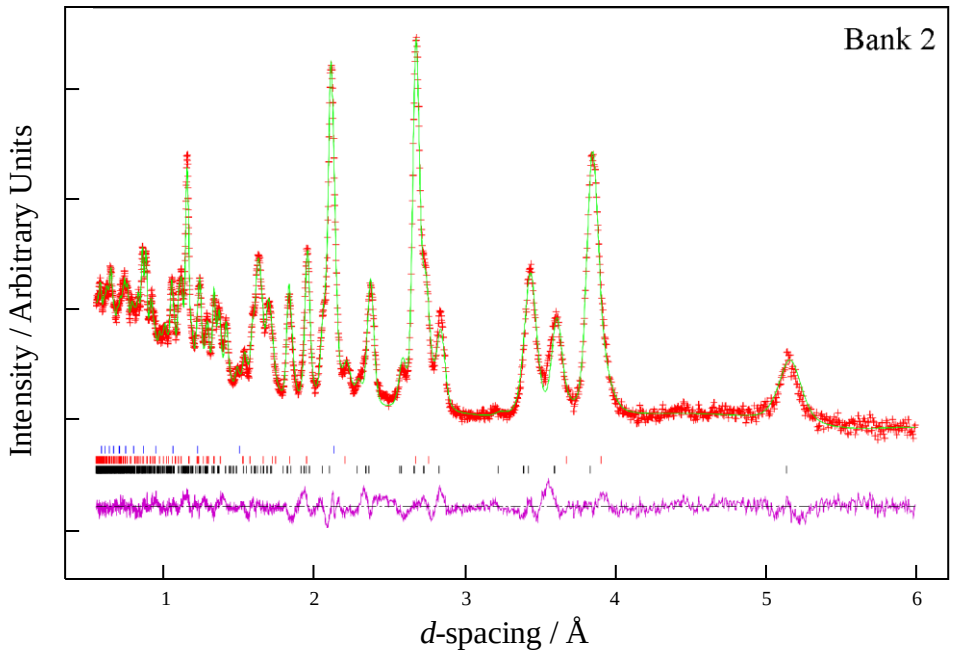

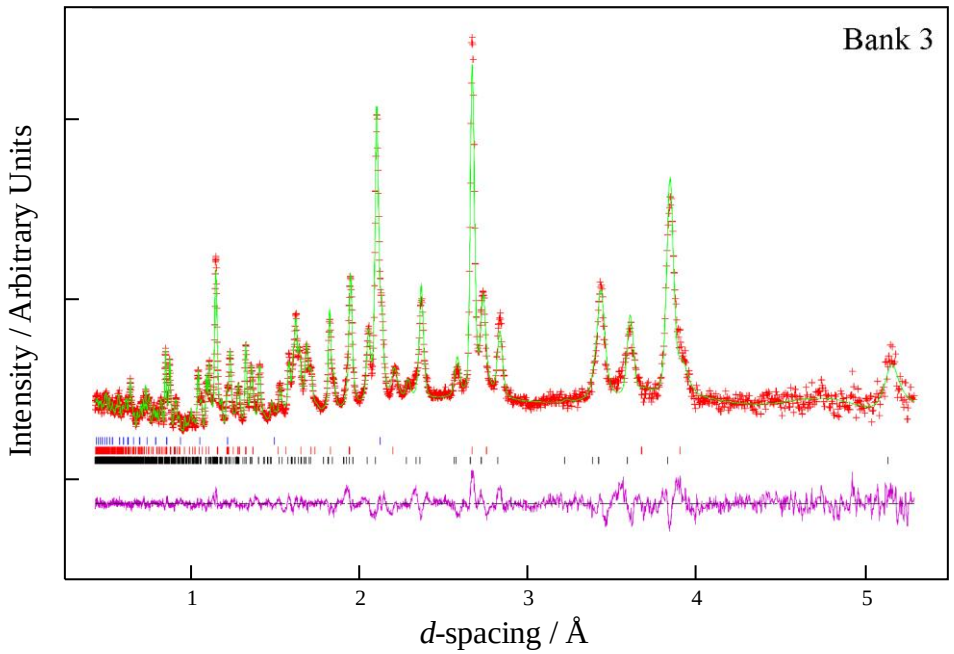

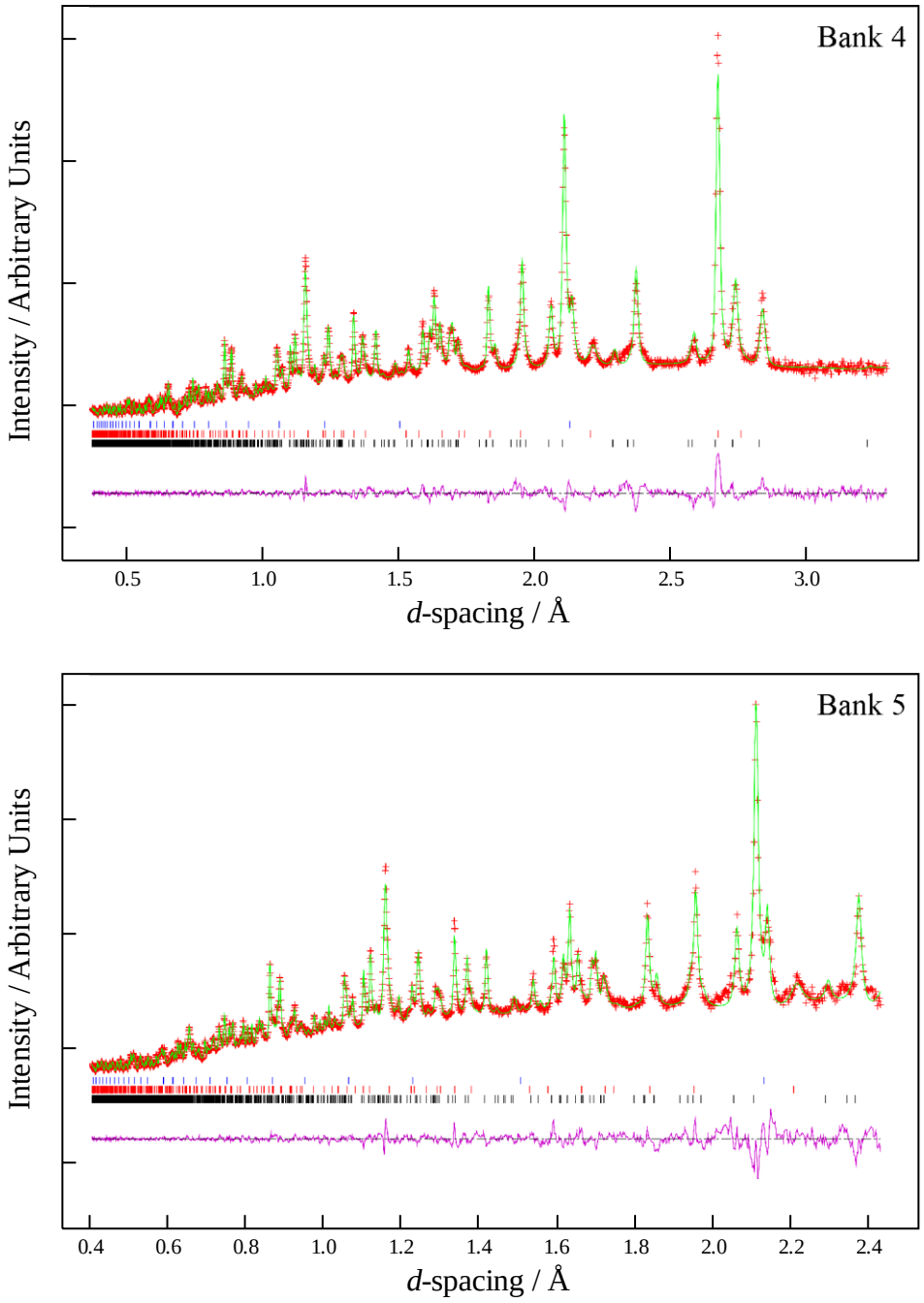

Figure 7.2: Observed, calculated, and difference plots for refinement of the structural model of $Sr_3V_2O_3H$ at 298 K against neutron powder diffraction data collected using the POLARIS instrument. The middle set of tick marks correspond to a 10.8(3)% by weight impurity of $SrVO_2H$. The upper set of tick marks correspond to contributions from the vanadium sample holder.

Appendix 7.3 $SrVO_2H$ 4 K Neutron Data

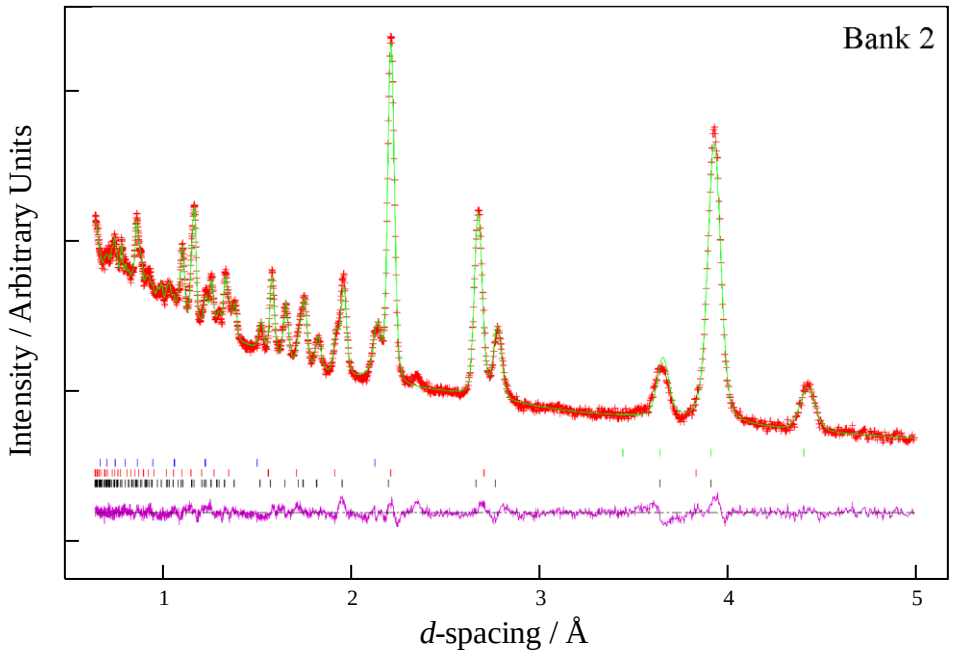

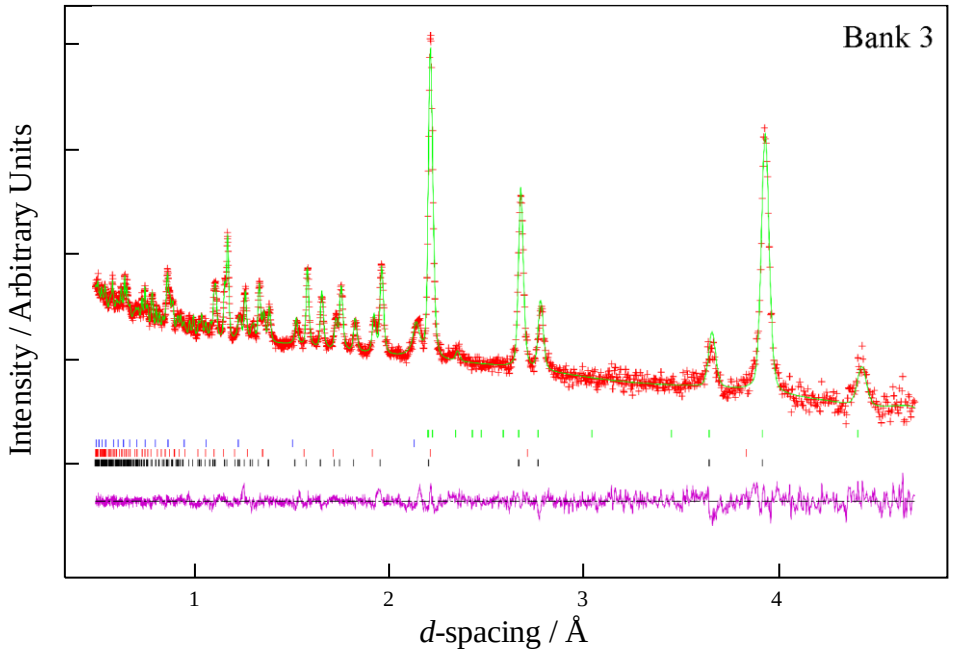

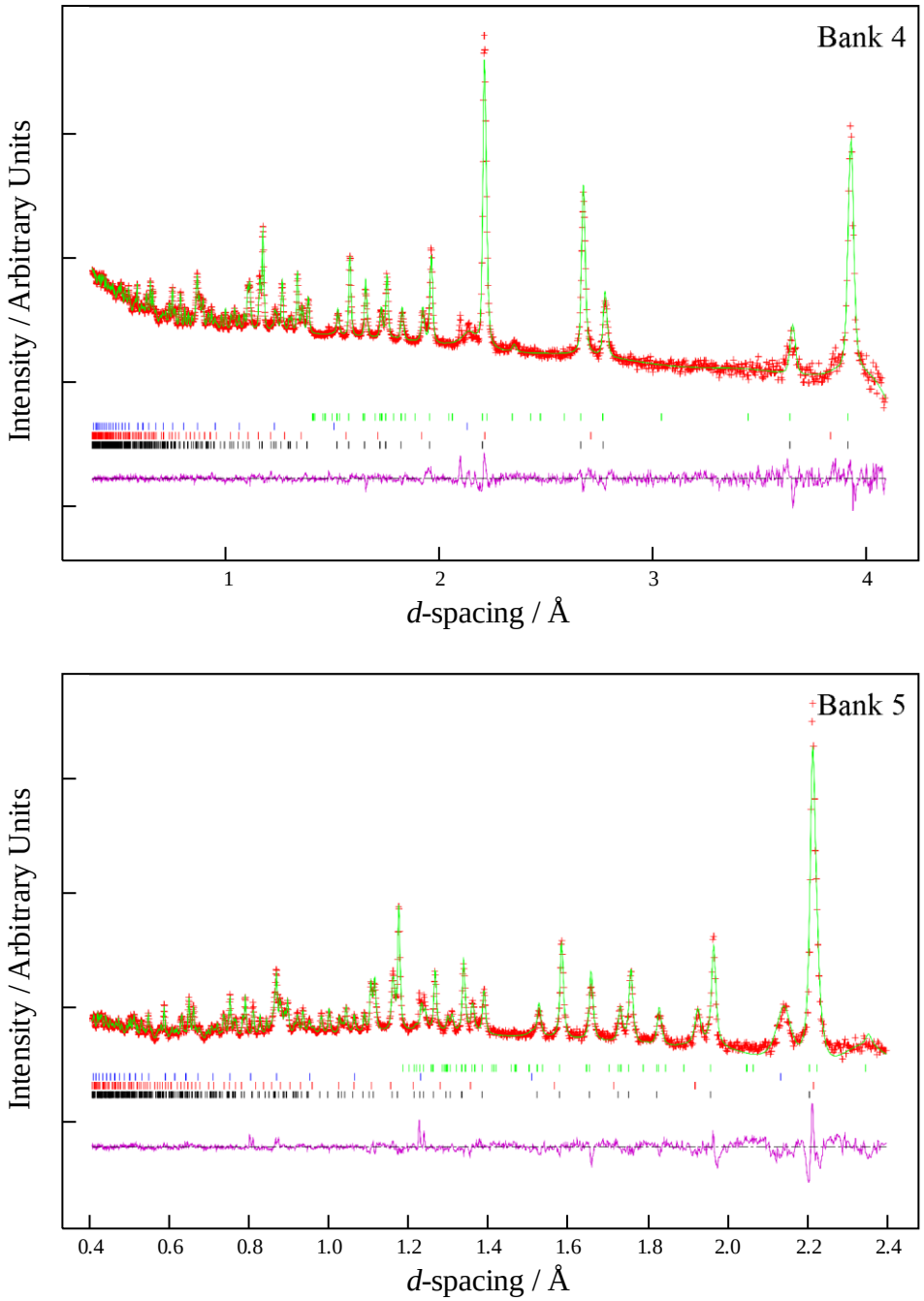

Figure 7.3: Observed, calculated, and difference plots for refinement of the structural model of $SrVO_2H$ at 4 K against neutron powder diffraction data collected using the POLARIS instrument. Red tick marks correspond to a $SrVO_{3-x}$ impurity. Blue tick marks correspond to contributions from the vanadium sample holder. Green tick marks correspond to the magnetic reflections.

Atom	Wyckoff Position	*x*	*y*	*z*	Fractional Occupancy	U_{iso} / Å^2
Sr(1)	4*i*	1/2	1/2	1/2	1	0.002(1)
V(1)	2*a*	0	0	0	1	0.002
O(1)	4*i*	0	1/2	0	1	0.002(1)
H(1)	2*b*	0	0	1/2	1	0.023(1)
Sr_2VO_3H: space group *P*4/*mmm*; *a* = 3.9291(6) Å and *c* = 3.6570(6) Å; cell volume = 56.46(3) Å^3; weight fraction = 87.3(3)%						
$SrVO_{3-x}$: space group *Pm*-3*m*; *a* = 3.8495(6) Å cell volume = 57.04(3) Å^3; weight fraction = 12.7(3)%						
Magnetic Model						
Atom		***x***	***y***	***z***	***Mz* / μ_B**	
V(1)		0	0	0	1.56(3)	
V(2)		1/2	1/2	0	-1.56(3)	
V(3)		0	0	1/2	-1.56(3)	
V(4)		1/2	1/2	1/2	1.56(3)	
Space group *P*1 *a* = 5.56(1) Å, *b* = 5.56(1) Å, *c* = 7.32(1) Å						
χ^2 = 1.950, wRp = 0.96%, Rp = 1.32%						

Table 7.1: Refined structural and magnetic parameters for $SrVO_2H$ at 4 K.

Appendix 7.4 Sr_2VO_3H 4 K Neutron Data

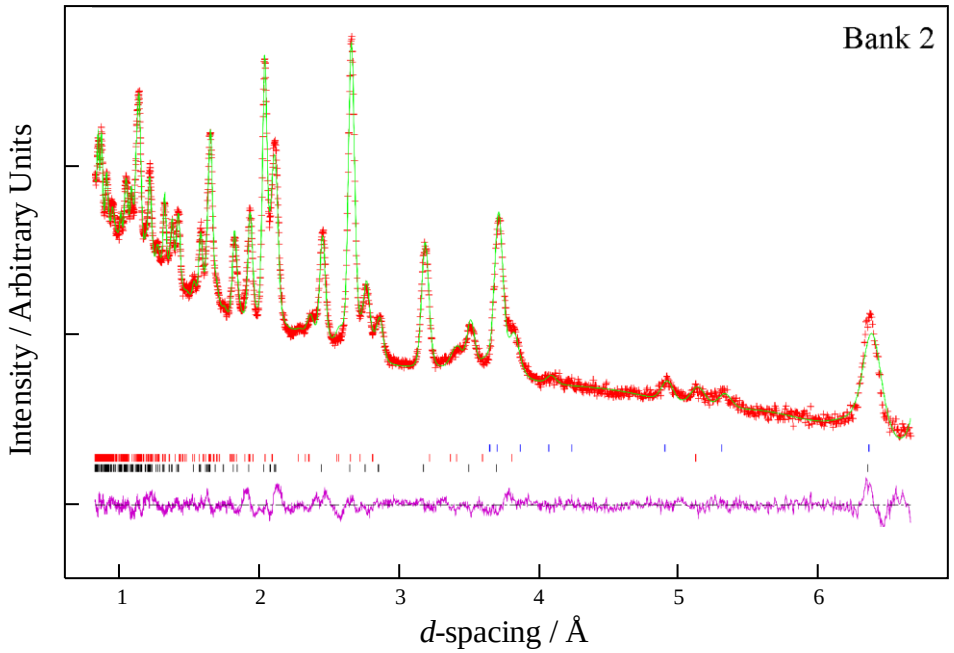

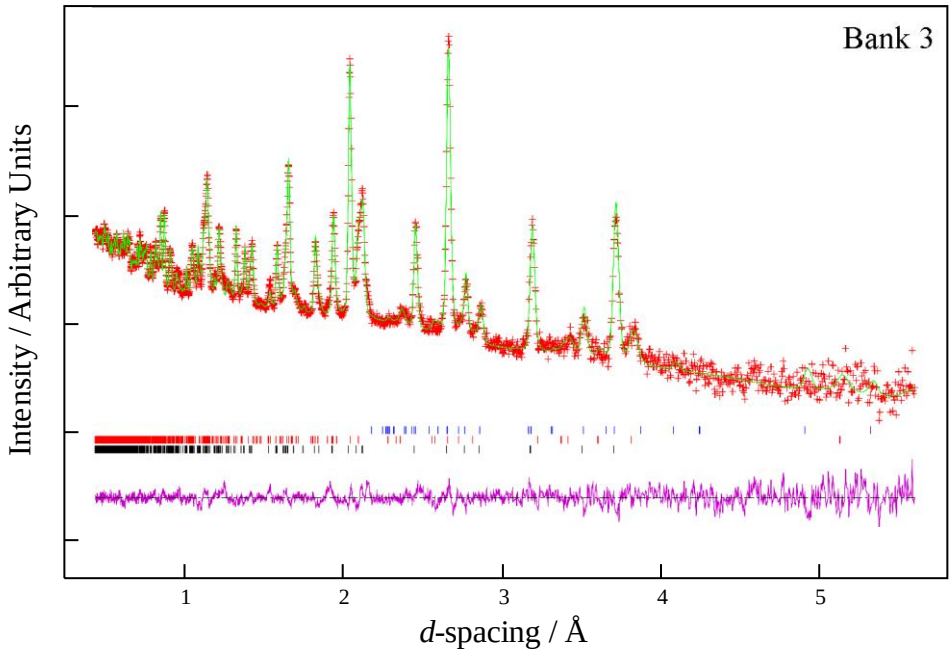
Bank 3
Intensity / Arbitrary Units
1
2
3
4
5
d-spacing / Å

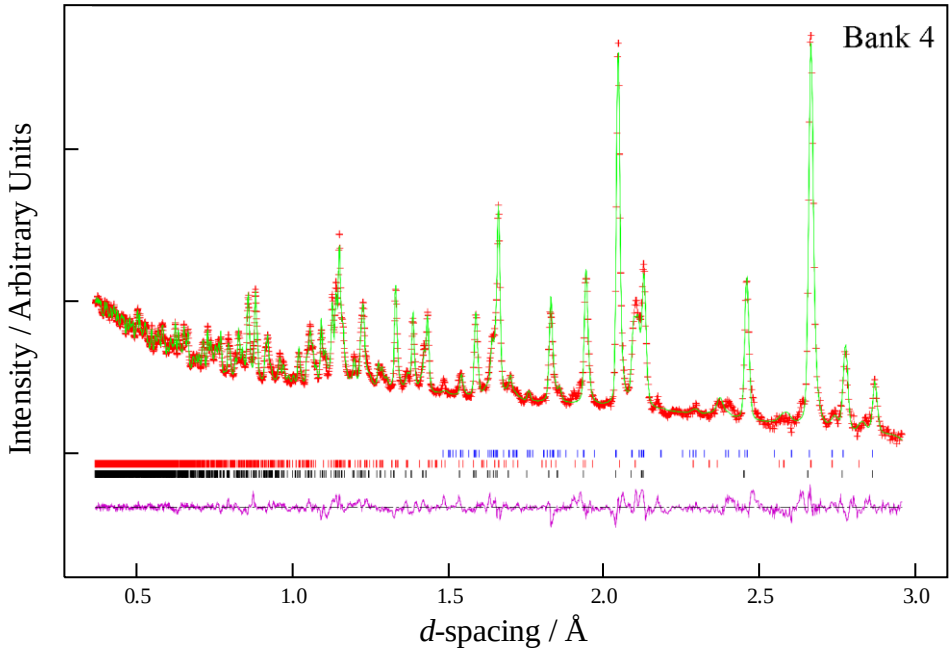
Bank 4
Intensity / Arbitrary Units
0.5
1.0
1.5
2.0
2.5
3.0
d-spacing / Å

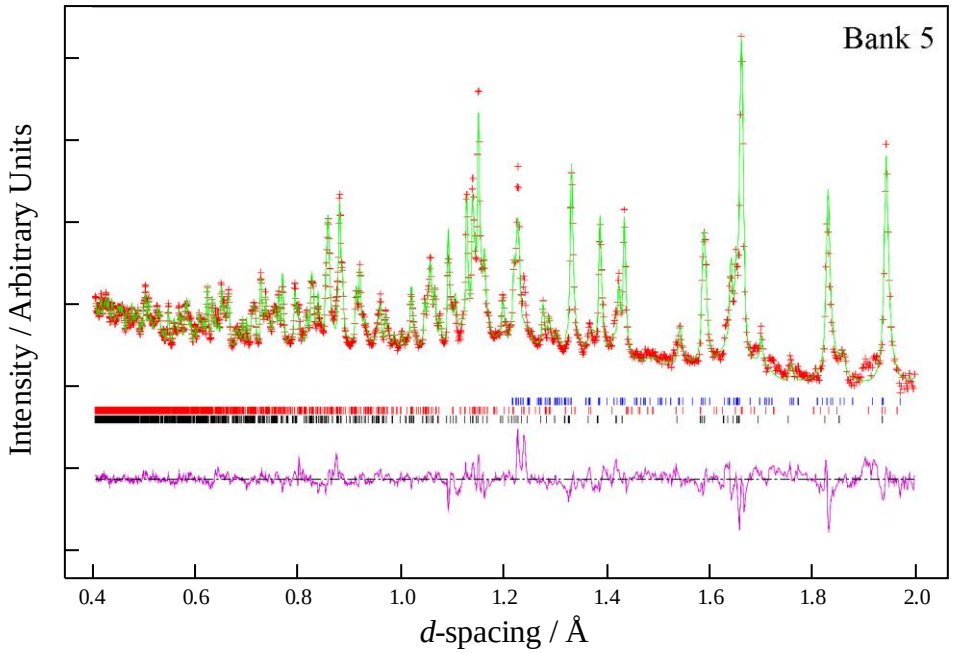

Figure 7.4: Observed, calculated, and difference plots for refinement of the structural model of Sr_2VO_3H at 4 K against neutron powder diffraction data collected using the POLARIS instrument. Red tick marks correspond to a $Sr_3V_2O_5H_2$ impurity. Blue tick marks correspond to the magnetic model.

Atom	***x***	***y***	***z***	**Fractional Occupancy**	**U_{iso} / Å^2**
Sr(1)	0	0	0.3518(1)	1	0.001(1)
V(1)	0	0	0	1	0.002
O(1)	0	0	0.1576(1)	1	0.002(1)
O(2)	1/2	0	0	1	0.002(1)
H(1)	0	1/2	0	1	0.025(1)
Sr_2VO_3H: space group *Immm*; *a* = 3.8853(8) Å, *b* = 3.6599(7) Å, and *c* = 12.7719(25) Å; cell volume = 181.61(10) Å^3; weight fraction = 73.4(4)%					
$Sr_3V_2O_5H_2$: space group *Immm*; *a* = 3.8959(11) Å, *b* = 3.6744(10) Å, and *c* = 20.5803(61) Å; cell volume = 294.61(19) Å^3; weight fraction = 26.6(4)%					
Magnetic model					
Atom	***x***	***y***	***z***	**Fractional Occupancy**	***Mz* / μ_B**
V(1)	0	0	0	1	1.45(7)
V(2)	1/2	1/2	0	1	-1.45(7)
V(3)	1/2	0	1/2	1	1.45(7)
V(4)	0	1/2	1/2	1	-1.45(7)
Space group *P*1 *a* = 5.345(1) Å, *b* = 5.345(1) Å, *c* = 12.778(1) Å, γ = 86.65(1)					
χ^2 = 3.287; wRp = 1.13%; Rp = 1.34%					

Table 7.2: Refined structural and magnetic parameters from Sr_2VO_3H at 4 K.

Appendix 7.5 $Sr_3V_2O_5H_2$ 4 K Neutron Data

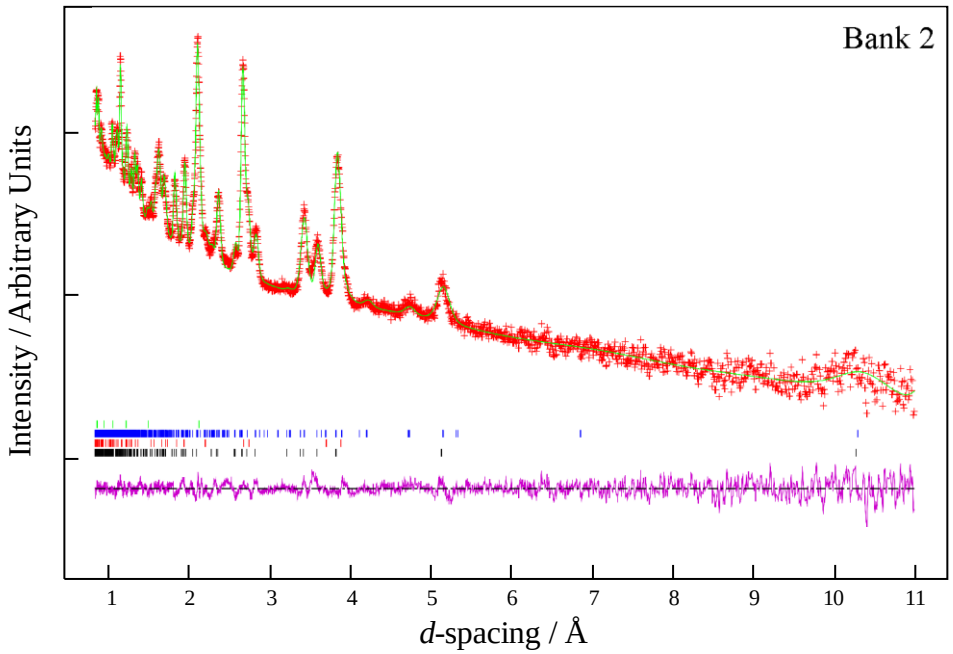

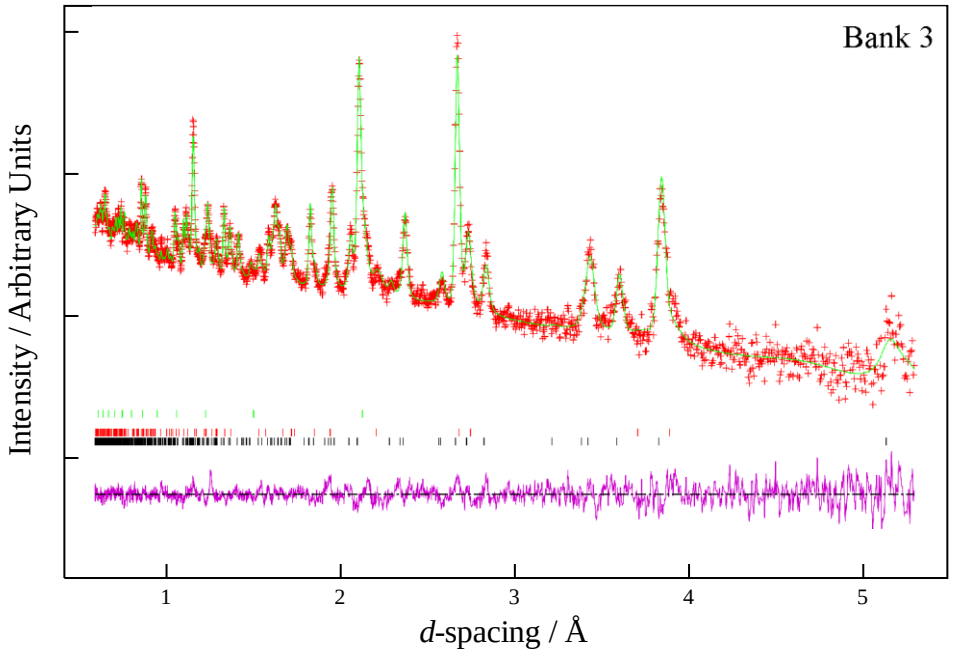

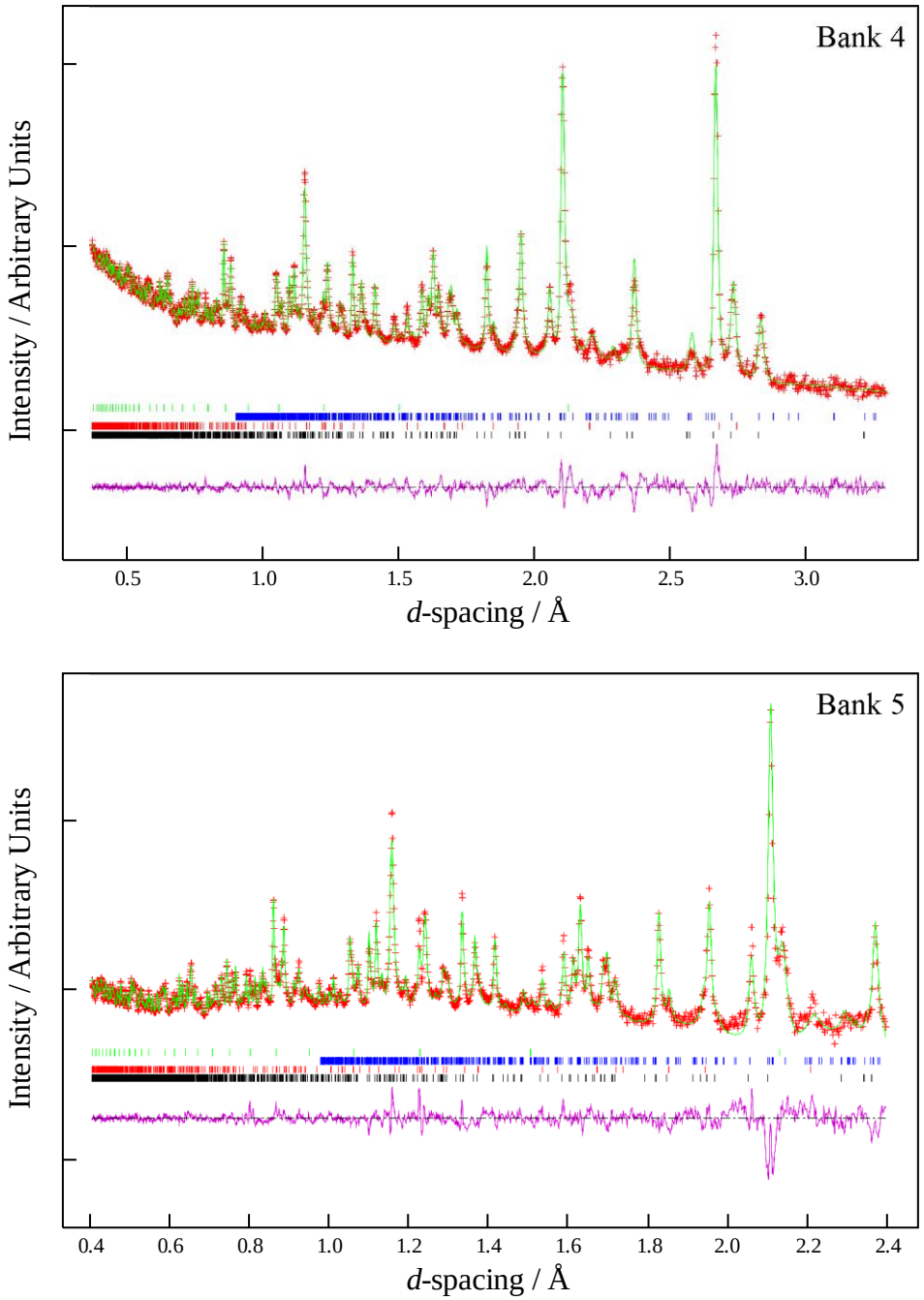

Figure 7.5: Observed, calculated, and difference plots for refinement of the structural model of $Sr_3V_2O_3H$ at 4 K against neutron powder diffraction data collected using the POLARIS instrument. Red tick marks correspond to a $SrVO_2H$ impurity. Blue tick marks correspond to the magnetic model. Green tick marks correspond to contributions from the vanadium sample holder.

Atom	***x***	***y***	***z***	**Fractional Occupancy**	**U_{iso} / Å^2**
Sr(1)	0	0	1/2	1	0.001(1)
Sr(2)	0	0	0.3127(1)	1	0.001(1)
V(1)	0	0	0.0938(15)	1	0.002
O(1)	0	0	0	1	0.002(1)
O(2)	0	0	0.1927(1)	1	0.002(1)
O(3)	1/2	0	0.0953(1)	1	0.002(1)
H(1)	0	1/2	0.0973(2)	1	0.02(1)
$Sr_3V_2O_5H_2$: space group *Immm*; *a* = 3.9115(6) Å, *b* = 3.6585(6) Å, and *c* = 20.6108(36) Å; cell volume = 294.95(15) Å^3; weight fraction = 85.5(3)%					
$SrVO_2H$: space group *P*4/*mmm*; *a* = 3.9043(17) Å and *c* = 3.7205(28) Å; cell volume = 56.71(6) Å^3; weight fraction = 14.5(3)%					
Magnetic model					
Atom	***x***	***y***	***z***	***Mx* / μ_B**	***My* / μ_B**	**$\lvert M\rvert$ / μ_B**
V(1)	0	0	0.0938	0.96(14)	-0.96(14)	1.35(20)
V(2)	0	0	-0.0938	-0.96(14)	0.96(14)	1.35(20)
V(3)	1/2	1/2	0.0938	-0.96(14)	0.96(14)	1.35(20)
V(4)	1/2	1/2	-0.0938	0.96(14)	-0.96(14)	1.35(20)
V(5)	1/2	0	0.5938	0.96(14)	-0.96(14)	1.35(20)
V(6)	0	1/2	0.5938	-0.96(14)	0.96(14)	1.35(20)
V(7)	1/2	0	-0.5938	-0.96(14)	0.96(14)	1.35(20)
V(8)	0	1/2	-0.5938	0.96(14)	-0.96(14)	1.35(20)
Space group *P*1 *a* = 5.366(1) Å, *b* = 5.366(1) Å, *c* = 20.652(1) Å, γ = 86.19(1)						
χ^2 = 2.168; wRp = 1.01%; Rp = 1.39%						

Table 7.3: Refined structural and magnetic parameters from $Sr_3V_2O_5H_2$ at 4 K.